

General Disclaimer

One or more of the Following Statements may affect this Document

- This document has been reproduced from the best copy furnished by the organizational source. It is being released in the interest of making available as much information as possible.
- This document may contain data, which exceeds the sheet parameters. It was furnished in this condition by the organizational source and is the best copy available.
- This document may contain tone-on-tone or color graphs, charts and/or pictures, which have been reproduced in black and white.
- This document is paginated as submitted by the original source.
- Portions of this document are not fully legible due to the historical nature of some of the material. However, it is the best reproduction available from the original submission.

"Made available under NASA sponsorship
in the interest of early and wide dis-
semination of Earth Resources Survey
Program information and without liability
for any use made thereof."

^{SEP}
E82-10398

CR-169187

Heat Capacity Mapping Mission

Investigation No. 25 (Tellus Project)

Principal Investigator:

Sergio Galli de Paratesi

FINAL REPORT

to

National Aeronautics and Space Administration

Goddard Space Flight Center

Preparation and editing

Sergio Galli de Paratesi

Peter Reiniger

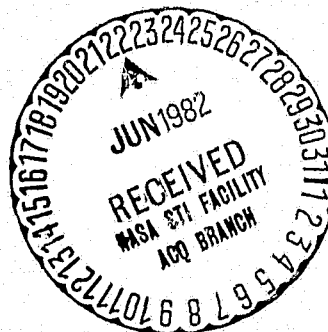
(E82-10398) HEAT CAPACITY MAPPING MISSION
INVESTIGATION NO. 25 (TELLUS PROJECT) Final
Report (Joint Research Centre of the
European) 249 p HC A11/MF A01

CSCL 08B

N82-32820

G3/43

Unclas
C0398



Commission of the European Communities
JOINT RESEARCH CENTRE
Ispra Establishment

1982

Heat Capacity Mapping Mission

Investigation No. 25 (Tellus Project)

Principal Investigator:

Sergio Galli de Paratesi

FINAL REPORT

to

National Aeronautics and Space Administration

Goddard Space Flight Center

Preparation and editing

Sergio Galli de Paratesi

Peter Reiniger

Original photography may be purchased
from EROS Data Center
Sioux Falls, SD 57198

RECEIVED

JUN 18, 1982

SIS/902.6

HCM-025

Type III Final



Commission of the European Communities
JOINT RESEARCH CENTRE
Ispra Establishment

1982

Acknowledgements

The present report is also the result of the efforts and cooperation of a great number of people who do not figure in the list of co-investigators. One cannot give a complete enumeration, but in naming a few we would like to tell them how much we appreciated their help, contribution or encouragement.

John G. Price, HCMM Project Scientist at NASA's Goddard Space Flight Centre, Greenbelt, proved to be the animator of the project and provided technical guidance and a stimulating exchange of ideas, as well as the «WINDOW» programme for atmospheric corrections.

Locke Stuart, HCMM Project Manager, and Richard Stonesifer, HCMM Technical Monitor, helped to iron out difficulties at Goddard and kept the project running smoothly.

R. Lasbleiz, Director of the Centre d'Etude de Météorologie Spatiale, Lannion, and his staff provided continuous assistance in acquiring HCMM data from ESA and answered questions promptly.

Jacques Gillot at the Directorate General for Agriculture, Brussels, supported TELLUS research action from the beginning, when his critical faculty was a help to it. The Delegation of the European Communities at Washington, and in particular Luigi Massher, provided most valuable assistance in keeping contacts with NASA and dispatching HCMM data.

The Projects Directorate, Friedrich Geiss and George Fraysse together with the Division staffs at the Research Centre of the European Communities, Ispra, gave their full support to the TELLUS investigation. Heinz P. Weber did a great part of the administrative work at Ispra, helped by Ulisse Devisioni who has been an irreplaceable stand-by.

Finally, we would like to thank Coletta Brovelli for her active secretarial work and for typing and collating the reports to NASA and co-investigators.

Contents

Summary	IX
Introduction	1
I. Project Organization	3
JRC Assignments and Role	5
Co-Investigators and Test Sites	5
Objectives of the Investigation	8
II. Data Delivery, Distribution and Quality	9
Type and Origin of Data	9
NASA / GSFC Data	9
Data Transmission and Distribution	
Preliminary Test Data	
Standing Order Data	
1. Delay in receiving SO data	
2. Distribution Anomalies, Quality Data	
Retrospective Order Data	
ESA / EARTHNET Data Delivery	15
Quick Look Data	
Retrospective Order Data	
Priority Coverage	15
III. Activity Performed and Results Obtained	17
Part 1 - Evaporation and Soil Moisture	19
Chapter 1 - Development and Test of Algorithms	
Introduction	19
Methodology	20
Test of Combined Aerodynamic Energy-Balance Approach	21
Models of Water and Heat Flow in the Soil-Plant- Atmosphere Continuum	22
The TERGRA Model	22
1. Description	
2. Test of the TERGRA Model	
2.1 Grassland	
2.2 Structured crops-potatoes	
The TELL-US Model	25
1. Description	
2. Test of the TELL-US model	
Other Models	27
1. The TELOP model	
2. The SEAL model	
The Operational Evaluation of ET-Algorithms	28
Comparison of Methods Involving Surface Temperature and Classical Methods	

Taylor's Expansion of the Surface Energy-Balance Equation	
Regional ET Estimates from HCMM Data	
1. Satellite Imagery and maps	
2. Surface temperature	
3. Albedo	
Conclusion	36
Composition of Working Group II	36
 Chapter 2 - Field Operations, Data Acquisition and Analysis	 40
Flight Experiments	40
The Netherlands	40
1. Description	
2. Results and conclusions	
France	41
1. Description	
2. Results and conclusions	
United Kingdom	41
1. Description	
2. Results and conclusions	
2.1 TELL-US model application	
2.2 TERGRA model application	
2.3 Spectral reflectance	
Italy	43
1. Description	
2. Results and Conclusions	
Germany	47
1. Description	
2. Results and Conclusions	
Continuous field measurement campaigns	48
Italy	48
1. Description	
2. Results and Conclusions	
 Part 2 - Effects of Topography, Soils and Land-Use on Surface Temperature Distribution	 54
Chapter 1 - The Influence of Topographic Structures on Night-Time Surface Temperatures in the South of Germany	54
<i>A. Processing of HCMM-Satellite Thermal Images for Superposition with Other Satellite Imagery and Topographic and Thematic Maps</i>	54
Introduction	54
Objectives	54
The Area under Investigation	55
Data Base	55
Maps	
LANDSAT Image Sources	
Preparation of Auxillary Data (Map Digitalization)	59
Processing HCMM Thermal Imagery	61
"Rough" Rectification	
"Fine" Rectification	
Quantitative Results and Precision of the procedure	
The Construction of the Multichannel Scene	67

B. Investigation on the Thermal Conditions of Different Parts of the Landscape	72
Night-Time Surface Temperatures and Relief	72
Surface Temperatures and Forest Distribution	76
Surface Temperature and Land-Use	79
Critical Evaluation and Treatment of the Data	
Application of Multiple Linear Regression Analysis	
1. The contribution of the type of land-use to the variance of the surface temperatures	
2. Modification of surface temperature with changing land-use	
3. The detection of night-time cold air reservoirs and cold air streams on the deviations from regression	
4. Deviations in the central parts of the Upper Rhine Plain	
 Chapter 2 - Interpretation Results from HCMM Digital Radiance Recorded over Belgium	 101
A. Optical Comparison of Thermal Map-Like Printouts with Soil Association and Forest Maps	101
Purpose of the Work	101
Application of Computer Programs	101
Optical analysis of digital printouts	102
Results	103
B. Ground Temperatures of General Land-Use Classes as registered by the HCMM Satellite	115
Introduction	115
Application of Computer Programs	115
Procedure and Results	115
Remarks	117
C. Thermal Inertia Applications	117
Introduction	117
Method and Procedure	119
Results	119
Thermal Inertia	119
D. Summary of Significant Results	120
 Chapter 3 - HCMM Potentialities for the Deduction of Physiographic Lineaments of the Po' Valley in Northern Italy	 122
Introduction. Basic Approach	122
Zone Investigated. HCMM Imagery and Maps Used	122
Method and Activity Performed	127
Instrumentation	
Analysis support of methodological process	
Superposition - Interpretation procedures	
Results	134
Classification of identified structures and probabilities of correlation with actual physiographic lineaments	
Discussion of results of HCMM Imageries interpretation	
1. DAY-VIS image (3 June 1978, 1.30 p.m.)	
2. DAY-IR image (3 June 1978, 1.30 p.m.)	
3. NIGHT-IR image (3 June 1978, 2.30 p.m.)	

Chapter 4 - Remotely Sensed Thermal Data for the Localization of Frost-prone Areas and the Evaluation and Monitoring of Low Altitude Breezes	137
--	-----

<i>A. Wind-Induced Microclimatic Differences Detected from Thermal Scanner Data</i>	137
---	-----

Introduction	137
--------------	-----

Interpretation of MSS Aircraft Data	137
-------------------------------------	-----

City of Freiburg

Rhine Valley

Conclusions	142
-------------	-----

<i>B. Thermal Imagery as a Tool to Delimit Vineyard Sites Liable to Cold-Air Damage</i>	147
---	-----

Introduction	147
--------------	-----

Methods and Data Used	147
-----------------------	-----

Delimitation of Cold Air Influence	148
------------------------------------	-----

Subregional scale. Entire Kaiserstuhl, ca. 100 km², 180-550 m a.s.l.

Local scale. The vineyards of a single Kaiserstuhl village, ca. 1 km²

Stagnant cold air on a single vine terrace, ca. 0,01 km²

Conclusions	154
-------------	-----

Chapter 5 - Geographic Measurements on METEOSAT and HCMM Imagery Recorded over Northern Africa	155
---	-----

Introduction	155
--------------	-----

Method

Quantimet 720 Image analyser

Procedure

Results	158
---------	-----

Conclusions	161
-------------	-----

Part 3 - Anthropogenic Heat Release	163
-------------------------------------	-----

Surface Temperature Distribution for the City of Freiburg	163
---	-----

Urban Agglomerations and Cold Air Accumulations and Stream in Germany	163
--	-----

Surface temperatures and settlements

Industrial complexes

Cold air reservoirs and cold air streams

Urban Heat Islands and Thermal Effluents in Belgium	167
---	-----

The city of Brussels

Schelde-river and Poel's nuclear plant

Part 4 - HCMM Satellite Data Calibration and Atmospheric Corrections	177
---	-----

Introduction	177
--------------	-----

Atmospheric Corrections	178
-------------------------	-----

The RADTRA model

The linear model

Data Calibration

Thermal Infrared data

1. Pine forest and fog surface
2. Grass-airfields
3. Lac Leman
4. Steinhuder Meer
5. Crau-grassland
6. Land and water surfaces. The Netherlands
7. Adriatic Sea

Comparisons with Thermal Data from Other Satellites	189
Conclusions	189

Part 5 - Development and Application of Auxilliary Methods and Techniques **193**

Chapter 1 - Usage of Filtering Techniques for Scaling-up Simulation **193**

Introduction	193
<i>Scale Effect: Theoretical Model</i>	193
Possible reduction methods	
Discrete image formation process	
Determination of scale-change function	
<i>Scale Effect: Operative Approach</i>	199
Determination of the scale change filter	
Comparison Techniques between True and Simulated Images	204
Application Example	205
Conclusions	216

Chapter 2 - An Active Method for Measuring Thermal Infrared Effective Emissivities. Implications and Perspective for Remote Sensing **218**

Introduction	218
Radiometry for Heterogeneous Media	218
Statement of the problem	
Effective parameters	
A Method to Measure Effective Emissivities	220
Principle of the method	
Advantages and disadvantages	
A simple Realization of the Required Instrumentation	
Implications and Perspectives for Remote Sensing Applications	222

Chapter 3 - Data Processing Methods **225**

<i>A. Digitizing of Grey Levels on Auxilliary Maps</i>	225
Introduction	225
Separation of Grey Levels for a Relief Map	225
Correction of Magnetic Effects in Map of build-up Areas	228

B. Geometric Rectification of HCMM Image and Auxiliary Maps	228
Methodology Adopted	228
C. Registration of Night Thermal Data over Day Thermal and Visible Data	229
Introduction	229
The Method Used	229
The Results Obtained	230
 IV. Conclusions	 231
List of TELLUS Newsletter	
List of Abbreviations	

Executive Summary

Motivation and Main Goals

In the period 1977 - 1981, seven countries of the European Community carried out a joint investigation into the applicability of air-and-space remotely sensed thermal data to some typical European zones of agricultural, hydrological and environmental interest. This activity was sponsored by various Directorates-General of the European Communities and was designed to clarify whether thermal satellite data, together with aircraft data, could present some advantages over - and possibly implement - conventional technical methods for providing the European Communities with the desired sectorial information. One such pilot experiment (TELLUS Project) was set up as a collaboration between several European institutes and organizations under the leadership of the Joint Research Centre of Ispra. It dealt with the use of the (0.5 - 1.1 μm)-day and the (10.5 - 12.5 μm)-day and/or night imagery from NASA's Heat Capacity Mapping Mission (HCMM).

TELLUS' main goals were :

- a) to ascertain whether remote sensing can contribute to synoptical evaluation of evapotranspiration and moisture in agricultural soils, and to what extent;
- b) to evaluate the influence of topography, soils, land-use and meteorology on surface temperature distribution
- c) to investigate anthropogenic heat release from space.

Co-investigators' research was developed over a broad range of significant test-areas, extending from e.g. semi-arid lands in Southern Italy to polders in the Netherlands, vine-growing hills in the Rhine Valley to grasslands in Buckinghamshire.

Research and Applications

Evapotranspiration and Soil Moisture

Objectives

1. In the interest of hydrology, climatology and agronomy, developing a mathematical modelling technique, whose parameters are obtained both from remote sensing and from conventional measurements, for the synoptical evaluation of evapotranspiration (ET) and soil moisture.
2. Contribution to a deeper understanding of the processes relating evapotranspiration (ET) and soil moisture to other meteorological and ground parameters.
3. Providing, throughout the systematic approach adopted in 2., a scientific basis for simple statistical (i.e. multivariate regression analysis) or empirical correlations.
4. Using HCMM thermal infrared and albedo data with the algorithms developed in 1. and 3. for the estimation of evapotranspiration (ET) on a mesoscale, filling in this way a gap which exists between local and continental ET estimation.

Basic Approach

The methodological approach to the estimate of ET is based on the energy balance at the soil surface. The R.S. platform provides surface temperature and albedo values which are used in calculating the sensitive heat flux and net radiation flux in this balance. The other conventional parameters are measured at ground level. Using a known relation between thermal inertia and soil moisture, the volumetric moisture content in the upper soil layer can be determined.

Field testing of models is performed through :

- a. Structural tests: flight experiments involving both MSS airborne and

- ground measurements with a duration of a few days;
- b. **Validation tests:** continuous field measurements lasting a number of weeks or even some months. Remote sensing data are obtained by means of field radiometers.

Main results and significance

A number of models have been developed for bare soils and soil covered by vegetation which permit the integration of instantaneous evapotranspiration (ET) obtained from remotely sensed surface temperature T, to yield cumulative daily ET. These models are TERGRA and SEAL which use the daily maximum surface temperature and the TELL-US model which uses both the daily maximum and minimum temperatures T. For the evaluation of daily ET the use of the minimum night temperature has no advantage but is rather a complicating factor. The knowledge of the daily temperature amplitude is however useful for the determination of the surface cover. From the thermal inertia the moisture content in the upper soil layer can be obtained although there is a tendency to underestimate it. Operational tests of the surface temperature method took place in the Netherlands, the United Kingdom, France, Italy and in Germany. On the top of this activity the Joint Flight Experiment (JFE) campaigns have taken place with the participation of many national field-teams; ground measurements and multispectral scanner flights were carried out on patches of homogeneous nature with regard to crop and soil. Evapotranspiration and soil moisture maps have been obtained.

In an operational test using HCM data on an irrigated and dry grassland area in Southern France the method agreed over a roughly 100-day period with ET measured by the Bowen ratio method to within $\pm 15\%$. The critical point is the evaluation of the "roughness" parameter which has to be defined for each zone.

A simplified approach proposed by Jackson et al.: $ET = R_n \cdot S + A \cdot B(T_n - T_a)$ was also tested. In spite of a pronounced dispersion ($r = 0.67$) it allows us to estimate ET within a ± 1.5 mm day precision. For long-term integration (100 days) the equation fits reference values of the Bowen ratio method by $\pm 12\%$ which may be considered quite satisfactory. However the empirical constants A and B obtained in this experiment are quite different from the original values proposed by the authors. Further experiments covering a wide range of natural surfaces would be necessary to establish whether a unique set of empirical constant could be used in practice.

Effects of topography, soils, land-use and meteorology on surface temperature distribution

Objectives

1. Correlation of the geographic reality of the various natural surfaces having a different physical constitution (forest, settling areas, farmland, etc.) with daily surface temperature T patterns;
2. Influence of daily T variations (resp. night/day temperature differences ΔT) on the correlation mentioned in 1.;
3. Influence of altitude, topography and meteorologic conditions on the temperature T of surface elements of the same kind and constitution;
4. Influence of static physiographic aspects (geology, hydrology, pedology) on surface temperature T patterns in relation to dynamic aspects (vegetation cover, land-use, etc.);
5. Impact of subsoil characteristics on apparent thermal inertia ATI through the variations of the characteristics of heat transfer (porosity, mineral composition, moisture content, etc.) and of soil coverage;
6. Correlation of surface T distribution with frost-prone areas and with low altitude breezes;
7. Correlation of distribution of surface albedo a with transitory phenomena such as flooding and grass fires.

Basic Approach and Main Results

A. Satellite data

The approach adopted was developed along three main parallel lines,

corresponding to co-investigators' backgrounds, trends and means available.

1. Analog deductive interpretation of HCMM transparencies.

Visible and Infrared imagery was superimposed upon "truth" physical maps and LANDSAT false-colour composites using an analog-anamorphic stereo-plotter.

Interpretation was based on the reciprocal inference between buried structures (HCMM) and surface patterns (LANDSAT and conventional maps). This approach was adopted for the deduction of the physiographic outlines of large areas (some hundreds of kilometers).

Procedure steps: a) finding control points for further cartographic approach; b) grey tones discrimination: boundaries between homogeneous tones are traced out (structure and texture). Without delimiting isophenic zones (i.e. creating genuine landscape families) one respects the intrinsic realities which have been recognized on the scene as much as possible. Oceanographic and urban boundaries are purposely considered separately; c) cartographic classification and deductive interpretation phase by stereo-plotter. Information from stereo-plotter and colour density slicing leads to the final interpretation.

Results and significance

The method was applied to a large hydrographic basin. It revealed many physiographic details. Thematic maps of a hydrological character have been obtained. The type of legend introduced illustrating the logical passage between geomorphological, vegetational and anthropic aspects of the identified surfaces and the buried hydrological aspects deduced is interesting. The role of the thermal inertia properties of materials appears obvious for interpretation and classification in the hydrological field, both structural and applied. It has been confirmed that the Day-IR imagery contribution is quite significant for the characterization of lithological and hydrological structure, but it gives only a slight contribution to the definition of humid areas. The Night-IR image appears to be a very significant contribution to the characterization of highly surface saturated zones. It is however less important for a structural recomposition (relief, morphology).

2. Combination of digital and optical interpretation

a) The approach consisted basically in an analog interpretation of computer classification print-outs after optical superposition with reference thematic maps and LANDSAT multispectral colour composites (band 5 and 7). It proved useful for a detailed analysis of HCMM data to delineate areas as distinguishable from surface temperature patterns which could correspond to soils and/or soil surface features. The computer analysis was performed using some routines of the ORSER software package of PSU / /. Some of the programs were rearranged and/or adapted by the TELLUS co-investigators.

Procedure steps : a) preparation of computer printouts after transcription of original HCMM CCTs into the ORSER format. Programs used: brightness classification, arithmetic combination of different channels, map symbols assignment to categories, according to specified class limits, statistical vectors calculation, etc.; b) optical superposition of computer printouts on different types of maps (topographic forest, roads, soils, etc.) and LANDSAT imagery with the aid of a Zoom Transfer Scope. Some major land-use classes were used for HCMM pixel identification and positioning; c) analog interpretation; d) calculation of apparent thermal inertia ATI from HCMM night, day and albedo data sets using the algorithm proposed by NASA, Goddard / /. Satellite data averaged for the considered segment areas.

b) A mixed analog-digital interpretation approach was also adopted for the intercomparison of mapping of albedo data of HCMM (0.5 - 1.1 μm , scale 1/4x10⁴) and METEOSAT (0.4 - 1.1 μm , scale 1/16x10⁴), which aimed to evaluate how small-scale synoptic imagery could assist in the monitoring of transitory phenomena on the ground (flooding, vegetation fires, etc.).

An electronic image analyser was used (epidiascope, vidicon camera and system control unit with variable frame-and-scale module).

Procedure steps: a) the limits of the considered soil units are drawn from a

geographic map on transparent paper; b) the areas to be evaluated are outlined on the video display with the aid of the electronic pen; c) patches which appear as homogeneous in grey tone on the satellite image for homogeneous patterns of such patches) are manually depicted after being previously identified on the imagery drawn from the geographic map; d) the scale of imagery is calculated by comparing distances between two reference points (e.g. coast-lines) both on the satellite image and on the soil map; e) correspondence between areas drawn on the satellite image and that on the mapped soil unit is evaluated; f) finally, calculation of the area extent from satellite digital data is obtained using a classification digital routine.

Results and significance

Using this method, on the Belgian area the delineation of large (regional scale) and smaller areas as distinguishable from temperature patterns and which correspond to soil and/or soil surface features was successful. Forests could generally be distinguished by their relatively high radiant temperature. However conifers and deciduous forest type or difference between species could not yet be detected. Coast lines, dunes, urban areas and small forests are well delineated.

Its results confirmed that special information from other satellite (such as LANDSAT) may contain recent information on land surface features or on land-use which may also be discernable through thermal properties. Spatial limits of some temperature classes do correspond fairly well with soil unit boundaries. Wetter polder areas may easily be distinguished: humid soil is generally cooler than dry soil (evaporation of absorbed water also lowers temperature). High moisture content of soil increases its heat capacity and a lower temperature will be sensed.

As for training areas it is concluded that they must meet the following requirements: they must be small but sufficiently large, easy to locate and their radiance must be relatively homogeneous over the entire surface. Because of the low pixel resolution of HCMM as well as to the high degree of parcelling over the areas studied, some spectral inhomogeneity may be expected for the selected training areas.

It has been confirmed that thermal infrared radiances and radiant temperatures derived from them largely depend on sun illumination conditions preceding the satellite overpass. These will not only vary during the daily cycle but also with season, meteorological conditions, etc.

The ATI for major land-use classes were calculated. As was expected, open water, forests, urban land, grassland and bare soil are easily distinguishable. Even forest species are found to be distinguishable (*Fagus*, *Quercus*, *Picea*, *Pinus*, etc.).

Recognition and quantification of flooded areas has been experimented with success in Africa (Tunisia) using HCMM transparencies. Measurements have been compared with corresponding METEOSAT imagery.

3. Analog Interpretation on high precision merged-multichannel scenes

A purely digital superposition method was adopted. HCMM scenes were geometrically rectified and superimposed pixel by pixel on other digital information, e.g. relief waterways, forest, population distribution and land-use. Interpretation of thermal conditions of the various parts of the landscape was made on such merged-multichannel scenes (mean superposition error of 1 pixel).

Procedure steps: a) choosing an appropriate auxiliary data base: map-type binary distribution of land-use categories and digital contour representation of land forms, together with LANDSAT image classification data; b) choosing an appropriate scale based on the correspondence between the smallest possible size of the map-picture element and the HCMM pixel; c) geometric rectification of HCMM thermal scene by the interpolation method ("rough" control points with respect to water-networks and forest distribution and "fine" rectification referring to the pre-assigned geographic coordinate reference system; d) preparing auxiliary data structure: densitometric digitization of maps with correction of distortion due to vignetting effects and fitting into the common geographic coordinate

system together with the LANDSAT image data; e) construction of the multi-channel scene using a special merged module; f) evaluation of some segments of the merged-multichannel scene in some possible different combinations. The successive examination of surface temperature T pattern referred to relief, land-use and build-up distributions is typical; g) applying multiple linear regression analysis to find contributions of larger classes to give an explanation of distribution of surface temperature T. For a correct interpretation of deviations from regression the entire area under investigation is divided into squares of 5x5 km.

Results and significance

It was found that this kind of methodological procedure is the most suited to the investigation of the influence of the thin structure of topography and land-use on surface temperature patterns. It was applied with success to HCMM night scenes of the Rhine Valley and surrounding highlands in Germany. LANDSAT data sets of eight classes were used (two-density urban build-up, water, crops and forests). Excellent rectification precision has been obtained on the HCMM image (roughly 1 pixel). The application proved to be very satisfactory with regard to the correlation between surface temperature and the water network as well as to the relationship between surface temperatures and the settlement pattern. However it should be noted that the resolution of HCMM is not sufficient to determine the boundaries of various geographic units or to establish the exact limits of topographic structures by means of the HCMM imagery. Nevertheless, it is essential to state that the thermal pattern of an HCMM image can be related to and explained by topographical structure.

A well-known rule of topoclimatology is the thermal tripartition of hilly or mountainous areas at night: cold elevations, warm slopes and cold valley bottoms. The HCMM data have allowed us to test the applicability of this law to the behaviour of surface temperatures in various spatial dimensions. In general, only the difference between cold valleys and lowlands on the one hand and warm slopes and mountain tops on the other, could be verified. Valleys tend to be considerably colder than slopes covered by comparable vegetation. The water network which follows the valley systems is all but congruent with the distribution pattern of particularly cold surfaces. The elevated areas proved to be as warm as the slopes, in some cases even noticeably warmer. Cold elevated areas can be found only in places where one of the following three conditions is met: grassland and cultivated fields in altitude above forested slopes, extended plateaux and extended surfaces in areas with small differences in elevation.

As far as correlation between surface temperatures and forest distribution is concerned, it is generally agreed that forests do not cool as rapidly at night as do unforested areas and that they, consequently, produce higher surface temperatures at night than adjoining grassland or cultivated fields. Therefore, it is surprising that a much more complex picture resulted from the examination of HCMM scenes. Some exhaustive explanations have been given for the distinctive behaviour of forested surfaces.

The HCMM surface temperature values for all areas below an altitude of 200 m were extracted for the whole zone under investigation, with the aid of the relief map. For this area, the HCMM values and the parts of the various land-use classes were linked to each other by a multiple linear regression. The following points were investigated in greater detail: which part of the surface temperature distribution may be explained by the land-use; in which way the surface temperature would change due to a 20% change in the land-use and which other influences on the surface temperature are included in the deviations from the regression.

B. Aircraft (8-14 μ m) data

Two parallel approach lines were developed corresponding to the sub-objectives of point 6:

1. Determination of vineyard sites liable to cold-air damage.

Data recorded at different altitudes in the hours before sunrise (clear sky) are submitted to a multi-step digital processing and interpretation procedure: a) image enhancement for a qualitative interpretation; b) false-colour equidensities of 1°C; c) transfer to a topographic and vegetation

map for delimitation of stagnant cold-air influence on the sub-regional scale; d) digital enlargement of lower-altitude flight images for delimitation on a local scale (single hill or slope and even single vine terrace); d) ground-check from mobile measurements of air temperature.

2. Wind induced microclimatic difference detection.

Data recorded at different altitudes (three times a day) are processed digitally: a) by means of digital low-pass filters the temperature ranges are split into grey tones corresponding to 1°C each; b) interpretation is made by comparison of thermal data sets with meteorological data (wind speed and wind direction, air temperature) from some local weather stations and taking into account the structure of the surface cover.

Results and significance

The usefulness of airborne remotely sensed data for the localization of frost prone areas and the monitoring of low altitude breezes has been demonstrated. The interpretation of aircraft thermal images can lead to the detection of wind microclimatic differences. Ground reference data prove to be essential for a correct interpretation.

Anthropogenic Heat Release

Objectives

1. Demonstration of the role of surface temperature T and its daily amplitude variation ΔT , measured from HCMM, as time-space information useful in evolving a thermal description of various man-induced heat sources.
2. Confirmation of the impact of anthropogenic heat release on the thermal behaviour of various physiotores and environmental units.
3. Preliminary indications on the introduction of T and ΔT as parameters in heat budget arguments.

Basic Approach

The approach adopted involved an analog-deductive interpretation both of digital satellite print-outs and auxiliary maps and of high precision merged-multichannel scenes.

HCMM : Description of day/night evolution of the thermal behaviour of urban settlements, industrial complexes and cold-air accumulations (and related outflows) was made in comparison with some corresponding detailed topographical maps: Digital temperature slicing at the limit of the satellite temperature resolution (0.4 K) is needed both for detailed thermal depiction of cities or for identification of small urban areas.

Procedure steps for description of thermal pollution of large water bodies:

- a. thermal infrared counting of pixels for all the considered area (ORSER programs);
- b. The pixel matrix so constructed is superimposed upon a local map for localization of thermal anomalies.

HCMM and aircraft: Check of spatial temperature distribution of urban heat islands by comparison with high-resolution thermal representation obtained by aircraft flights. This procedure involves geometric corrections and smoothing of satellite pixel edges.

Main results and significance

The spatial radiometric resolution of HCMM proved sufficient for the detection of anthropogenic heat release both at meso and local scale in assessing dynamic heat budgets. In this respect the different response of heat sources on consecutive day-and-night IR scenes proves to be very useful. During night, cities and even small urban areas (1 or 2 pixels) can be distinguished due to their relatively high radiant response. Urban agglomerations (e.g. cities of Brussels and Freiburg) can be marked out individually. It was to be expected that heat islands from large cities would be depicted in the HCMM scenes. However it became obvious that much smaller settlements can evoke a signal, under favourable circumstances, down to a size of 2000 inhabitants. Prerequisites for this phenomenon are a densely built-up village centre and placement in a horizontal, unforested environment. Otherwise the weak signal emitted by the settlement would be masked by other effects on the thermal pattern. The situation is less equivocal when we consider larger villages and

smaller towns with an average size of approximately 10,000 inhabitants. The core area of every larger city with tens of thousands of inhabitants is registered as a heat island with temperatures a few degrees higher than its surroundings. The area of higher surface temperature extends beyond the urban build-up area to the surroundings because of the flow of warm air in the boundary layer. The suburban area is much warmer on the leeward than on the windward side of the cities. On comparing different industrial areas, it becomes apparent that different levels of energy consumption are identified on the thermal image.

HCMM imagery has given useful information for the detection of thermal pollution of large water bodies also. It has allowed the evaluation of the temperature difference (some K) between the water discharge point of a nuclear power plant (e.g. Schelde river) and the rest of the river. The high surface temperatures recorded over industrial areas, located on the right riverbank, as compared to the mean temperature of the polderland have also been evaluated.

HCMM Satellite Calibration and Atmospheric Corrections

Objectives

1. Correcting shifts in absolute level of the satellite measured surface temperature T due to atmospheric absorption;
2. Compensating "smoothing" of the actual spatial and temporal differences in surface temperature ΔT by atmospheric corrections for relative measurements, including thermal inertia.
3. Calibrating satellite measured surface temperature T after atmosphere correction.

Basic Approach

The atmospheric corrections were calculated in most cases using the WINDOW model which proposes a linear relationship between a radiometric temperature measured on the ground T_g and the temperature T , "seen" by the satellite. Radiosonde data from meteorological stations were used.

The calibration procedure consisted in comparing the satellite measured surface temperature T , with the ground measured surface temperature T_g , measured after atmospheric correction by the satellite.

Main results and significance

Forty five data points from five countries, covering a period of 34 days after launch of the satellite, to 761 days after launching, were provided for calibration. The radiometric surface temperatures ranged from -3°C to 53°C . The following conclusions could be drawn: 1) From 34 to 528 days after launching there seemed to be no long time trend in the calibration of the HCMR. 2) The onset of 5.5°C which had been introduced into the calibration equation of the HCMR after the validation study by NASA was not valid during the whole period investigated. The differences between $7-12^{\circ}\text{C}$ with temperatures measured by NOAA-5 and TIROS-N point in the same direction. 3) The linear regression of T_{sat} , the theoretically correct satellite temperature of T_{sat} , and the actual temperature given by the HCMR is represented by an equation whose intercept of 7.55 shows that the offset of 5.5°C should be abandoned. The low regression coefficient $R^2 = 0.64$ indicates that the relation is not linear or that either the ground or satellite measurements, or both, do not form homogeneous populations. This could point to sporadic changes in scanner performance. 4) The assumption that the calibration of the HCMR is not linear is statistically supported by the parabolic regression of T_{sat} on T_g with a regression coefficient $R^2 = 0.89$. 5) The hypothesis of sporadic changes in the calibration is not to be excluded, as 38 days after launching calibration results over a pine forest in Germany and over Lake Geneva agreed with those of NASA at White Sands. This was no longer the case 54 days after launching.

Introduction

The aim of the TELLUS Project was the development and presentation, on a European basis, of techniques using remotely sensed thermal data of earth resources.

This effort was centered around the Heat Capacity Mapping Mission (HCMM) of the National Aeronautics and Space Administration, Goddard Space Flight Center, Maryland (U.S.A.). The special feature of the HCMM satellite measuring the day-night temperature cycling of objects on the earth's surface made it attractive for hydrological, geological and environmental prospection.

The general objective of TELLUS was to investigate whether, and to what extent, such temperature cycling or diurnal temperature only can be related to evaporation and moisture in agricultural soils, to physiographic characters of land and to anthropogenic heat release.

These goals, while partially fulfilling a number of requests by some Directorates General, Brussels of the European Communities (EC) in matter of policy for agriculture and environment correspond also to the specific research objectives of the Co-Investigators.

PRECEDING PAGE BLANK NOT FILMED

I Project Organization

II HCMM Data Delivery, Distribution and Quality

I. Project Organization

PRECEDING PAGE BLANK NOT FILMED

JRC Assignments and Role

Starting in 1976, the Joint Research Centre of Ispra, Italy (JRC), was assigned to:

- . Developing an EC research action (TELLUS), aimed at learning how HCMM data, together with other aircraft and/or satellite data, present some advantages over - and possibly complement - conventional technical methods for providing the European Communities with the requested sectorial information. This action should be developed as a pilot experiment covering a significant range of typical applications.
- . Taking opportunity of TELLUS for contributing to Remote Sensing applied to land resources within the European scientific community through the coordination of diversified national competences and support facilities.

The Project was set up as a collaboration between several Institutes and Organizations of the EC's Member Countries under the leadership of the JRC.

JRC's role in TELLUS was divided into two distinct parts:

- 1) A coordination activity for the contribution

from the Co-investigators working on different topics and test sites. This included liaison activities with NASA and dispatching HCMM data from GSFC, Greenbelt and CMS Lannion of ESA/EARTHNET to Co-investigators.

- 2) An experimental activity, essential in itself, in the South of Italy (Test site No. 1) and organization and direct participation in the Joint Flight Experiment (JFE) campaigns on various test sites in Europe.

Co-Investigators and Test Sites

The Co-investigators were divided into six groups, i. e. :

EC General Directorates and JRC, Ispra
Establishment,
Be-Ne-Lux Institutes,
British Institutes,
French Institutes,
German Institutes,
Italian Institutes.

The names and abbreviations of the Organizations and Institutes who contributed to the TELLUS Investigation (HCM-025) are reported in Table I.1, together with the names of the Co-investigators.

TABLE 1.1: List of Organizations and Institutes Participating in the TELLUS Project (HCM-025)

Test-Site Coordinators (TSCs)	Co-Investigators (COIs)		
DIRECTORATES OF THE EUROPEAN COMMUNITIES			
		<ul style="list-style-type: none"> Directorate General for Agriculture, Brussels Directorate General for Research, Science and Education, Brussels Joint Research Centre, Ispra EC Delegation, Washington 	GD-VI DG-XII JRC DG-1/WD
NATIONAL ORGANIZATIONS AND INSTITUTES			
Feddes R.A.	D'Hoore J.M.	Belgium <ul style="list-style-type: none"> Fakulteit der Landbouwwetenschappen, Katholieke Universiteit, Leuven 	KUL/LBB
	Eckardt F.E.	Denmark <ul style="list-style-type: none"> Institutet for Okologisk Botanik, University of Copenhagen 	UK/OB
Gollot Ch.	Gollot Ch. Sarloy E. Seguin B. Perrier A. Becker F.	France <ul style="list-style-type: none"> Service de Télédetection, INRA Versailles Station d'Amélioration des Plantes, INRA Rennes Station de Bioclimatologie, INRA Montfavet Station de Bioclimatologie, INRA Versailles Groupe de Recherches en Télédetection Radiométrique, Université de Strasbourg 	INRA/ST INRA/SAP INRA/CRASE/SE INRA/SB ULP/GRTR
Gossinann H.	Gossmann H. Van der Ploeg R.	F.R. Germany <ul style="list-style-type: none"> Geographisches Institut der Universität Freiburg Institut für Bodenkunde und Waldernährung 	UF/GI UG/IBW
Callandro A.	Borriello L. Cavazza L. Milella A. Callandro A., Pacussi G. Maracchi G. Fosa F. Marcolongo B. Pietracaprina Lechi G.M. Tombesi L. Possini E.	Italy <ul style="list-style-type: none"> Centro Studi Applicazioni Tecnologiche Avanzate, Bari Istituto di Agronomia Generale e Coltivazioni Erbacee, Università di Bologna Istituto di Agronomia e Coltivazioni Arboree, Università di Sassari Istituto di Agronomia e Coltivazioni Erbacee, Università di Bari Istituto di Agronomia Generale e Coltivazioni Erbacee, Università di Firenze Istituto di Fisica, Università di Bari Istituto di Geologia Applicata, CNR Padova Istituto di Mineralogia e Geologia, Università di Sassari Istituto per la Geofisica della Litosfera, CNR Milano Istituto Sperimentale per la Nutrizione delle Piante, Roma Ufficio Centrale di Ecologia Agraria, Roma 	CSATA UBO/IAGCE USS/IACA UBA/IACE UFI/IAGCE UBA/IF IGA USS/IMG IGL ISNP UCEA
Feddes R.A.	Feddes R.A. Van Ulden A.P.	Netherlands <ul style="list-style-type: none"> Instituut voor Cultuurtechniek en Waterhuishouding, Wageningen Koninklijk Nederlands Meteorologisch Instituut, De Bilt 	ICW KNMI
McCulloch J.G.	Kirkby M.J. Savigear R.A.G. McCulloch J.G.	United Kingdom <ul style="list-style-type: none"> Department of Geography, University of Leeds Department of Geography, University of Reading Institute of Hydrology, Wallingford 	UL/DG UR/DG IHW

Geographic as well as technical considerations led to arranging the fourteen test sites (TS) into five groups as originally proposed by the Co-investigators. No particular test site was proposed by the JRC Ispra because its research staff were designated to working in collaboration with the Co-investigators on their national test sites. A Test Site Coordinator (TSC) was designated for each Test Site Group (TSG) in agreement with the Institutes involved.

The arrangement in groups of TELLUS test sites is reported in Table 1.2. Fig. 1.1 shows the distribution of the test sites proposed by Co-investigators within the overall test area

TABLE 1.2: TELLUS Test Sites, Arranged in Groups

Test Site Group	Test Sites	No.
ITALY	Puglia	1
	Sardinia	2
	Emilia	3
FRANCE	Bouches du Rhône	4
	Brittany	13
GERMANY	Rhine Valley A	5
	Rhine Valley B	6
	Northern Alps	7
	Northern Germany	14
UNITED KINGDOM	England A	8
	Wales	9
	England B	10
	England C	11
BENELUX	Belgium	12
	Netherlands	
	Luxemburg	

HEAT CAPACITY MAPPING MISSION (HCLMM) COVERAGE EUROPE DAY

ORIGINAL PAGE IS
OF POOR QUALITY



Fig. I.1: Spatial Distribution of TELLUS Test Sites within the Overall Test area "EUROPE".

"Europe" which was proposed by NASA for allotment of HCMM imagery.

Objectives of the Investigation

According to the interests of the EC's Commission and the proposals made by the national Institutes, three main thematic lines of investigation were singled out:

- 1) Evapotranspiration and moisture content in bare soils and in soils covered by vegetation

Motivation

Evapotranspiration and soil moisture are among the most important parameters in agriculture and in land management because of their obvious impact on cultivation choice, crop yield, planning of water supply for irrigation, etc. and on the occurrence of flooding, erosion, etc.

- 2) Effects of topography, soils and land-use on surface temperature distribution
- 3) Mesoscale distribution of anthropogenic heat release

Motivation

The possibility of registering the spatial distribution of surface temperatures, their daily amplitude variation and the so-called Apparent Thermal Inertia (ATI) derived from it is the basis for a variety of application studies ranging from the discrimination of landscape physiographic characters to the introduction of surface temperature as a parameter in heat budget deliberations.

Many of these research projects are difficult to realize in the European area due to the complexity, the different type of topography and the many overlapping factors which influence surface temperatures. But if TELLUS merely succeeded in evolving a description of the thermal behaviour of various physiotopes and environmental units on a regional scale and in representing this information spatially on maps, then this can be regarded as an important contribution to classic climatological and environmental research in the mesoscale.

ORIGINAL PAGE IS
OF POOR QUALITY

II. HCMM Data Delivery, Distribution and Quality

A Hubaux and E. Scheffer Joint Research Centre, Ispra, Italy

ORIGINAL PAGE IS
OF POOR QUALITY

Type and origin of data

HCMM data received by HCM-025 Investigation can be divided into three groups:

- 1) Preliminary Test (PT) data
- 2) Data as stipulated in the Provisions for Participation (1976), i. e. :
 - Standing Order (SO) data
 - Retrospective Order (RO) data
- 3) Data as agreed upon at Freiburg Meeting (1978) between NASA/GSFC, ESA/CMS Lannion and EC, JRC, i. e. :
 - Quick Look (QL) data.

Technical characteristics of PT, SO, RO and QL data are summarized in [1] and [2].

All data have been produced and sent by:

NASA/GSFC (data received by the Madrid Station), or
ESA/EARTHNET (data received by the CMS Lannion).

NASA / GSFC Data

Data Transmission and Distribution

Figure II.1 represents a flow chart of data transmission from GSFC Greenbelt to JRC Ispra, subsequent distribution to Co-investigators and JRC Research Sectors, and filing.

Travel time from GSFC Greenbelt to JRC Ispra, via EC Delegation in Washington, did not exceed 18 days, while dispatching to Co-investigators, via Test Site Coordinators, needed 14-40 days depending on various factors (e. g. efficiency of local mailing services).

Preliminary Test Data

After HCMM satellite launch on April 26, 1978, PT data were sent to European Investigators to familiarize them with SO data. PT data on Chesapeake Bay, USA, arrived at JRC Ispra in Autumn 1978 in the form of transparencies and tapes.

Some interpretation of PT transparencies was attempted by TELLUS Co-investigators. Studies were made using pre-existing LANDSAT imagery and conventional thematic maps as "ground truth" (GT).

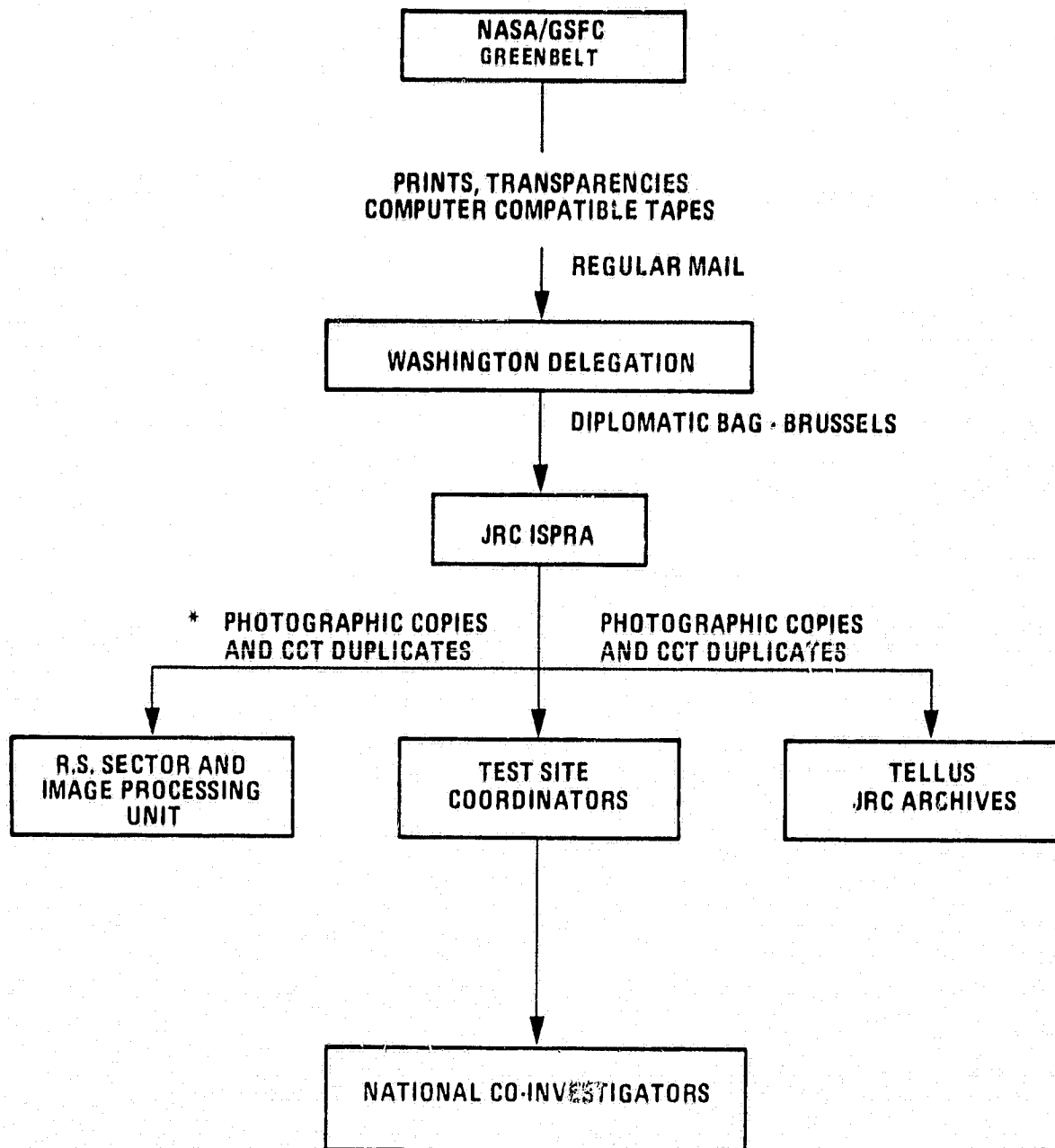
The quality of PT data was good regarding scanning, but densitometrically poor and of low contrast.

Standing Order Data

1. Delay in Receiving SO Data

The situation of SO data delivery to JRC can

ORIGINAL PAGE IS
OF POOR QUALITY



* On specific request

Fig. II.1: HCMM Data Distribution from NASA GSFC Greenbelt through to TELLUS Users.

be summarized as follows:

Jan. 1979 No SO data received yet at JRC, Ispra.

Febr. 1979 A Priority Processing List (PPL) was agreed upon between GSFC and JRC, in order to put an end to such a delay situation. 81 sets of consecutive night-day (N/D) scenes were selected by TELLUS Co-investigators.

March 1979 SO data started arriving at JRC Ispra.

Sept. 1979 The 20% response to PPL by GSFC consisted of night (N) or day (D) scenes, not systematically consecutive. Only one consecutive N/D set was delivered. Some 50 extra scenes not specified in the PPL, were received too.

March 1980 56% of PPL delivered (20 D+N sets). This situation seems to be partially explained by the following reasons:

- . random cutting of orbits (we happened to receive northern part of orbit when asking for southern part and vice versa);
- . some tracks had two N orbits - East and West - or two D orbits overflying HCM-025 test sites. When asking for the first one, the second one was sometimes delivered instead.

Sept. 1980 End of SO distribution for a total of 368 orbits.

Table II.1 shows the actual distribution of SO data to Co-investigators. A comparison between the situation of the response to the PPL and the actual RO distribution per country may offer some interesting indications (Tables II.2 and II.3).

2. Distribution Anomalies. Quality of Data

The poor organization of processing and delivering SO data by the Master Data Processing Facility (MDPF) at GSFC had a negative impact on the HCM-025 Investigation. The following drawbacks should be pointed out:

- A. Irregular delays and unorganized assortments of shipments. This resulted in:
- . PI's extra-burden for promotion, coordination and control of interpretation by Co-investigators,
 - . considerable complication in distributing and filing by JRC staff and Test Site Coordinators,
 - . loss of confidence and difficulties for a sound interpretation by Co-investigators. Multitemporal interpretation was particularly affected by such distribution anomalies.
- B. Errors in image processing and uncorrected deliveries such as:
- a) the same scene (same orbit, same exposure time) processed at different periods had different coordinates,
 - b) physically identical scenes - with identical cloud pattern - had completely different exposure dates,
 - c) copies of the same image sent several times,
 - d) processed images announced but not included in packages,
 - e) delivery of unrequested extra-copies.

This resulted in:

- an extra-burden for control, distribution and filing by Ispra staff,
- perplexity and loss of confidence by Co-investigators.

The quality of SO data was densitometrically better compared to PT data. Contrast was good, but scanning was sometimes affected by a periodical line-effect.

ORIGINAL PAGE IS
OF POOR QUALITY

TABLE II.1: Status of Priority Processing List (PPL) on 31 August, 1980.

MONTH	REQUESTS					DELIVERIES					FAILED	
	G	BNL	F	UK	I	G	BNL	F	UK	I	TRACKS	
	N D	N D	N D	N D	N D	N D	N D	N D	N D	N D	N D	N D
May 78	3 3		2 2		4 4	3 2		1 2		2		1
June	1 1		1 1		7 7	1 1		1		3 2		1
July		2 2	2 2	2 2	9 9		2 2	2	1	6 2		5
August	1 1		4 4		10 10			1 4		4 3		2
September			5 5	3 3	7 7			5 5	1 2	4 4		1
October	5 5		2 2		2 2	5		2		1		3
November	1 1		4 4	1 1	3 3	1 1		2 3	1	1 2		
December	1 1		2 2			1		2				2
Jan. 79	1 1					1						
TOTAL	13 13	2 2	22 22	6 6	42 42	5 11	2 2	11 19	2 3	18 16		5 10

DELIVERIES = 63.4%
REQUESTS

Legend: G Germany
BNL Benelux
F France
UK United Kingdom
I Italy

Retrospective Order Data

Retrospective Order (RO) data had to be requested by Co-investigators (via JRC) only after reception of SO data. Obviously, the interpretation activity of RO data was affected by the delays and drawbacks which affected the SO data.

The greatest part of RO data was requested as Computer Compatible Tapes (CCT's) of SO scenes. CCT's processing and delivery by GSFC generally occurred about 1.5 months after JRC's request. CCT's delivery operation by GSFC appeared to be always regular. No particular complaints were received at JRC by Co-investigators.

The situation of RO delivery on SO requests is shown in Table II.3. Some ATI data were only available in the last period of TELLUS investigation. Some scenes of Temperature Difference (TD) and Apparent Thermal Inertia (ATI) were requested by Co-investigators. A few Middle European Institutes were interested in their utilization for correlation to topography, soils and land-use.

TABLE II.2: Distribution of Standing Order (SO) Scenes per Test Site and Country, Made by JRC Ispra.

Test Site Group	Test Site No.	No. of SO Scenes	Repeatedly Processed Scenes	Scenes per Country
Italy	1	75	6	259
	2	135	11	
	3	127	13	
	others	1		
France	4	185	15	319
	13	123	6	
	others	90	5	
Germany	5	81	2	185
	6	77	4	
	7	77	4	
	15 others	2		
Benelux	12	136 6	13	142
United Kingdom	8	77	3	173
	9	78	4	
	10	69	3	
	11	64	4	
	others	39	1	

TABLE II.3: Retrospective Order (RO) Scenes on CCTs on 31 August, 1980.

	NASA/GSFC	EARTHNET/CMS Lannion	Total
Ordered	101	74	175
Received	95	71	166
Still not received	6	3	9

Total Distribution per Country: Benelux 31
France 41
Germany 73
Italy 15
United Kingdom 12

TABLE II.4 - Quick Look Distribution by CMS Lannion to TELLUS Test Sites Groups

NIGHT ORBITS							DAY ORBITS						
Track	JRC	I	G	BNL	F	UK	Track	JRC	I	G	BNL	F	UK
2.1	X	X					18.3	X					
13.1	X	X					8.1	X	X	X			
8.1	X	X					3.1	X	X	X			
3.1	X	X					14.1	X	X	X			
14.1	X	X					9.1	X	X	X	X		
9.1	X	X	X				4.1	X	X	X	X		
4.1	X	X	X				15.1	X	X	X	X		
15.1	X	X	X		X		16.1	X	X	X	X	X	
10.1	X	X	X		X		5.1	X	X	X	X	X	
5.1	X	X	X	X	X		16.1	X	X	X	X	X	X
16.1	X	X	X	X	X		11.2	X	X	X	X	X	X
12.2	X	X	X	X	X		6.2	X	X	X	X	X	X
16.2	X		X	X	X		1.2	X	X	X	X	X	X
1.2	X		X	X	X	X	12.2	X			X	X	X
12.2	X		X	X	X	X	7.2	X			X	X	X
7.2	X		X	X	X	X	2.2	X				X	X
2.2	X		X	X	X	X	13.2	X				X	X
13.2	X			X	X	X	8.2	X				X	X
8.2	X			X	X	X	3.2	X				X	X
3.2	X				X	X	14.2	X				X	
14.2	X				X	X	Total D Tracks						
4.2	X					X	19	12	11	11	13	10	
15.2	X					X	OVERALL NUMBER OF N/D TRACKS						
Total N Tracks	24	12	12	10	15	11	Track	JRC	I	G	BNL	F	UK
							Night	24	12	12	10	15	11
							Day	19	12	11	11	13	10
							N+D	43	24	23	21	28	21

ORIGINAL PAGE IS
OF POOR QUALITY

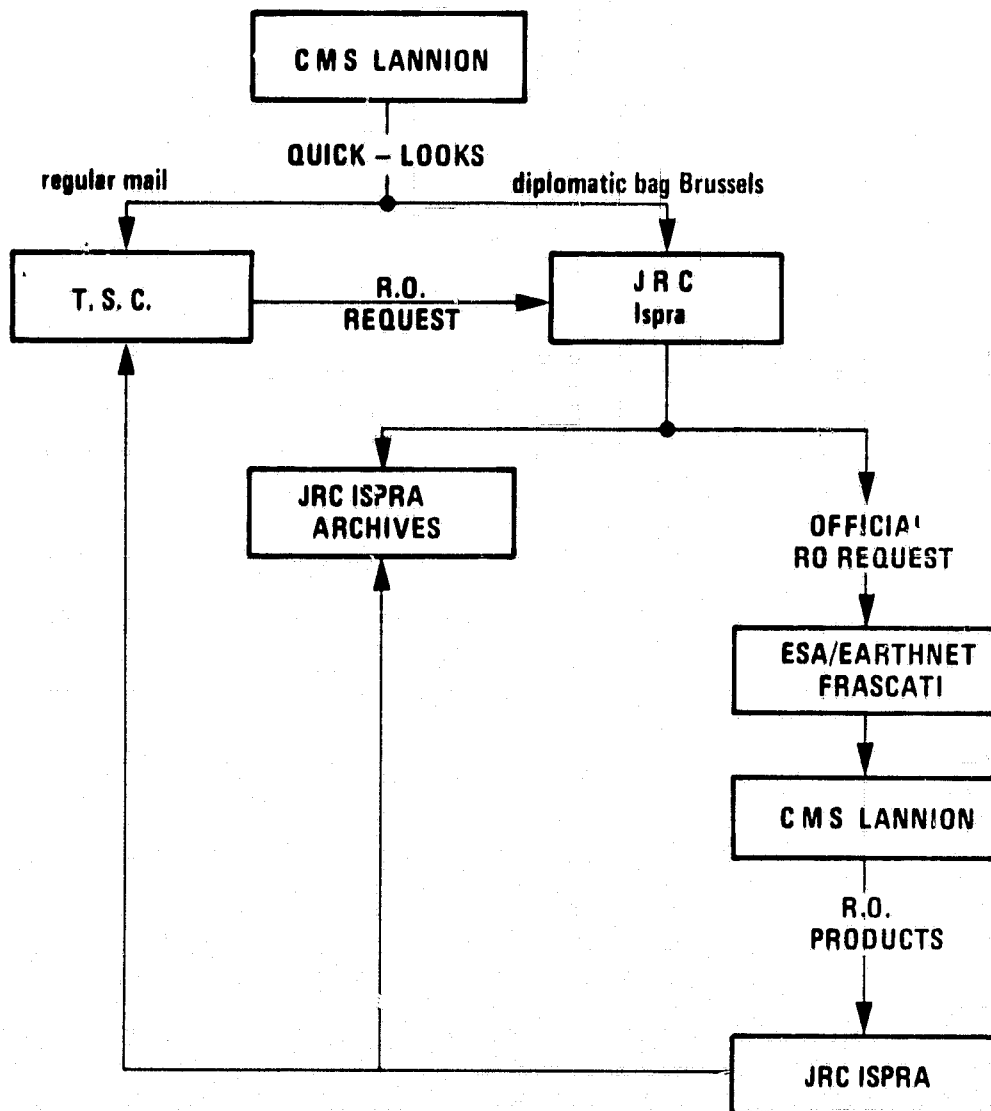


Fig. II,2: HCMM Data Distribution from ESA/CMS Lannion Through to TELLUS Users.

ESA / EARTHNET Data Delivery

Quick Look Data

Since May 1979 CMS Lannion has been producing and regularly distributing Quick Look (QL) data for the whole HCMM trackings of the Lannion station receiving area. Fig. II. 2 shows the flow diagram of QL data distribution to Co-investigators. The QL data distribution scheme to TSCs, according to track number, is indicated in Table II. 4. Quality of these QL data was rather good.

Retrospective Order Data

RO data request had to be made to CMS Lannion after reception of QL data by Co-investigators. The flow diagram of RO request to ESA/EARTHNET and delivery to Co-investigators by CMS Lannion is shown in Fig. II. 2. The overall time for request and delivery to Co-investigators was faster as for RO data on SO requests. No particular problems arose in processing and distributing RO data. TELLUS Co-investigators asked for 74 CCTs. Table 3 presents the overall situation of RO delivery on QL requests. The distribution within national Test Site Groups is also indicated.

Processing routines of TD and ATI data were available to CMS Lannion in the very last phase of HCM-025 Investigation only. This explains the small number of TD and ATI requested.

Priority Coverage

A series of priority HCMM satellite coverage was requested by some Co-investigators and by JRC to be matched with concomitant ground measurements, aircraft flights or other satellites' passes. However, a correct switching-on of HCMM satellite was not always easy to obtain for various reasons. In 1978 the situation was particularly difficult owing to congestion at the Madrid Station for other satellites' transmission. Sometimes HCMM satellite switching-on could not be organized at all. After March 1980 due to a lowering of HCMM orbit it was difficult to know the actual track pattern and ask for correct priority switching-on.

References

1. Provisions for Participation of HCM-025 Investigation, NASA/GSFC and EC/JRC, 1976.
2. Minutes WG-3 Meeting, Freiburg, 30 Nov. - 1 Dec., 1978.
3. HCMM Data Users Handbook, NASA/GSFC, Dec. 1978.
4. Minutes of WG-2 Meeting, Rome, 20/21 Nov., 1979.
5. TELLUS NEWS, periodical of the TELLUS Project, Ispra, 1980-81.
6. TELLUS NEWSLETTERS, No. 23.
7. A. STEIN; Programme for Filing and Archiving of Data at JRC, SAD, TD2, TCARD (A. Stein), dialogue input program, Ispra, 1979.

PRECEDING PAGE BLANK NOT FILMED

III. Activity Performed and Results Obtained

Part 1 : Evaporation and Soil Moisture

1. Development and Test of Algorithms

Working Group : Evaporation and soil moisture (P. Reiniger , JRC Ispra ed.

PRECEDING PAGE BLANK NOT FILMED

ORIGINAL PAGE IS
OF POOR QUALITY

Introduction

According to the field of application, soil moisture and evaporation can be expressed at various time and spatial scales.

The meaningful interpretation of an average soil moisture content and soil water properties is complicated by the three-dimensional nature of this parameter and is actually limited to about field size (SIMMONS et al. 1979, RUSSO and BRESLER 1980).

On the contrary, evaporation or evapotranspiration (ET) is a well defined and useful concept on time scales ranging from a few minutes to about a month and on spatial scales from a field plot to the size of a continent. The time and spatial scale are usually not independent of each other. Specific methods for measuring evaporation are being used, and are still being developed at the various scales (SEGUIN 1980).

On a local scale, ranging from a few square meters to fields of about 1 ha, ET can be estimated from measurements in the atmosphere (BOWEN 1926) or from a water balance in the soil (DAIAN and VACHAUD 1971). The corresponding time scale runs from a few minutes to a few days and the precision is in

the order of 10 - 20%.

At the other extreme, on the very large scale ranging from vast drainage basins and up to continents ($10^4 - 10^6 \text{ Km}^2$), evaluation is possible using atmospheric vapour flux analysis and the laws of the planetary boundary layer (RASMUSSEN 1977, BRUTSAERT and MAWDSLEY 1976). The corresponding time scale runs from about a month down to a few days and the precision of the estimate is about 20 - 30%.

Between the continental and the local scale there exists a gap at what one may call the regional scale from about 1 Km^2 to $10^3 - 10^4 \text{ Km}^2$, which is the width of the synoptic meteorologic network in large parts of Europe. The corresponding time scale would go from one to about 10 days, according to the potential users (SEGUIN 1980). These potential users of regional evaporation data could be found:

- in agronomy for predicting crop yields and scheduling irrigation (MALET and GUYOT 1978, IDSO et al. 1978);
- in hydrology for establishing a regional water balance (VAN DER PLOEG et al. 1976);
- in regional climatology where the latent heat

of evaporation is an important factor for the repartition of energy at the surface (SEGUIN 1978a).

Actually, estimates of ET on the regional scale are being carried out using Penman's equation (THOM and OLIVER 1977), the conception approach of MORTON (1977) or the relation between local and regional ET derived by BOUCHET (1963). Routine estimates from data provided by the synoptic meteorologic network are established in France (CHOISNEL 1977) and in the U.K. (WALES-SMITH and ARNOTT 1979). The difficulty with these methods lies in determining which surface is exactly concerned by their results and in interpolating correctly between the measuring points of the synoptic network.

The Heat Capacity Mapping Radiometer (HCMR) with its spatial resolution of approximately 500 x 500 m should be well suited to find solutions for this difficulty.

Therefore, in the HCM-025 investigation a systematic approach was used through the development of theoretical models, their testing in long-time measurement campaigns on the ground and during aircraft flights, and, finally, in their tentative application to HCMM-satellite data.

Methodology

The basic equation containing a relation between surface temperature T_s and the evaporation ET is the energy balance equation

$$ET = R_n - H - S \quad (1.1)$$

where

ET = latent heat flux
 R_n = net radiative flux
 H = sensible heat flux
 S = ground heat flux

In the combined aerodynamic energy-balance approach, already used by BROWN and ROSENBERG (1973) and STONE and HORTON (1974), the sensible heat flux H is calculated by the aerodynamic equation (1.2) relating flux to the difference between air and surface temperature.

$$H = \rho C_p h (T_s - T_a) \quad (1.2)$$

where ρ is the density of the air, C_p the specific heat of the air, h is the sensible heat exchange coefficient and T_a and T_s are the air and surface temperatures.

Combining equations (1.1) and (1.2) and re-writing one obtains

$$ET = (1 - \alpha) R_G + \epsilon (R_1 - \sigma T_s^4) - \rho C_p h (T_a - T_s) - S \quad (1.3)$$

where α is the albedo for solar radiation, R_G is the global incoming solar radiation flux, R_1 the long wave sky radiation flux, ϵ is the surface thermal emissivity and σ the Stephan-Boltzmann constant.

The HCMR should make two contributions to the solution of eq. (1.3). Its sensor in the visible near-infrared-range (0.55 - 1.1 μm) should provide a value for the albedo, contributing to an evaluation of the net radiation flux, and its thermal sensor (10.5 - 12.5 μm) should give a value of the surface temperature, contributing to the calculation of the sensible heat flux and of the thermal component of the net radiation flux.

Three critical points of the method can be identified:

1. The air temperature is measured as the kinetic temperature, while the surface temperature is measured by the HCMR as the radiative temperature and, therefore, a knowledge of the thermal emissivity is necessary to avoid errors which could amount

- to 2 ± 3 degrees (BECKER et al. 1980).
2. The calculation of the sensible heat exchange coefficient h is rather delicate and depends on the knowledge of a roughness parameter of the surface which is difficult to evaluate.
 3. The meaning of a remotely sensed surface temperature in eq. (1.3) is open for discussion as even in a short grass cover important horizontal and vertical temperature gradients can be measured and discrepancies between T_s measured and calculated by eq. (1.2) have been noted (KEIJMAN and DE ERUIN 1979).

Test of the Combined Aerodynamic Energy-Balance Approach

The performance of this approach expressed in eq. (1.3) was tested on a grassland area of Test Site no.4 at Montfavet, Southern France (SEGUIN 1978b). The grassland area was composed of a Northern and a Southern field with a different irrigation schedule, but due to the wet summer of 1977 there was little effective difference in the water regime of the two fields.

Over a 67-day period of July-September 1977 all components of the energy balance equation were measured at 1-minute intervals on this area. For a two-week period in July, hourly and daily ET was calculated by the aerodynamic energy-balance method (ET_{Ts}) and was compared with the Bowen ratio method (ET_{β}) which served as a standard reference.

As shown in Figs. III 1.1 and III 1.2, the values of this comparison were spread around a 1 : 1 relation line both for hourly values at the time of the daily maximum surface temperature (Fig. III 1.1) and for daily values of ET (Fig. III 1.2).

Despite the considerable spread, these results seemed to be encouraging and the problem of

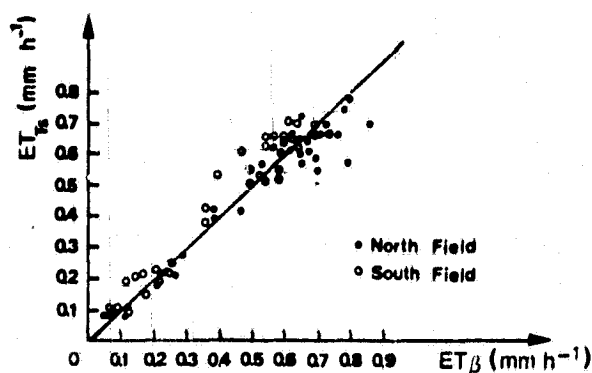


Fig.III.1.1. Relation between hourly values (12-13 hr UT) of ET_{Ts} and ET_{β} during the experiment of summer 1977 (SEGUIN 1978).

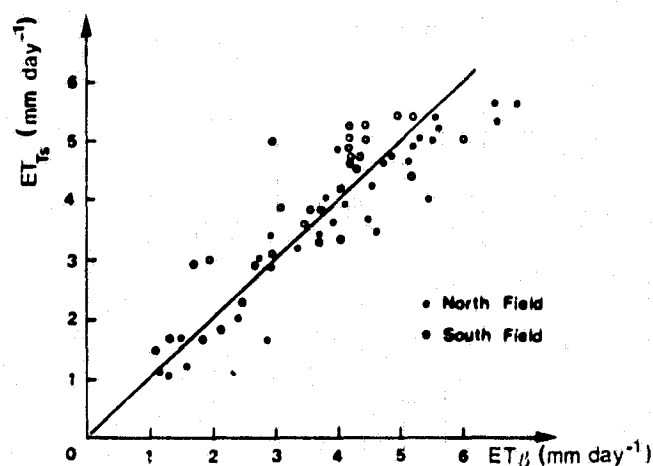


Fig. III.1.2. Relation between integrated daily values of ET_{Ts} and ET_{β} during the experiments of summer 1977 (SEGUIN 1978).

the calculation of the daily ET from the integration of only one (day) or two (day/night) instantaneous values given by HCMM had to be solved. This was attempted by modelling the evapotranspiration flux in the soil-plant-atmosphere continuum.

**ORIGINAL PAGE IS
OF POOR QUALITY**

Models of Water and Heat Flow in the Soil-Plant-Atmosphere Continuum

The TERGRA Model

1. Description

In the TERGRA model (SOER 1977) the evapotranspiration flux ET is also written as a transport equation:

$$ET = -\frac{\rho C_p}{\gamma} \frac{e_c^*(T_c) - e_a}{r_{av} + r_s} \quad (\text{W.m}^{-2}) \quad (1.4)$$

where γ is the psychrometric constant (Pa.K^{-1}), $e_c^*(T_c)$ the saturated water vapour pressure (Pa) at temperature T_c , e_a the water vapour pressure (Pa) in the air, r_{av} the turbulent diffusion resistance for water vapour (s.m^{-1}) and r_s the crop diffusion resistance for vapour transport (s.m^{-1}).

Combining equation (1.3) and (1.4) the crop water vapour flux is set equal to the liquid water flux in the soil-plant system:

$$E = \frac{1}{g} \frac{\psi_{\text{soil}} - \psi_{\text{leaf}}}{R_{\text{soil}} + R_{\text{plant}}} \quad (\text{kg.m}^{-2}.\text{s}^{-1}) \quad (1.5)$$

where ψ_{soil} and ψ_{leaf} are the water pressures (Pa) in the soil and the leaves respectively, and R_{soil} and R_{plant} the resistances (s) in the soil and the plant respectively, and g is the acceleration due to gravity. The two processes are coupled by the relation:

$$r_s = f(\psi_{\text{leaf}}) \quad (1.6)$$

With this model the daily behaviour of crop temperature and energy balance components is simulated for different soil moisture conditions, resulting in a family of curves of ET or of the surface temperature (Fig. III 1.3). The curve which corresponds at the time of the daily maximum with the remotely sensed surface temperature is assumed to represent the time curve of the energy balance components for this day and consequently gives also the daily evapotranspiration.

ORIGINAL PAGE IS
OF POOR QUALITY

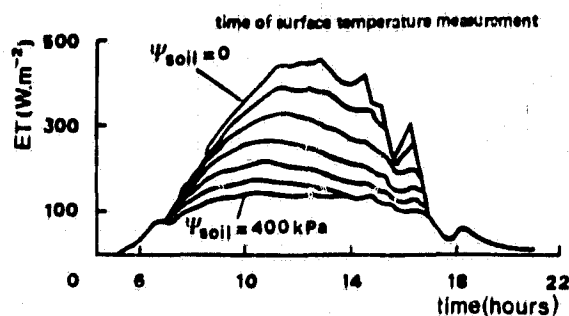


Fig.III.1.3. TERGRA-simulation of the daily course of actual evapotranspiration ET at different soil moisture pressure values ψ_{soil} (SOER 1980).

2. Test of the TERGRA model

2.1 Grassland

As a first approximation, a short grass cover may be considered a relatively simple and unstructured surface, i.e. one may assume that the remotely sensed surface temperature coincides with the surface temperature at the height of zero windspeed in eq. (1.3) and (1.4). A test of the TERGRA model based on this assumption was carried out in the Netherlands (NIEUWENHUIS and KLAASSEN 1978).

While the total daily ET calculated by the TERGRA model agreed with the Bowen ratio reference method to within 4% as shown in Fig. III 1.4, the maximum difference for the instantaneous ET reached 25%.

The importance of this instantaneous difference is considerable for remote sensing purposes if one remembers the fact, that one instantaneous surface temperature value at the time of flight or satellite overpass is used to calculate daily ET.

As was to be expected, ET at night was close to zero or even negative, i.e. condensation was taking place.

A comparison of measured surface tempera-

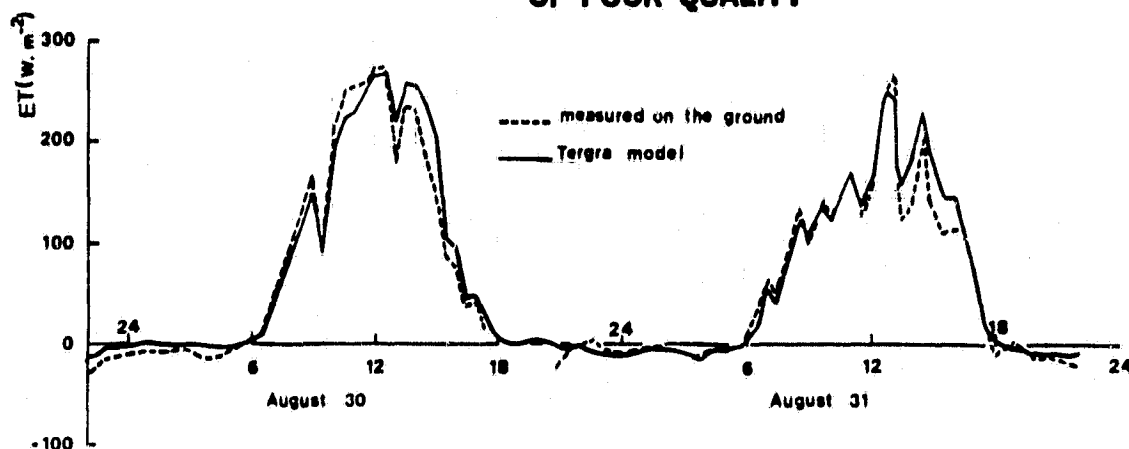


Fig.III.1.4. Daily course of the evapotranspiration ET calculated with the TERGRA-model and measurements according to the Bowen ratio-method for August 30 and 31, 1977 NIEUWENHUIS and KLAASSEN 1978).

tures and those calculated by the TERGRA model (Fig. III 1.5) shows that the model tends to underestimate actual surface temperature by up to 2°C during daytime. As will be shown later, this discrepancy corresponds approximately to the temperature difference between well watered and water stressed crops observed in the summer climate of Western Europe.

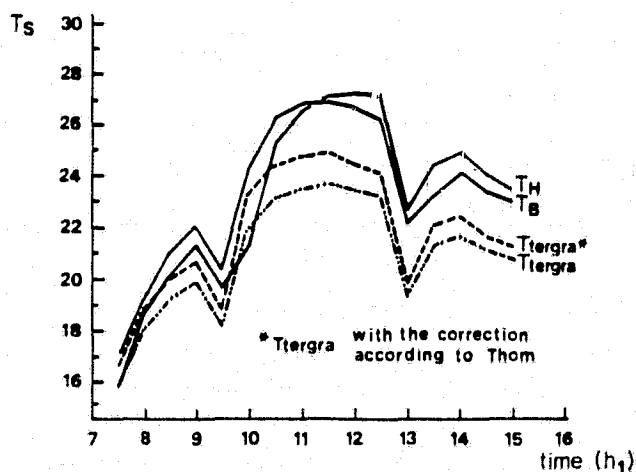


Fig.III.1.5. The simulated crop temperature with and without the correction according to THOM and the radiation temperature measured by the KNMI with a Barnes (T_B) and a Heimann (T_H) radiometer for August 30, 1977 (NIEUWENHUIS and KLAASSEN 1978).

Without the Thom correction for the difference between flux of momentum and latent heat (THOM 1972), the difference between measured and calculated surface temperature in Fig. III 1.5 reached even 3.5°C .

On the contrary, in another test of the TERGRA model carried out on two $30 \times 60 \text{ m}$ grass plots in July 1978 at Policoro in the South of Italy ($40^{\circ}14'N$, $16^{\circ}40'E$), the TERGRA model overestimated crop surface temperature around the time of the daily maximum (13.00 hrs) by $2 - 6^{\circ}\text{C}$ (CARLONI et al. 1981). As shown in Table III 1.1, the daily evapotranspiration calculated by the TERGRA model agreed to within 16% or better with the daily ET calculated by the Bowen ratio, but its estimates were always lower than ET. Unfortunately, during the period of the test there was no, or only a slight, difference in the water regime of the dry and irrigated plot and in both plots ET was close to potential ET. Furthermore, due to the size of the plots and the surrounding ground cover, an oasis effect is not to be excluded.

DATE (1978)	ET , mm d ⁻¹				T _s wet, °C			T _s dry, °C			T _A , °C
	TERGRA		Bowen ratio	Class - A pan	TERGRA calculated	MEASURED	Δ	TERGRA calculated	MEASURED	Δ	
	wet	dry									
30.6		7.0	7.3	8.7	30.4	25.4	5.0	29.9	26.9	3.0	27.4
1.7		6.6	6.7	7.9	28.7	24.3	4.4	28.6	25.7	2.9	25.5
3.7		5.6	6.4	6.1	30.1	25.9	4.2	30.0	27.0	3.0	26.4
4.7		5.9	7.0	8.2	31.6	26.5	5.1	31.4	27.9	3.5	25.6
5.7		5.8	6.1	7.3	30.9	28.0	2.9	30.9	29.0	1.9	25.8
8.7	5.5		5.5	5.8	29.3	24.9	4.4	29.9	25.6	4.3	26.1
9.7	5.4		5.4	5.8	30.4	25.0	5.4	30.9	26.0	4.9	24.7
10.7	6.0		6.0	7.1	31.8	25.2	6.7	32.6	26.9	5.7	27.4
11.7	6.3		6.2	7.8	32.8	28.5	4.3	32.7	29.0	3.7	27.6
12.7	6.3		6.2	7.3	33.3	28.1	5.2	33.2	28.9	4.3	28.5

Table III.1.1. Daily cumulative evapotranspiration (ET) calculated by the TERGRA model and the Bowen ratio, class-A pan evaporation, crop surface temperature (T_c) and air temperature (T_a) for two test plots at Policoro, Southern Italy (CARLONI et al 1981).

2.2 Structured crops - Potatoes

For higher, structured crops the simplifying assumption made for short grassland can no longer be made and the temperature distribution inside the canopy has to be taken into account when solving eq. (1.3). In fact, as pointed out before, even in short grassland important temperature gradients were measured by KEIJMAN and DE BRUIN (1979).

A solution for structured crops, i.e. considering the temperature distribution inside the crop canopy, has been worked out by KLAASSEN (1979). In this case, the turbulent diffusion resistance for heat transport in eq. (1.3) $r_{ah} = \frac{z}{h}$ has to be composed of two terms:

$$r_{ah} = r_{am} + r_l \quad (\text{s. m}^{-1})$$

where r_{am} is the atmospheric resistance for momentum transfers and

$$r_l = 80 \left(\frac{w}{u^*} \right) 0.5 \quad (\text{s. m}^{-1})$$

with w being the leaf width (m) and u^* the friction velocity (m. s^{-1}). This approach is also valid for the short grass surface treated previously.

Likewise, for potatoes the relation given by eq. (1.6) had to be replaced by constant values

of the crop resistance r_s , with an r_s value of 50 being characteristic of a well watered crop and a value of 120 being valid for water stressed potatoes.

A comparison of daily ET calculated by this method and measured by the Bowen ratio is given in Table III 1.2, while the corresponding measured and calculated surface temperatures at the time of the daily maximum are compared in Table III 1.3.

One may note that the results are very sensitive to the value of the crop resistance r_s , a parameter difficult to evaluate. Furthermore, in order to arrive at absolute daily ET values corresponding to measured ET crop resistance, values had to be used which led to overestimate crop surface temperature by up to 4°C.

On the other hand, as shown in Tables III 1.2 and III 1.3 for the two days with a relatively high evaporative demand, the temperature difference between well irrigated and water stressed potatoes was about 2°C both measured and calculated. This difference corresponded to 0.9 and 1.6 mm of daily ET.

This temperature difference of 2°C could be detected by the HCMR and one may therefore conclude that the TERGRA model should not

Date	Measured		Simulated r_s ($s \cdot m^{-1}$)			
	ET (mm)	dew (mm)	50	90 ET (mm)	120	dew (mm)
12 July 1979	3.3	0.5	4.7	3.6	3.1	0.1
13 July 1979	1.1	0.4	1.4	1.1	1.0	0.2
14 July 1979	3.1	0.2	3.0	2.4	2.1	0.1

Table III. 1.2. Daily evapotranspiration (ET) and dew of irrigated potatoes as measured by the TERGRA - model (NIEUWENHUIS et al. 1980).

Date	Measured				Simulated r_s ($s \cdot m^{-1}$)		
	T_a (°C)	Irr. (°C)	non-Irr. (°C)	ΔT (°C)	50 (°C)	120 (°C)	ΔT (°C)
12 July 1979	21.5	21.4	23.8		23.6	25.7	2.1
13 July 1979	20.5	18.8	19.3		20.5	21.5	1.0
14 July 1979	20.5	20.6	22.7		23.3	25.0	1.7

Table III.1.3. TERGRA simulated and measured radiation temperature of potatoes and air temperature T_a at 14.00 hours UT (NIEUWENHUIS et al. 1980).

be used for an absolute calculation of ET, but the temperature difference between comparable surfaces should serve to identify water stressed crop surfaces.

The TELL-US Model

1. Description

The TELL-US model (ROSEMA and BIJLEVELD 1977) is also based on a solution of eq. (1.1) but it was specifically designed for bare or sparsely vegetated soil and for the HCMH satellite, as it uses not only the daily maximum but also the daily minimum temperature.

Transient heat flow in a homogeneous soil is described by a finite difference equation. As a lower boundary, a soil depth outside the daily temperature cycle is taken, while the upper boundary is given by a level in the atmosphere where windspeed, air temperature

and air specific humidity have to be measured hourly. The atmosphere and the soil regime are coupled by eq. (1.1).

As two surface temperatures measured at proper times are used as input, the model can give a solution for two unknowns. One of the two must have a strong influence on the course of the surface temperature during daytime, while the other must govern the nighttime surface temperature course.

A parameter combination that satisfies these criteria is formed by surface relative humidity and thermal inertia. In the model, these two unknowns have to be assumed to be constant during the daily cycle.

In applying the model, daily maximum and minimum temperatures are simulated for a series of combinations of surface relative humidity and thermal inertia, producing look-up graphs as shown in Fig. III 1. 6. By entering the remotely sensed daily maximum and minimum temperature in Fig. III 1. 6a, one obtains the surface relative humidity which by the relation in Fig. III 1. 6b permits to obtain daily cumulative ET.

From the thermal inertia and using a known relation between thermal inertia and soil moisture, the volumetric moisture content in the upper soil layer can be determined.

The TELL-US model was also adapted to soils covered by vegetation (KLAASSEN and ROSEMA 1979). In this version, the assumption of a constant surface relative humidity was either replaced by that of a constant plant resistance r_p , or by the assumption of this plant resistance being proportional to the water vapour deficit.

2. Test of the TELL-US model

A first test of the TELL-US model (ROSEMA et al. 1978) showed reasonable agreement between measured and calculated average soil

ORIGINAL PAGE IS
OF POOR QUALITY

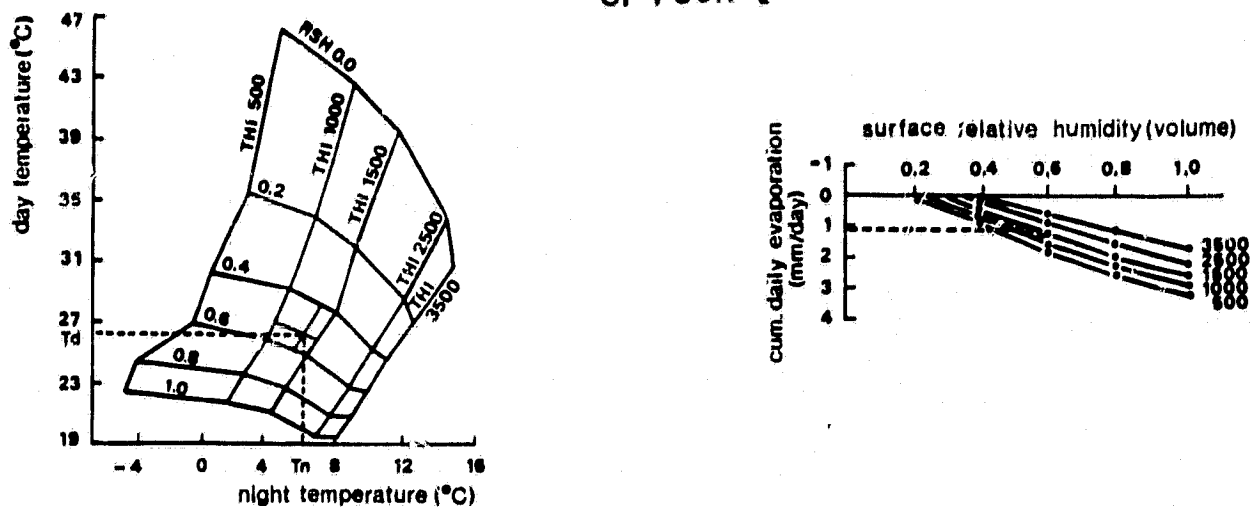


Fig.III.1.6. Look-up graphs calculated by Tell-us in the case of bare soil with albedo 0.09 (DEJACE et al, 1979).

moisture content in the top soil layer (Fig. III 1. 7a and b).

Comparing daily cumulative ET measured in a lysimeter and ET calculated by the model (Table III 1. 4), one notices a rather large discrepancy which seems to a certain extent to be caused by the assumption of a constant surface relative humidity.

Further analysis of the model with data from the Joint Flight Campaign at Grendon, U. K. (HUYGEN and REINIGER 1979) showed the model to be very sensitive to the value of the

Days after irrigation	Measured by lysimeter	Calculated with TELL - US
2	-5.84	-6.48
6	-1.43	-0.59
14	-0.68	+1.63

(+ : condensation)

Table III.1.4. Total Daily evaporation (mm day) (ROSEMA et al. 1978)

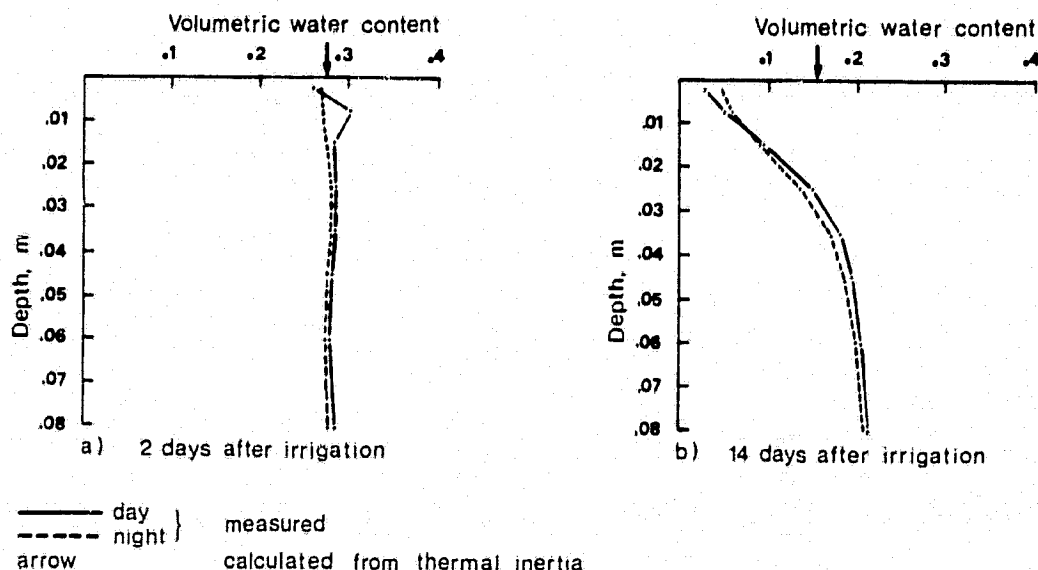


Fig.III.1.7. Soil moisture profiles of Avondale loam (ROSEMA et al. 1978).

soil heat capacity and to spatial changes in air temperature which are frequent during nights with low windspeed. Modifications were introduced into the model to permit the use of correct values of the soil heat capacity combined with short calculation times (HUYGEN 1979a).

One may conclude that these difficulties and the assumption of a constant surface relative humidity make the use of the TELL-US model for the estimation of cumulative evaporation rather problematic. This evaluation does not necessarily include the estimate of soil moisture by the same method. It is furthermore evident that the model should be tested more extensively under different climatic and soil moisture conditions.

As the night time contribution to the daily ET can in most cases be neglected, the difficulties arising from a use of the night temperature should be avoided and the evaluation of the daily ET should be based on one or more remotely sensed daytime surface temperatures (BECKER and HECHINGER 1979).

On the contrary, the daily temperature am-

plitude was more effective in distinguishing the type of surface cover than either the minimum or maximum surface temperature alone. This is shown in Fig. III 1.8 presenting thermal data obtained during the Joint Flight Experiment, France, 1977 (PERRIER et al. 1980).

Other Models

Two simplified models which have been developed as part of the Tellus Project should briefly be described.

1. The TELOP model

This model (GREGOIRE, 1980) is based on the assumption that cumulative daily ET is a function of cumulative daily net radiation (HLAVEK et al. 1974). This function is different above and below a "critical" soil moisture content. Cumulative daily net radiation is calculated as a sinusoidal function from R_{n13} the net radiative flux at the time of the daily maximum surface temperature, i.e. the time of the HCMM overpass. This net radiative flux is derived from eq. (1.7).

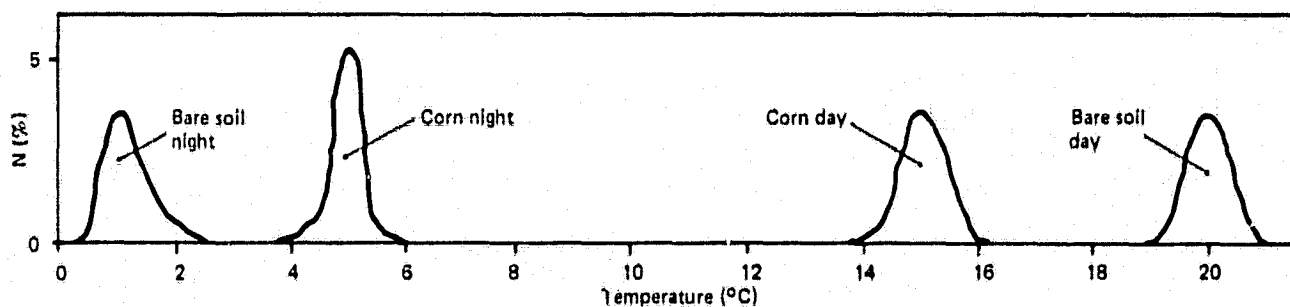


Fig.III.1.8.a. Frequency distribution of the day and night time surface temperature of two contiguous fields of corn and bare soil.

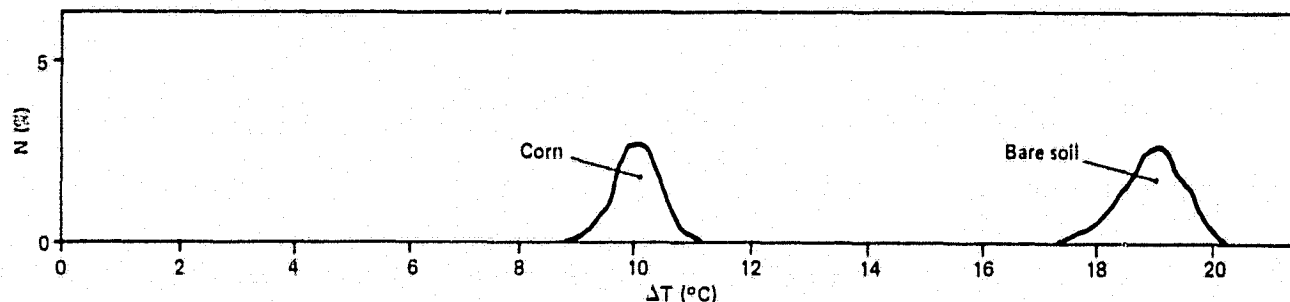


Fig.III.1.8.b. Frequency distribution of the day/night surface temperature difference for the 2 fields (PERRIER et al. 1980).

$$Rn_{13} = (1-\alpha)RG_{13} + Rl_{13} - R_{le13} \quad (1.7)$$

where the subscript 13 refers to 13 hours UT, or the time of the satellite overpass and R_{le} is the emitted long wave radiation.

The remotely sensed surface temperature serves to calculate the emitted long wave radiation as in eq. (1.3), RG_{13} is either measured on the ground or is calculated from the reflected visible & NIR radiation measured by the satellite if the albedo of the surface is known.

Using data from the Policoro Experiment 1978 (Test Site no. 1) over a 10-day period, cumulative ET calculated by the TELOP model differed from values obtained with the TERGRA model by 9%. Maximum differences in daily ET were 25%.

2. The SEAL model

This Simplified Evapotranspiration Algorithm (HUYGEN 1979b) is an adaptation of the TELLUS model to surfaces covered by vegetation. Accordingly, the following changes have been introduced into the model:

The simulation period is reduced to the time between sunrise and sunset.

The ground heat flux is assumed to be 10% of the net radiation.

The course of the daily surface temperature is calculated for different but constant values of bulk stomatal resistance, instead of surface relative humidity and thermal inertia.

For a certain stomatal resistance there will be agreement between the remotely sensed surface temperature close to the daily maximum and the simulated crop surface temperature at that time. The stomatal resistance thus obtained permits the calculation of the daily evapotranspiration. In addition, the crop surface temperature corresponding to potential evapotranspiration is being calculated. A first result obtained by the algorithm agreed

to within 5% with the daily evapotranspiration calculated by the TERGRA model, but no further tests with experimental field data have yet been carried out.

The Operational Evaluation of ET-Algorithms

Comparison of Methods Involving Surface Temperature and Classical Methods

An operational evaluation of ET-algorithms was carried out in 1978-80 on Test Site no. 4 in the Crau (43°50'N, 4°56'E), Southern France (SEGUIN and PETIT 1980).

The site on flat land consists of 10 - 30 km² of irrigated pasture and about 100 km² of non-irrigated grassland. Two identical monitoring stations were established, one in the irrigated and the other in the dry zone. The following parameters were measured in each station every 10 minutes:

- net radiation
- soil heat flux
- wet and dry bulb temperature of the air at 0.3 and 2 m
- surface temperature (HEIMANN KT-24)
- windspeed at 2 m
- soil temperature at 0.1, 0.5 m depth.

Global radiation was measured at Montfavet (30 km from the site). The measurements covered the period July-October 1978 and April 1979 - March 1980.

Evapotranspiration was calculated for both the dry and irrigated zone by four methods which were compared with the Bowen ratio method serving as a reference.

Two of the four methods did not involve the surface temperature. They were the approximations $ET_{Rn} = Rn$ (HLAVEK et al. 1974), liable to be valid under wet conditions and $ET_{eq} = (\Delta / (\Delta + \gamma)) Rn$, i. e. the first term of

Penman's equation, adapted to moderately dry conditions (PERRIER 1977).

The methods using surface temperature were the combined energy balance-aerodynamic approach (ET_{Ts} , eq. (1.3) and a simplified approach (ET_{JT}), proposed by JACKSON et al. (1977). The equation used for ET_{JT} had the form:

$$ET = (R_n - S_g) + 1.0 - 0.25 (T_s - T_A) \quad (1.8)$$

(mm d⁻¹)

The difference between the values in this equation and in the one originally proposed by Jackson can most probably be explained by the local advective conditions of the Arizona test plots.

Comparing the results obtained by the four methods with the Bowen ratio reference standard (ET) for the irrigated zone (Fig. III 1.9) and for the dry zone (Fig. III 1.10), one can draw the following qualitative conclusions:

- The two methods based on thermal infrared data, ET_{Ts} and ET_{JT} , give results which both for the dry and irrigated zone are arranged rather symmetrically along the 1:1 relation line, despite an important scatter of the single measurement points.
- Of the two classical methods, each one provides an estimate of comparable precision only for one of the two zones. While ET_{Rn} is rather evenly distributed along the 1:1 line for the irrigated zone, though with a tendency to overestimate ET , it completely

ORIGINAL PAGE IS
OF POOR QUALITY

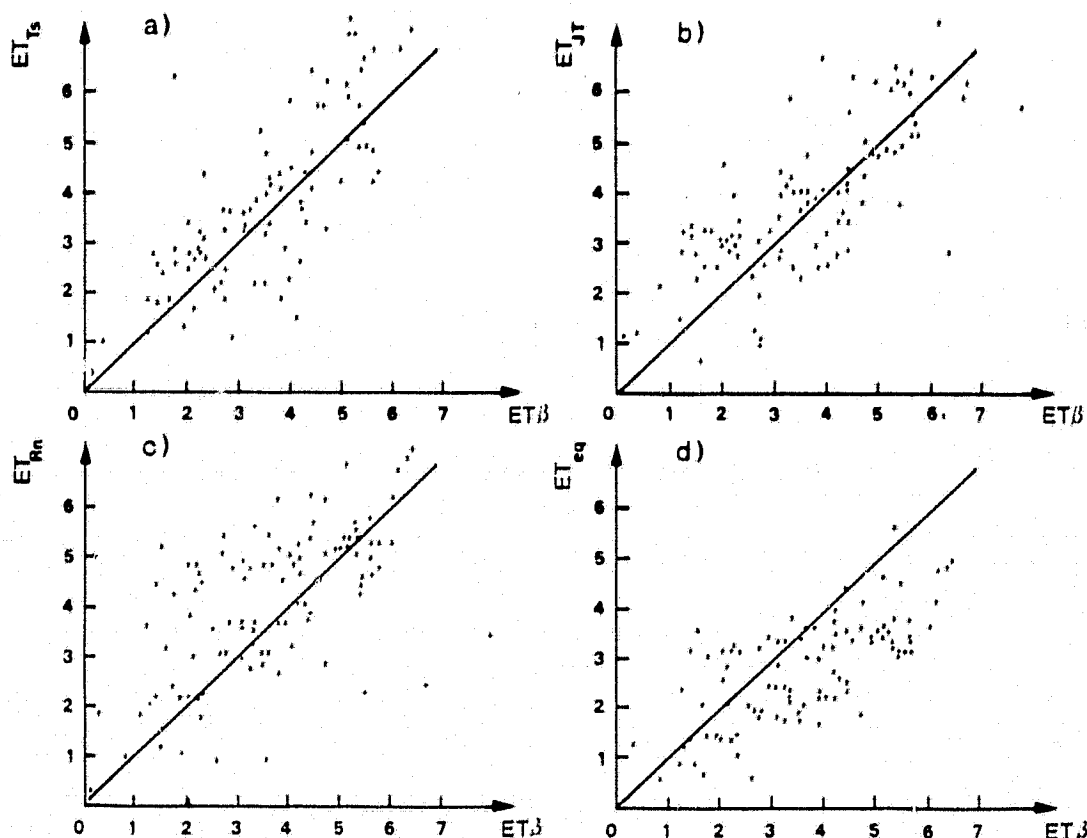


Fig. III.1.9. Comparison of daily ET obtained by four different methods with the standard Bowen ratio method (ET_{β}): a) ET_{Ts} , b) ET_{JT} , c) ET_{Rn} , d) ET_{eq} . The line represents the 1:1 relation (SEGUIN and PETIT 1980).

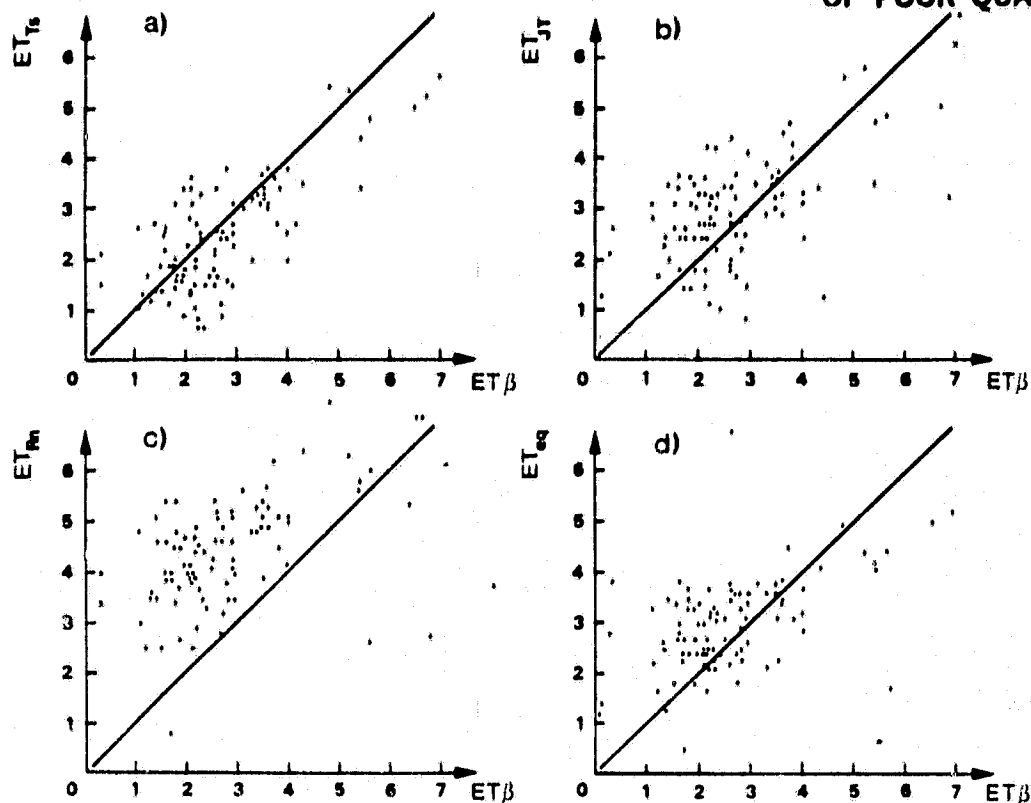


Fig.III.1.10. Dry zone, 98 days in the summer of 1979. Comparison of daily ET obtained by four different methods with the standard Bowen ratio method (ET_{β}): a) ET_{Ts} , b) ET_{JT} , c) ET_{Rn} , d) ET_{eq} . The line represents the 1:1 relation (SEGUIN and PETIT 1980).

overestimates ET for the dry zone. On the contrary, ET_{eq} follows the 1 : 1 line for the dry zone, but underestimates ET for the irrigated zone.

These qualitative conclusions are quantitatively supported by the seasonal mean daily ET (mm d^{-1}) given by the four methods and presented hereunder together with the Bowen ratio reference method (ET_{β}) and the potential evapotranspiration (ETP). It should be noted,

though, that the seasonal mean daily ET is a much less sensitive parameter than daily ET (Table III 1.5).

Taylor's Expansion of the Surface Energy Balance Equation

The energy balance equation (1.3) can be approximated by a first order Taylor's expansion (MENENTI 1980). By using the partial derivative of eq. (1.3) with respect to

Season	Zone	mmd \cdot 1					
		ETP	ET	ET_{Ts}	ET_{JT}	ET_{Rn}	ET_{eq}
Summer 78	Irrigated	4.7	3.5	4.2	4.0	4.1	2.7
Summer 79	Dry	6.7	2.6	2.4	2.9	4.4	3.0

Table III.1.5. Seasonal mean daily ET calculated by five methods and potential evapotranspiration. (SEGUIN and PETIT 1980).

ORIGINAL PAGE IS OF POOR QUALITY

surface radiation temperature T_s and albedo and employing the reference value of ET on the ground, the following relationship between ET, T_s and α was obtained for a desert area in Libya.

$$ET(T_s) = -0.125T_s - 8.5\alpha + 43.73 \quad (1.9)$$

(mm d⁻¹)

Some of the estimated values were corrected because of relevant differences in aerodynamic resistance r_a and air temperature T_a , as compared with the other data points. The corrections were calculated by taking other first order partial derivatives of eq. (1.3). The values measured by the Bowen ratio method were used only for comparison.

As shown in Fig. III 1.11, the results of the calculations with eq. (1.9) were spread around a 1 : 1 regression line on the ET measured by the Bowen ratio method. The standard deviation was ± 1 mm/d which represents about 20% of the mean daily evaporation rate encountered in the experiment.

Equation (1.9) would have to be site-calibrated

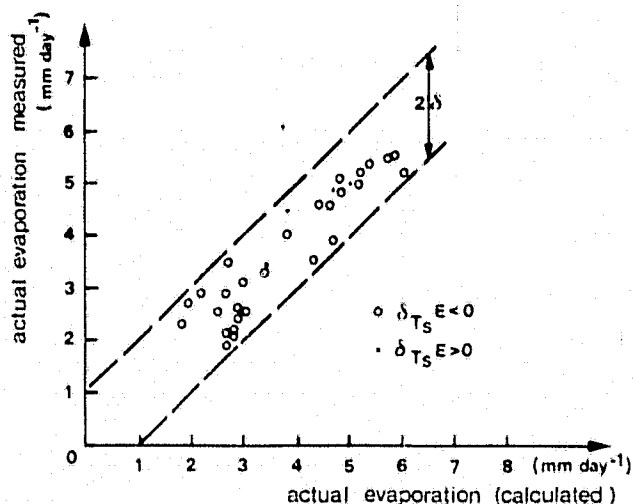


Fig.III.1.11. Measured (ET) versus calculated eq.(1.9) evaporation rates. Corrections included relate to surface aerodynamic resistance and air temperature. A scatter equal to twice the standard deviation is shown by the broken lines (MENENTI 1980).

and could be used to transform maps of surface radiation temperature and albedo into evaporation maps.

Regional ET Estimates from HCMM Data

1. Satellite imagery and maps

A first evaluation of regional ET from HCMM thermal and albedo data was attempted for the Crau site in Southern France. Three night/day passes of the summer of 1978 were used in this attempt. The scenes were:

17.7.78	28.7.78	12.8.78
AA-0082.020.0.3	AA-0093.02.12.0.3	AA-0108.01.51.0.3
AA-0082.1303.0.1.2	AA-0093.13.07.0.1.2	AA-0208.1247.0.1.2

The scenes were geometrically rectified and superimposed on a topographic map on a scale 1 : 250,000 (Fig. III 1.12). The irrigated and dry zones of the Crau were delimited on a Landsat image on a scale 1 : 50,000 (BAELZ 1980) and the boundaries were transferred to the 1 : 250,000 map with a zoom transfer-scope (Fig. III 1.13).

2. Surface temperature

The location of the two ground measuring stations was marked on the map which permitted a comparison of ground and satellite measured surface temperatures of the same area. At the same time the mean surface temperature and albedo of the dry and irrigated areas was extracted with a suitable statistical program. It had been shown earlier (PERRIER et al. 1980) that the mean temperature of a number of fields having the same surface characteristics could be used for the calculation of ET and that this calculation had not to be carried out for each individual field. The satellite surface temperatures were corrected for the offset of the radiometer and the effect of the atmosphere was calculated with the "Window" program (PRICE 1980) using radiosonde data (0 and 12 hrs UT) from Nimes, distant about

30 km from the site.*

The resulting surface temperatures are presented in Tables III 1. 6 and III 1. 7 and are confronted with the ground measured surface temperatures.

Turning first to the night time surface temperature in Table III 1. 7, one observes both a good agreement between satellite and ground measured temperatures (in 4 out of 5 cases better than 1°C) and a very small temperature contrast between the irrigated and the dry zone with a maximum difference of 1. 8°C.

The daytime data in Table III 1. 6 being the key to the use of remotely sensed surface temperatures for the evaluation of ET, they deserve a more extensive comment:

1. The effect of the atmospheric corrections on the absolute surface temperatures is extremely important and had, on the three days investigated, values from 3. 9 to 14. 9°C.
2. The atmospheric corrections also largely affect the temperature difference between the dry and wet zone. In the case of 28. 7. 1978, this difference was 4. 5°C without and 8. 4°C with the atmospheric corrections and a difference of 11. 7°C was measured on the ground.
3. Even after atmospheric correction there remained a discrepancy between satellite and ground measured temperatures of 5 - 6°C (the difference of 13. 0°C on 12. 8. 78 is probably due to a failure of the radiometer on the ground).

Date	Zone	Extension	T _{sat} °C	Atm. corr. °C	T _{sat} corr. °C	T _G	T _G -T _{sat}
17.7 1978	Irrig.	Point	30.5	3.9	34.4	39.8	5.4
		Area	32.1 ±3.1	4.6	36.7		
	Dry	Point	36.4	6.3	42.7	49.0	6.3
		Area	35.2 ±2.7	5.8	41.0		
28.7 1978	Irrig.	Point	26.3	9.0		41.3	6.0
		Area	26.3 ±2.4	9.6	36.5		
	Dry	Point	33.0	14.9	47.9	53.0	5.1
		Area	31.4 ±3.1	13.3	44.9		
12.8 1978	Irrig.	Point	24.9	5.3	29.0	28.9	-0.1
		Area	24.7 ±3.5	5.2	28.7		
	Dry	Point	31.1	6.2	37.3	50.3	12.0
		Area	30.9 ±3.4	6.3	37.2		

Table III.1.6. Satellite and ground measured daytime radiometric surface temperatures and atmospheric corrections for the irrigated and dry zone of the Crau (REINIGER et al. 1981)

Date	Zone	Extension	T _{sat} °C	Atmos. Corr. °C	T _{sat} Corr. °C	T _G	T _G -T _{sat}
17.7 1978	Irrig.	Point	16.0	-1.7	14.3	15.7	1.4
		Area	17.1 ± 1.1	-1.0	16.1		
	Dry	Point	17.8	-0.8	17.0		
		Area	17.3 ± 1.0	-0.9	16.4		
28.7 1978	Irrig.	Point	14.2	0.2	14.4	15.1	0.7
		Area	14.7 ± 0.7	0.6	15.3		
	Dry	Point	15.6	1.5	17.1	17.7	0.6
		Area	15.7 ± 0.9	1.4	17.1		
12.8 1978	Irrig.	Point	11.6	-1.2	10.4	9.9	-0.5
		Area	12.3 ± 1.3	-0.8	11.5		
	Dry	Point	13.4	-0.3	13.1	13.6	0.5
		Area	13.4	-0.3	13.1		

Table III.1.7. Satellite and ground measured nighttime radiometric surface temperatures and atmospheric corrections for the irrigated and dry zone of the Crau (REINIGER et al. 1981).

* The radiosonde data were provided by the Zentralamt des Deutschen Wetterdienstes, Offenbach am Main.

ORIGINAL PAGE IS OF POOR QUALITY

Therefore, it is impossible to apply models for the calculation of ET which had been developed for surface temperatures measured on the ground as long as no correspondance between ground and satellite measured surface temperatures has been established. Even the simplified relation ET_{JT} cannot be applied as it was derived with the aid of ground measured surface temperatures. As it should be extremely difficult, if not impossible, to relate the temperature of a few square meters of land surface to the temperature of a pixel of approximately 25 ha, an alternative solution would consist of deriving a relation of the type ET_{JT} for satellite measured surface temperatures. For this purpose, a larger number than the present three HCMM scenes of the Crau would have to be analysed. The problems enumerated above have little incidence on the use of HCMM thermal data to delimit zones of different ET measured on the ground. At present it seems that the major contribution of HCMM thermal data to the evaluation of regional ET is given by determining the extent of the zone for which point measurements of ET are valid, rather than by calculating ET from remotely sensed surface temperatures.

3. Albedo

Only little attention has been given so far to the albedo values in the 0.55 - 1.1 μ m band provided by the HCMM. Table III 1.8 presents the satellite measured albedo for the irrigated and the dry zone of the Crau for the three scenes investigated. As a comparison, the albedo of approximately 425 km² of the Mediterranean Sea off the coast of France is indicated for two of the scenes.

As can be seen on Table III 1.8, there was no difference between the albedo of the dry and irrigated zone which came somewhat as a surprise.

Zone	Extension	17.7.1978	26.7.1978	12.8.1978
Irrig.	Point	0.18	0.17	0.13
	Area	0.16 \pm 0.012	0.16 \pm 0.012	0.14 \pm 0.017
Dry	Point	0.18	0.17	0.15
	Area	0.16 \pm 0.010	0.16 \pm 0.010	0.14 \pm 0.012
Mediterranean Sea		-	0.03 \pm 0.004	0.04 \pm 0.007

Table III.1.8. Satellite measured albedo for the irrigated and dry zones of the Crau and an area of 1806 pixels in the Mediterranean Sea (REINIGER et al. 1981).

Unfortunately, no albedo was measured in the ground measuring stations and for commenting the absolute values of the albedo one has to fall back on data in the literature and on albedo measured at INRA Montfavet, about 30 km from the site of the Crau. At Montfavet, albedo of short grass was measured as 0.19 - 0.20, while for a slightly drier, but also continuous grass cover, a higher albedo of 0.25 - 0.27 was observed (SEGUIN 1978b). Measurements of the albedo of natural pasture in Israel carried out from a helicopter gave values of 0.19 in the dry season, and of 0.29 in the rainy season (STANHILL 1970). This form of vegetation should be comparable to that of the dry zone of the Crau.

Compared with these values, the albedo given by the HCMM is somewhat low, especially on 12.8.78. This discrepancy may be due to atmospheric attenuation which could amount to 20 - 40%, and to the difference in the wavelength band, conventional albedo being measured in the 0.4 - 3.0 μ m band compared to 0.55 - 1.1 μ m for the HCMM.

Likewise, the albedo of water was lower by 20 - 40% than the rather constant value of 0.05 given in the literature (MONTEITH 1973). This reduction could eventually be used to correct the albedo of the land surfaces.

The values in Table III 1.7 compare well to the albedo measured by NIMBUS II over the



Fig. III.1.12. Day Thermal Image of the Crau (12.8.78) Geometrically Corrected at a Scale 1:250,000. The Location of the Ground Measuring Stations is Marked with a Cross and "D" for the Dry and "I" for the Irrigated Zone. (Bright is Hot, Dark is Cold) (REINIGER et al., 1981).

ORIGINAL PAGE IS
OF POOR QUALITY

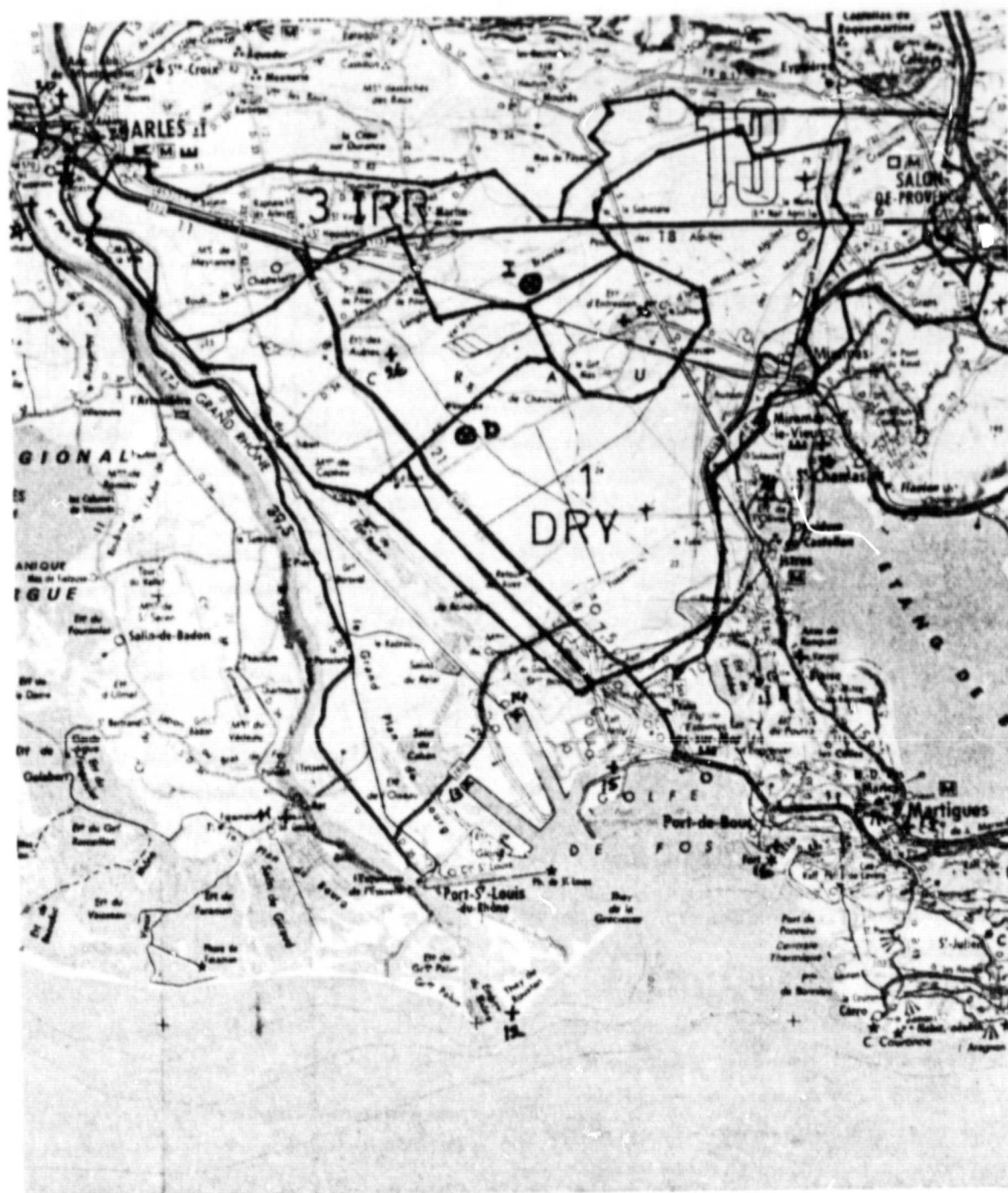


Fig. III.1.13. The Dry (1) and Irrigated Zone (3) of the Crau Delimited on a Topographic Map 1:250,000. The Measuring Stations are Marked D for the Dry and I for the Irrigated Zone (REINIGER et al., 1981).

ORIGINAL PAGE IS
OF POOR QUALITY

coastal region of northern Israel with values of 0.15 - 0.20 on 30 June 1966, and 0.10 - 0.15 on 5 July 1966 (POUQUET and RASCHKE 1968).

Conclusion

From the state of the art in general, and in particular from the results presented in this report, one may conclude that the use of crop surface temperatures does not give better local estimates of evapotranspiration than other, conventional, methods. On a regional scale, the use of HCMM, or similar satellite daytime surface temperatures, necessitates the elimination of atmospheric effects if any useful estimation of ET is to be attempted.

For the evaluation of ET, the use of consecutive night/day temperatures showed to have no advantage over the use of the daily maximum temperature only, but four or five temperature measurements during the daily cycle should provide a better estimate of ET.

Furthermore, if ET models developed for ground measured surface temperatures are to be employed, satellite measured surface temperatures have to be firmly correlated with these ground measured data. An alternative solution could be seen in establishing simplified relations of the ET_{JT} -type directly between ET and satellite measured surface temperatures.

On the other hand, HCMM daytime thermal images showing temperature differences between comparable surfaces, should permit to identify water stressed areas. They should also permit to delimitate zones of ET by interpolating between the network of ground measuring stations.

Composition of Working Group II :

Permanent Members:

F. E. Eckard, Institute of Plant Ecology, University of Copenhagen, Copenhagen, Denmark.

B. Seguin, INRA - Station de Bioclimatologie, Montfavet, France.

R. R. van der Ploeg, Institut für Bodenkunde und Waldernährung der Georg-August-Universität, Göttingen, Germany.

G. Maracchi, Istituto di Agronomia Generale e Coltivazione Erbacee, Università di Firenze, Firenze, Italy.

R. A. Feddes, Instituut voor Cultuurtechniek en Waterhuishouding (ICW), Wageningen, The Netherlands.

R. J. Gurney, Institute of Hydrology, Wallingford, U.K.

P. Reiniger (Coordinator), Commission of the European Communities, Joint Research Centre (JRC), Ispra (Italy).

Collaborating Members:

F. Becker, Université Louis Pasteur, Strasbourg, France.

A. Perrier, INRA - Station de Bioclimatologie, Versailles, France.

A. Rosema, Engineering Consultants for Environmental Analysis and Remote Sensing (EARS), Delft, The Netherlands.

G. Tassone, Commission of the European Communities, Joint Research Centre (JRC), Ispra (Italy).

ORIGINAL PAGE IS
OF POOR QUALITY

References

- BAELZ S., 1980. Utilisation de thermographies infrarouge recueillies par satellite pour le calcul de l'évapotranspiration à l'échelle régionale. Thèse du doctorat 3ème cycle, Univ. Paris VI - Pierre et Marie Curie, Dec. 1980, 124 pp.
- BECKER F. and HECHINGER E., 1979. Potentialités de la télédétection pour l'étude des mécanismes de transfert et la mesure des flux échangés entre sol et atmosphère. Tellus Project, 4th Meeting of Working Group II, Monterotondo, November 20-21, 1979.
- BECKER F., NGAI W. and STOLL M. P., 1980. An active method for measuring thermal infrared effective emissivities: Implications and perspectives for remote sensing. Tellus Newsletter 21, JRC, Ispra, 18 pp.
- BOUCHET P. J., 1963. Evapotranspiration réelle et potentielle: Signification climatique. Gen. Ass. Berkeley. Inter. Ass. Sci. Hydro. Publ. 62, 134-142.
- BOWEN J. S., 1926. The ratio of heat losses by conduction and by evaporation from any water surface. Phys. Rev. 27, 779-787.
- BROWN K. W. and ROSENBERG N. J., 1973. A resistance model to predict evapotranspiration and its application to a sugar beet field. Agron. J. 65 (3), 341-347.
- BRUTSAERT W. and MAWDSLEY J. A., 1976. The applicability of planetary boundary layer to calculate regional evapotranspiration. Water Resources Res. 12, 852-859.
- CARLONI E., TASSONE G. and TOSELLI F., 1981. Actual evapotranspiration of a grass field in southern Italy. Applications and validity of an agrobioclimatological model. Technical Note No. 1.06.10.81.52, JRC, Ispra.
- CHOISNEL E., 1977. Le bilan d'énergie et le bilan hydrique du sol. La météorologie, No. spécial "Evapotranspiration", VIe Série, No. 11, 108-159.
- DAIAN J. F. and VACHAUD G., 1971. Méthode d'évaluation du bilan hydrique in situ à partir de la mesure des teneurs en eau et des suctions. Proc. IAEA-FAO Symp. "Isotopes and radiation in soil-plant relationship including forestry", Vienna, Dec. 13-17.
- DEJACE J., MEGIER J., KOHL M., MARRACCI G., REINIGER P., TASSONE G. and HUYGEN J., 1979. Mapping thermal inertia, soil moisture and evaporation from aircraft day and night thermal data. 13th Int. Symp. on Remote Sensing of Environment; Ann Arbor, USA, 23-27 April, 1979.
- GREGOIRE J. M., 1980. Détermination de l'évapotranspiration d'un couvert végétal herbacé et de l'humidité de surface du sol: Apport de la télédétection. Thèse 3ème cycle, Université Louis Pasteur de Strasbourg. Jan. 1980, 164 pp.
- HLAVEK R. et al., 1974. Essai d'estimation de l'évapotranspiration réelle à l'échelle du bassin versant: considérations théoriques et applications pratiques. Bull. AIMS, 19 (4), 449-485.
- HUYGEN J., 1979a. Further developments of the TELL-US model: I. An implicit finite difference scheme for the numerical approximation of the ground heat flux. Tellus Newsletter No. 11, JRC, Ispra, 8 pp.
- HUYGEN J., 1979b. Further developments of the TELL-US model: II. A simple algorithm for estimating the actual and potential evapotranspiration of vegetated surfaces from one remotely sensed surface temperature near the daily maximum. Tellus Newsletter No. 11, JRC, Ispra, 8 pp.
- HUYGEN J. and REINIGER P., 1979. A test of the TELL-US model for the conditions of the Grendon Test Site (JFE/UK - 1977). Tellus Newsletter, No. 8, JRC, Ispra, 16 pp.
- IDSO S. B., JACKSON R. D. and REGINATO R. J., 1978. Remote sensing for agricultural water management and crop yield prediction.

Agric. Water Manage., 1, 229-310.

JACKSON R.D., REGINATO R.J. and IDSO S.B., 1977. Wheat canopy temperature: a practical tool for evaluating water requirements. Wat. Resources Res. Vol. 13 (3), 651-656.

KEIJMAN I.Q. and DE BRUIN H.A.R., 1979. A comparison of measured and calculated temperatures of a grass covered surface. 5th European Geophysical Society Meeting, Vienna.

KLAASSEN W., 1979. Resistance for sensible heat flux of vegetation as derived from radiometrically measured crop temperatures. Nota 1067, ICW, Wageningen, The Netherlands.

KLAASSEN W. and ROSEMA A., 1979. Generalisation of the TELL-US model to vegetated surfaces. EARS, Delft, The Netherlands. Report to the Commission of the European Communities, Joint Research Centre, Ispra, under contract no. 943-78-10 SISPN, 18 p.

MALET Ph. and GUYOT G., 1978. Principes de détermination des systèmes culturels et de leur potentiel de production par télédétection. Proc. Int. Symp. Remote Sensing for Observation and Inventory of Earth Resources and the Endangered Environment. July 2-8, 1978. Freiburg. Vol. III, 1665-1670.

MENENTI M., 1980. Defining relations between surface characteristics and actual evaporation rate. Tellus Newsletter No. 15, JRC Ispra, 21 pp.

MONTEITH J.L., 1973. Principles of Environmental Physics. Edward Arnold (Publishers) Ltd., London, 241 pp.

MORTON F.I., 1975. Estimating evapotranspiration from climatological observations. Appl. Meteorol. 14, 448-497.

NIEUWENHUIS G.J.A. and KLAASSEN W., 1978. Estimation of the regional evapotranspiration from remotely sensed crop surface temperature. Part I: Grass land. Tellus

Newsletter No. 2, JRC, Ispra, also Nota 1055 ICW, Wageningen, 21 pp.

NIEUWENHUIS G.J.A., MENENTI M. and FEDDES R.A., 1980. Soil moisture and heat budget evaluation by remote sensing (TELLUS Project). Report of ICW, 13 pp.

PERRIER A., 1977. Projet de définition concernant l'évapotranspiration en fonction de considérations théoriques et pratiques. La météorologie, VIe Série, No. 11, 7-16.

PERRIER A., ITIER B., BOISSARD P., GOILLOT C., BELLUOMO P. and VALERY P., 1980. Etude des températures radiométriques: fluctuations, repartitions, significations. Tellus Newsletter No. 13, JRC, Ispra, 34 pp.

POUQUET J. and RASCHKE E., 1968. A preliminary study of the detection of geomorphological features over northeast Africa by satellite radiation measurements in the visible and infrared. NASA, TND. 4648.

PRICE J.C., 1980. On the atmospheric correction to satellite thermal infrared measurements. Communication to HCMM investigators, Goddard Space Flight Center, Maryland.

RADMUSSEON E.M., 1977. Hydrological application of atmospheric vapour flux analysis. WMO Operational Hydrology. Rep. 11, 50 pp.

REINIGER P., HUYGEN J., MEGIER J. and SEGUIN B., 1981. Estimates of regional evapotranspiration in south-eastern France using thermal and albedo data from the Heat Capacity Mapping Mission satellite. 1st Thematic Conference: Remote Sensing of Arid and Semi-Arid Lands", Cairo, Egypt, Nov. 1981.

ROSEMA A. and BIJLEVELD J.H., 1977. Test of algorithm for the determination of soil moisture and evaporation from remotely sensed surface temperatures. EARS, Delft, The Netherlands, Report to the Commission of the European Communities, Joint Research Centre, Ispra, under contract no. 752-77-08 SISPN, 33 p.

- ROSEMA A., BIJLEVELD J.H., REINIGER P., TASSONE G., BLYTH K. and GURNEY R.J., 1978. "Tell-us", a combined surface temperature, soil moisture and evaporation mapping approach. 12th Int. Symp. on Remote Sensing of Environment, Manila, Philippines, 20-26 April, 1978.
- RUSSO D. and BRESLER E., 1980. Scaling soil hydraulic properties of a heterogeneous field, *Soil Sci. Soc. Am. J.* 44, 681-684.
- SEGUIN B., 1978a. Modélisation des échanges d'énergie et de masse à l'interface-sol-atmosphère: problèmes posés par l'extension des modèles locaux à l'échelle régional (100 km). Séminaire de l'ASP "Evolution des Clirnats", Paris, 11-12 December, 19 pp.
- SEGUIN B., 1978b. Estimates of regional ET from HCMM data: Summary of 1977 experiment and final arrangement for 1978 in South-eastern France Test Site. 2nd Meeting of Tellus Project Working Group II, Wallingford, February 21-22, 1978.
- SEGUIN B., 1980. Détermination de l'évapotranspiration réelle ETR dans les bilans hydrologiques par télédétection en thermographie infrarouge. *Bull. Sci. Hydrol.* 25 (2), 143-153.
- SEGUIN B. and PETIT V., 1980. Utilisation de la thermographie infrarouge pour l'estimation de l'évaporation: Analyse critique des résultats de mesures sur le site de la Crau. *Tellus Newsletter* No. 16, JRC, Ispra, 12 pp.
- SIMMONS C.S., NIELSEN D.R. and BIGGAR J.W., 1979. Scaling of field-measured soil-water properties. I. Methodology II. Hydraulic conductivity and flux, *Hilgardia* 47 (4), 77-173.
- SOER G.J.R., 1977. The TERGRA model - A mathematical model for the simulation of the daily behaviour of crop surface temperature and actual evapotranspiration. NIWARS Publ. No. 46, Delft, The Netherlands, 44 pp.
- SOER G.J.R., 1980. Estimation of regional evapotranspiration and soil moisture conditions using remotely sensed crop surface temperature. *Rem. Sensing of Env.* 9, 27-45.
- STANHILL G., 1970. Some results of helicopter measurements of the albedo of different land surfaces. *Solar Energy* 13, 59-66.
- STONE L.R. and HORTON M.L., 1974. Estimating evapotranspiration using canopy temperatures: Field evaluation. *Agron. J.* 66, 450-454.
- THOM A.S., 1972. Momentum, mass and heat exchange of vegetation. *Quart. J. Royal Met. Soc.* 98, 124-134.
- THOM A.S. and OLIVER H.R., 1977. On Penman's equation for estimating regional evaporation. *Quart. J. Royal Met. Soc.* 103, 345-357.
- VAN DER PLOEG R.R., BEESE F. and BENECKE P., 1976. Simulationsmodelle von Wald-Ökosystemen: Wasser. *Verhandlungen der Gesellschaft für Ökologie*, Göttingen, 1976, p. 29-41.
- WALES-SMITH B.G. and ARNOTT J.A., 1979. The rainfall and evaporation calculation system used in Great Britain. W.M.O.

2. Field Operations. Data Acquisition and Analysis

R.A. Feddes
Instituut voor Cultuurtechniek en Waterhuishouding
Wageningen, Nederland

P. Reiniger, Physics Division
G. Tassone, F. Toselli, Electronics Division
Commission of the European Communities, Joint Research Centre, Ispra, Italy

ORIGINAL PAGE IS
OF POOR QUALITY

Field operations carried out on various test-sites had the purpose of testing the algorithms, to be used for the interpretation of HCMM data. The data collected by the JRC and the Coinvestigators served to prepare the necessary data processing routines and acquainted the co-investigators with handling and interpretation of this type of data.

Field operations were of two kinds:

- flight experiments involving both airborne and ground-based measurements of a duration of a few days,
- continuous field measurements lasting a number of weeks or even one month.

Flight Experiments

Five campaigns took place at the request of national Coinvestigators. While the Dutch flights were organized by the National Institutes, the U.K., French, Italian and German flights were Joint Flight Experiments (JFE) with the participation of both National Institutes and the Joint Research Centre.

The Netherlands

(Instituut voor Cultuurtechniek en Waterhuishouding, Wageningen; Koninklijk Nederlands Meteorologisch Instituut, De Bilt)

1. Description

Flights with an airborne MSS having 10 channels between 0.38 and 1.1 μm and one thermal infrared channel from 8-14 μm were performed over two areas. The first area, located in the Lopikerwaard (51° 38' N, 4° 55' E) consisted mainly of grassland on clay soil. The second area was situated in the IJssel Lake Polder (50° 13' N, 7° 3' E) and was occupied by various agricultural crops, especially wheat, sugar beet and potatoes. The soil was a silty clay.

Flight altitude was 1200 m resulting in 2.5 x 3 m resolution elements on the ground. The flights were carried out at the maximum of the daily temperature amplitude between 12 and 14 h solar time. The dates were May 15, June 14 and August 31, 1977 for the Lopikerwaard and May 17 and June 14, 1977 for the IJssel Lake Polder.

The purpose of the flights was testing of the TERGRA model for evaluating ET and soil moisture from crops surface temperatures. Details of the operation, as well as a description of the instrumentation on the ground is given in TELLUS NEWSLETTER No. 2 [1].

2. Results and Conclusions

On thermal scanner images the relation scan angle/sun angle considerably influenced the temperature measured.

For grassland, as well as for wheat, calculation of evapotranspiration from remotely sensed surface temperatures only was unreliable. Crop (wheat) temperatures simulated with the TERGRA model were higher, by a few degrees, than measured temperatures.

France

(Joint Research Centre, Ispra; Institut National Recherches Agronomiques, Station Avignon; Institut National Recherches Agronomiques, Service Télédétection, Versailles)

1. Description

A Joint Flight Experiment (JFE/France) was carried out on Sept. 30, 1977 on the French test site of the Beauce along a flight axis of 20 km centered on a point south of Chartres ($48^{\circ} 13' 49''$ N, $1^{\circ} 36' 01''$ E). The flight axis crossed a mixed agricultural area covered mainly by corn, sugar beet, stubble and bare soil.

One experimental plot on wheat stubble was equipped for measurements of the energy balance. Surface temperatures were measured on the ground with a mobile PRT-5 infrared thermometer.

Two flights at 1700 m altitude were carried out along the same axis, the night flight at 00.52 h and the consecutive day flight at 13.05 h local time. On-board instrumentation consisted of a 10-channel Daedalus MSS, a Daedalus thermal scanner 8-14 μ m, a PRT-5 infrared radiometer and a 4-channel SAT thermal scanner.

The purpose of the JFE was an investigation of the surface temperature distribution in various

types of vegetation. Details of the operation including a description of the instrumentation are given in TELLUS NEWSLETTER No. 13.

2. Results and Conclusions

Surface temperature variations were found to be larger inside one crop than between various fields of the same crop. During the day, meteorological data needed for the interpretation of remotely sensed surface temperatures should be obtained at exactly the same time as the surface temperature.

Thermal data from this flight was used to simulate HCMM resolution over a mixed agricultural area. The result of this simulation is reported in TELLUS NEWSLETTER No. 1.

United Kingdom

(Joint Research Centre, Ispra; Institute of Hydrology, Wallingford; Geography Institute, University of Leeds; Geography Institute, University of Reading)

1. Description

A Joint Flight Experiment (JFE/UK) was carried out on Sept. 13 on the U.K. test site along two flight axes of 10 km each. The first flight axis was over the Grendon-Underwood Experimental Catchment (1° W, $51^{\circ} 53'$ N) composed of gently sloping land with fields of up to 15 ha. The second flight axis passed over the Newbury area ($1^{\circ} 44'$ W, $51^{\circ} 20'$ N) with fields up to 12 ha. Soils on the two sites ranged from brown calcareous soils and surface water gley to clays. Land-use was cropland (cereals) and grassland with some forest and market gardening.

Grassland and bare soil were instrumented on the Grendon site, measuring points on arable soil, grassland and bare soil were established on the Newbury site.

Two consecutive flights at an altitude of 1000 m

were carried out along the same flight path: A night flight between 04.25 and 05.15 GMT and a day flight between 12.45 and 13.55 GMT. On-board instrumentation consisted of a Dae-dalus DS-1250 MSS with a thermal channel from 8-14 μm . A Barnes PRT-5 infrared thermometer coupled to a Hasselblad camera and a RC-883 camera.

The purpose of the JFE was acquiring experience in the interpretation of thermal imagery of agricultural land surfaces. In particular, data were obtained to test the algorithms TERGRA and TELL-US for the evaluation of soil moisture and evapotranspiration from remotely sensed surface temperatures.

2. Results and Conclusions

The thermal and VIS-IR airborne MSS data obtained during the campaign were of excellent quality. They were used to develop data processing routines such as geometric corrections and the superposition of day and night images. They also served as data for speeding up the execution of the TELL-US algorithm and for testing the sensitivity of both the TERGRA and TELL-US model.

An important part of this work has been carried out at the JRC-Ispra, Image Processing Laboratory.

2.1 TELL-US Model Application

Soil moisture and evaporation was mapped by processing in the TELL-US model pixel by pixel values of day and night surface temperature and albedo, together with ground data (e. g. surface roughness) varying field by field and meteorologic data (e. g. solar radiance, windspeed, air temperature) valid for the whole flight strip. To this purpose, a tabulated version of the algorithm was prepared which used multiple interpolations within tables to reduce processing time to a few msec per pixel.

The scanner data were first corrected for scan angle effect and for geometry to permit superposition of night thermal data on day visible thermal data (see Part 5, Ch. 3 C) [2].

Three types of thematic maps were obtained representing thermal inertia, soil moisture and cumulative daily evaporation of bare or vegetated areas (bare soil, burnt and unburnt stubble, stubble with some green shoots). Each of the three parameters had five to seven classes of magnitude and was presented with a ground resolution of 2.5 x 2.5 m, equal to that of the scanner data.

It could be confirmed that a detailed mapping of thermal inertia, soil moisture and cumulative daily evaporation was possible using a complex model like TELL-US. Obviously, the data processing scheme developed is independent of the intrinsic performance of the model and each further improvement of the latter will bring some corresponding improvement of the thematic maps produced.

The comparison with measured soil moisture values suffers from experimental uncertainties, but it seems to indicate a tendency to underestimate soil moisture content. Direct measurements of evaporation were not available at Grendon, but independent calculations of ET agree, within 10%, with the values obtained by TELL-US. In inhomogeneous areas, like burnt stubble, where temperature, albedo and surface roughness vary considerably in space, these variations tend partially to mask the smoother evolution of moisture and evaporation.

Figs. III.1, 14 to 22 are displays of mapped temperatures, albedo, cumulative daily evaporation, soil moisture and thermal inertia for the overflown area of Grendon, U. K. [2].

An analysis of the sensitivity of the TELL-US

model to various input parameters and to the value of the soil heat capacity used in the model was presented in TELLUS NEWSLETTER No. 8. In calm air, as often found at night, the variations in air temperature due to topography and ground-cover may have an important influence on the thermal inertia calculated with the TELL-US model.

2.2 TERGRA Model Application

A sensitivity analysis of the model carried out for the grassland site at Grendon showed the model not to be sensitive to soil parameters at the soil moisture range found on the site.

Cumulative daily evapotranspiration agreed, to within 10%, with ET calculated from Bowen ratio measurements on the Newbury site. The same agreement was found between calculated and measured soil moisture on grassland.

2.3 Spectral Reflectance

The spectral reflectance in the four Landsat bands was measured on the ground on four surfaces during the flight. The surfaces were bare soil, stubble, grassland and burnt stubble. These reflectances were compared with the airborne MSS measurements.

At lower wavelengths good agreement was found between airborne and ground measure reflectance factors. At higher wavelengths, especially on grassland, there was an increasing discrepancy between the two measurements. A systematic error in the calibration of the airborne multispectral scanner seems to be largely responsible for this discrepancy.

Italy

Joint Research Centre, Ispra; CSATA, Bari; Institute of Agronomy, University of Bari; Institute of Agronomy, University of Florence; Institute of Physics, University of Bari; UCEA, Ministry of Agriculture, Rome; LAREV, Consiglio Nazionale delle Ricerche, Rome)

Description

The first Joint Flight Experiment after the HCMM launch was carried out on July 1979 on an area of 2x3 Km of a semiarid region along the Joanian coast (Sibari, Southern Italy; 39°N, 16°E). The area investigated, parcelled in fields of 3 ha each, is flat and devoid of trees, bushes and buildings. The general texture of all the profiles is silty loam with increase of the clay fraction in depth. There is no superficial water table. The purpose of this experimental campaign was to investigate on the possibility to use air-and-space remote sensing as a help to evaluate quantitatively evaporation (and soil moisture) in semi-arid lands referring to local types of soil and vegetation. The use of models such as TELL-US and TERGRA (or similar) which were preliminarily tested during the preceding Dutch and Britain flight experiments, was considered, having in mind to obtain possibly some handy particular algorithms.

The flights were performed at three different altitudes (500 m, 1000 m, 3000 m) on two consecutive days (July 30 and 31) at a 14 and 3 hrs respect., nearly corresponding to the HCMM overpasses. The aircraft (Dornier 28 D2) was equipped with an 11-channel MSS Bendix, a Zeiss RMK camera for FC photos and a PRT-5 radiometer. General weather conditions were very good with no haze before sunrise.

Ground measurements were taken on two sugar-beet fields and on two bare soil fields with different moisture contents. Heat balance components were measured continuously and data logger-recorded before, during and

ORIGINAL PAGE IS
OF POOR QUALITY

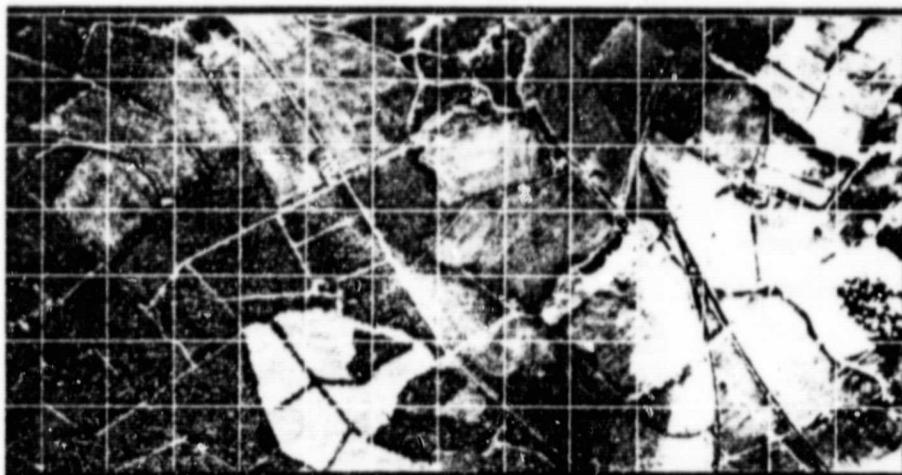


Fig. III.1.14. Mapped night temperatures, original data. Range of variation 0° C - 18° C (radiative values).

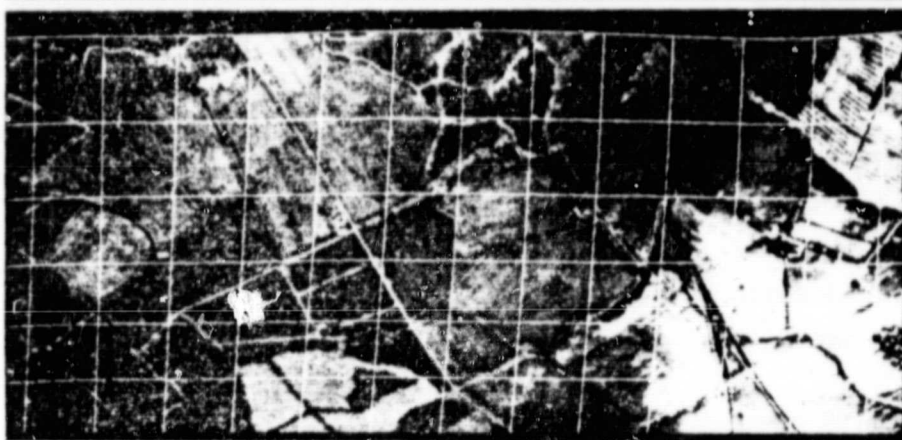


Fig. III.1.15. Mapped night temperatures. Data geometrically corrected. The transformation is visible through the grid deformation.



Fig. III.1.16. Mapped day temperature. Range of variation 8° C - 44° C (radiative values).



Fig. III.1.17. Mapped albedo values. Range of variation 0.02 - 0.20 in the investigated fields.

ORIGINAL PAGE IS
OF POOR QUALITY

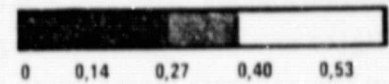


Fig. III.1.18. Cumulative daily evaporation calculated by TELLUS and mapped in 5 grey levels (mm).
1: bare soil; 2: stubbles; 3: burnt & unburnt stubbles; 4: stubbles with green shoots; 5: stubbles & cropped cereals.

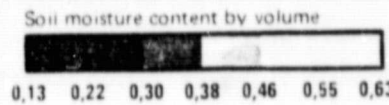


Fig. III.1.19. Thermal inertia and soil moisture calculated by TELLUS and mapped in 6 grey levels.

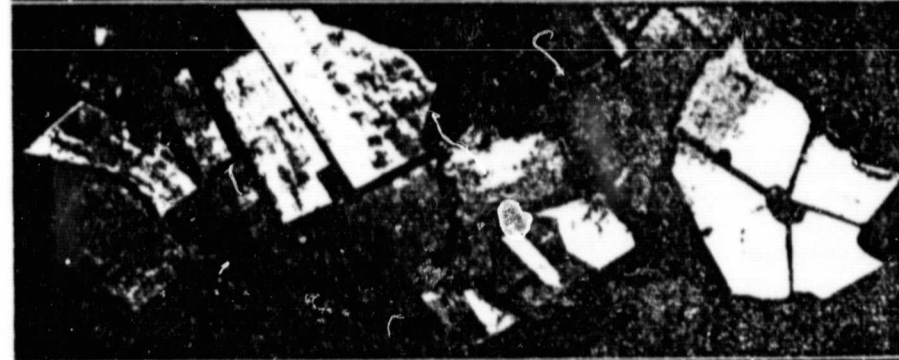


Fig. III.1.20. Difference between Fig. 9 and Fig. 8 mapped in 5 grey levels.

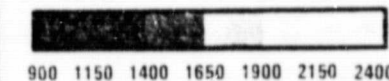


Fig. III.1.21. Apparent thermal inertia mapped in 6 grey levels.

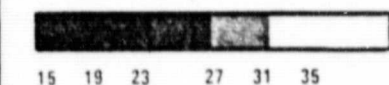


Fig. III.1.22. Temperature differences ($T_d - T_n$) mapped in 6 grey levels.

after flights. VIS-NIR and IR radiometric measurements were taken during the over-flights on a regular array of prefixed spots by two separate teams using portable instruments (EXOTECH 100 and PRT-5). Soil moisture contents were then determined by weighting soil samples taken on each field at different points and depths.

To take into account atmospheric effects, a calibration panel of 10x10 m was built (see Fig. III.1.23). Its known optical behaviour was continuously monitored both in the VIS-NIR and IR bands by means of three radiometers on ground.

Details of the operation including a description of the instrumentation are given in Progress Report No. 2.

Results

The MSS data were preprocessed to correct for geometric distortions, atmospheric effects and emissivity and to superpose thermal day-to-night images. 803 samples and 1536 lines, taken from the 1000 m-high flight line were utilized having a resolution on ground of 2.5x2.5 m² at nadir sub-point. The "Sigmoid curvature" was corrected by tabulating the geometric transformation and resampling with the "nearest neighbouring" technique which allowed to maintain the same input radiometric values. Fifty ground points of the same targets in the two images were selected with an iterative procedure by utilizing the flickering option between the two images to be registered. Taking the day image as a reference, the coefficients of a cubic polynomial function were derived and used for the transformation of the night image.

As a first step, to obtain soil real temperatures, thermal data were corrected for the atmosphere absorption using an empirical approach consisting in calculating the differences between the radiative temperatures of the panel and soil, given by the two local mounted PRT-5 radiometers, and the cor-

responding MSS temperature. A curve giving temperature corrections versus ground temperatures was so obtained (see Fig. III.1.24). It showed to be in good agreement with the simplified Becker's model results. For the conversion of radiative temperatures into real temperatures, an emissivity mean value of 0.965 was used.

To produce thematic maps, the TELL-US model was used which calculates, for a given set of agro-meteorological parameters, a look-up table (see Fig. III.1.6). A search and an interpolation must be carried out if thermal inertia (THI), surface relative humidity (SRU) and cumulative evaporation (CE) are needed for values of T_{max,min} other than the 30 ones provided by the look-up tables. As the controlled soil fields at Sibari were composed by 5480 pixels, a faster procedure was adopted by using the following relationship

$$THI = A_1 T_{max} + A_2 T_{max}^2 + A_3 T_{min} + A_4 T_{min}^2 + A_5$$

SRU

whose coefficients were calculated by a least square multiple regression analysis. The 30 values contained in each look-up table were fitted and correlation coefficients better than 0.996 were obtained. THI, SRU and CE were then built into image form knowing T_{max,min} for each preprocessed pixel. The pixels of the wet and dry fields were identified analysing the T_{max} histogram which showed a bimodal distribution corresponding to different hydrological conditions.

Highest frequency values were found to be at a 42.5°C and 37 °C resp. for the dry and wet fields with very low variances. Frequency values near zero resulted to be at 39°C. They were then adopted to discriminate between pixels of the two fields.

Conclusions

The results obtained proved that the procedure adopted allows mapping of soil thermal inertia and evapotranspiration using air remote sensed

data. Ground measured data, still necessary at this stage of modelling and interpretation, burdens heavily the work; when not available it would make quantitative evaluation almost impossible. The importance of thermal remote sensing data results to be confirmed to provide useful qualitative information on soil/plant status over large agricultural areas. An extension of the investigation on the applicability of the models with HCMM data could not be performed because no HCMM imagery was available from NASA/GSFC in spite of the priority coverage requested.

**ORIGINAL PAGE IS
OF POOR QUALITY**

Germany

(Joint Research Centre, Ispra; Institut für Bodenkunde und Waldernährung, Universität Göttingen; Bundesanstalt für Geowissenschaften und Rohstoffe, Hannover; Institut für Meteorologie und Limnologie, Universität Hannover; Institut für Pflanzenbau und Pflanzenzüchtung, Universität Göttingen; Niedersächsisches Landesamt für Bodenforschung, Hannover; Systematisch-Geobotanisches Institut, Universität Göttingen; ZAF von Deutscher Wetterdienst, Braunschweig; Department of Geography, University of Leeds; Department of Geography, University of Reading; Institute of Hydrology, Wallingford)

Description

The campaign in West Germany, 3 - 27 June 1979, concluded the Joint Flight Experiments of the TELLUS Project. It was carried out at Pattensen (52°15'N), near Hannover on a 5x4 Km large agricultural area (nearly 70 HCMM satellite pixels). This test area offers many favourable features with respect to water and energy budget evaluation. It is rather parcelled out: the individual fields have an average size of nearly 7.5 ha and the land shows practically no relief in an open landscape without trees, bushes and buildings. The soils, which are developed in a pleisto-

genic-loess layer of nearly 2 m thick, are quite homogeneous. The water table is at a depth of 2-3 m.

The original purpose of this experiment was to collect some comprehensive sets of concurrent space, air and ground data over a wide agricultural area which would be sufficiently homogeneous on the HCMM resolution point of view. This would have enabled TELLUS to test the existing evapotranspiration (and soil moisture) algorithms at HCMM scale and to perform some scale effect studies.

At the moment of the flight experiment about 2/3 of the test area was covered with cereals (wheat and barley) and 1/3 with sugar-beet. Seven fields were chosen by Coinvestigators for detailed agrometeorological, radiometric and soil measurements. One test plot was located in a bare soil field. As test plots some either wheat, barley and sugar-beet fields were selected. Moreover an irrigation pond was specifically monitored during the flight time to be used as a calibration surface for the aircraft MSS data (see Fig. III.1.25).

The campaign was characterized by a continual atlantic perturbation. Nevertheless the aircraft experiment could regularly take place in clear weather conditions on June 21 from 12.30 to 14.30 hrs and on June 22 from 1.58 to 3.11 hrs. The aircraft utilized was an Air-commander Twin. Flight altitudes were nearly 500, 1000 and 3000 m resp. The on-board remote sensing equipment consisted of an 11-channel MSS Daedalus and a Zeis MRK camera for FC photos.

Details of the operation, including description of the instrumentation and experimental data are given in Progress Report No. 3.

Results and conclusions

The air flights were performed corresponding to two day/night consecutive HCMM overpasses. Unfortunately, still in this case, the full satellite switch-on was not obtained. Nevertheless, despite the interest of such last campaign has rather fallen off, processing and

interpretation of data is going to be performed by Coinvestigators at lower priority level. The data have been treated for heat transfer, roughness determination and Bowen ratio. In spite of the instability of weather conditions during the experiment, the resulting thermal inertia values are in good agreement with soil moisture measurements (gravimetric and tensiometric) and the evaporation values are in agreement with those calculated out of the heat budget.

The application of the model for bare soil (TELL-US) is then expected to confirm that the agreement with the experimental data is good and can lead to the production of the thematic maps at a larger scale.

Continuous Field Measurement Campaigns

Among the field measurement campaigns carried out by TELLUS coinvestigators, three of them can be considered as long term ones. The first two, organized by INRA Montfavet, covered the period July - October 1978 and April 1979 - March 1980 and are extensively reported in Chapter 1. The third campaign is described hereunder.

Italy

(Joint Research Centre, Ispra; Institute of Agronomy, University of Bari; CSATA Bari)

The JRC, Ispra organized this long term field campaign at Policoro, Basilicata (Southern Italy, $40^{\circ}13'N$; $16^{\circ}40'E$) in an experimental farm (nearly 45 ha) of the University of Bari. The Policoro soil can be classified as a silty-clay-loam soil of good structure with water table at a depth greater than 2.5 m.

Measurements were taken continuously from June 24 to July 21, 1978, on a 60 x 60 m field very densely covered by grass. The field was subdivided into two sections submitted to different irrigation regimes. The aim of this campaign was to check in semi-arid regions the evapotranspiration

models, which had been previously tested in Middle European humid conditions, as those at Grendon Underwood (JFE/UK). A complete set of ground instrumentation was installed (see Fig. III.1.26 and Table III.1.9). Sensors were connected with data logger and tape recorder. Measurements were taken every 10 minutes.

Results and conclusions

The model used (TERGRA) confirmed to underestimate (16%) the evapotranspiration as compared with the Bowen ratio and to systematically overestimate the grass temperature during the period of maximum evapotranspiration, which ranges 7.30 - 19.30 hrs. Within the Policoro area the air temperature was nearly continually higher than the crop temperature. The Bowen ratio showed that evapotranspiration ET is higher than the net radiation R_N . This trend was confirmed by direct measurements of R_N and sensible heat flux H (via wind speed and Businger-Dye relationship) showing that H contributed significantly to the ET process.

A sensitivity analysis was carried out aimed at explaining such behaviour of TERGRA. It was found that the soil parameters were un-influential on the Policoro conditions (soil moisture at potential ET) and that measurement accuracy of some other parameters (i.e. air temperature (wet/dry), solar and long wave radiation and wind speed) ruled out their responsibility on those temperatures' discrepancies. It appeared clearly that crop and aerodynamic resistances brought up crop temperature values and that the model indicated a water stress status (never observed in Policoro) bringing consequently to a reduced evapotranspiration. From calculations on Policoro conditions, a difference of $3^{\circ}C$ in crop temperatures would bring a $\Delta ET = 20\%$. It resulted also that crop temperature values calculated by means of TERGRA might lead to a considerable error in ET estimation.

References

- Commission of the European Communities, Joint Research Centre of Ispra, 1979, HCMM Satellite follow-on investigation No. 025. Soil Moisture and Heat Budget evaluation in selected European zones of agricultural and environmental interest (TELLUS Project). First Progress Report, April 1st - August 31st, 1979.
- Id. Second Progress Report, April 1st - August 31st, 1979.
- Id. Third Progress Report, April 1st - August 31st, 1980.
- J. Huygen and P. Reiniger, 1978. A test of the TELL-US model for the conditions of the Grendon test-site (JFE/UK, 1977) TELLUS Newsletter No. 8, Ispra, May 1979.
- G. Maracci, 1979. Comparison of spectral reflectances measured by airborne scanner and on the ground, TELLUS Newsletter No. 8, Ispra, August 1979.
- A. Perrier, B. Iher, P. Boissard, C. Goillot, P. Belluomo and P. Valery, 1979. Etudes de temperatures radiométriques: Fluctuations, repartitions, significations. TELLUS Newsletter 13, Ispra, Feb. 1980.
- G. J. A. Nieuwenhuis, 1979. Application of HCMM satellite and airplane reflection and heat maps in agro-hydrology. TELLUS Newsletter 19, Ispra, 1980.
- E. Carloni, G. Tassone and F. Toselli, 1981. Actual evapotranspiration of a grass field in Southern Italy. Applications and validity of an agrobioclimatological model. Technical Note No. 1.06.10.81.52, JRC Ispra.
- J. Dejace, J. Megier, M. Kohl, G. Maracci, P. Reiniger, G. Tassone and J. Huygen, 1979. Mapping thermal inertia, soil moisture and evaporation from aircraft day and night thermal data. 13th Int. Symp. on Remote Sensing of Environment; Ann Arbor, USA, 23-27 April, 1979.
- L. Boriello, E. Carloni, T. Caroppo, G. Tassone and F. Toselli, 1981. Processing of remotely sensed data for mapping thermal inertia, soil moisture and EVT on semi-arid areas. First Conf. on Remote Sensing of Arid and Semi-arid Lands, El Cairo, Jan. 1982.
- G. Maracci, G. Tassone and F. Toselli, 1981. The use of a reference panel in airborne multispectral scanner. Proc. of the Int. Colloquium on Spectral Signatures of Objects in Remote Sensing; Avignon, 8-11 Sept. 1981.
- F. Becker, 1977. Thermal infrared remote sensing. Principles and Applications. Adv. Seminar on Remote Sensing, Joint Research Centre, Ispra, Italy, 1977.
- A. Callandro, S. Galli de Paratesi, G. Tassone and F. Toselli, 1979. Metodologia ed applicazione del telerilevamento per il bilancio idrologico dei terreni agricoli, 3^o Convegno Naz. AIGR, Catania, 16-19 Maggio 1979.
- R. R. Van Der Ploeg, G. Tassone and J. Von Hoyningen-Huene, 1980. The Joint Measuring Campaign 1979 in Ruthe (West Germany). Description and preliminary data (Internal Report).

ORIGINAL PAGE IS
OF POOR QUALITY



Fig.III.1.23. Joint Flight Experiment, Sibari 1976. Aerial view from the 500 m altitude of the bare soils fields:
1) $10 \times 10 \text{ m}^2$ calibration panel; 2) dry; 3) wet field parts.

ORIGINAL PAGE
COLOR PHOTOGRAPH

ORIGINAL PAGE IS
OF POOR QUALITY

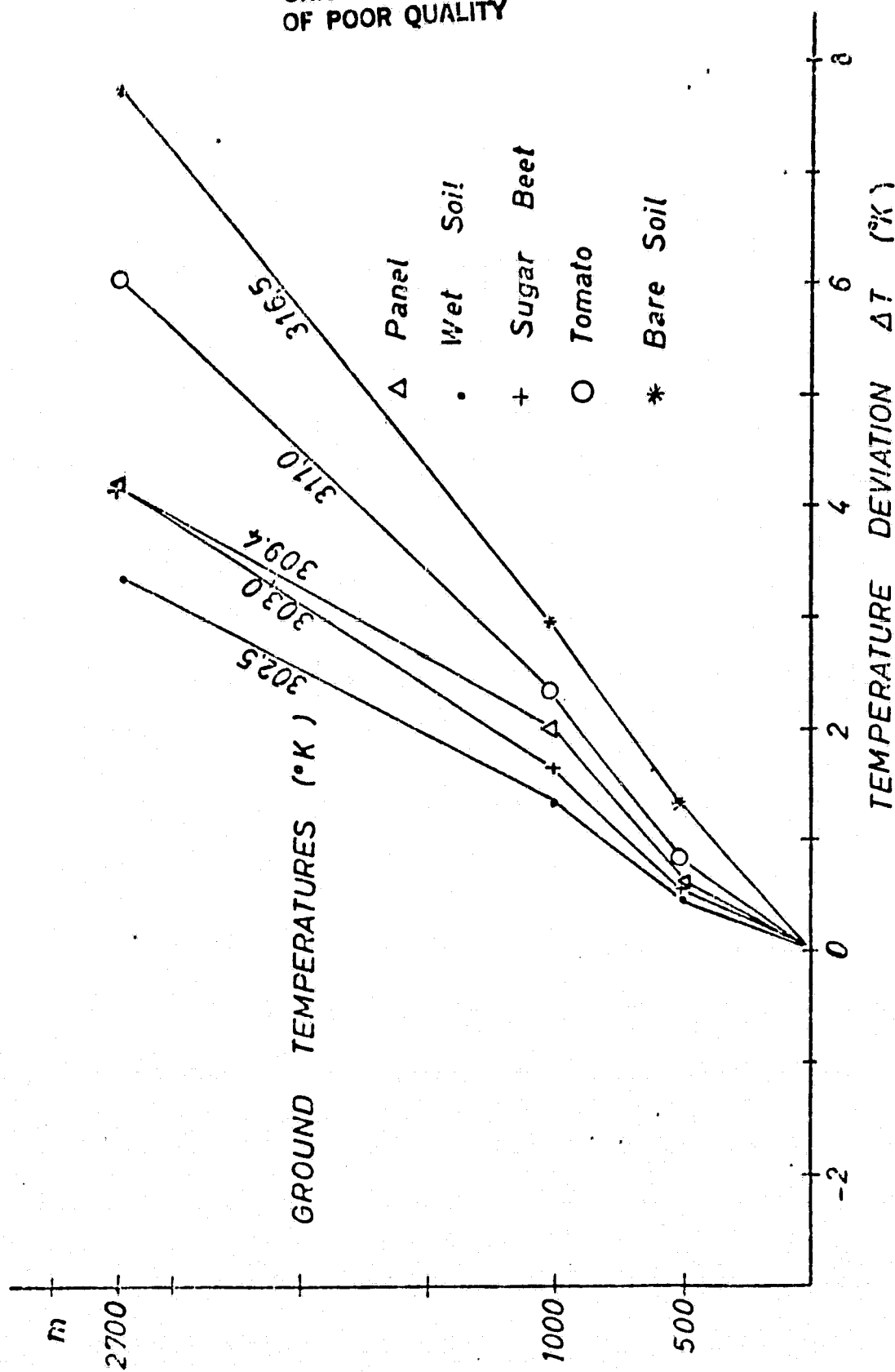


Fig.III.1.24. Radiative temperature deviations at various flight altitudes obtained out of the use of a 10x 10 m reference panel.

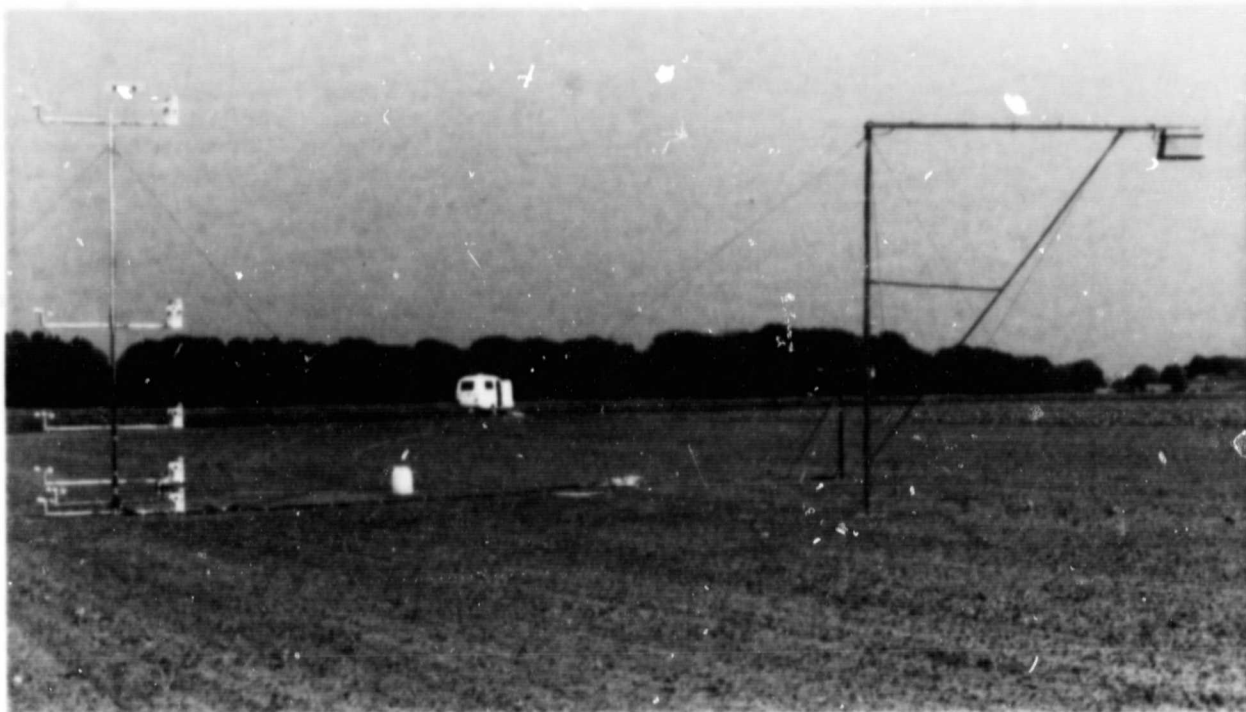


Fig.III.1.25. Joint Flight Experiment, Pattensen 1979. View of a part of JRC's ground instrumentation on arable land. The radiometers group (EXOTECH 100 and PRT-5) and an anemometers pole are visible on the sides. The day logging system is lodged in the van visible on the background.



Fig.III.1.26. Long term measurement campaign at Policoro, 1979. One of the two radiometers assemblies stands out on the background. Installations of albedometers, net radiometers and tensiometers are visible on the grass.

ORIGINAL PAGE
COLOR PHOTOGRAPH

TABLE III.1.9. Pollicoro campaign. List of parameters measured on ground and instrumentation

Measured parameters	Instruments
MICROMETEOROLOGY	
<ul style="list-style-type: none"> • net radiation (1m) • shortwave incoming radiation (1m) • longwave incoming radiation (1m) • albedo (1m) • wind velocity (2m) • psychrometry (0.4 m, 1.5 m) • air pressure • evaporation 	<ul style="list-style-type: none"> net radiometer solarimeter net radiometer with cup albedometer anemometer psychrometer barometer class A pan evaporimeter
RADIOMETRY	
<ul style="list-style-type: none"> • reflectance (VIS + NIR)FOV 20° on a 5 m mast • crop temperature (TIR)FOV 20° on a 5 m mast 	<ul style="list-style-type: none"> radiometer radiometer
SOIL	
<ul style="list-style-type: none"> a) Field measurements: <ul style="list-style-type: none"> • humidity (various depths) • temperature profile (till 50 cm depth) • heat flux (-4 cm, -10 cm) b) Soil physical properties: <ul style="list-style-type: none"> • density • pF curve • specific heat • granulometry • organic matter • heat diffusivity and conductivity • water conductivity 	<ul style="list-style-type: none"> tensiometer, sampling thermocouples heat plates laboratory techniques on field
VEGETATION	
<ul style="list-style-type: none"> • roots distribution 	<ul style="list-style-type: none"> on field

Part 2 - Effects of Topography, Soils and Land-Use on Surface Temperature Distribution

1. The Influence of Topographic Structures on Night-Time Surface Temperatures in the South of Germany

A. Processing of HCMM-Satellite Thermal Images for superposition with other Satellite Imagery and Topographic and Thematic Maps

H. Gossmann
Geographisches Institut der Universität Freiburg, Deutschland
P. Haberäcker
DFVLR, Institut für Nachrichtentechnik, Oberpfaffenhofen, Deutschland

Introduction

The topics of interest for the utilization of the HCMM imagery taken over the German test sites were the following:

- Connection between the patterns of surface temperatures respectively day/night temperature differences and the geographic reality of various natural surfaces with a different physical constitution (forests, farmland, settling areas, etc.) by comparison with already available special maps mainly in the scale 1 : 1,000,000.
- Correlation between surface temperatures or their variations and the nature of surface coverage.
- Analysis of the influence of altitude, topographic situation and regional meteorologic

conditions on the temperature of surface elements of the same kind.

- Thermal behaviour of different regional units in Southern Germany.

Objectives

Two questions, both of primary importance for the application of HCMM-image material with regard to the above mentioned goals, were examined:

- 1) how exact a regionally bounded HCMM-scene can be rectified with respect to a pre-assigned coordinate system (in this case the Gauss-Krüger System for the official maps of the Federal Republic of Germany).
- 2) Related to this problem is the question of the scale to which excerpts from HCMM-data can be sensibly enlarged or, conversely, how large natural topographic structures must be in order to be identified accurately in a satellite thermal image. This information is a prerequisite for all evaluations in which HCMM data are related to terrestrial observations or measurements.

Furthermore, a procedure was set up to superimpose computationally point by point the HCMM image data with other information, especially

relief and forest and population distribution maps, but also with a land-use map, which had been derived from Landsat data. Here it is necessary, on the one hand, to digitize the maps and to rectify them, likewise with respect to the Gauss-Krüger coordinate system, and, on the other hand, to combine the various information levels in a single multi-channel data-structure. The consequent requisite methodological steps and the accompanying difficulties, as well as some evaluations of the resultant data-structures, are presented below.

The Area under Investigation

For this study a section was chosen from the southwestern part of Central Europe between the cities of Basel and Frankfurt (Fig.III.2.1). This section comprises the so-called Upper Rhine Valley and the surrounding highlands. There are several reasons for this choice:

Both sides of the Rhine river are exemplified by a variety of landscape types: the holocene flood plain with residual forests; the intensely cultivated quarternary accumulation plain, interspersed in some places with forested sand and gravel terrain, the orchards and vineyards of the foothill zone; the strongly dissected forested ascent to the mountainous flanks of the Graben; forested plateaus, extending away from the Upper Rhine Valley and divided by large valleys, and which on the side away from the Rhine are bounded by a well-marked rock formation and thereafter replaced by a relatively unforested farm landscape.

In the following, the area in question will be considered as a whole as well as in some of its parts. These parts correspond to the sheets of the official maps of the Federal Republic of Germany, scale 1 : 200,000 (TÜK 200; Fig.III.2.1).

As the result of a study on the evaluation of Landsat data for the preparation of land-use data to be used in regional planning, there is already available a digital map of the Mannheim area with the territory classified into eight land-use classes. This allows a direct combination with HCMM data.

Flights carried out in 1976 by the German Aerial Surveying Program made available day and night thermal images for several sections of the area in question. These images can also be combined with HCMM data.

Data Base

Maps

Of all the types of existing thematic maps showing distribution patterns of specific phenomena, two are of special interest with regard to superimposing with satellite images. The first type is the distribution pattern of land-use types, in which the illustrated area is composed of "sub-surfaces", each class of sub-surface representing a particular geographic quality, as is the case with land-use maps. The binary distribution maps of a land-use category (binary mosaic map), such as those for forest distribution or the distribution of tilles or settled acreage in a given area, are special cases of this type.

The second map-type is comprised of the iso-line representation of a continuum, i.e., of a continuous field which fills the observed area, as e.g. the contour representation of land forms. On the other hand, maps constructed on the basis of a network of linear elements, such as the network of rivers, streams, lakes, etc., of an area, can only be used for orientation purposes or as a framework of reference, since, because of the ex-

ORIGINAL PAGE IS
OF POOR QUALITY

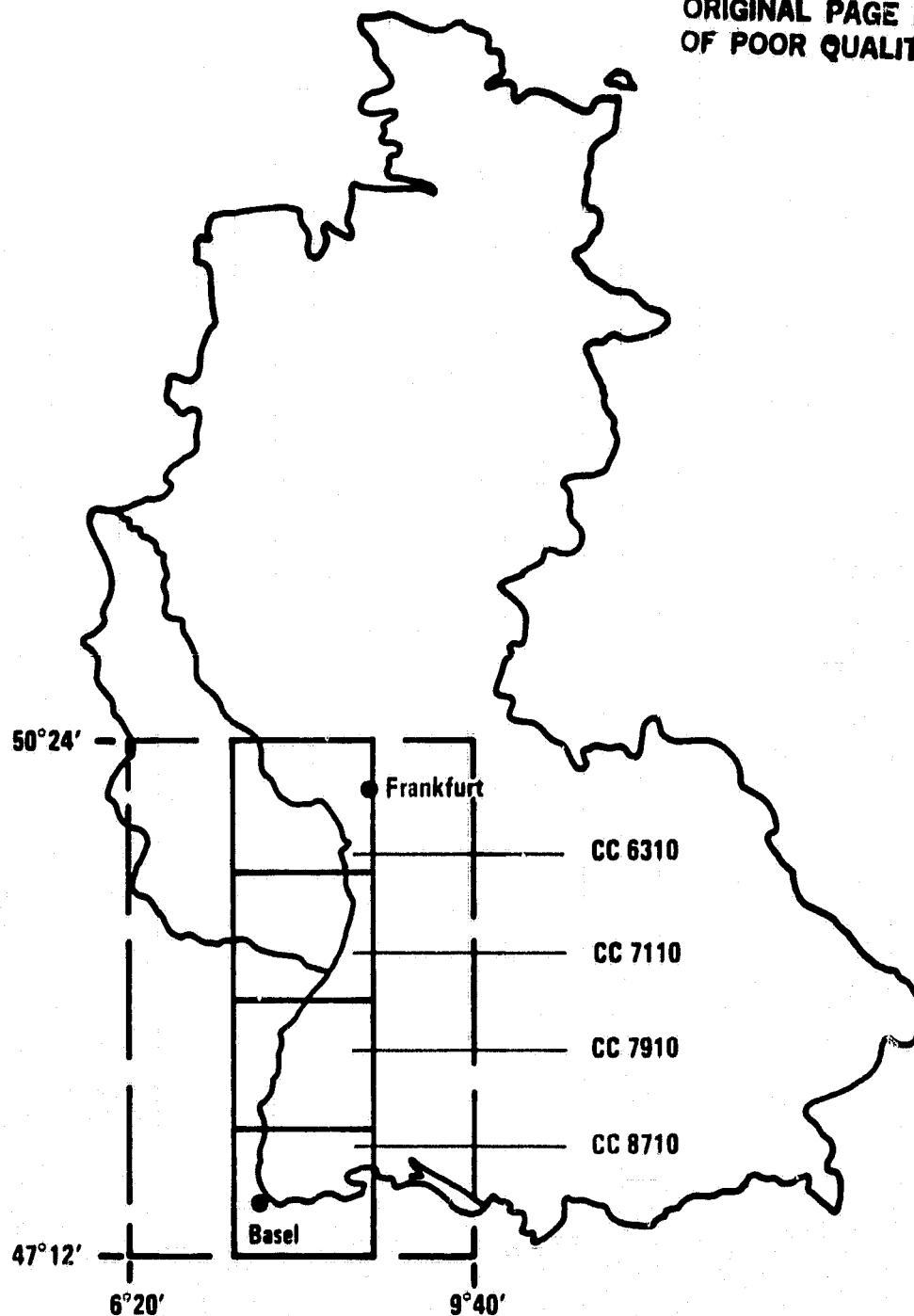


Fig. III.2.1. The area under investigation. CC 6310, CC 7110, CC 7910 and CC 8710 are sheet-numbers of the official Topographical Map 1:200,000 of the FRG.



Fig. III.2.2. Forest Distribution in South-West Germany from Hydrologischer Atlas der Bundesrepublik Deutschland.

ORIGINAL PAGE IS
OF POOR QUALITY

traordinary broadness of the line, the image-elements which appear on the map as water bodies must not necessarily represent water in the satellite image, too.

One example of each of these two map-types was selected for the investigation (Table III.2.1.a). In choosing an appropriate scale the geometric resolution of the satellite thermal-image was the decisive factor. Assuming the smallest possible size of the map-elements to be 0.3 x 0.3 mm, the pixel size of 600 x 600 m corresponds to a scale of 1 : 2,000,000. Therefore, in the digitalization maps of the scale 1 : 1,000,000 and 1 : 2,000,000 were employed. Fig.III.2.2 shows, as an example, the forest distribution map which was used in this study. The relevant sheets of the Topographical Map of the Federal Republic of Germany, scale 1 : 2,000,000 (TUK 200, Fig.III.2.1), served as the basis for the geometric rectification and the fitting of the entire data-structure to the Gauss-Krüger Coordinate System.

LANDSAT Image Sources

As mentioned above Landsat image data were used as a further data base. Specifically, the data sources are two Landsat scenes of South-western Germany, the one dated 8/9/1975, the other 8/28/1975, both of which were geometrically rectified and adapted to the Gauss-Krüger coordinate system. Segments of both scenes were fitted together so as to form a mosaic which covers the map CC 7110 (Mannheim, scale 1 : 200,000). Each pixel of the rectified and CC 7110-fitted scenes describes a surface of 100 x 100 m² (1 ha). The following 8 classes were established by multispectral classification: high-density urban built-up areas, low-density urban built-up areas, water, pastures and orchards, tilled acreage, vineyards, deciduous forest and coniferous

forest. The so classified scene is available as a data-structure which can be combined with other data sources. Fig.III.2.1 demonstrates the combination of the classified scene with the information of the topographical map for the same region. In the present investigation the combination was carried out using the infrared data of the HCMM satellite.

Preparation of Auxiliary Data (Map Digitalization)

Map digitalization was achieved by scanning 6 x 6 cm² slides with a DICOMED-Flying-Spot-Scanner (DIBIAS System). This system allows a resolution of the image in 1024 x 1024 pixels. Considering the extension of the Upper Rhine Valley and its surroundings, this results in a pixel size of approx. 350 x 350 m². This resolution corresponds approximately to the accuracy of the map: 350 m = 0.35 mm and 0.175 mm in scales of 1 : 1,000,000 and 1 : 2,000,000, respectively. At the same time it is somewhat better than the geometric resolution of the thermal-image.

The digitizing of grey levels which appear on the maps presented considerable difficulties. It proved to be impossible to carry out the digitalization of a grey tone scale with more than two levels in one step. Furthermore, because of vignetting effects the binary black and white prints also show a strong distortion of the image contents. Using the relief map as an example, the solution to this problem is described in Part 6, Ch. 3, A.

The maps representing the distribution of forests, built-up areas and rivers were digitized similarly. Special mention must be made of the type of vignetting effect in the distribution map of built-up areas and the corresponding correction procedure.

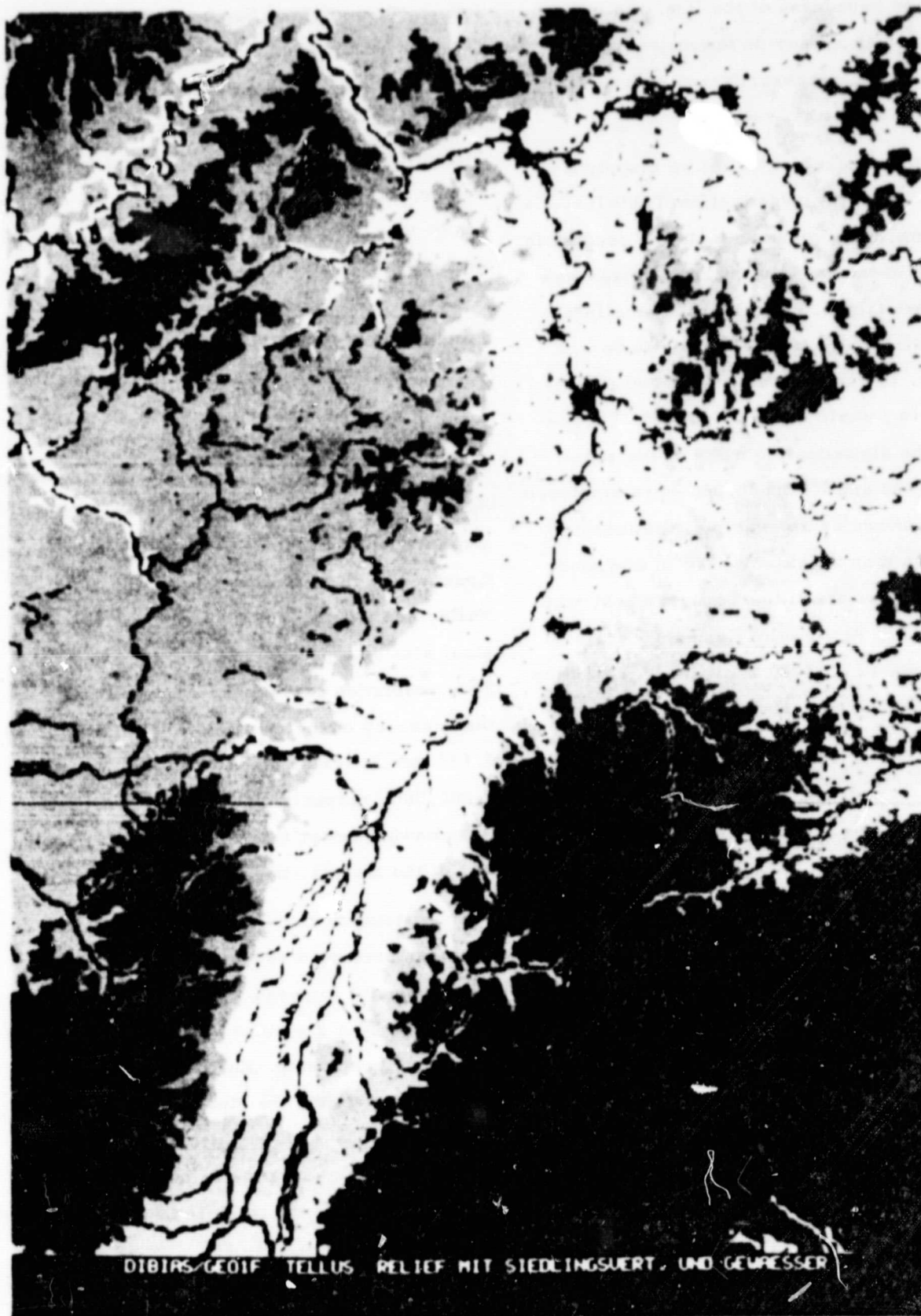


Fig. III.2.3. Result of the digitalization of different maps. Superposition of the relief with the distribution-pattern of urban built-up areas and the river network.

ORIGINAL PAGE IS
OF POOR QUALITY

Afterwards all maps were fitted to the Gauss-Krüger coordinate system and in this way to each other. This occurred according to the same procedure which was used to rectify the thermal-image. Finally, with the corner points having been given in Gauss-Krüger coordinates, similar "windows" were cut from the individual maps and digitally superimposed; this served as a quality control of the processing procedure. Fig.III.2.3 shows the relief map superimposed with the urban built-up distribution and water network which were produced in this way (the former represents only the German part of the territory investigated).

Processing HCMM Thermal Imagery

Geometric adjustment to the Gauss-Krüger coordinate network. The geometric rectifications were carried out by the interpolation method by which some control points on the distorted scene are related to the reference image (see Part 5, Ch. 3, B).

The data base for this investigation was provided by a segment of HCMM scene AA 0034. 0213.0.3 of May 30, 1978. As mentioned in Ch. 3, it encompasses the Upper Rhine Valley between Basel and Frankfurt and the surrounding highlands.

"Rough" Rectification

In order to achieve the highest possible degree of precision the determination of the control points proceeded in two steps. First, the thermal image was corrected with respect to water-networks and forest distribution ("rough" rectification). From this corrected image, which already represents a good geometric approach to the topographical map, the control points for the final rectification were determined using Gauss-Krüger coordinates ("fine" rectification).

The determination of the control points for the first step of rectification was carried out on the DIBIAS-monitor screen. Here the thermal-image as well as the digitized and pointwise correlated forest distribution and water-network maps were deposited in the image memory of the system. In this way one can rapidly compare the images and easily identify their corresponding structures. As an auxiliary aid to the present investigation a relief map was also used. Although large-area landscape-structures (the Upper Rhine Valley, Kaiserstuhl, large cities) were easy to recognize in the contrast enhanced thermal-image, the detection of control point pairs remained difficult. It turned out, for example, that in the monitor-screen comparison of structures for the region of the Upper Rhine Valley no control points - except a few well-marked structures of the Rhine itself - could be determined. The search was easier in the highlands which surround the plain. Here the valleys with their pastures contrast strongly with the forested mountains and hills. They show a lower surface temperature at night due to differences in the heat budget between pastures and forests and the accumulation of cold air on the valley bottoms. One can therefore define, as control points, the bends in a valley or the confluences of several valleys. This clear pattern of a valley network in the thermal-image is lacking in landscapes with unforested plateaus or only partially forested valley slopes, because here the influences of the relief and vegetation distribution on the surface temperature run in opposite directions.

Seven of the 17 control points used for the "rough" rectification lie on the Rhine river, 2 on prominent corners of forests, and 8 in the bends of valley confluences of the highlands. Of the Rhine control points, two or three were



ORIGINAL PAGE IS
OF POOR QUALITY

DIBIAS HCM 30.5.78 NACHT IR

Fig. III.2.4. A section of the thermal infrared HCM-satellite image (5/30/78, 2:13 GMT). The section shows the Rhine Valley between Basel and Frankfurt and the surrounding highlands (bright = warm, dark = cold).

produced by the river alone, in some the strip of forest along the river banks was of assistance and in the case of two others on the Middle Rhine the influence of the (relatively warm) Rhine Valley slopes which follow the bends of the river was evident.

"Fine" Rectification

As mentioned above the control points for the "fine" rectification were determined using Gauss-Krüger coordinates. In order to achieve an average residual error of less than one pixel in the line as well as in the column-direction, it was attempted, on the basis of the topographical overview map, scale 1 : 200,000 (TÜK 200), to determine the coordinates for 50 to 100 control points with an error of less than 600 m. This requirement means the determination of these points on the map with an accuracy of 3 mm. To do this the "rough" rectified images were projected onto the corresponding map sections. By shifting the maps on a magnetic wall, the structures which correspond to the recognizable patterns in the thermal image, namely, relief, forest distribution, water-network, urban built-up areas, were assigned in sub-regions of 20 to 40 km in diameter. Corresponding details of the thermal image and the map were then identified in these partial regions. It became clear along the way that the control points which had been used in the preliminary rectification could, for the most part, not be identified on the map with the necessary accuracy (3 mm). This is true especially for the control points which were taken from the forest distribution data. The corresponding forest distribution patterns are indeed present on the map TÜK 200; however, the relevant corners and edges could only be defined with precision to about 1 cm. The same is true for the "heat islands" of large cities, which are

conspicuous in thermal-images and useful in small scale classification. But when blown up they are structureless and have such diffuse edges that it is difficult to assign control points within them. On the other hand the relief provides a good reference system, but not the bends or confluences of the large valleys (as was the case with the "rough" rectification), and, particularly, the many small forms in the upper parts of the drainage basins. Several control points on the Rhine river could thus be taken over from the "rough" rectification, directly.

The 86 detected control points, for which a definition within the afore mentioned margin of error was possible, are distributed among the different classes according to the following list:

Water bodies (5 points): Three well-marked bends in the Rhine river, one in the Mosel river, and a corner of a lake which had a rather conspicuous shape. Many of the river-bends have to be disqualified, since it cannot be unequivocally determined whether or not the structure which appears in the thermal image is produced by the river itself or by the adjoining strips of forest.

Urban built-up areas (5 points): Although there were numerous cities with populations of up to 10,000, which evoke a thermal signal, it was possible only in a few cases (Endingen, Waldshut) to distinguish the respective town centres. In two other cases, however, the corner points of large industrial built-up areas could be determined.

Land-use boundaries (18 points): The determination of land-use boundaries was more difficult than expected. Forest-clearings (2), small wooded expanses (3), forest-edges which jut out into or sharply recede from the adjoining landscape (9), etc., can apparently be iden-

TABLE III.2.2. Numerical results of the geometrical rectification.

Area	Reference map	Control points No. Determination	Solution approach	Size of the pixels Original (m), Image (m)	r.m.s.				Calculating Time
					x-axis		y-axis		
					b _i	m	b _i	m	
I. "Rough" Rectification									
entire scene 1)	forest	10 monitor screen	linear	1200	1.5	1800	12.6	15000	
	water, network	10 monitor screen	linear		1.2	1440	2.95	3540	
	relief	10 monitor screen	linear		1.3	1560	1.98	2376	
	1:1,000,000 1:2,000,000	11 monitor screen	linear		0.9	1080	1.1	1320	
entire scene (northern portion)	1:2,000,000	9 monitor screen	linear	600	1.8	1080	2.05	1230	
entire scene (southern portion)	1:2,000,000	10 monitor screen	linear	600	2.5	1500	1.99	1194	
II. "Fine" Rectification									
entire scene	TUK 200	50 GK ²⁾	linear	600	1.03	618	0.78	468	18 min.
entire scene	TUK 200	50 GK	quadratic	600	1.01	606	0.77	462	35 min.
CC 7110 (Mannheim)	TUK 200	14 GK	linear	600	1.04	624	0.74	444	13 min.
OC 7910 (Freiburg North)	TUK 200	17 GK	linear	600	0.98	588	0.66	396	13 min.
OC 8710 (Freiburg South)	TUK 200	17 GK	linear	600	0.87	522	0.76	456	12 min.

1) entire scene: Upper Rhine Region with surrounding highlands.

2) GK: Gauss-Krüger coordinates.

tified only when the borders of the pixel coincide with the land-use boundaries. In 4 cases land-use boundaries could be recognized by a prominent corner of a dam on the Rhine.

Relief (51 points): With some reservation one can say that the nightly appearing pattern of various sorts of concavities was the most effective aid in identifying the control points on the map TUK 200. The valley network of the highlands thus served, in addition to its application for the "rough" rectification, as reference for the projection of the thermal-image onto TUK 200. But essentially important here were the small but numerous forks (31) in the upper valley regions, which could be assigned to a definite image-point. Furthermore, in some places it was possible to define, with sufficient accuracy, the junctions at which small peripheral valleys combine with major ones (8) as well as larger junctions (3) or bends (3) in the valleys.

It should be noticed that for all defined categories or classes only a few of many geographically equivalent situations were recorded in the thermal-image. This is due to smearing in mixed signatures caused by averaging the temperatures of the different objects which contribute to the pixel. From this point one can derive two consequences:

Firstly, the fact of this "smearing" reinforces trust in those control points which were finally selected. Exactly those situations were captured in which the phenomenon producing the signal was located centrally in the respective pixel. Secondly, it is to be expected that some of the control points which were employed here will not always be useful for the rectification of other images of the same territory, even if they are taken at the same time of day. This is because due to different arrangement of the

pixels, the same geographic phenomenon can be reproduced clearly in one image but less prominent in another one.

Quantitative Results and Precision of the Procedure

With the control points thus defined, the entire scene (linear and quadratic polynomials) as well as different selected parts of it were rectified with respect to the format of TUK 200 in several computing runs. Table III. 2. 2 shows that for the "rough" rectification the best results reveal an rms error of somewhat more than 1000 m in both the line and column directions, for the "fine" rectification the values are 618 and 606 m in line and 468 and 462 m in the column direction. The insignificant difference between the residual errors of the linear and quadratic approaches 618 and 468 m vs. 606 and 462 m, respectively, suggests that, with regard to the size of the investigated area (about 300 x 150 km), the increased time-consumption of the quadratic approach (35 min. calculating time vs. 18 min. for the linear approach) is not yet compensated by the relatively small gain in efficiency.

The rms errors from the individual rectifications of the three TUK-plates are with one exception all significantly smaller than one pixel of the original data. The somewhat better values for the plates CC 7910 (Freiburg-North) and CC 8710 (Freiburg-South) can well be attributed to the investigators' long experience with this area, especially by the previous work with aircraft scanner thermal imagery, which facilitates the selection of control points in this region.

The fact that after the linear rectification no more essential systematic distortions are present in the image is shown in the rms vector

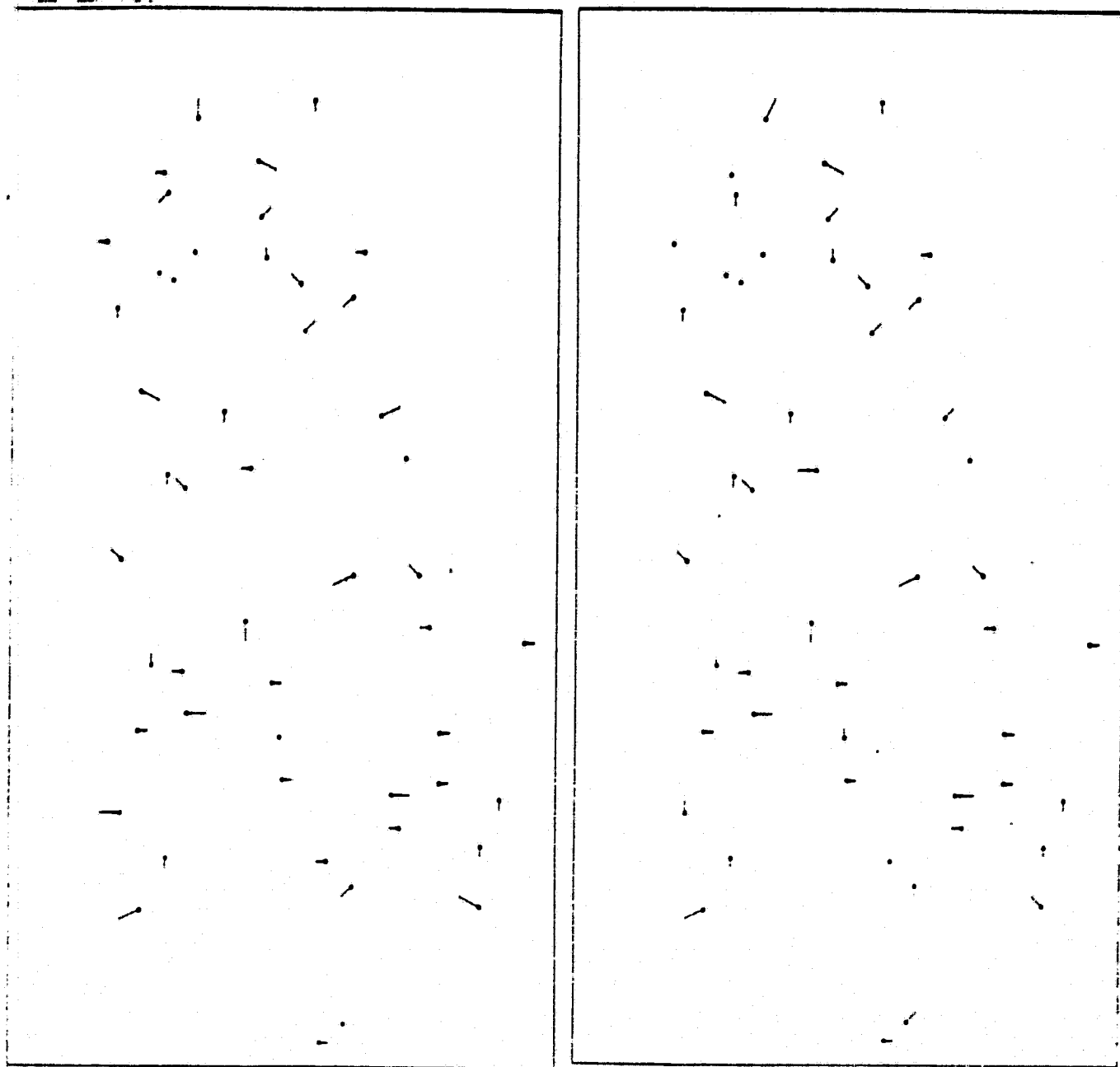


Fig. III.2.5. Diagram of the r.m.s. vectors in the "fine" rectification of the entire scene; left, **quadratic** and right **linear**. For a clear representation of the vector length have been stretched by a factor of 8 relative to the scale of the drawings.

diagrams of the individual control points (Fig. III.2, 5 and 6): the vectors in the different parts of the image exhibit no specific tendencies. On the other hand a systematic additive error (translation) cannot be revealed by this argumentation.

In Figs. III.2, 7 to 8 the results of the rectification are presented by using images as examples. They show respectively the entire scene following the preliminary rectification and the section of CC 7110 (Mannheim) following the "fine" rectification, overlaid with the corresponding topographic pattern.

Fig. 1, Part. 3 shows the surface temperature distribution within the city boundaries of Freiburg-im-Breisgau as recorded in a satellite thermal-image and after "fine" rectification with respect to Gauss-Krüger coordinates and "smoothing" of the pixel edges. Fig. 2, Part. 3 is taken from an aircraft scanner thermal-image of the same region produced under comparable conditions.

Construction of the Multi-Channel Scene

As a result of the processing steps described above the following spatially correlated, digitized, and rectified image-information from the investigated area was derived:

- the HCMM night-infrared image data with calibrated grey values,
- the HCMM night-infrared image data with calibrated grey values which were also adapted to the temperature pseudo-colour scheme,
- the network of urban built-up areas,
- the forest distribution,
- the relief for the area represented in map CC 7110,
- and the classified image data described in section 2.

By means of the ME-module (Merge-Modul) the individual scenes were transformed into two multi-channel scenes: one for the entire area under investigation and a second for the region represented in CC 7110.

The content of the various channels in the first multi-channel scene is sketched in Fig. III.2, 9. A pixel g of this scene is thus a vector in six dimensions ($g_1, g_2, g_3, g_4, g_5, g_6$); the vector components correspond to the following categories:

g_1 :	= 230	elevation	0 - 200 m
	= 180	"	200 - 400 m
	= 130	"	400 - 700 m
	= 80	"	700 - 1000 m
	= 30	"	> 1000 m
g_2 :	= 0	urban built-up area	
	= 255	no urban built-up area	
g_3 :	= 0	forest	
	= 255	no forest	
g_4 :	= 0	water body	
	= 255	no water body	
g_5 :	= 0 ≤ g_5 ≤ 255	HCMM night-IR data, calibrated	
g_6 :	= 0 ≤ g_6 ≤ 255	HCMM night-IR data, calibrated and adapted to the temperature pseudo-colour scheme.	

The second multi-channel scene overlays a portion of the map CC 7110. It was produced in a procedure similar to the one described above and consists of the following eight channels:

K_1	Landsat classification according to section,
K_2	HCMM night-IR data, calibrated,
K_3	HCMM night-IR data, calibrated and adapted to the temperature pseudo-colour scheme,
K_4	HCMM night-IR data, calibrated,

ORIGINAL PAGE IS
OF POOR QUALITY

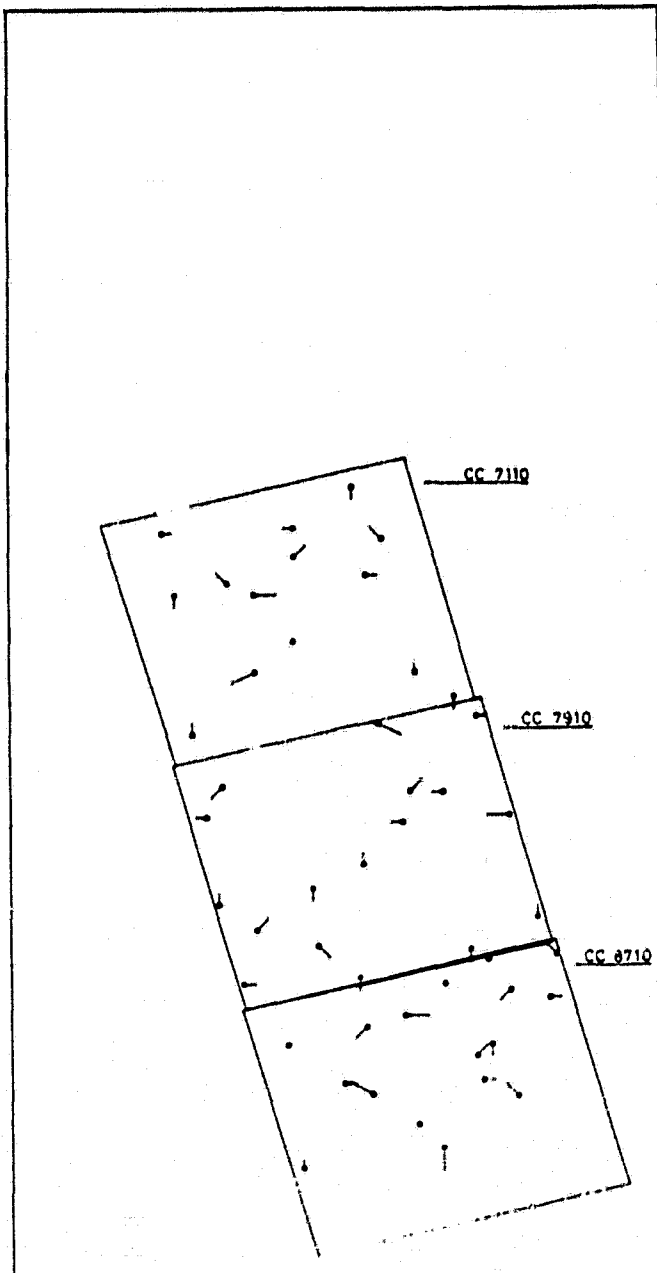


Fig.III.2.6. Diagram of the residual vectors in the "fine" rectification in accordance with TUK 200 map plates (cf. the last 3 lines in Table III.2.2). As in Fig.III.2.5 the vector lengths have been increased by a factor of 8.

ORIGINAL PAGE
BLACK AND WHITE PHOTOGRAPH



Fig.III.2.7. Thermal-image (entire scene) after the first step in the rectification ("rough" rectification, line 4 in Table III.2.2). The water-ways are overlaid.

ORIGINAL PAGE
COLOR PHOTOGRAPH

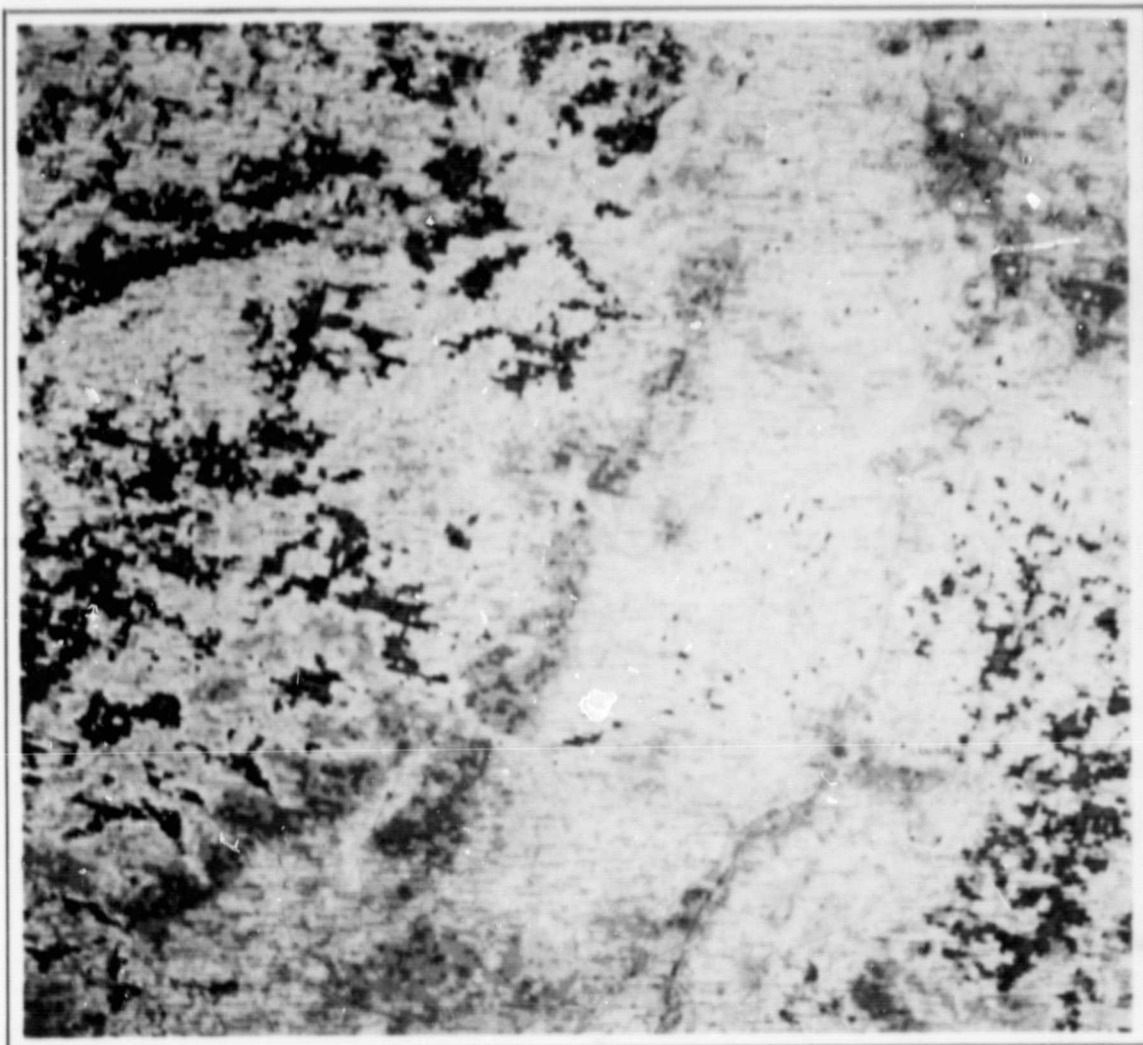


Fig. III.2.8. Thermal-image (a section, of TUK 200, sheet CC 7110 Mannheim) after the second step in the rectification ("fine" rectification, third to the last line in Fig. 8a). The superimposed information is from a topographical map.

ORIGINAL PAGE
COLOR PHOTOGRAPH

ORIGINAL PAGE IS
OF POOR QUALITY

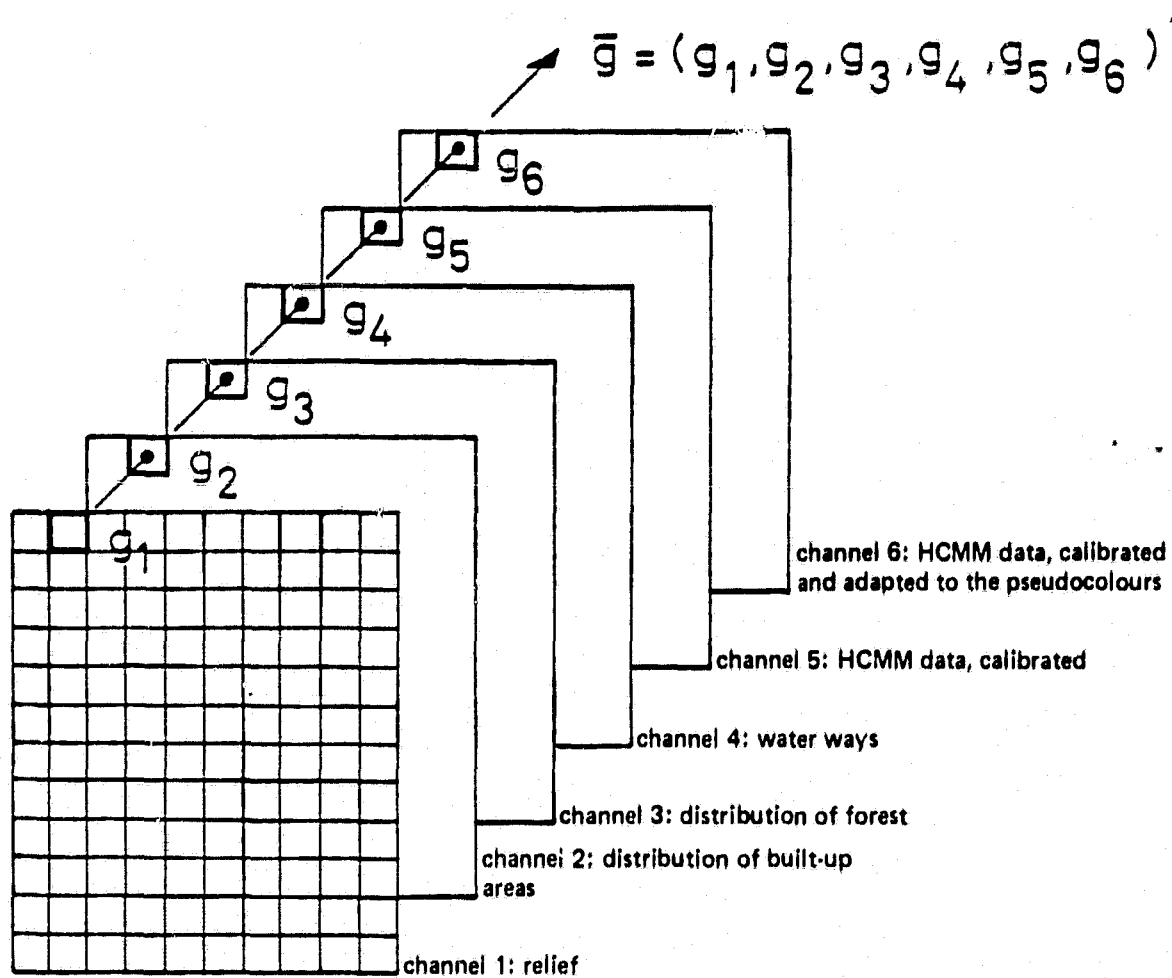


Fig. III.2.9. Data structure of the multi-channel scene for the whole area under investigation.

averaged, and adapted to the temperature pseudo-colour scheme,

- K₅ relief,
- K₆ urban built-up area,
- K₇ water ways,
- K₈ forest distribution.

References

1. NASA; "Heat Capacity Mapping Mission (HCMM) Data Users Handbook for Applications Explorer Mission-A (AEM).
2. H. GOSSMANN; "The Thermal Behaviour of Natural and Cultural Landscape Regions in Southern Germany as Derived from Satellite Imagery." Publication in preparation; 1980.
3. W. SCHIKARSKY et al.; "Das Abwärmeprojekt Oberrheingebiet - Aufgaben und Ziele". Bericht des Kernforschungszentrums Karlsruhe, Laboratorium für Aerosolphysik I, März, 1977.
4. P. HABERÄCKER et al.; "Auswertung von Satellitenaufnahmen für die Landnutzung". Schriftenreihe "Raumordnung" des Bundesministers für Raumordnung, Bauwesen und Städtebau, Bonn, 1980.
5. S. FERNANDEZ et al.; "DIBIAS-Handbuch", DFVLR, Institut für Nachrichtentechnik, Oberpfaffenhofen, 1976.

ORIGINAL PAGE IS
OF POOR QUALITY

B. Investigation on the Thermal Conditions of Different Parts of the Landscape

H. Gossmann
Geographisches Institut der Universität Freiburg, Deutschland

Night-Time Surface Temperature and Relief

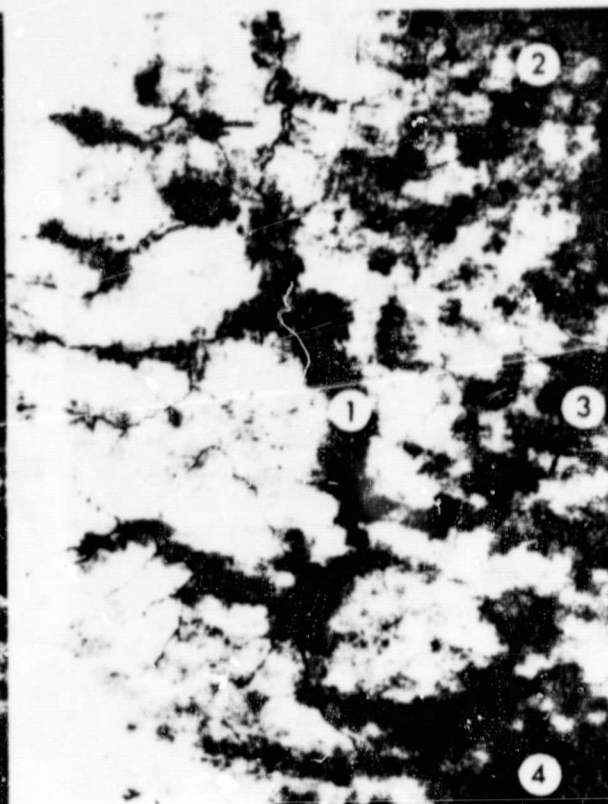
A well-known rule of topoclimatology is the thermal tripartition of hilly or mountainous areas at night: cold elevations, warm slopes and cold valley bottoms. The data allowed us to test the applicability of this law to the behaviour of surface temperatures in various spatial dimensions.

In general, only the difference between cold valleys and lowlands on the one hand, and warm slopes and mountain tops on the other, could be verified. Valleys are considerably colder than slopes if covered by comparable vegetation. The water network which follows the valley systems is all but congruent with the distribution pattern of particularly cold surfaces (Fig.III.2.10). This applies not only to the valleys in the highlands carved to a depth of hundreds of metres, but also to differences in elevation amounting to less than one metre on the alluvial and diluvial plains of the Upper Rhine Valley (Figs.III.2.11a and 12). Nevertheless, the elevated areas proved to be as warm as the slopes, in some cases even noticeably warmer (Soonwald, Pfälzer Wald, West-Taunus, edge of the Black Forest near Offenburg) in most of the image sections presented here. Cold elevated areas can be found in these samples only in places where one of the following three conditions is met:

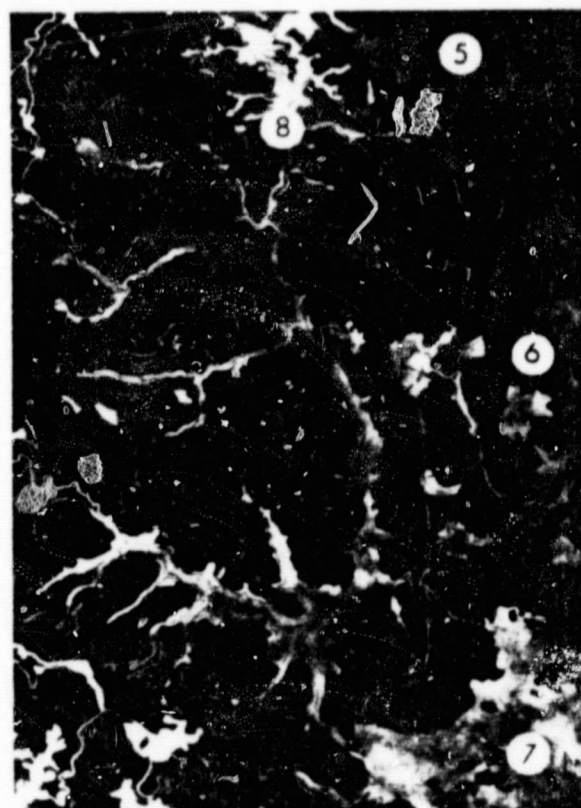
1. Grassland and cultivated fields in altitude above forested slopes,
2. Extended plateaus (Fig.III.2.10a),
3. Extended surfaces in areas with small dif-



a) Relief and water-ways



b) Water-ways



c) Forest

ORIGINAL PAGE IS
OF POOR QUALITY

- 1 Murg
- 2 Grosse Enz
- 3 Nagold
- 4 Glatt
- 5 Murg-Enz-Platte
- 6 Enz-Nagold-Platte
- 7 Freudenstädter Graben
- 8 Enge von Forbach

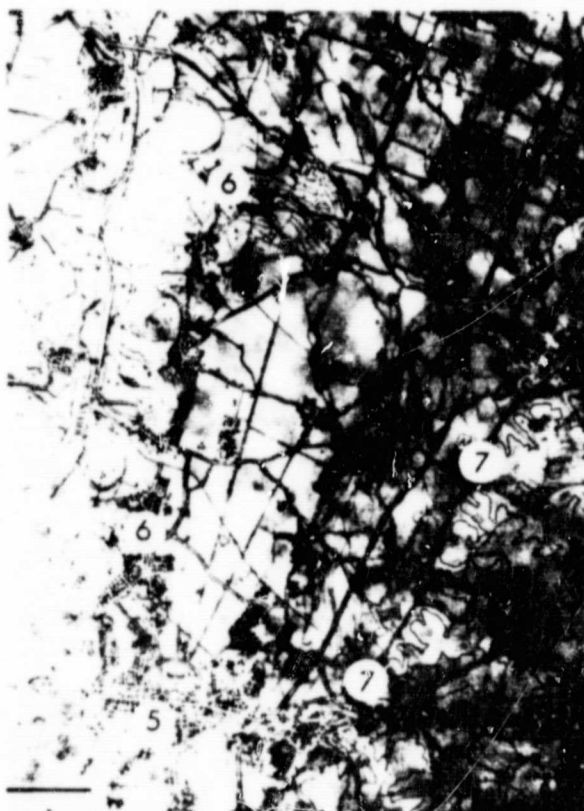
Fig. III.2.10. Murgtal im Nordschwarzwald. Grey: HCMM data (light = warm, dark = cold). Black: excerpts from TUK 200, CC 7910.



a) Water ways and relief



b) Water-ways, relief and forest

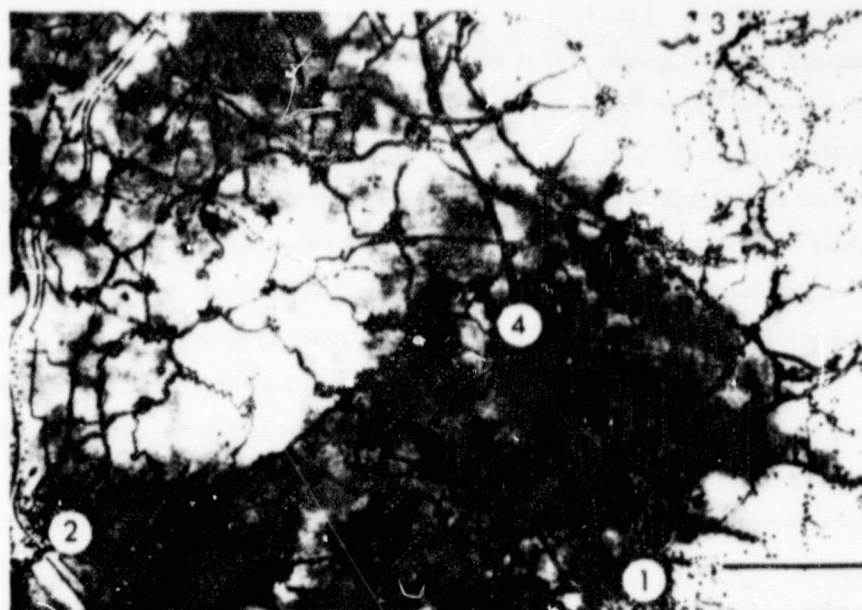


c) Water-ways, relief and urban agglomerations

ORIGINAL PAGE IS
OF POOR QUALITY

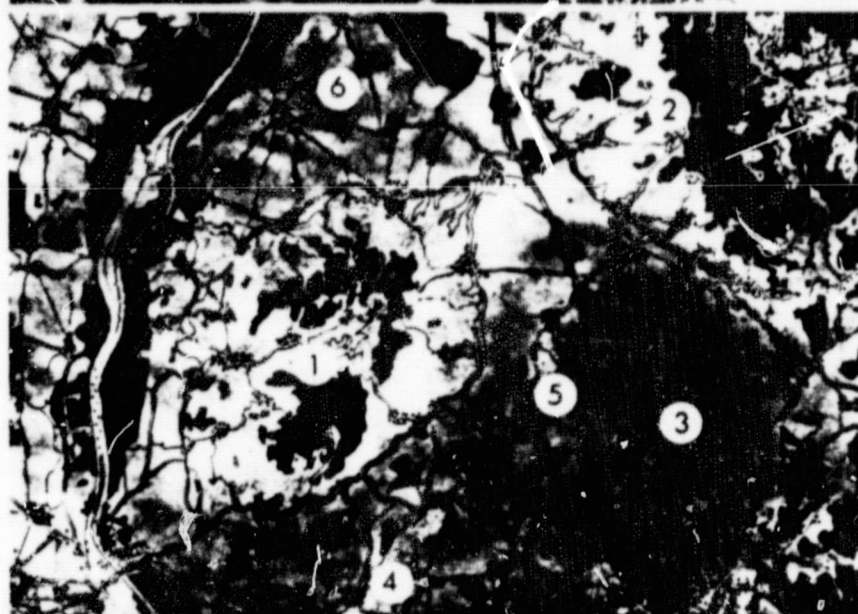
- 1 Kraichgau
- 2 Randniederung
- 3 Hardwälder
- 4 Bellheimer Wald
- 5 Karlsruhe (276,000 eW)
- 6 Rheinzeile
- 7 Bergzeile

Fig. III.2.11. Plain of Oberrhein and Outskirts of Kraichgau near Karlsruhe. Grey: HCMM data (bright = warm, dark = cold). Black: excerpts from TUK 200, CC 7110.



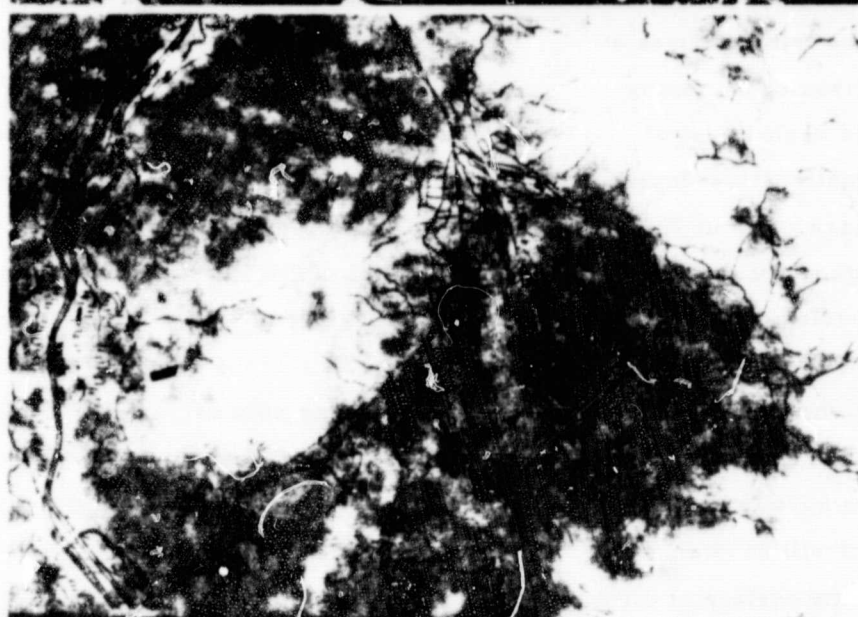
a) Settlements, roads and railways

- 1 Freiburg
- 2 Breisach
- 3 Ottoschwanen
- 4 Motor-road



b) Relief, forest, settlements

- 1 Kaiserstuhl
- 2 Emmendinger Vorbergzone
- 3 Freiburger Bucht
- 4 Tuniberg
- 5 Nimberg
- 6 Forchheimer Niederterrasse



c) Waterways

**ORIGINAL PAGE IS
OF POOR QUALITY**

Fig. III.2.12. Breisgau and Kaiserstuhl. Grey: HCMM data (bright = warm, dark = cold). Black: Excerpts from TUK 200, CC 7910.

ferences in elevation (Fig. III.2.13. b).

At the mesoscale, if we do not consider each mountain or valley individually, but designate the whole Upper Rhine Valley as the "cold low-land", the entire, strongly dissected highland fringe as the "warm slope" and the highland plateau which declines slightly towards the edges of the image, as the "cold elevation", we can establish virtual congruence between the model and reality.

One possibility to investigate the correlation between relief and surface temperature is the extraction of the thermal data for several elevation levels of HCMM image.

The thermal images of the different elevation levels produced by this procedure (Fig. III.2.14) demonstrate what kind of parameters influence the surface temperatures. Thus the highest surface temperatures (without consideration of the large cities) do not occur in the Rhine Valley (0 - 200 m) but on the slopes of the highlands.

These are in the northern part of the Rhine Valley, mainly the regions between 200 and 400 m and in the southern part those between 400 and 700 m. Very warm we find isolated elevations between 400 and 700 m, e. g. in the northern part of the Vosges mountains. Relatively high, however, are the temperatures of the Rhine Valley in comparison to the plains of the highlands, e. g. in the region east of the Black Forest. In the great shallow depressions which can be found there at about 700 m, the lowest surface temperatures of south-west Germany occur. This discussion could be continued, but the above mentioned hints already demonstrate that the thermal images of different elevation levels can be used in order to investigate how the altitude of the surface and how the relief of its environment will have an influence on the temperature of the surface at night.

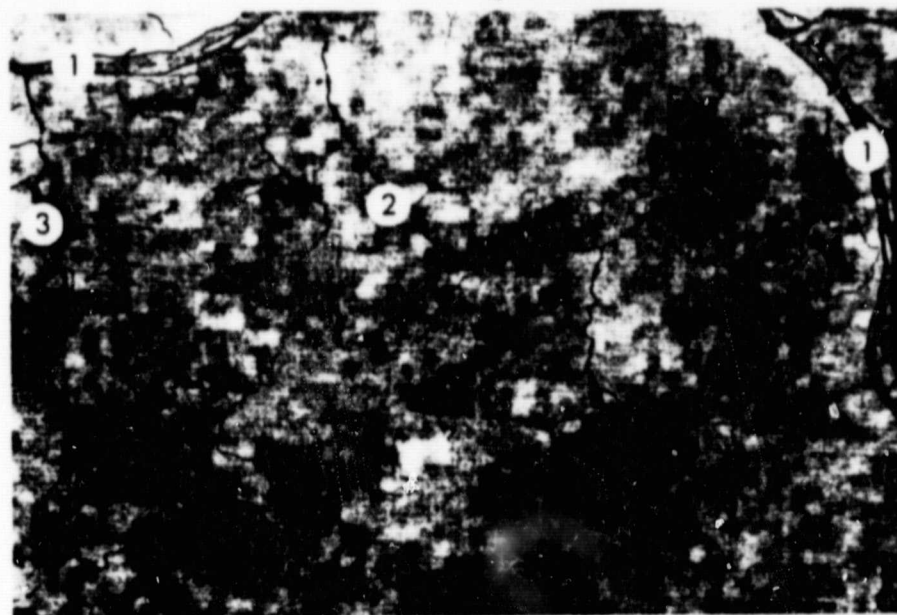
Surface Temperatures and Forest Distribution

It is generally agreed that forests do not cool off as rapidly at night as do unforested areas and that they, consequently, produce higher surface temperatures at night than adjoining grassland or cultivated fields. Therefore, it is surprising that a much more complex picture resulted from this study:

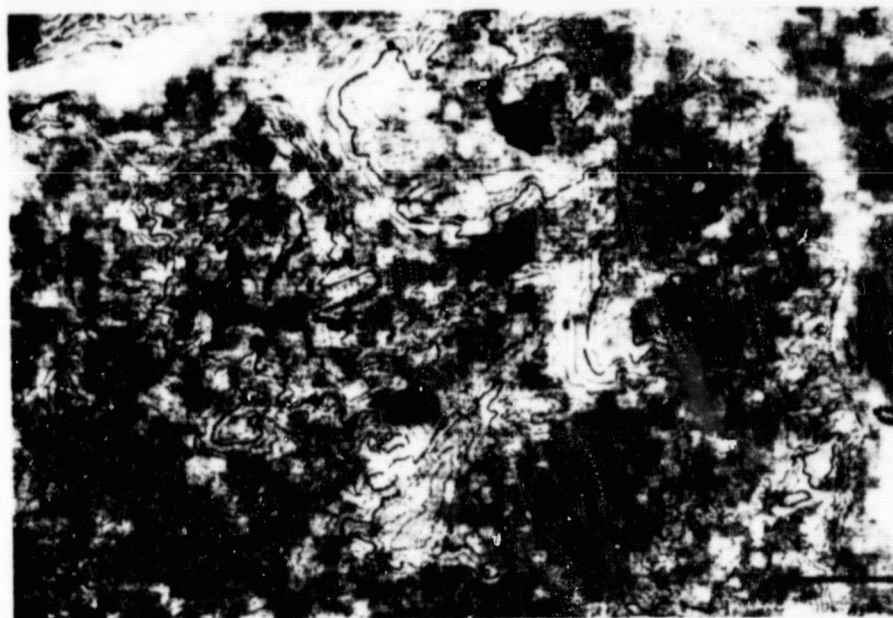
1. Forest on steep slopes or convex terrain shows very high temperatures (as warm as city centres).
2. All forests on the plateau of highland display slightly lower temperatures but are definitely warmer than scattered clearings or adjoining unforested terrain. With the exception of the Upper Rhine Valley, the contrast between forested and unforested terrain is the most essential factor of the distribution of warm and cold surfaces everywhere, unless, of course, the relief determines the thermal pattern.
3. In the Upper Rhine Valley, the picture is very complex. The residual forests on the holocene flood plain of the Rhine are depicted as being relatively warm but only in places where they have not lost their characteristic features due to canalization of the Rhine River and the subsequent drop of the ground water level. The forests on the diluvial and alluvial fans in front of the Pfälzer Wald and the northern Vosges Mountains also seem to be warmer than their surroundings. On the other hand, most of the Hardt forests on the Rhine's quaternary accumulation plain and in part on the gravel fans of the rivers of the Black Forest, are as cold as, or even colder than neighbouring unforested areas. This is most evident in the southern part of the Upper Rhine Valley north of Basel.

If one ignores the behaviour of the residual

ORIGINAL PAGE IS
OF POOR QUALITY



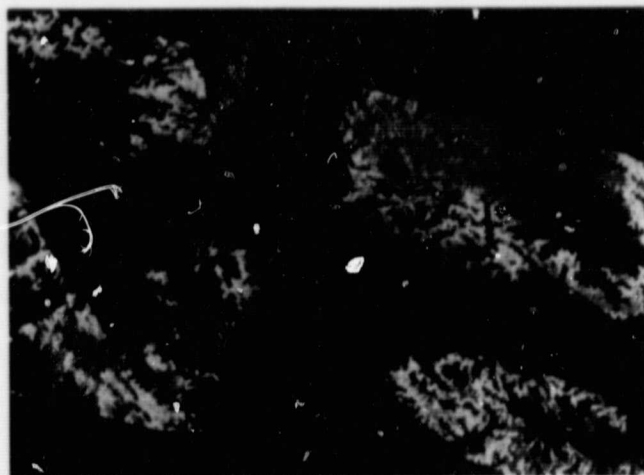
- a) Water-ways
- 1 Rhein
 - 2 Selz
 - 3 Nahe



- b) Relief and forest

Fig. III.2.13. Rhein-Hesse hill-land. Grey: HCMM data (bright = warm, dark = cold). Black: Excerpts from TUK 200, CC 6310.

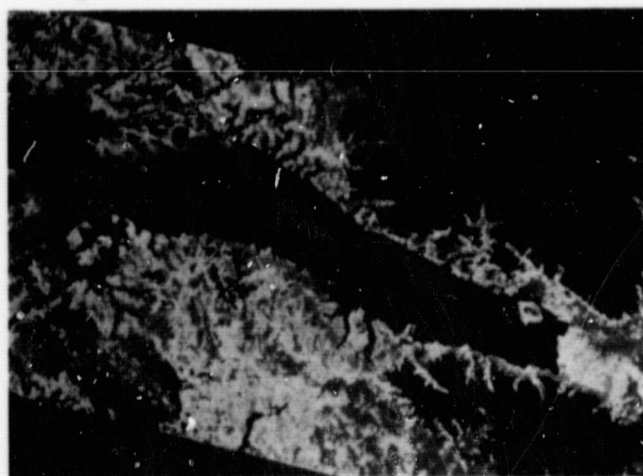
400 -
700 m



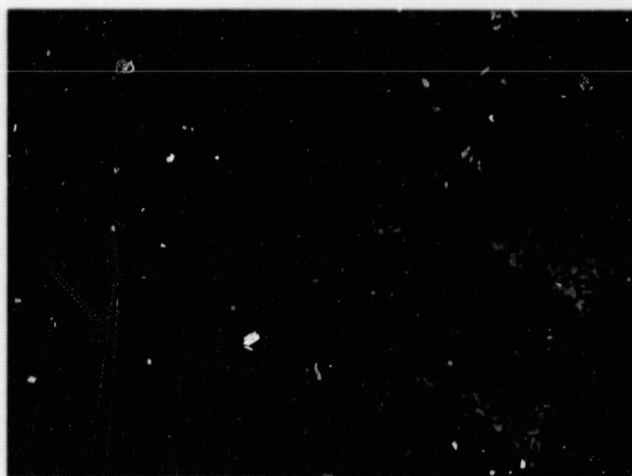
ORIGINAL PAGE
COLOR PHOTOGRAPH

Fig. III.2.14. Surface temperatures at different elevations of the investigated area as recorded 5/30/78 by the HCMM satellite (preliminary calibration). Red: warm; blue: cold. 1-degree levels; cyan/green 2°C.

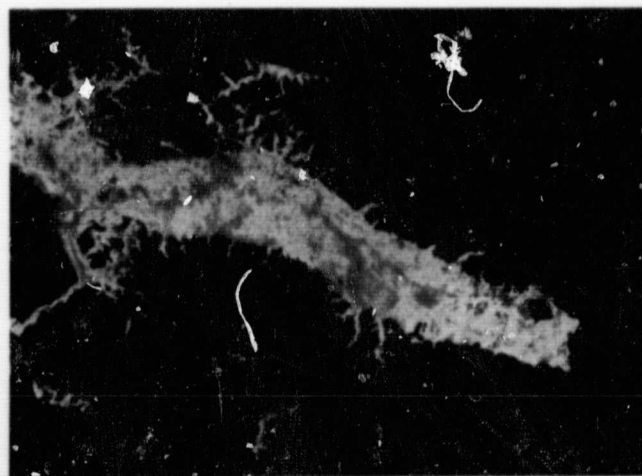
200 -
400 m



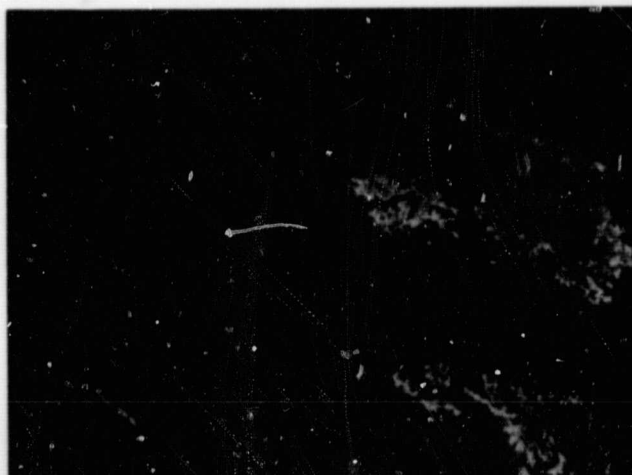
> 1000 m



0 -
200 m



700 -
1000 m



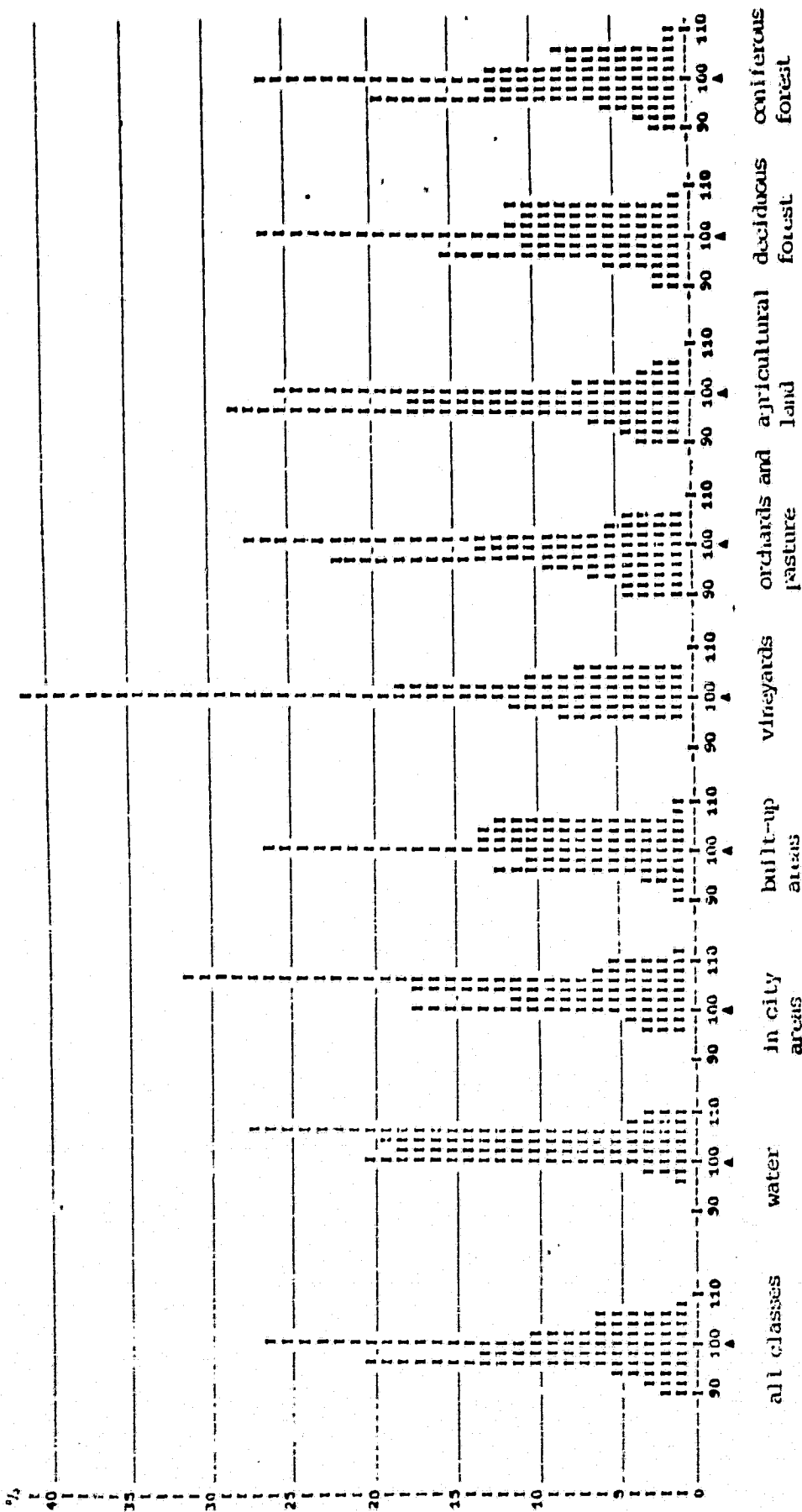
forest on the Rhine's holocene flood plain, a general tendency for great contrast between forested and unforested areas on convex land-forms and for reduction of this contrast between the two types of surfaces in concave terrain prevails. As we have stated repeatedly, the highest surface temperatures are found on forested mountain ridges and steep slopes. There must be several reasons for the distinctive behaviour of forested surfaces:

1. The low surface temperature of the Hardt forests can only be understood if it is assumed that there is a relatively homogeneous layer of cold air extending beyond the actual height of the trees (inversion in the boundary layer).
2. The differing behaviour of forests on plateaus can then be explained by the fact that a sufficiently extended layer of inversion could not be created there because of stronger dynamic turbulences caused by winds at relatively high speeds. The sensible heat flux to the forested surfaces thus remains greater than on adjoining grassland and arable fields.
3. All this signifies that the much higher surface temperatures of forests at night cannot be attributed to, or at least not completely explained, by the capacity for heat storage within the forest but rather also by the sensible heat flux between the air and the forest.
4. The explanation for the relatively high temperature of the residual forests on the holocene flood plain of the Rhine can be derived from the fact that, on the one hand, a greater heat capacity is available below the surface of the forest because of numerous residual water bodies and that, on the other hand, inversion in the boundary layer is interrupted or at least weakened, as in large cities. These residual water areas

were especially large and numerous at the time of the satellite overpass, as the Rhine had had a particularly high water level a few days earlier in May 1978.

Surface Temperature and Land-Use

Besides the relief, different land-use types will be reproduced in the thermal image, depending on their individual heat budget. Thus, in Fig.III.2.13 the cities of Basel, Strasbourg, Mannheim and Frankfurt appear as warm areas, similar to extended forest areas in the Rhine Valley or in the highlands. Using this fact, the data structures can be used to separate individual land-use types and to quantify the influence of the special type of land-use on the surface temperature. For the region of the topographical map CC 7110 (1:2,000,000, Mannheim), for which the Landsat derived land-use classification was integrated into the data-structure, statistics of the surface temperature for each land-use type can be calculated. Without regarding the influence of the relief, this evaluation was calculated for the elevation level 0 - 200 m, according to the elevation of the Rhine Valley (Fig.III.2.15). The grey values 90, 100 and 110 of the abscissa in Fig.III.2.15 correspond to the temperatures 2.5, 5 and 7.5°C. For a better understanding of the evident correlation of the surface temperature with the type of land-use, the whole region of CC 7110 was overlaid with a grid of 5x5 km² (Fig.III.2.16). For each of these squares the distribution of the different land-use classes can be calculated. Fig. III.2.17 is an example of this calculation for four of these squares, containing the distribution of the classification, the parts of built-up and forest areas derived from the digitized maps and the mean surface temperature of the HCM data. The values demonstrate that high surface temperature coincides with large portions of built-up areas and that low surface tem-



ORIGINAL PAGE IS
OF POOR QUALITY

Fig. III.2.15. Temperature-histogram of all surfaces less than 200 m in elevation in the region of the TUK 200 OC 7110 (Mannheim). Land-use classes as in Fig. III.2.23.

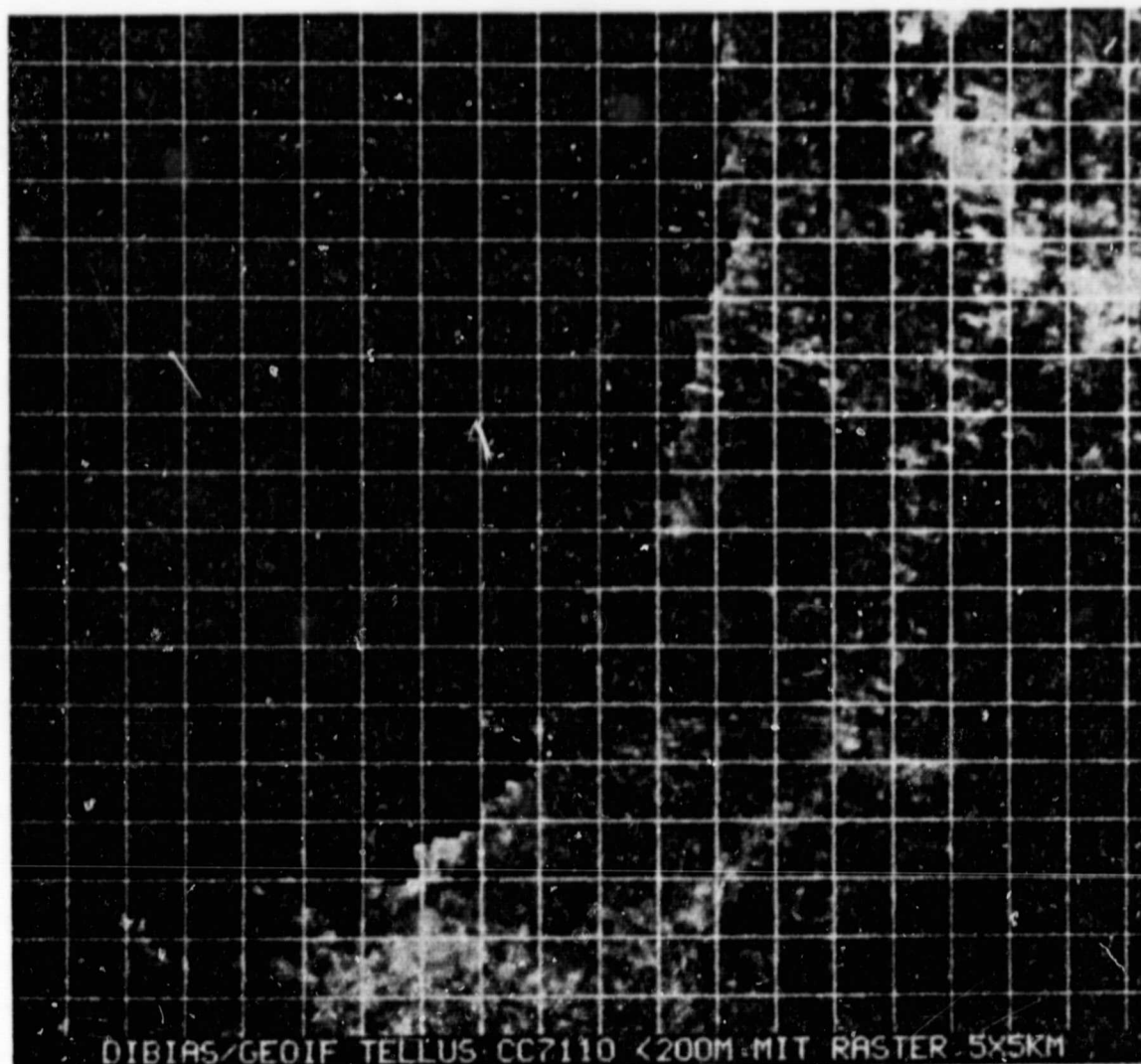


Fig. III.2.16. This figure represents temperatures of all surfaces with elevations of less than 200 m in the region of CC 7110 (Mannheim). Grid-distance 5 km. This will be used in order to derive the correlation between the average surface temperature of a square element of landscape and the relative distribution of the land-use classes within this square.

ORIGINAL PAGE IS
OF POOR QUALITY

perature coincides with large portions of agricultural land. On the other hand the question arises of why the large area of forest in square No. 3 (Bienwald) does not produce high temperatures.

To investigate these problems more carefully, the data of the nearly 150 squares were evaluated using regression analysis.

Critical Evaluation and Treatment of the Data

Histogrammes of the HCMM-temperature values for the various land-use classes show that, as expected, some types of surfaces have a trend for higher temperatures (Fig.III.2.17). This is true especially for densely built-up urban areas and areas covered by vineyards. On the other hand, we noticed that such a clear trend was missing in other land-use classes, for instance in woodland.

Woodland, sparsely built-up areas, arable land, as well as horticultural land and pastures showed nearly the same spread in the histogramme of HCMM values as was shown in the histogramme of the entire data set. There seem to be two reasons for this result. Firstly, even in the rather narrow deviation range selected, the various land-use classes form different surface temperatures as a result of the different geographic surroundings. This fact must be kept in mind when interpreting the deviations from regression. Secondly, the large spread in the HCMM-temperature values in the various surface classes is caused by sources of errors in the data themselves. Their influence on the present study had to be eliminated, or had at least to be limited. These sources of error are the following:

1) The geometrical smoothing of the Landsat, and even more so of the HCMM data is afflicted with a residual error which may pos-

sibly falsify the point-by-point classification at the margins of the land-use categories.

- 2) The size of the picture elements is 600 x 600 m for the HCMM data and is about 100 x 200 m for the land-use data. This means that, as a rule, HCMM values average out various types of land-use. When setting up the data structure, the individual HCMM picture elements were subdivided, if necessary, and the different parts were each assigned to one particular land-use class.
- 3) The basic land-use classification is in itself afflicted with a residual uncertainty. Most errors occur in areas with small plots of land, and at the boundaries of large land-use units.

In order to reduce these sources of errors, the data were treated as follows:

- 1) The comparison between HCMM-temperature values and land-use was not carried out for single HCMM values, but for larger areas, and their mean HCMM-temperature value was compared with the distribution of land-use classes in this area.
For this purpose, the entire area was divided into quadrangles of 5 x 5, resp. 10 x 10 km (Fig.III.2.16). The mean radiative temperature and the percentages of the various land-use classes were determined for each square (Fig.III.2.17). Thus, the influence of the residual errors of the geometric correction and the effect of the different size of the picture elements of Landsat and HCMM data were largely eliminated, more so in the larger (10 x 10 km) than in the smaller (5 x 5 km) squares.
- 2) All calculations were performed in two different ways. In the first one, the percentages of the eight land-use classes were inserted as separate variables. In the second method, six land-use classes were combined in pairs

Fig. 11.2.17. Surface temperatures and relative distribution of land-use classes in various grid-quadrants of the Upper Rhine Plain in the area of Mannheim.

Fig. 11.2.17. Surface temperatures and relative distribution of land-use classes in various grid-quadrants of the Upper Rhine Plain in the area of Mannheim.

Fig. 111.2.18. Multiple linear regression of the surface temperature (HCMM) on the percentage of land-use classes for quadrangles of sheet 7110 (Mannheim) of TUK 200. Dependent variable (V_3): HCMM-temperature value (mean of the square in standardized grey values); Independent variable: percentages of land-use classes (V_4 sparsely built-up, V_5 densely built-up, V_6 arable land, V_7 pastures and horticultural land, V_8 vineyards, V_9 coniferous forests, V_{10} deciduous forests, V_{11} water); A_1 built-up, A_2 open land, A_3 forests.

Fig. 111.2.18. Multiple linear regression of the surface temperature (HCMM) on the percentage of land-use classes for quadrangles of sheet 7110 (Mannheim) of TUK 200. Dependent variable (V_3): HCMM-temperature value (mean of the square in standardized grey values); Independent variable: percentages of land-use classes (V_4 sparsely built-up, V_5 densely built-up, V_6 arable land, V_7 pastures and horticultural land, V_8 vineyards, V_9 coniferous forests, V_{10} deciduous forests, V_{11} water); A_1 built-up, A_2 open land, A_3 forests.

to form three variables, i. e. : sparsely and densely built-up areas were combined to one variable named "built-up areas", pasture, horticultural and arable land to a variable named "open areas", and coniferous and deciduous forests to one variable "forests". As the accuracy of the classification increased from values of under 70% for the single land-use classes to values of over 80% for the combined land-use classes, the second calculation run served to control the results derived from the calculations with the single variables.

Moreover, on account of the particular situation at the edge of the Upper Rhine Plain and at the mouths of the valleys it was felt to be advantageous to perform all calculations with two different data sets. Therefore, we formed one data set with only those squares that were entirely below an altitude of 200 m and another data set featuring all the squares with at least part of their surface below 200 m. This set contained values of variables only from that part of their surface which was actually at an altitude below 200 m. Thus, a total of four data sets (large and small squares, squares entirely below 200 m and squares at least partially below 200 m) were evaluated in two calculation runs, i. e. single variables, respectively, part of the variables combined (Fig.III.2.18).

Application of Multiple Linear Regression Analysis

The HCMM temperature values were taken as the dependent variable y , the percentages of the land-use classes as the independent variables $X_1, X_2, X_3, \dots, X_8$, respectively, X_1, \dots, X_5 . The multiple linear regression of Y on X_1, \dots, X_K was calculated with the

program "REGRESSION" from the program package SPSS of the Computer Centre of Freiburg University.

The variables were introduced into the calculation one by one, creating the prediction equations: Y_1, \dots, Y_K .

1. The Contribution of the Type of Land-Use to the Variance of the Surface Temperatures

The part of the total variance of the surface temperature accounted for by land-use varied between 19 and 50.5% for the different data sets used (see Fig.III.2.18). Accordingly, also the corresponding standard deviations varied between 3.09 and 1.80 (which corresponds to 0.77°C , respectively 0.45°C).

Apparently, the better results from calculation runs 7 and 8 (Fig.III.2.18) are mainly based on the greater homogeneity of the data sets used in these two runs. They exclude two areas where, as will be shown in the later discussion on the deviations, other influences on the HCMM-temperature values, which do not result from land-use, are particularly intense. These areas are the valley bottoms and the mouths of the valleys on both sides of the Upper Rhine Plain, and the agricultural and wooded area to the south-east of Mannheim. The high surface temperatures of the latter cannot be explained on the basis of its land-use. Therefore, the following conclusions were based mainly on runs 7 and 8.

Figs.III.2.19 and 20 show the results for the different calculation steps for these two runs.

The linear regression model with five land-use classes accounts for the spread of surface temperatures to 26.6%, with built-up areas, to 11.7% with water surfaces to 2.1%, with open areas and to 1.2% with vineyards. The model with eight land-use classes accounts for 34.1%

Step	Variable included	Variance explained	Increase in the variance explained	r	$(1-r)^2$ for the variables not included						
1	V ₅ (Densely built-up)	34.1%	34.1%	0.584	V ₄	V ₆	V ₇	V ₈	V ₉	V ₁₀	V ₁₁
2	V ₁₁ (Water)	43.1%	9.0% (23.4%)	0.656	0.35	0.95	0.87	0.98	0.98	0.85	0.87
3	V ₁₀ (Deciduous)	44.7%	1.6%	0.669	0.35	0.93	0.65	0.91	0.88	0.86	
4	V ₈ (Vineyards)	46.4%	1.7%	0.681	0.31	0.23	0.55	0.75	0.58		
5	V ₆ (Arable)	48.9%	2.5% (5.9%)	0.699	0.25	0.17	0.51	0.58	0.47		
6	V ₄ (Sparsely built-up)	50.3%	1.4% (16.7%)	0.710	0.17		0.42	0.46			
7	V ₇ (Pastures and horticulture)	50.5%	0.2%	0.711			0.25	0.004			

Fig. III.2.19. Stepwise multiple linear regression of the HCMM-temperature values on the percentage of the various land-use classes (calculation run 7, eight land-use classes). The percentages in parentheses are the part of the variance which the corresponding variable would explain in a simple linear regression.

Step	Variable included	Variance explained	Increase in the variance explained	r	$(1-r)^2$ for the variables not included			
1	A ₁ (Built-up)	26.6%	23.6%	0.516	A ₂	A ₃	V ₈	V ₁₁
2	V ₁₁ (Water)	38.3%	11.7% (23.4%)	0.619	0.80	0.86	0.96	0.91
3	A ₂ (Open land)	40.4%	2.1% (9.9%)	0.635	0.79	0.84	0.90	
4	V ₈ (Vineyards)	41.6%	1.2%	0.645	0.09	0.88		

Fig. III.2.20. Stepwise multiple linear regression of the HCMM-temperature values on the percentage of the various land-use classes (calculation run 8, five land-use classes). The percentages in parentheses are the part of the variance which the corresponding variable would explain in a simple linear regression.

of the spread with densely built-up areas, and 9.0% with water surfaces. The part of each of the remaining land-use classes was 2.5% or less (deciduous forests 1.6%, vineyards 1.7%, arable land 1.4%, sparsely built-up areas 1.4%, horticultural areas and pastures 0.2%).

Both models showed the dominant role on night-time surface temperatures of urban built-up areas on one hand, and water surfaces on the other. This is true for densely, as well as for sparsely built-up urban areas. Though variable V_4 (sparsely built-up) appears only in sixth place in Fig.III.2.20 with an increase in variance accounting for only 1.4%, this is caused by the high correlation between the percentages of sparsely and densely built-up areas ($r = 0.81$). A simple linear regression between V_3 and V_4 alone would result in 16.7% of the variance accounted for. The same is true for water surfaces, the contribution of which, on account of the many cities along the Rhine, is weakly correlated with the part of urban surfaces ($r = 0.35$ for V_5 and V_1 , resp. $r = 0.31$ for A_1 and V_{11}). A simple linear regression for V_3 and V_{11} would result for both data sets in 23.4% of the variance accounted for. In addition, this particular effect was only found in agricultural pastures and horticultural areas. In a simple regression, the arable land V_6 , accounts for 5.9%, and the collective variable open land, A_2 for 9.9% of the variance of the surface temperature.

It is rather conspicuous that all forests, especially coniferous forests, furnished only small contributions to an explanation of the distribution of surface temperatures, although in the thermal picture, the edges of forest land may be identified in many cases as borderlines between warm and cold zones. This results was not caused by their late inclusion into the cal-

culation or their correlation with other variables. Even with a simple regression, the forest areas would furnish only a very small part of the variances (A_1 2.25%, V_9 1.25%, V_{10} 3.13%). The cause is, as was confirmed by observing the deviations, that the forests in the test area had a wide range of surface temperatures, i.e. they showed relatively high and also relatively low values. Deciduous forests seemed to show a clearer tendency for higher surface temperatures.

2. Modification of Surface Temperature with Changing Land-Use

The previous part of the study showed, respectively confirmed, that besides the different forms of land-use, there were other factors which strongly determined night-time surface temperatures. Therefore, even in the case of such relatively homogeneous data sets as 7 and 8, the part of the land-use classes accounted only for 40 - 50% of the variance of the surface temperature. However, it would be worthwhile to use the present model correlating surface temperature and land-use to answer another important question, i.e. how and to what degree a change in land-use would affect the surface temperature. We think this would be a much needed contribution of remote sensing in predicting the possible climatologic consequences of man-made changes of large parts of the landscape. Therefore, we should like to anticipate, with a few remarks on the validity of the results, what could be expected to be obtained:

- 1) The model is valid only for the area covered by the data set. Without further study, it is not possible to transfer it to other areas with different boundary conditions.
- 2) The model is valid only for the same weather conditions as those at the time of and during the last few hours prior to the HCMM passage. A different wind regime, for instance,

or a different degree of incoming long wave radiation would have led to other temperatures of the various surface types, as well as to entirely different regression coefficients. Evidently, the model is valid for the corresponding time of the day.

It should also be noted that in the following discussion the influence of the emissivity of the various surfaces has not yet been taken into consideration. This will be done elsewhere in connection with the absolute calibration of the HCMM data, and may also lead to certain corrections of the temperature differences given below.

Calculation run 7, after the 7th calculation step furnished the following regression equation:

$$V_3 = 0.2111 \cdot V_5 + 0.5649 \cdot V_{11} + 0.1624 \cdot V_{10} + 0.1539 \cdot V_8 + 0.0807 \cdot V_6 + 0.0960 \cdot V_4 + 0.0154 \cdot V_7 + 90.285$$

With this equation we may estimate how V_3 would change if one of the variables V_5, \dots, V_{11} were decreased by 20%, while another variable was increased by 20%. The results of this calculation, converted into centigrades, are depicted in Fig.III.2.21, and the corresponding results for run 8 are given in Fig.III.2.22. These figures permit an easy determination of the changes in surface temperature, also for other changes in land-use.

How can these figures be interpreted? First, we should ask whether the temperature modification in question really results only from the above mentioned change in land-use, or if it was caused by other phenomena coupled to the corresponding land-use. This seems particularly to be the case when vineyards are involved. The increase in temperature from 0.19 to 0.77°C when changing from arable

land, pastures and horticulture, and conifers, or in the combined form, open land and forests, to vineyards is easily explained by the more favourable thermal location of vineyards in comparison with other agricultural and wooded areas. Accordingly, the mean surface temperature of an area near Karlsruhe occupied by conifers is not going to increase by 0.77°C, if we cut down 20% of the trees and start to plant grapes instead, as we are led to believe from looking at Fig.III.2.21. This means that the model is not applicable to the same extent for predictive purposes as the distribution of the various present land-use classes was determined by thermal conditions, either favourably or unfavourably. Otherwise, to realize the changes in surface temperature derived from the regression model would not only necessitate the corresponding change in land-use, but also the realization of the particular thermal conditions in the environment. This objection, or rather this limitation, is, fortunately, not true for the relations between urban areas and the various open land types, as at least the expansion of larger settlements during the course of the last 100 years has taken place without any consideration of, and without being influenced by thermal conditions. Should the current discussions, e. g. over fresh air currents, influence to a large extent the future expansion pattern of settlements, then in one hundred years a similar study would result in a different picture. However, at present it may be assumed that the values in the first two columns of Fig.III.2.21 are to be explained solely by their different land-use. Therefore, they may well be used to predict temperature modifications due to changes in land-use.

This means that a change of 20% of sparsely built-up areas to densely built-up (column 2 in Fig.III.2.12) would raise the surface tempera-

	20% Decrease	Increase 20%	Sparsely built-up V_4	Densely built-up V_5	Arable V_6	Pastures and horticulture V_7	Vineyards V_8	Conifers V_9	Deciduous V_{10}	Water V_{11}
Sparsely built-up	V_4			0.576	- 0.076	- 0.403	0.290	- 0.480	0.332	2.345
Densely built-up	V_5	- 0.576			- 0.652	- 0.979	- 0.286	- 1.056	- 0.244	1.769
Arable	V_6	0.076	0.652			- 0.327	0.366	- 0.404	0.408	2.421
Pastures and horticulture	V_7	0.403	0.979	0.327			0.693	- 0.077	0.735	2.748
Vineyards	V_8	- 0.290	0.286	- 0.366	- 0.693			- 0.770	0.042	2.055
Conifers	V_9	0.480	1.056	0.404	0.077	0.770			0.812	2.825
Deciduous	V_{10}	- 0.332	0.244	- 0.408	- 0.735	- 0.042	- 0.812			2.013
Water	V_{11}	- 2.345	- 1.769	- 2.421	- 2.748	- 2.055	- 2.825	- 2.013		

Fig. III.2.21. Change in the night-time surface temperature ($^{\circ}\text{C}$) due to a modification of the land use by 20%. Estimate, taken from the results of the linear multiple regression of the HCM-temperature values on the percentage of land-use classes for squares of 10 x 10 km. 8 land-use classes (calculation run 7).

	20% Decrease	Increase 20%	Built-up A_1	Open land A_2	Forests A_3	Vineyards V_8	Water V_{11}
Built-up	A_1			- 0.552	- 0.245	- 0.054	2.038
Open land	A_2	0.552			0.307	0.498	2.590
Forests	A_3	0.245	- 0.307			0.191	2.283
Vineyards	V_8	0.054	- 0.498	- 0.191			2.092
Water	V_{11}	- 2.038	- 2.590	- 2.283	- 2.092		

Fig. III.2.22. Change in the night-time surface temperature ($^{\circ}\text{C}$) due to a modification of the land use by 20%. Estimate, taken from the results of the linear multiple regression of HCM-temperature values on the percentages of the land-use classes for squares of 10 x 10 km in the Upper Rhine Plain between Mannheim and Karlsruhe. 5 land use classes (calculation run 8).

ture by at least $0.5 (0.58)^{\circ}\text{C}$. If the expansion of densely built-up areas takes place at the expense of agricultural surfaces, the surface temperature would increase by at least $0.6 (0.65)^{\circ}\text{C}$, at the expense of pastures and horticultural land almost $1 (0.98)^{\circ}\text{C}$, woodland (dependent on the type) between 0.25 and 1°C . Only if urban settlement were to spread by 20% at the expense of water surfaces then the surface temperature would decrease by about $1.8 (1.77)^{\circ}\text{C}$.

For an expansion of sparsely built-up areas by 20% (Fig.III.2.22 column 1) the thermal effect may be different depending on the initial situation. Settlements in agricultural areas would not considerably change the surface temperature. Settlements, instead of pastures and horticultural areas, would lead to a temperature increase of about 0.4°C , settlements instead of deciduous forests to a decrease in temperature by 0.3°C . A corresponding spread of settlements at the expense of water surfaces would result in a drop in temperature of about 2.3°C .

Similarly, we may look at the consequences of deforestation and its change to another type of land-use (Fig.III.2.21, 2nd line from below). An extension by 20% of agricultural surfaces at the expense of deciduous forests would decrease the surface temperature by about $0.4 (0.4)^{\circ}\text{C}$ and a change to pastures and horticultural land by about $0.8 (0.7)^{\circ}\text{C}$, whereas an extension of vineyards at the expense of deciduous forests would have almost no thermal consequences (0.04°C).

The corresponding numbers for coniferous forests (Fig.III.2.21, 3rd line from below) should be looked at rather cautiously, as the reasons for the low temperatures of the coniferous forests indicated in the HCMM scene of the control area are not sufficiently clear. Similar to vineyards, a thermal discrimination in

the location of coniferous forests could have taken place, with in this case the forests occupying the locally colder sites. In the control area, the conifers are represented mostly by pine trees on dry locations. One might also consider the effect of the thermal emissivity, assuming that pine trees, due to the waxy surface of the needles have a significantly lower thermal emissivity than the other types of vegetation prevalent in this area. No conclusion can be reached at this moment.

The thermal effect of the increase, respectively decrease of water surfaces is also of interest, as in the past there was considerable human interference along the Rhine River in the form of the regulation of the water way, and the same can be predicted for the future. There is evidence (Fig.III.2.21, last line, respectively last column) that with 20% change in water surface (except for a change to a densely built-up area) there is always a change in surface temperature by $2-3^{\circ}\text{C}$, i. e. it increases by that amount when the water part is enlarged, and it decreases by that amount when the water part is reduced with regard to the total surface.

3. The Detection of Night-time Cold Air Reservoirs and Cold Air Streams Depending on the Deviations from Regression

An analysis of the deviations from regression in Figs.III.2.23 and 24 shows that extreme values are generally not isolated but grouped. This confirms the assumption that the deviations from regression not only form a random part of the data set, but that they can be explained by a causal relation.

Assuming that the influence of land-use is largely and exhaustively represented by the regression, we must attribute the deviation from regression to the effect of other factors on the surface temperature. It is therefore of

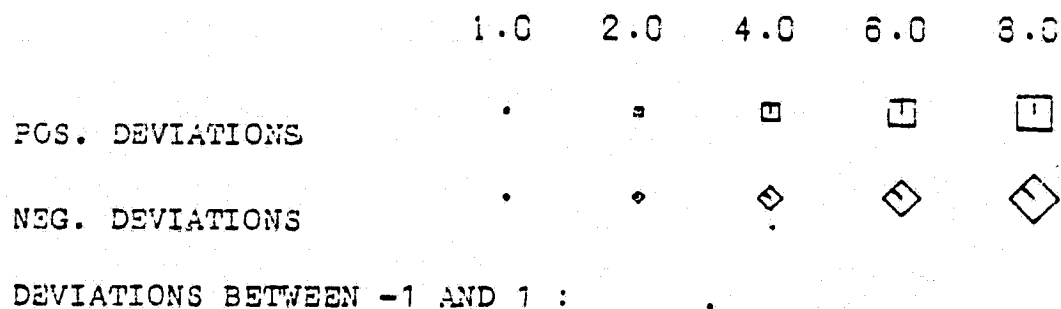
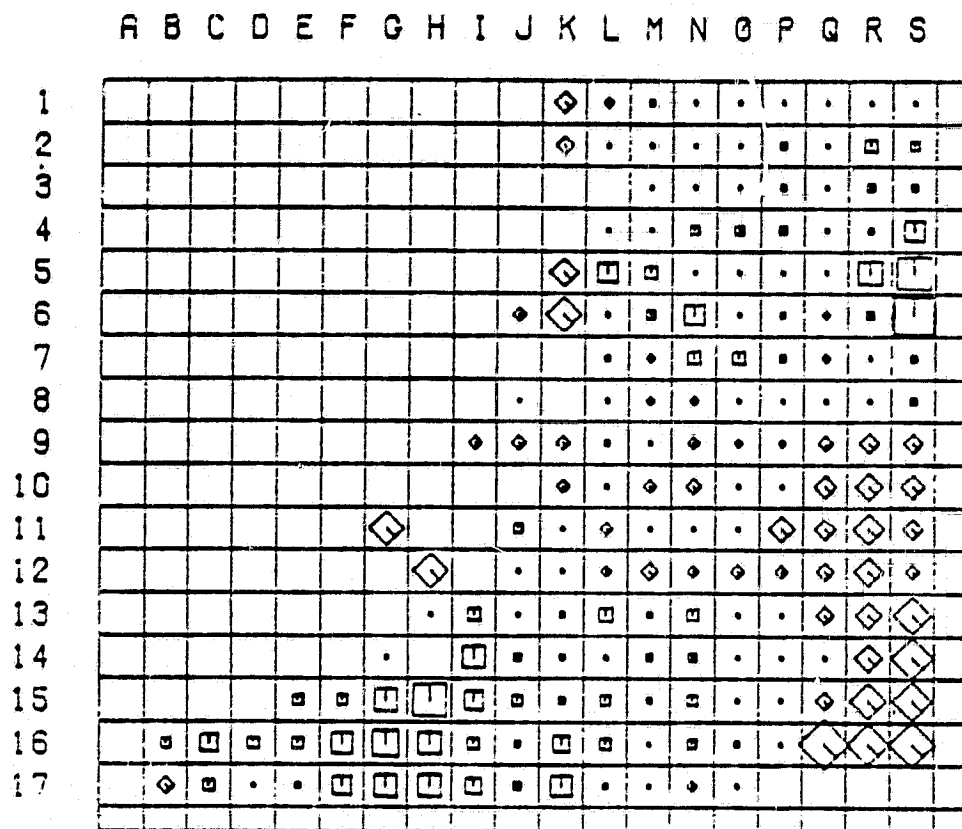


Fig. III.2.23. Deviations from the multiple linear regression of HCM-temperature values on the land-use classes (calculation run 1). Four units correspond to one degree centigrade.

ORIGINAL PAGE IS
OF POOR QUALITY

ORIGINAL PAGE IS
OF POOR QUALITY

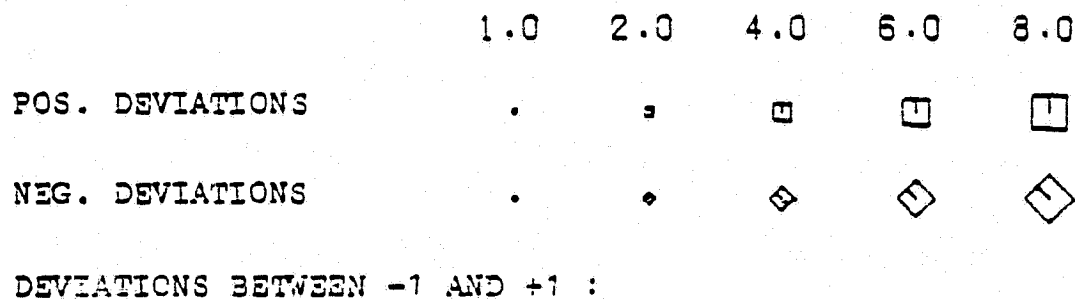
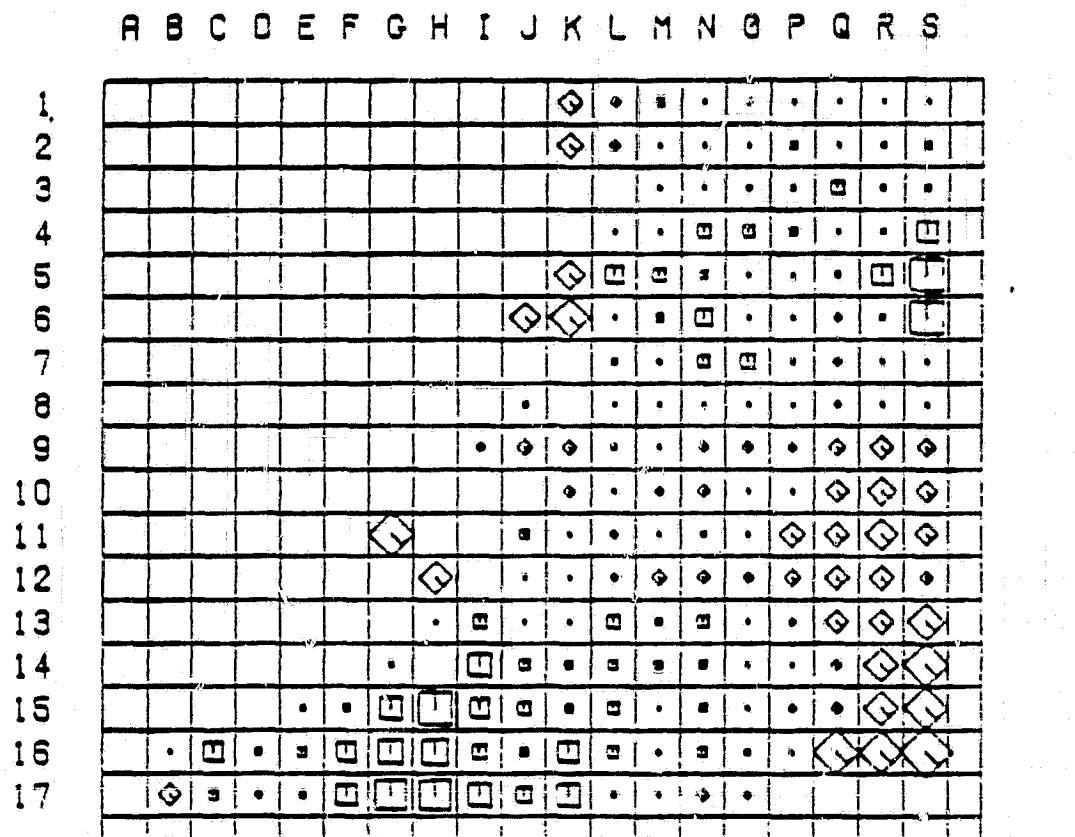


Fig. III.2.24. Deviations from the multiple linear regression of HCMH-temperature values on the land-use classes (calculation run 2). Four units correspond to one degree centigrade.

interest to investigate the relations of the deviations from regression to other environmental factors.

This investigation seems to be especially valid for the deviations from regression of the calculations with all squares of 5 x 5 km which have at least parts of the surface at an altitude below 200 m (Figs. III.2, 23 and 24).

They also include the foot-of-the-hill area at the edges of the gravel and the bottom of the valleys dropping down into the Upper Rhine Plain. This makes it possible to study the particular situation at the edge of the Upper Rhine Plain and furnishes a contribution to the question, how effectively these valleys may function as reservoirs for cold air on the one hand, and as cold air corridors on the other, and thus as night-time sources of fresh air for the settlements at the mouths of these valleys. It should further indicate to what degree HCMM images may help to clarify these phenomena.

Valley as Cold Air Reservoirs: It has been known for a long time that valley bottoms cool off during the night, and this phenomenon has been registered repeatedly on infrared thermal images. Usually, though, it is not possible to decide to which degree the two factors "relief" and "surface cover" (or vegetation) are involved in the particular night-time cooling-off process of the valley bottoms. In many cases, the low temperatures may be attributed to the concave relief as well as to the large part of meadows on the valley bottom, i. e. to the collection of cold air flowing down from the slopes, as much as to the low thermal capacity of meadows and the resulting heat loss of grass surfaces during the night. As the latter effect is largely taken into account by the above regression analysis, the negative deviations on both sides of the Upper Rhine Plain result from the effect of cold air streams from the

slopes. They are largely a function of the shape of the valleys and the temperature regime of the slopes.

One may note that the largest negative deviations in both calculation runs occur in the south-eastern part of sheet CC 7110, especially the valley area of the "Pfinz" (R 15, R 16, S 15, S 16) and of the "Saalbach" (S 14) which, coming from the "Kraichgau" enter the Upper Rhine Plain east of Karlsruhe. These valleys have a depth of about 50 - 100 m with slopes of no more than 8°, half of them being free of forests, i. e. being arable land.

The negative deviations are somewhat smaller (1.0 - 0.5°C) in the valleys of the Palatine Forest (Pfälzer Wald), i. e. that of the "Lauter" (G 11, H 12) and those of the "Cueich" and the "Speyerbach" (K 6, K 7). In contrast to the valleys of the "Kraichgau" these valleys cut 200 - 300 m deep into the bottom of the "Pfälzer Wald", and have slopes of more than 20°. With the exception of the valley bottoms they are usually completely covered by forests. These observations correct and complete, in a rather important way, the first impressions obtained from the untreated thermal image. In these images, the deeply cut valleys with their meadow grounds between the wooded hills stand out by their low surface temperatures, while in strictly agricultural areas like the "Kraichgau" the valleys are rather difficult to identify. Nevertheless, the conclusions drawn above strongly support the theory that the cooling effect of the cold night air coming down from the hills is greater in these valleys with large tracts of arable land.

Valleys as Conducts of Fresh Air: Another question of interest concerns the possibility to deduce from the deviations valid information about the role of these valleys as sources of cold and fresh air for the settlements at the

mouths of the valleys. FEZER, respectively GEIGER, both in 1977, gave us a description of such night-time mountain winds at the valley exit of the "Pfälzer Wald". The map of wind registrations at the time of the HCMM passage shows (Fig.III.2.25) a cold air current at the junction of the "Speyerbachtal" near Neustadt (L 6) with the Upper Rhine Plain and we may well expect other valleys to produce the mountain winds as described by FEZER and GEIGER.

However, studying the deviations of the squares located in front of these valleys exists (compare in Figs.III.2.16, 23 and 24 the squares M 1, M 4, M 6, L 9, L 10, J 13, etc.) we find either very small, or slightly positive deviations.

For none of these valleys do they really show a cooling effect of the fresh air current on the surface temperatures directly in front of the mouth of the valley.

We conclude that the spread and extension of these cold air currents is relatively small in comparison to the order of magnitude of the 5 x 5 km squares. However, it could be possible that a certain whirl-pool effect with increased wind speed at the ground occurred in the mixing zone between the mountain wind and the north-south current which prevailed at the moment of the HCMM passage in the Upper Rhine Plain (compare Fig.III.2.25). This effect may have, in part, prevented the decrease of the surface temperatures.

The situation in the eastern part of the Upper Rhine Plain, i.e. the valleys of the "Kraichgau" is somewhat different and the squares at the mouths of these valleys (Q 13, R 12, and S 11) have negative deviations of 3 to 5 points ($0.75 - 1.25^{\circ}\text{C}$). This result could possibly, in part, be attributed to the cold air currents from these valleys. Further meteorologic measurements would be needed to prove this

assumption, as not only the quadrangles in front of the valley exits, but also the entire area of the so-called "Randniederung" and the Hardt-Forests north-east of Karlsruhe (P 11, Q 9, 10, 11, 12; R 9, 10, 11, and S 10) show corresponding negative deviations from regression.

One may conclude that the deviations from the multiple regression based on 5 x 5 km squares describe rather well the ability of valleys at the edge of the Upper Rhine Plain to form cold air reservoirs. They do not reflect the influence of the cold air flowing out of the valley into the plain, or, it is rather impossible to distinguish between this influence and other factors.

4. Deviations in the Central Parts of the Upper Rhine Plain

The calculation runs 5 and 6 (Figs.III.2.26 and 27) contain only the quadrangles of size 5 x 5 km which lie entirely below an altitude of 200 m. This excludes the areas of the valley bottoms and the mouths of the valleys, as well as the lower slopes on both sides of the Upper Rhine Plain.

First, one has to keep in mind that quadrangles with large negative or positive deviations belong nowhere to urban built-up areas. Thus, the quadrangles covering the large cities Mannheim/Ludwigshafen (P 2, P 3, Q 2, Q 3) and Karlsruhe (O 13, O 14, P 14) have very small deviations.

This corresponds to the assertion made above, i.e. that for the built-up areas the regression represents, especially well, the influence of the land-use on the surface temperature. In areas with a high percentage of urban construction the estimate of the surface temperatures from the percentage of the land-use classes is, therefore, the least disturbed by

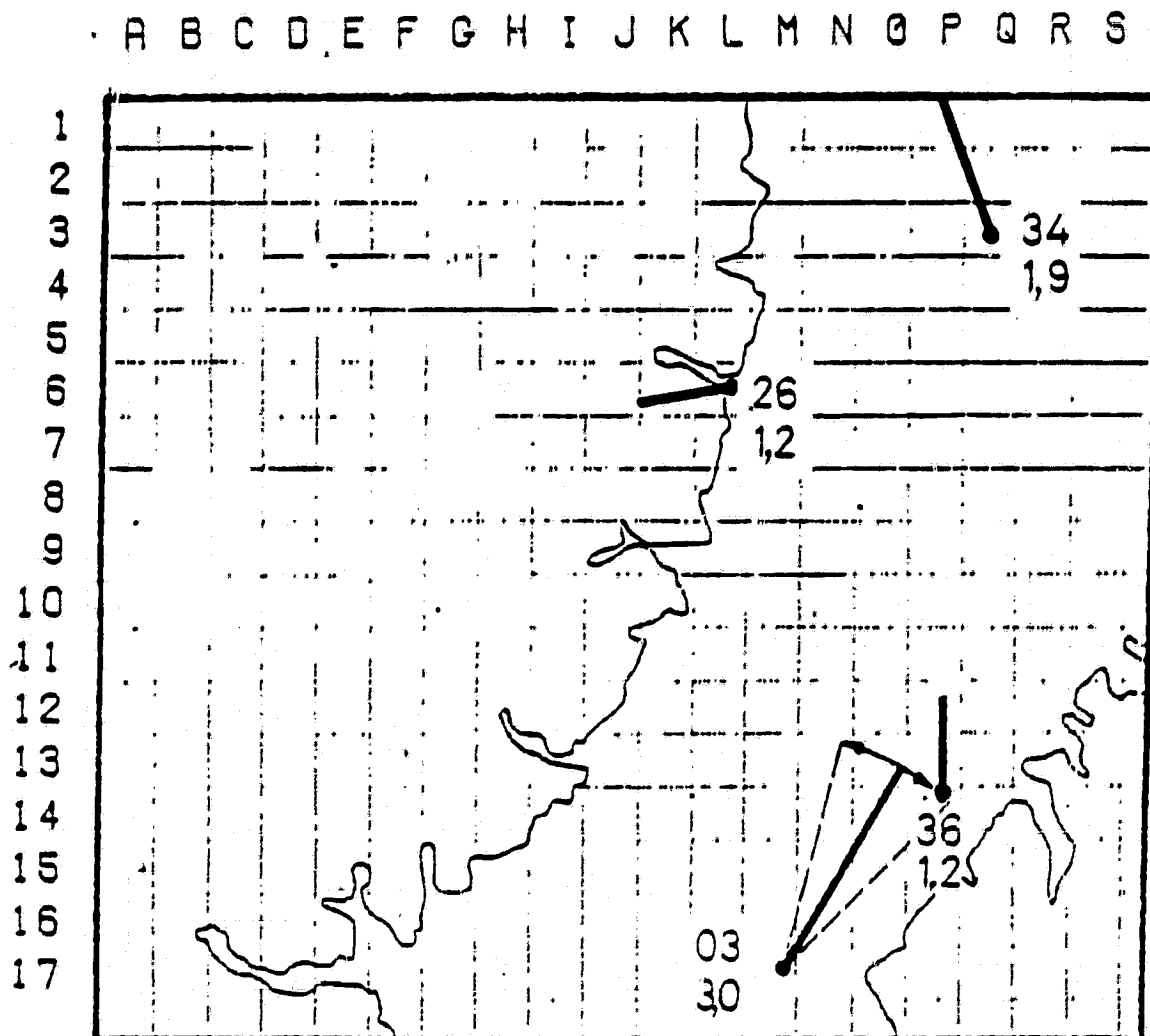
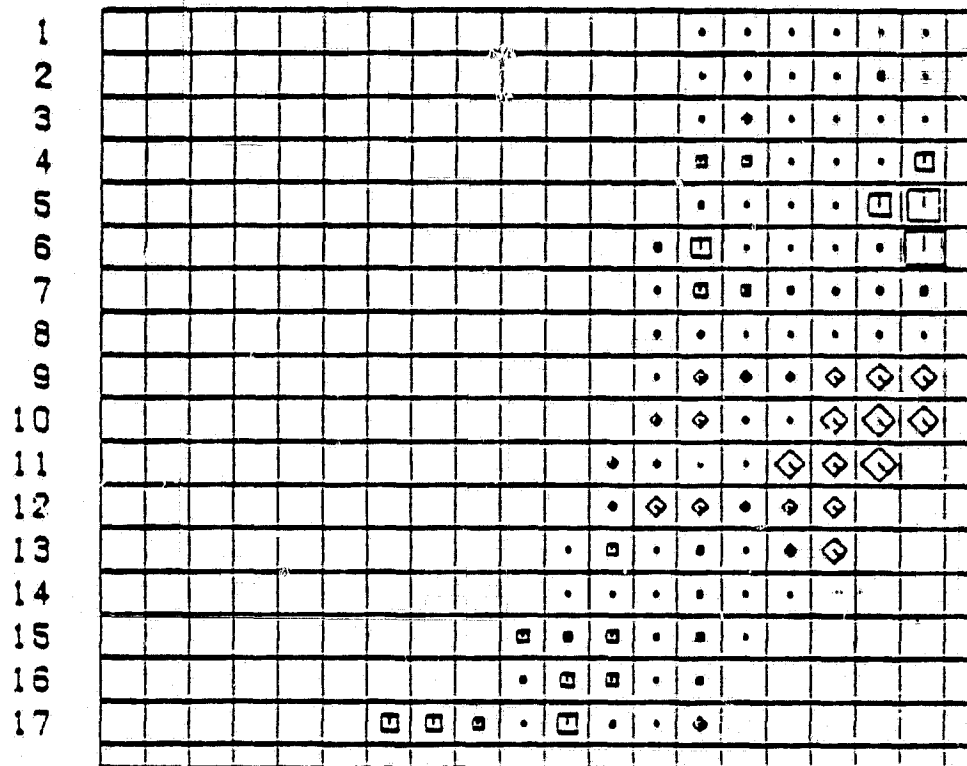


Fig. III.2.25. Average hourly values of the wind direction and wind speed on May 30, 1978, 2-3 GMT (3-4 MEZ). Stations: Mannheim (Q3), Karlsruhe (P13), Rastatt (M17), Neustadt (L6). Upper number: wind direction (0 ... 36); lower number: speed of the wind (m/s). These data were kindly provided by the Deutschen Wetterdienst and Landesanstalt für Umweltschutz, Karlsruhe.

ORIGINAL PAGE IS
OF POOR QUALITY

A B C D E F G H I J K L M N O P Q R S



1.0 2.0 4.0 6.0 8.0

PCS. DEVIATIONS

NEG. DEVIATIONS

DEVIATIONS BETWEEN -1 AND +1 :

Fig. III.2.28. Deviations from the multiple linear regression of the HCMM-temperature values on the percentage of the land-use classes (calculation run 5). Four units correspond to one degree centigrade.

ORIGINAL PAGE IS
OF POOR QUALITY

ORIGINAL PAGE IS
OF POOR QUALITY
SMALL SQUARES, COMPLETELY BELOW AN ALTITUDE OF 200 METERS.
5 LAND USE CLASSES.

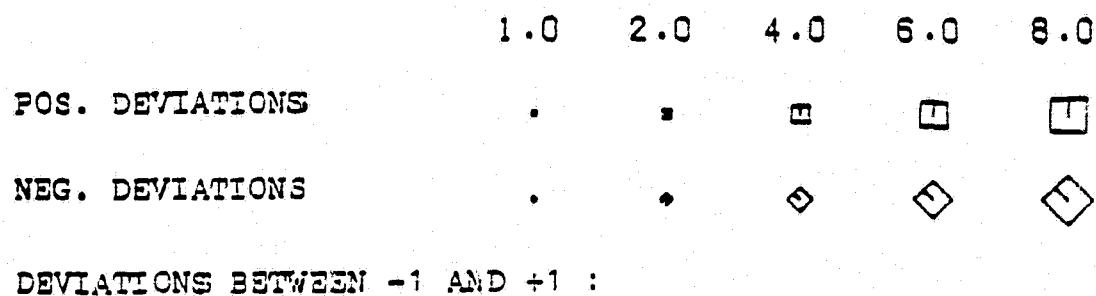
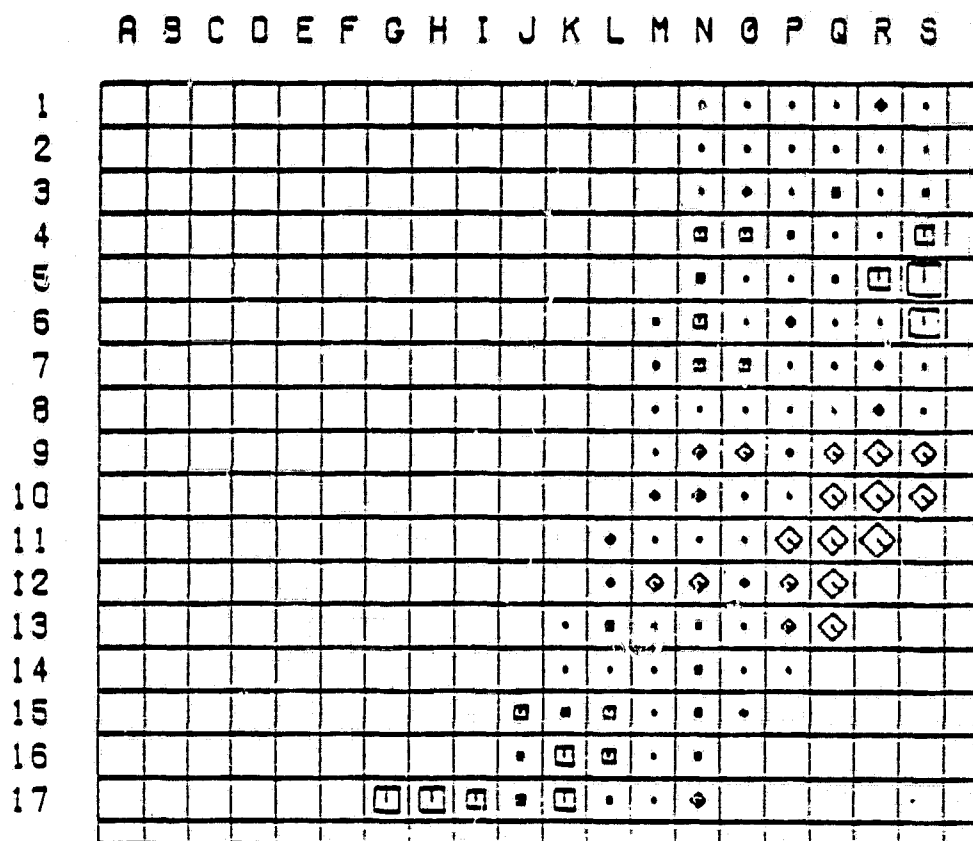


Fig. III.2.27. Deviations from the multiple linear regression of the HCMM temperature values on the percentage of the land-use classes (calculation run 6). Four units correspond to one degree centigrade.

ORIGINAL PAGE IS
OF POOR QUALITY

SMALL SQUARES, COMPLETELY BELOW AN ALTITUDE OF 200 METERS.
3 LAND USE CLASSES.

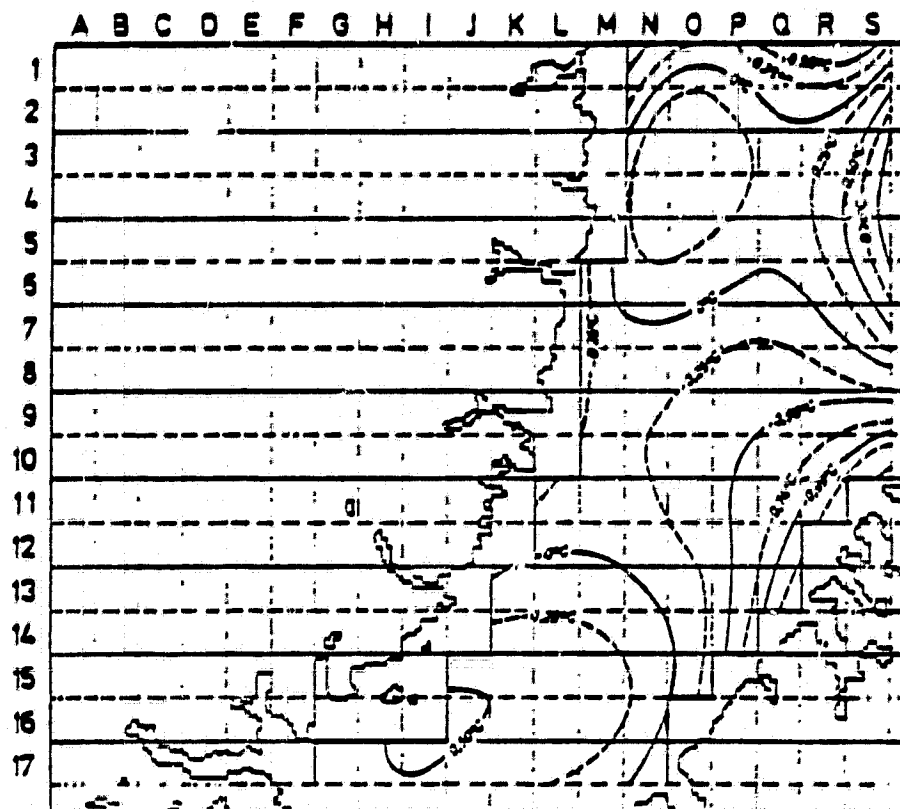


Fig. III.2.28. Trend surface (4th degree) of the deviations from the multiple linear regression of the HCM temperature values on the percentage of land-use classes. (Calculation run 5). The trend surfaces were calculated with the TREND programme of the GEO-GEO programme library at the Computing Centre of Freiburg University. The cooperation of Dr. Güssefeld in permitting use of this programme is gratefully acknowledged.

ORIGINAL PAGE IS
OF POOR QUALITY

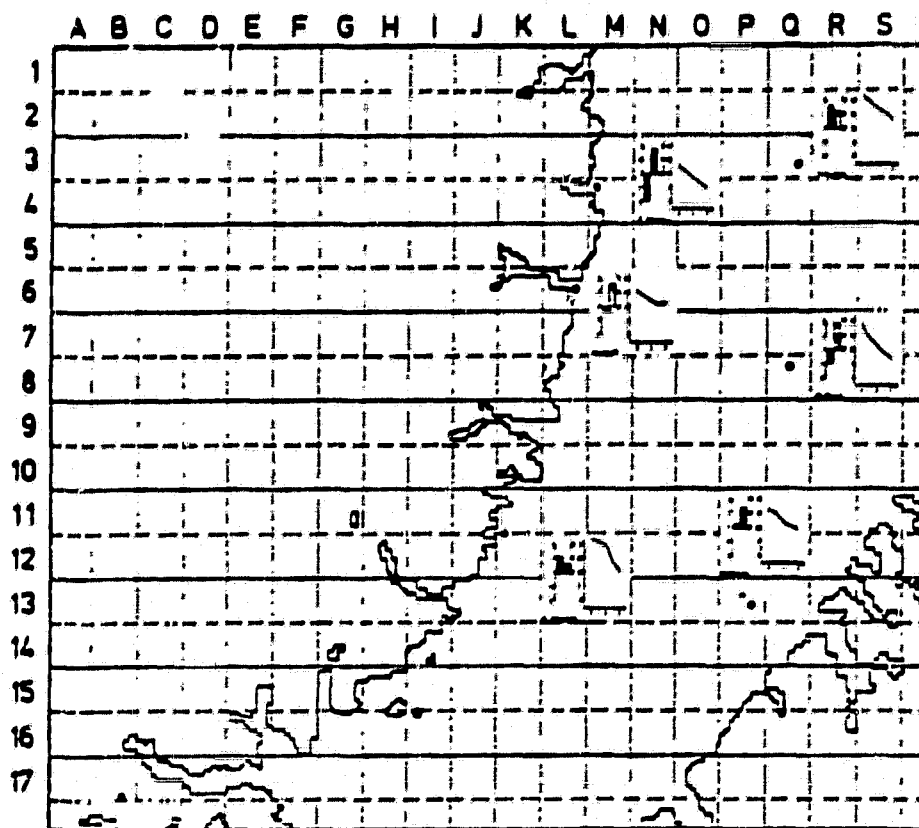


Fig. III.2.29. Meteorological data from the Upper Rhine Plain between Mannheim and Karlsruhe on May 30, 1978, at 2.13 GMT (3.13 MEZ). Left column: deviation of the air temperature from the value measured in Karlsruhe ($^{\circ}\text{C}$); right column: humidity of the air (%); curve: course of the air temperature between 0 and 4 MEZ; climatological stations: Karlsruhe (P13), Philippsburg (Q8), Mannheim (Q3), Heidelberg (to the right, outside), Bad Dürkheim (M4), Neustadt (L6), Bad Bergzabern (L11/12). (These data were kindly provided by the Deutschen Wetterdienst and Landesanstalt für Umweltschutz, Karlsruhe.)

other factors.

The same is true, with only two exceptions (P 11 and R 5), for the quadrangles which follow the course of the Rhine, crossing the Upper Rhine Plain at about its centre from south to north (L 17, L 16, M 17, N 14, O 13, O 12, P 11, P 10, P 9, P 8, Q 8, Q 7, Q 6, Q 5, R 5, Q 4, Q 3, Q 2, P 1). These are the quadrangles which contain a usually small percentage of water surfaces. Both these surface categories (urban built-up areas and water surfaces), due to the large heat capacity of their materials, react rather slowly to the short-term oscillations of meteorological parameters. It is therefore obvious to look at the areas with large deviations for a relation to meteorological factors such as air temperature, humidity, and wind.

For this purpose, trend surfaces were calculated for the deviations in the various calculation runs (compare the example in Fig.III.2.28) which can be better related to meteorological data than the single deviations. Their comparison with the air temperature, air humidity, and the course of the air temperature during the last hours before the HCMM-passage shown in Fig.III.2.29 helps to explain which deviations can be grouped together.

Thus, the trend surface in Fig.III.2.28 fits in well with:

- the high air temperature and low air humidity in Mannheim, Heidelberg and Bad Bergzabern,
- the low temperature and high humidity in Philippsburg,
- and the important decrease of air temperature between 0 and 4 MEZ in Philippsburg, and the somewhat lesser decrease and subsequent rise at 2 MEZ of the temperature in Heidelberg.

But the comparison of the various trend surfaces with the data collected so far still does not give us a definite picture of the correlation of surface temperatures with meteorological events. As there will probably be additional meteorological data to be included in this study, we should like to postpone to a later report further elaboration of this point.

References

1. H. GOSSMANN, and P. HABERÄCKER; "Image Processing of HCMM-Satellite Thermal Images for Superposition with Other Satellite Imagery and Topographic and Thematic Maps." TELLUS Newsletter No. 12, Ispra 1980.
2. P. HABERÄCKER et al.; "Auswertung von Satellitenaufnahmen für die Landnutzung" Schriftenreihe "Raumordnung" des Bundes-Ministers für Raumordnung, Bauwesen und Städtebau, Bonn, 1980.
3. S. SCHNEIDER; "Auswertung von Satellitenaufnahmen bei der Gewinnung von Flächennutzungsdaten für die räumliche Planung." Bul. 47 (1979), 179-182.
4. F. FEZER and R. SEITZ; "Klimatologische Studien im Rhein-Neckar-Raum. Studien zur Regional- und Siedlungsplanung". Heidelberger Geogr. Arbeiten, 47 (1977).
5. M. GEIGER; "Das Geländeklima an der Weinstrasse und im vorder-pfälzischen Tiefland". In: Klimatologische Untersuchungen im Rhein-Neckar-Raum. Heidelberger Geogr. Arbeiten, 47 (1977), 105-134.

Part 2

2. Interpretation Results from HCMM Digital Radiance Data Recorded over Belgium

R. Gombeer
Laboratorium voor Bodemgenese en Bodemgeographie,
Katholieke Universiteit te Leuven, België

General Introduction

Referring to the general mission objectives of Part 2, the results over Belgium may contribute to studies which are placed under the following headings:

- a) Relations between soil type, soil moisture and remotely sensed surface temperature.
- b) Mapping of surface thermal gradients on land and for water bodies.
- c) Calculation of apparent thermal inertia (ATI) and correlation with different land-use classes or land surface types.

The present part reports on interpretation results from HCMM-data acquired until November, 1980.

The following HCMM-scenes have been used for analysis:

- 1) 30 May 1978 night-IR
AA-0034-02130-3 (Belg.)
- 2) 28 July 1978 night-IR
AA-0093-02100-3 (Belg.)
- 3) 16 Sept. 1979 day-VIS + IR
orb. 7527 79 259
(11.46.55 GMT) sub-image 5 (Belg.)
- 4) 16 Sept. 1979 day-VIS
AA-0508-12000-1 (Belg.)
- 5) 16 Sept. 1979 day-IR
AA-0508-12000-2 (Belg.)

- 6) 16 Sept. 1979 night-IR
orb. 7520 79 259
(00.26.32 GMT) sub-image 5 (Belg.)
- 7) 16 Sept. 1979 night-IR
AA-0508-01002-3 (Belg.)
- 8) 5 Dec. 1979 day-VIS + IR
orb. 8712 79 339
(11.34.55 GMT)
(N-Africa)
- 9) 6 Dec. 1979 day-VIS + IR
orb. 8727 79 340
(11.52.52 GMT)
(N-Africa)

All interpretations were performed on digital data except for both recordings in December (5th and 6th) 1979, from which quick-look imagery was also used.

A. Optical Comparison of Thermal Map-Like Printouts with Soil Association and Forest Maps

Purpose of the Work

Some of the preliminary results on thermal data from a HCMM night-pass (2.13 GMT) on 30 May 1978, are here presented.

The purpose of this work was primarily:

- a) to visualize the digital thermal scanner data for Belgium (10.5 - 12.5 μm , resolution cell: approx. 500 x 500 m)
- b) to look for the optical location of thermal

pixels by comparison with different maps and also with Landsat imagery

- c) to delineate large (regional scale) and smaller areas as distinguishable from temperature patterns on map-like computer printouts and which correspond to soil and/or soil surface features.

Although this HCMM thermal recording only represents a momentary aspect of a rapidly evolving situation, it may be considered as rather unique being a cloud-free night view of the entire Belgian territory.

Application of Computer Programs

The computer analysis was performed with the ORSER program software (Pennsylvania State University, USA), some of the programs being rearranged or adapted by the Joint Research Centre, Ispra and the Centrum voor Landbouwkundige en Ecologische Interpretatie van Teledetectiegegevens at Leuven (CLEIT, KUL). The following programs were applied after transcription of the original HCMM digital data into the ORSER-format:

- NMAPW-program

This program is essentially a brightness classification program. It automatically calculates class limits and visualizes the pixel values in each class on each scanline as a maplike printout. This operation proved essential for the positioning of pixels on the maps as each pixel can now be identified by its scanline and element number.

- EXIO-program (Extended Ratio Mapping)

This program calculates arithmetic combinations of different channels and also assigns map symbols to categories according to specified class limits. These limits can be obtained by the STATS-program. The EXIO-

program produces a maplike printout of pixels on successive scanlines.

- STATS-program

For homogeneous test areas delimited on the NMAPW-print, the program calculates the vector of the mean, the vector of the standard deviation and the variance-covariance matrix, using the information contained in one or several spectral bands. The program also produces numerical (pixel) data and frequency histograms for specified channels.

Optical Analysis of Digital Printouts

Computer printouts (NMAPW, EXIO) were optically superposed and compared with different types of maps (road, topographic, forest, soil maps...) and corresponding limits were drawn depending on the application. Superpositions were all achieved with the aid of a Zoom Transfer Scope (ZTS) which allows for scale adjustments and anamorphic corrections.

The ZTS also allows for the projection of Landsat multispectral colour composites (MSS bands 5 and 7) on HCMM thermal printouts. In this manner the Landsat image is more or less considered as the ground truth information needed for the specific interpretation.

The following major land-use classes recognized on Landsat multispectral colour composites were used for pixel identification and positioning on the HCMM printouts:

<u>Class</u>	<u>Colour on Landsat Composite</u>
water	dark purple
dunes	whitish
urban land	blue
forests	purplish
pastures and agricultural crops	red

It should be noticed that the computer printouts

and the smaller interpretation maps derived therefrom, which appear in this paper, though all slightly stretched perpendicularly to the HCMM satellite scan direction, all sufficiently coincide when superposed to allow easy comparison.

Results

Digital HCMM-data were visualized by the NMAPW program for the entire Belgian territory (Fig.III.2.30). On a line-printer the whole area (approx. 30,000 km²) could be represented as a printout at approx. scale of 1:200,000. After its photographic reduction (about 50%) the national boundary could be drawn stepwise using a road map, each step resulting from an adjustment by means of the B & L Zoom Transfer Scope. Coast-lines, large river courses (Schelde), cities, small urban areas, small lakes (Blankaart, Gileppe, Bütgenbach) and forests were taken as reference points for optical adjustment. Boundaries within the Belgian territory were delineated from the optical distinctions of temperature patterns and from their location and/or orientation with respect to other surrounding areas. In Fig.III.2.30 warm signatures (light tones) and cool signatures (dark tones) are not only related to topographic relief (Condroz, Famenne, Ardennes), but also to land-use (Kempen, Polders, Leemstreek) or other surface features (cities as urban heat islands, open water, forests). Apparently, the delineated greater units do correspond to the Belgian geographic regions: Kustvlakte, Kempen, Zandleemstreek, Leemstreek, Condroz, Famenne, Ardennes and Lorraine. A more detailed study of the NMAPW-print also revealed good correlations with parts of the soil association map of Belgium. Fig.III.2.31 shows its corresponding limits

and also indicates the greater soil associations (see also Fig.III.2.30).

The NMAPW-printout was also optically compared with forest maps on the north and south Ardennes. In Figs.III.2.32 and 33 only the larger forest boundaries have been delineated as they appeared from surface temperature contrasts with surrounding areas. Homogeneous thermal areas were circumscribed by hand under the Zoom Transfer Scope and labelled through comparison with the forest maps. Forests could generally be distinguished from their relatively high radiant temperatures. However, the difference between coniferous and deciduous forest types or differences between species could not be inferred from the NMAPW-printout. It was attempted to slice out and represent forested areas in the northern part of the Ardennes by means of the EXIO-program. The class (temperature)limits for running this program were established from the statistical analysis of forest training areas by the STATS-program. The EXIO-printout is represented in Fig.III.2.34. In order to compare and correlate the HCMM-data with recent ground information, the EXIO-maplike printout was optically superposed on Landsat-imagery recorded on 17/5/76 and 10/4/76. In Fig.III.2.34 forest limits as interpreted on these Landsat images, may be compared with those from the EXIO temperature slicing.

Landsat imagery recorded on 23 March 1973 and on 22 May 1977 was also compared with an EXIO-temperature range printout of the Belgian polders (Fig.III.2.35). Class limits were obtained with the STATS-program which calculates the average pixel values and their standard deviation, within the training areas. On these printouts, coast-lines, dunes, urban areas and small forests are well marked out and correspond fairly well with limits dis-

ORIGINAL PAGE IS
OF POOR QUALITY



Fig.III.2.30. The NMAPW-visualization printout of HCMM-data over Belgium as obtained from collage.

ORIGINAL PAGE IS
OF POOR QUALITY

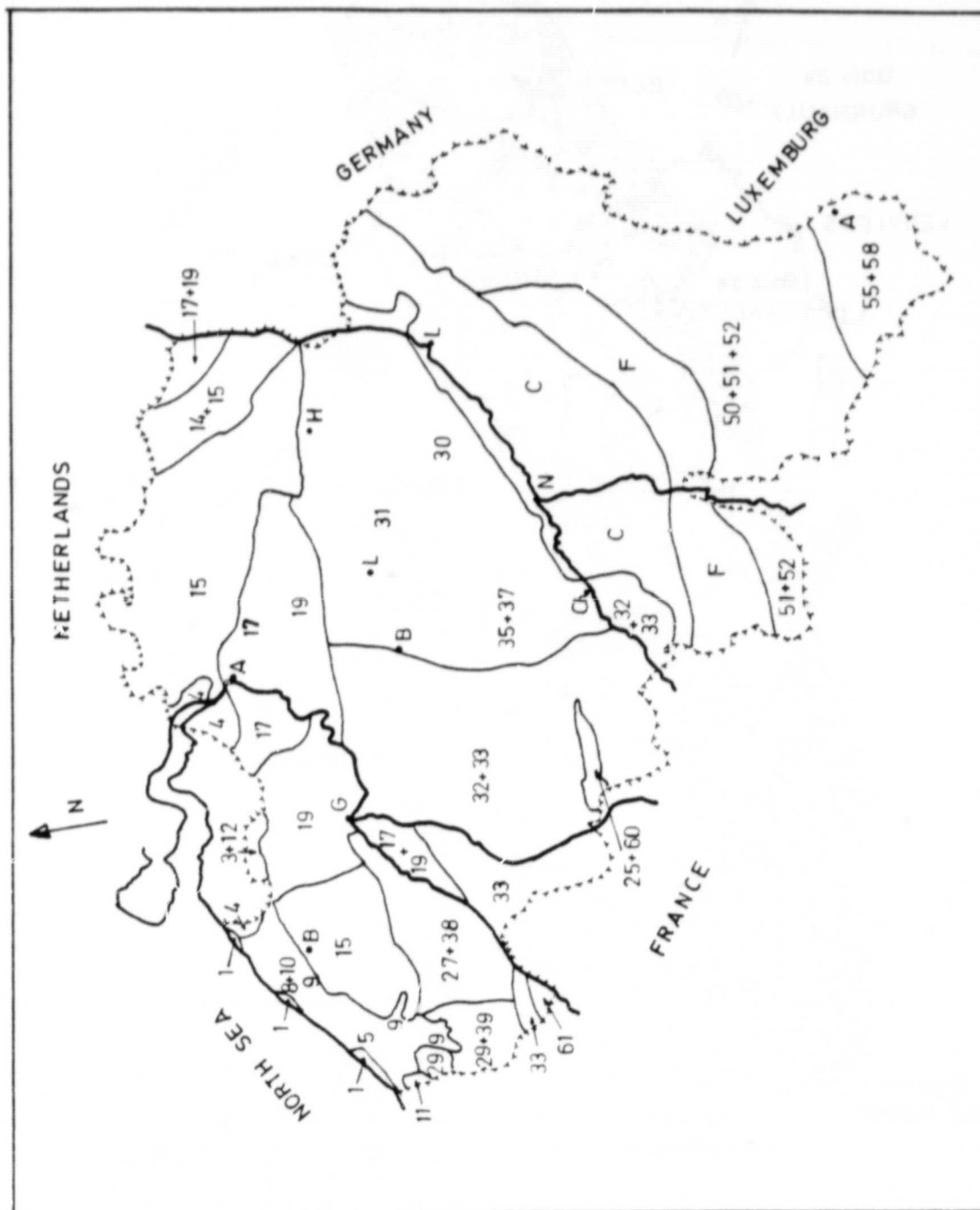


Fig. III.2.31. Optical delineation of greater units on the NMAPW printout and its comparison with the soils association map.

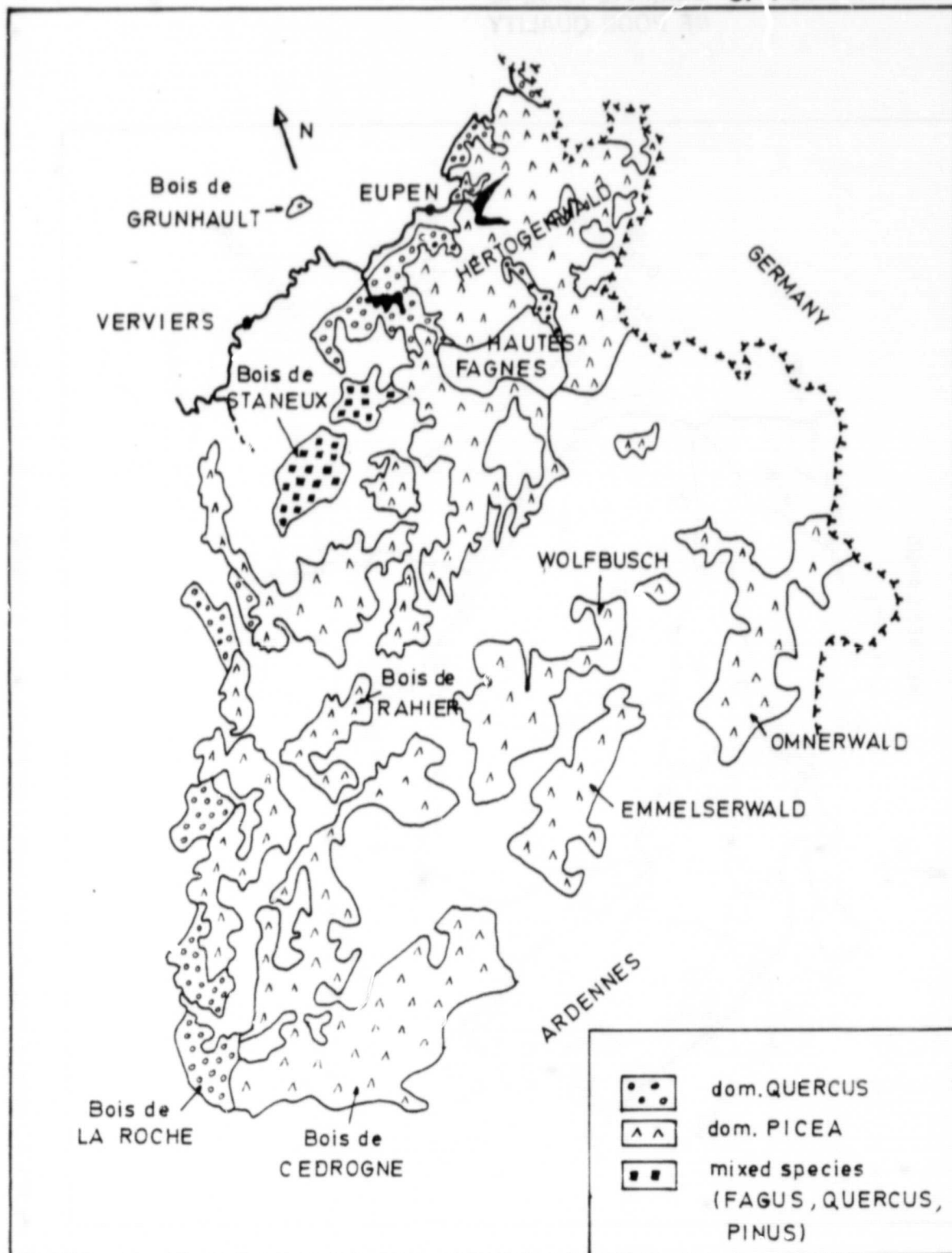


Fig. III.2.32. Forest limits delineated by optical comparison of a NMAPW-printout with a forest map of the North Ardennes (Belgium).

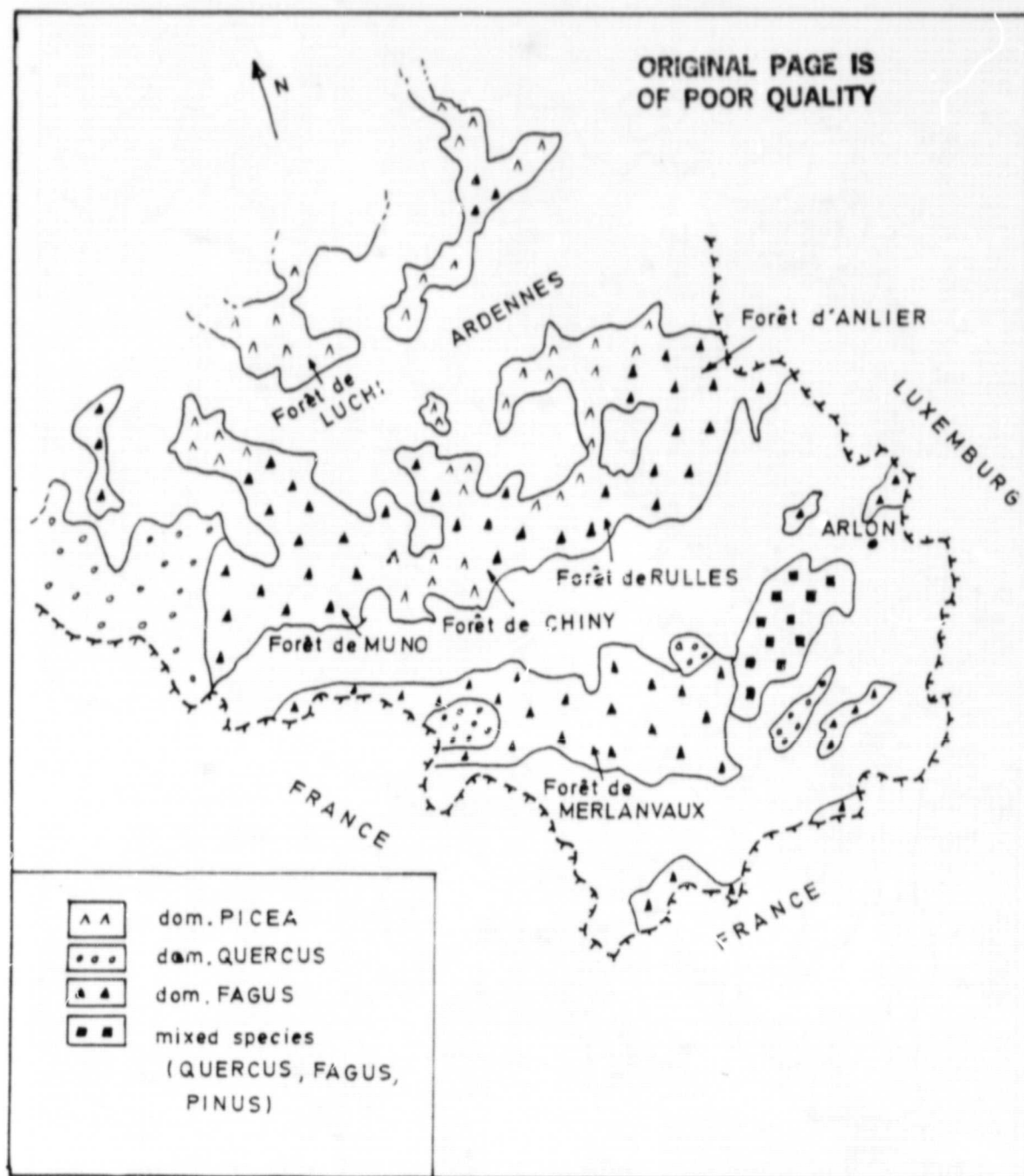
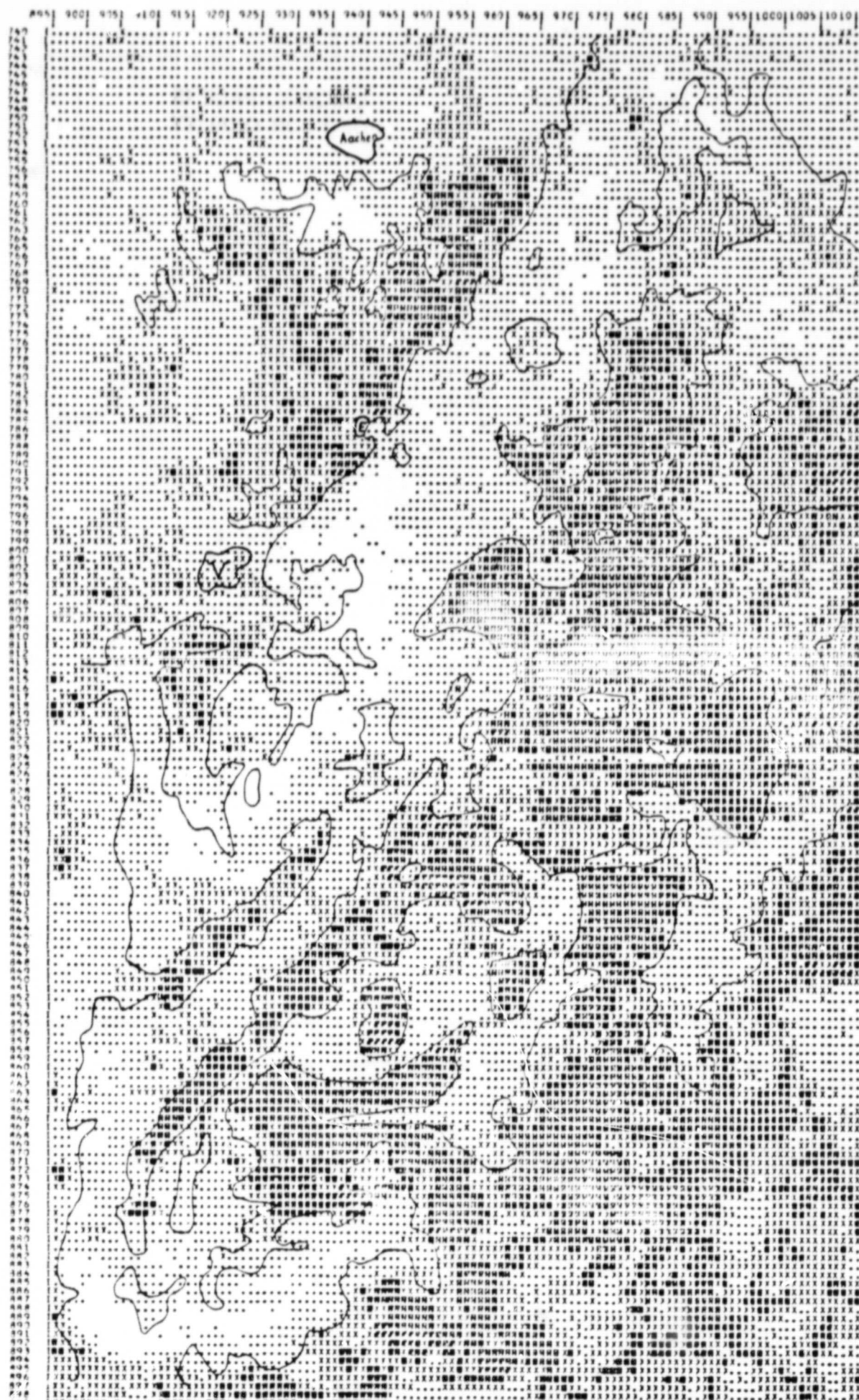


Fig. III.2.33. Forest limits delineated by optical comparison of a NMAPW-printout with a forest map of the South Ardennes (Belgium)



ORIGINAL PAGE IS
OF POOR QUALITY

Fig. III.2.34. Comparison of forest limits obtained by EX 10 temperature slicing with limits interpreted on Landsat imagery (N-Ardennes, Belgium) (legend see list of figures.).

7725
7726
7727
7728
7729
7730
7731
7732
7733
7734
7735
7736
7737
7738
7739
7740
7741
7742
7743
7744
7745
7746
7747
7748
7749
7750
7751
7752
7753
7754
7755
7756
7757
7758
7759
7760
7761
7762
7763
7764
7765
7766
7767
7768
7769
7770
7771
7772
7773
7774
7775
7776
7777
7778
7779
7780
7781
7782
7783
7784
7785
7786
7787
7788
7789
7790
7791
7792
7793
7794
7795
7796
7797
7798
7799
7800
7801
7802
7803
7804
7805
7806
7807
7808
7809
7810
7811
7812
7813
7814
7815
7816
7817
7818
7819
7820
7821
7822
7823
7824
7825
7826
7827
7828
7829
7830
7831
7832
7833
7834
7835
7836
7837
7838
7839
7840
7841
7842
7843
7844
7845
7846
7847
7848
7849
7850
7851
7852
7853
7854
7855
7856
7857
7858
7859
7860
7861
7862
7863
7864
7865
7866
7867
7868
7869
7870
7871
7872
7873
7874
7875
7876
7877
7878
7879
7880
7881
7882
7883
7884
7885
7886
7887
7888
7889
7890
7891
7892
7893
7894
7895
7896
7897
7898
7899
7900

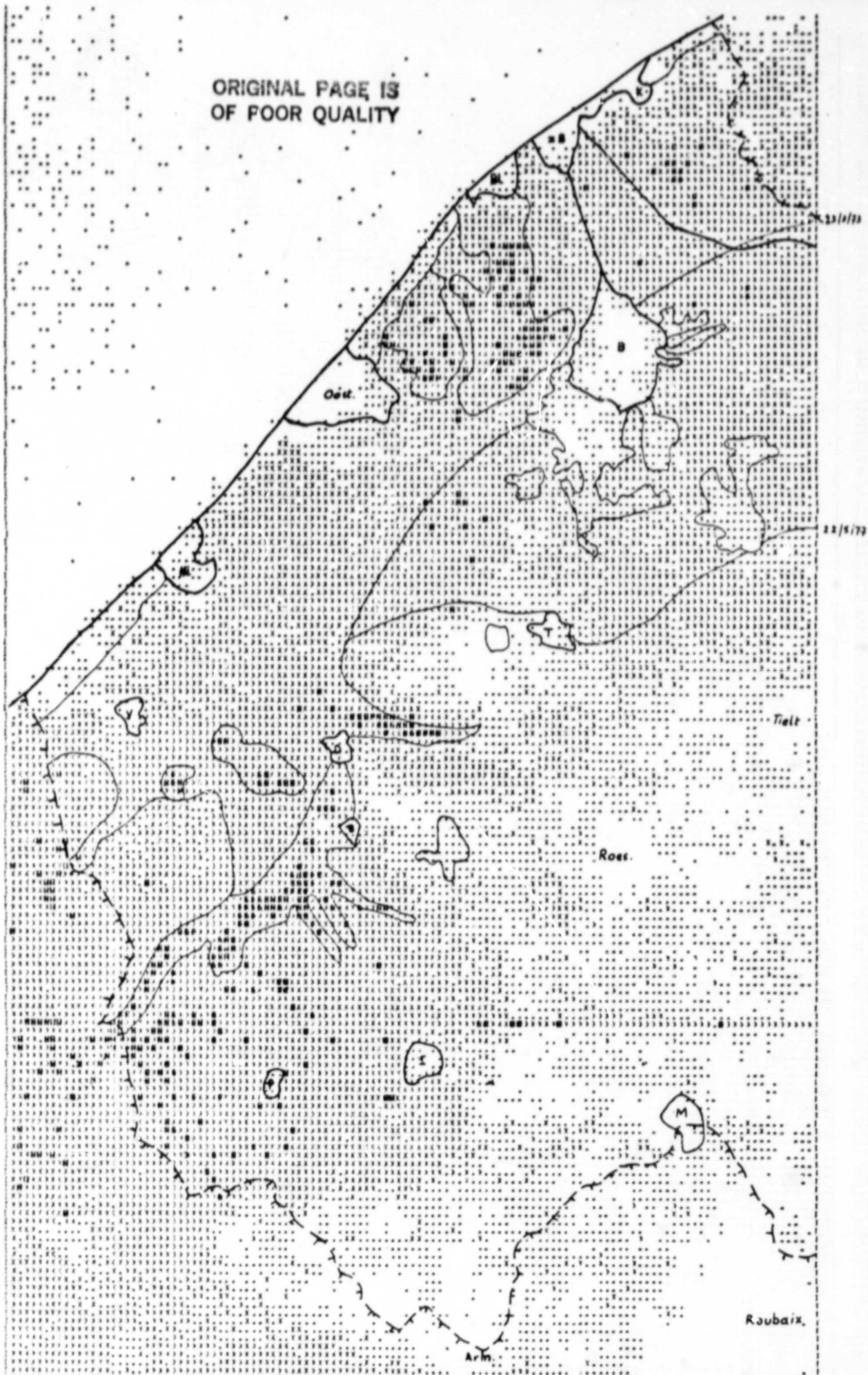


Fig. III.2.35. EXIO-printout of four surface temperature ranges for the Belgian polders compared with Landsat imagery (legend see list of figures).

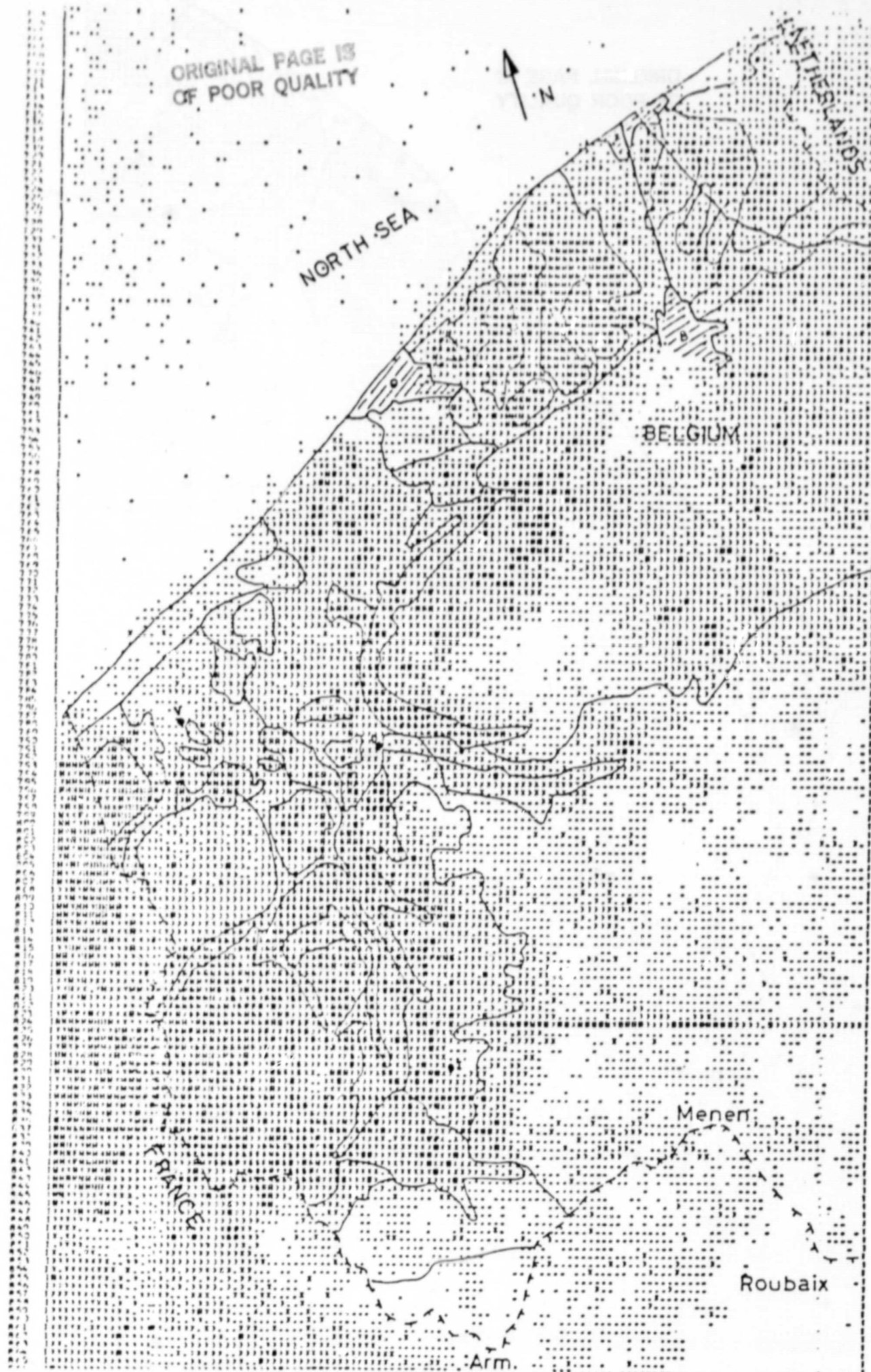


Fig. III.2.36. Comparison of an HCOMM EXIO-printout with the soils association map of the Belgian polders (legend see list of figures)

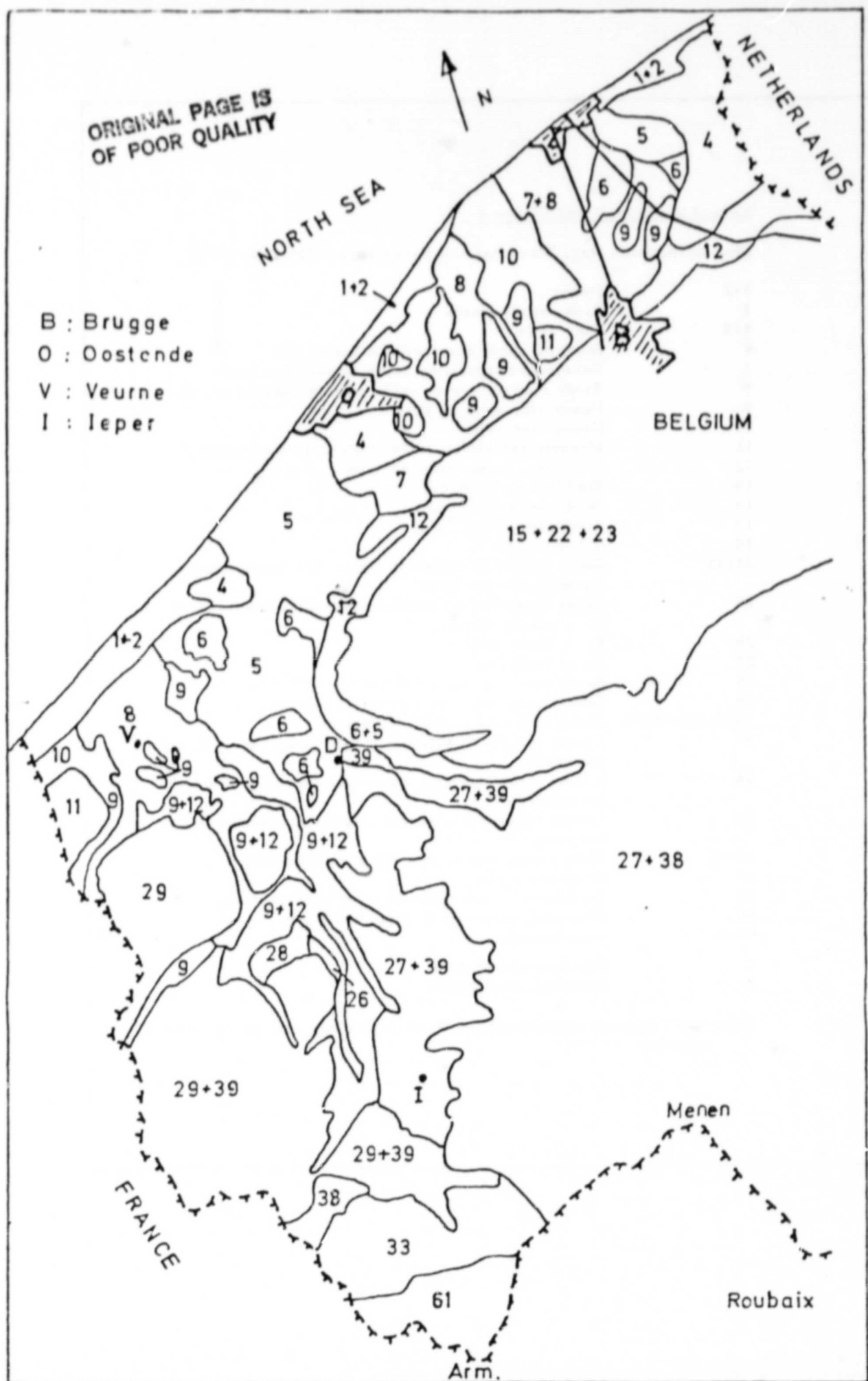


Fig. III.2.37. Soil associations of the Belgian polders. (schematized from Maréchal and Tavernier 1970).

ORIGINAL PAGE IS
OF POOR QUALITY

Legend of Figure 2 and Figure 8

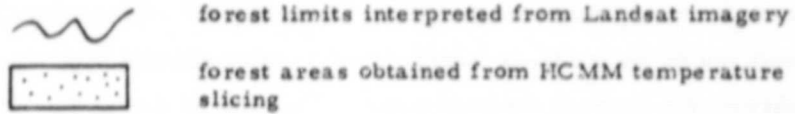
(Soil Association Map, Maréchal and Tavernier, 1:500,000, 1970)

1+2	Dunes
3	Sand, sandy loams
4+5	Clay soils
6	Sandy to sandy clay soils on heavy clay
7	Decalcified topsoil on heavy impervious clay
8	Sandy clay to clay on sand (ancient channel soils)
9	Heavy clay soils on peat
10	Heavy clay soils
11	Moeren (reclaimed soil complex, 17th century)
12	Clay soils on pleistocene sand
14	Sand/loamy sand (dry)
15	Sand/loamy sand (wet)
17	Sand/sandy loam (wet)
19	Complex 15+17
22+23	Sandy topsoil of different origin than deeper layers (on sand or clay/sand)
25	Sandy topsoil of different origin than deeper layers (on chalk or mar.)
26	Sandy loam (dry)
27	Sandy loam (wet)
28	Sandy loam with clay illuvial B-horizon (dry)
29	Sandy loam with clay illuvial B-horizon (wet)
30+31+32+33+35	Loam with clay illuvial B-horizon
37	Loamy topsoil of different origin than deeper layers (on sand)
38	Loamy topsoil of different origin than deeper layers (on sand/clay)
39	Loamy topsoil of different origin than deeper layers (on clay)
50+51	Stony loam, mixed with shale or sandstone
52	Stony loam (dry)
55	Sand/sandy loam with clay illuvial B-horizon
58	Clay soils with clay illuvial B-horizon
60+61	Alluvial soils
C	Condroz-association
F	Famenne-association

Note: The English translation of the Dutch terms has only an explicative meaning





Legend of Figure 5

Comparison of forest limits obtained by EXIO-temperature slicing
with limits interpreted on Landsat imagery (N-Ardenne, Belgium)



Legend of Figure 6

EXIO-printout of four surface temperature ranges for the Belgian
polders compared with Landsat imagery

<u>Symbol</u>	<u>HCMM-count</u>
	0 - 51
	52 - 57
	58 - 60
	61 - 255

Legend of Figure 7

Comparison of an HCMM EXIO-printout with the soil association
map of the Belgian polders

<u>Symbol</u>	<u>HCMM-count</u>
	0 - 53
	54 - 57
	58 - 60
	61 - 255

cernable on a Landsat multispectral colour composite of the area (MSS bands 5 and 7). Landsat imagery used in conjunction with HCMM data proved particularly useful for pixel location purposes. Furthermore, spectral information from other satellites such as Landsat may contain recent information on land surface features or on land-use which may also be discernable through thermal properties. On the Landsat scene of 23 March 1973 the limits of the polder area may be easily distinguished. When this image is optically superposed on the HCMM, EXIO-printout of Fig.III.2.35, it appears that polder pixels (counts ≤ 51) in the polder area more or less coincide with the wetter soils and with associations having a relatively high clay content (cfr. soil association map). These soils are permanently under grass cover. On Landsat composites recorded in early spring such areas stand out as bright red. They can be exactly located, delimited and optically transferred to a digital printout. The temperature range limit visualized by EXIO in Fig.III.2.35 as 22/5/77, was also clearly visible on the Landsat recording of 22 May 1977. North of this limit, lands are largely occupied by pastures whereas lands in the southern part are being used mainly for cultivation of industrial crops. In this southern area the relatively high proportion of soil surfaces not yet covered by vegetation at the time of the thermal recording, accounts for higher radiant temperatures. From the comparison with the soil association map it was also found that the limit coincides with the distinction between sandy soils (north of the limit) and sandy loam soils, south of the limit (Fig.III.2.37).

Fig.III.2.36 shows a further attempt to slice out those polder areas which all have a lower radiant temperature range (counts ≤ 53). The

location of such areas was then compared with the soil association map (somewhat schematized after optical superposition on the EXIO-computer printout). From this, it could be concluded that the spatial limits of some temperature classes do correspond fairly well with soil unit boundaries. Dune areas especially showed high radiant temperatures whereas the polder soils with high clay content (poelgronden) and also some of the more humid soil associations formed part of classes with lower temperature range (Fig.III.2.37). Humid soil is generally cooler than dry soil, evaporation of absorbed water also lowers the temperature. High moisture content of a soil increases its heat capacity and a lower temperature will be sensed.

References

- J. R. BOHSE, M. BEWTRA and W. L. BARNES; "Heat Capacity Mapping Radiometer (HCRM) Data Processing Algorithm, Calibration and Flight Performance Evaluation", NASA Technical Memorandum 80258 (1979).
- A. CEUSTERS, R. GOMBEER, H. GULINCK, N. SOUGNEZ and J. D'HOORE; "Applications of Computer-Aided Analysis of Landsat Data to Land-Use Studies in Belgium. The Ciergnon Test Site (Famenne)". Proc. Int. Symp. on Remote Sensing for Observation and Inventory of Earth Resources and the Endangered Environment, Freiburg, BRD (1978).
- R. GOMBEER; "Analysis of Thermal Infrared Digital Data Recorded over Belgium by a Heat Capacity Mapping Mission (HCMM) night-pass". TELLUS NEWSLETTER No. 10, 10-28 (1979).
- J. SUBBARAYUDU; "Heat Capacity Mapping Mission. Validation Study Final Report No. R-SAG-3/79-01". Systems and Applied Sciences Corporation, Riverdale, MD, USA (1979).
- B. TURNER, D. APPLGATE and B. MEREMBECK; "Satellite and Aircraft Multispectral Scanner Digital Data User Manual". ORSER, Pennsylvania State University, USA, (1978).

**ORIGINAL PAGE IS
OF POOR QUALITY**

B. Ground Temperature of General Land-Use Classes as Registered by the HCMM Satellite

Introduction

Earth surface temperatures may be calculated and mapped from the infrared radiances (wave-length band: 10.5 - 12.5 μm) measured by the HCMM-radiometer. The data obtained by the HCRM are digitized to 8 bits units of energy (255 levels), equivalent to a temperature range of 260° to 340°K. In this range, the byte (pixel) counts can be converted to temperature using a formula derived from the Planck function and from calibration procedures, representing radiometer performance (Subbarayudu, 1979). However, in the 11 μm atmospheric window, the slight absorption by water vapour, atmospheric gasses and aerosols causes the temperatures registered by the satellite to be lower than the true surface temperature.

Some preliminary results (HCMM night-pass, 2.13 GMT on 30 May, 1978) giving calculated ground temperatures for various terrain classes are presented. Temperatures were all derived from the digital count of infrared measurements and no atmospheric correction was applied. Notwithstanding their momentary aspect, surface temperatures may be associated with certain land surface features and also with certain subsoil characteristics influencing heat transfer (soil moisture content, porosity, mineral composition).

Application of Computer Programs

Computations were performed by means of the ORSER software package (Pennsylvania State University) (Turner et al., 1978) after transcription of the HCMM-tape format into ORSER-

format NMAPW and STATS programmes were mostly used.

Procedure and Results

Test areas, whose general land-use was known, were first located on an NMAPW visualization printout. Small training areas were then optically identified through superposition of the NMAPW-printout on topographical, road, soil and forest maps.

This operation was greatly facilitated by the use of a B & L Zoom Transfer Scope which allows for anamorphic correction so that differences in scale and deformations in printout can be amended. Certain recognizable landmarks were taken as references: major agglomerations, forests, lakes, coast-lines. Line and element numbers (NMAPW) delimiting the selected polygon areas were then entered into the STATS-program.

From the pixel count average of each training area, surface temperatures were calculated with the formula of Bohse et al., 1979, established according to the performance evaluation of the Heat Capacity Mapping Radiometer (HCRM):

$$T(I) = K_2 / \ln \left[K_1 / (I - K_3) + 1 \right]$$

where I is the calibrated count and K_1, K_2, K_3 are constant.

In this study it was intended to evaluate the temperature range for some of the larger land-use classes, recognizable on NMAPW-printouts and which could be related to some general surface or subsoil characteristics. In Table III.2,3 radiant temperatures may be compared for selected classes.

Agglomerations (urban heat islands) are generally distinguished by their relatively high radiant temperature range. Apparently, the

largest cities also have the highest temperature range. The lower temperature for Eupen might partly be explained by its elevated topographic situation. Effects of topographic relief are also illustrated by a temperature difference for the grassland training areas, one positioned in the Herve depression and the other one on the Herve Plateau. The lowest temperature was observed for the Hoge Venen (Hautes Fagnes) the highest plateau in the Belgian territory.

Stagnant waters (Blankaart, Gileppe) are observed to be relatively cooler than coastal (Oostende) or navigable waters (Westerschelde). The temperature decrease of seawater surfaces as measured offshore from Oostende, at approximately 25 and 50 km from the coastline, should also be noticed.

Forests generally display a higher temperature range than the surrounding area and could thus be located on an NMAPW-printout. However, differences between species cannot be inferred although it appears from Tab.III-2.3 that deciduous forests are somewhat higher in radiant temperature as compared to coniferous forests.

Temperature differences in the polder areas could, in general, be attributed to soil humidity (Gombeer, 1979). The lowest temperatures were observed especially for units described as heavy clay soils on peat (poelgronden) and other soil associations with inadequate drainage or high clay content (sandy to sandy/clay soils on heavy clay: overdekte poelgronden). The heating and cooling characteristics of a soil largely depend on its thermal conductivity (i.e. on its heat capacity which will depend on moisture content). Moist soil also has a cooler signature than dry soil because of the cooling effect as absorbed water

is evaporated.

Table III 2.3. Comparison of Radiant Surface Temperatures ($^{\circ}\text{C}$) for Training Areas of Various Land-Use Classes (HCMM night-pass on 30 May 1978 at 2.13 GMT)

Class 1 - Agglomerations

Antwerp	13.64 $^{\circ}\text{C}$	(121 pixels)
Brussels	13.50	(")
Gent	12.36	(")
Luik	12.36	(")
Mechelen	12.55	(36 pixels)
Hasselt	12.44	(9 ")
Leuven	12.07	(36 ")
Doornik	12.07	(36 ")
Aalst	11.92	(36 ")
Tienen	11.81	(9 ")
Bruges	11.63	(36 ")
Ieper	11.18	(9 ")
Vervier	10.19	(36 ")
Eupen	8.69	(9 ")

Class 2 - Open Water

Blankaart (Lake)	11.15 $^{\circ}\text{C}$
Gileppe (Lake)	11.78
Westerschelde	
(Hontenisse)	12.73
Coastal water	
(Oostende)	12.09
Offshore water (25 km)	11.07
Offshore water (50 km)	9.90

Class 3 - Grassland

Herve (depression)	8.50 $^{\circ}\text{C}$
Herve (plateau)	10.38

Class 4 - Forests

Forêt de Grunhault	10.62 $^{\circ}\text{C}$	(mixed species, 2 pixels)
Heverlee-bos	11.00	(mixed species)
Meerdaal-bos	10.69	(")
Hertogenwald	10.56	(Picea)
Cedrogne (Bois de)	10.85	(")
Omner Wald	9.93	(")
Zoniën-woud	11.79	(Fagus)
Forêt de Freyr	11.07	(")
Forêt de Merlanvaux	10.86	(")
Forêt de la Roche	11.98	(Quercus)

Class 5 - Polderland

Moeren	8.82 $^{\circ}\text{C}$
Dekkleigronden	9.08
Poelgronden-1	7.44
Poelgronden-2	7.13
Polders (Nederland)-1	11.02
Polders (Nederland)-2	11.36

Class 6 - Agricultural Land (Leemstreek)

Waremmes (East)	9.74 $^{\circ}\text{C}$	(45 pixels, 11 km ²)
Landen (East)	9.89	(60 pixels, 15 km ²)

Class 7 - Miscellaneous

Hoge Venen (Hautes Fagnes) 6.10°C
Dunes (Veurne) 10.92

Remarks

Although certain temperature ranges may be used for the purpose of comparison among different land-use classes, the following remarks should be taken into account:

- Training areas, in general, must meet the following requirements: small but sufficiently large, easy to locate and their radiance must be relatively homogeneous over the entire surface. Due to the low pixel resolution (500 x 500 m) of the Heat Capacity Mapping Mission as well as to the high degree of parcelling over the areas studied, some spectral inhomogeneity may be expected for the selected training areas.
- Atmospheric absorption causes the radiant temperatures observed by the satellite to be lower than the true surface temperatures. Satellite recorded temperatures can only be (and then only approximately), correct using meteorological observations at the various air pressure levels by balloon radiosonde ascent. Moreover, the effects of atmospheric changes are usually so great that observations should be made over each test site at the time of satellite overflight. Obviously, atmospheric correction data are generally acquired for few, relatively small surfaces mostly at random times.
- Thermal infrared radiances and radiant temperatures derived from them, largely depend on the insolation conditions preceding the satellite overpass. These will not only vary during the daily cycle but also with season, meteorological conditions, etc.

- The study of general thermal characteristics of land surfaces and the more so if it is to be performed at a regional or even larger scale, can best be approached by intercomparison of relative temperature ranges. Results from such comparisons are likely to be more related to surface and/or sub-surface characteristics than to the momentary absolute temperature (radiance) level of a particular feature of land-use class.

C. Thermal Inertia Applications

Introduction

Studies on thermal behaviour of soils can provide useful information on subsoil characteristics and on soil moisture. In such studies, the use of the thermal inertia product is particularly interesting as it is more a volume property rather than a surface property which can be sensed by remote sensing devices. It permits discrimination between different materials with similar surfaces which can only be difficultly separated by their reflectance properties. The thermal inertia effect is related to the diurnal surface temperature variation, having maximum and minimum values, which can be remotely measured by the HCMR through its appropriate orbit configuration (day/night overpasses). This paper presents the results on thermal inertia calculated for various land-use classes distributed over the Belgian territory.

Many of the local environmental changes are due to changes in land-use. The removal of vegetation may locally influence micro-climatic conditions at the surface of the land (radiation budget, wind velocity, etc.).

From a change of vegetation to an artificial cover, many by-products of industrialization

TABLE III.2.4. Apparent Thermal Inertia (ATI) of Land-use Classes calculated from HCMM day/night Digital Data recorded over Belgium on September 16, 1979.

Land Use Class	$1 - \alpha$ (α =apparent albedo)	T_{day} °K	T_{night} °K	$\Delta T(^{\circ}K)$ ($T_D - T_N$)	ATI Apparent thermal inertia
Urban land					
Gent	0.9426	289.0241	272.1262	16.8979	58.1360
Brugge	0.9357	287.2390	270.3583	16.8807	57.7693
Oostende	0.9269	286.6472	274.2750	12.3722	78.0794
Antwerpen	0.9475	289.1540	271.7142	17.4398	56.6224
Brussel	0.9487	288.6748	272.6836	15.9912	61.8295
Verviers	0.9263	286.7274	269.3374	17.3900	55.5140
Forest					
Fagus: Area 1	0.9166	280.5825	270.5167	10.0658	94.9035
Area 2	0.9174	280.9796	270.8326	10.1470	94.2263
Quercus: Neuville	0.9225	280.3871	269.5383	10.8488	88.6208
Esneux	0.9190	280.4425	269.3374	11.1051	86.2470
Picea: Hertogenwald	0.9298	279.4867	266.8554	12.6313	76.7171
Ommerwald	0.9350	278.9683	265.5110	13.4573	72.4110
Pinus: Gemeentebos	0.9272	282.1007	267.8191	14.2816	67.6624
Pijnven	0.9333	281.8388	267.2798	14.5590	66.8098
Kapellenbos	0.9263	282.1697	267.4348	14.7349	65.5172
Mixed species:					
Meerdaalbos	0.9167	280.8474	268.9754	11.8720	80.4737
Heverleebos	0.9265	281.8643	268.9590	12.9053	74.3372
Open water					
O-Schelde: Bergen op Zoom	0.9798	280.4720	278.1765	2.2955	444.8475
W-Schelde: Hontenisse	0.9724	281.7550	278.9010	2.8540	355.0929
Coastal water: Oostende	0.9674	281.2326	279.9212	1.3114	768.8152
Grassland					
Herve 1	0.8705	283.8168	267.7607	16.0561	56.5040
Herve 2	0.8733	283.7273	267.5059	16.2214	56.1081
Bare soil					
Dunes: Nieuwpoort	0.9186	287.7000	270.1875	17.5125	54.6675
Oostduinkerke	0.9049	287.8037	270.3624	17.4413	54.0720
De Panne	0.9058	287.3605	270.3786	16.9819	55.5900
Sandy surface: Leopoldsburg	0.9039	287.4403	267.8899	19.5504	48.1854

Note: Temperatures are given without atmospheric correction.

ORIGINAL PAGE IS
OF POOR QUALITY

may also alter the local composition of the atmosphere, soil and water bodies (pollutants). The concrete and brick surface of cities, for example, affects temperature conditions and urban "heat islands" are observed to be much warmer than rural areas. Some results of the Brussels "heat island" are presented in the second part of this paper, whereas the third part reports on some thermal anomalies observed in the vicinity of a nuclear power plant.

Method and Procedure

The HCMM-data were visualized and further analysed by applying the computer programs NMAPW, EXIO and STATS and following pixel (test area) positioning procedures (optical superpositions with ZTS) described in detail in Sections A and B. Thermal inertia was calculated from day/night recordings over Belgium on 16 Sept., 1979, using the algorithm proposed by NASA (1979):

$$ATI = \frac{NC(1-a)}{\Delta T} \quad (\text{Apparent Thermal Inertia})$$

In the ATI algorithm it is assumed that the factor (1-a) corrects the variable energy reflection of different surface materials (given solar incidence). The factor C attempts to compensate for seasonal variation of solar input (HCMM User's Guide, 1979).

Results

Thermal Inertia

Table III.2.4 summarizes thermal inertia calculations for different land-use classes of Belgium. It should be noticed that all day and night temperature values are given without atmospheric corrections. Referring to the calibration procedure of Part 4, real surface temperatures (day) are expected to be about 9.28°K higher.

The following general conclusions are drawn from Table III.2.4 hereinafter reported:

- for all land-use categories studied, T_{day} temperatures are higher than T_{night} temperatures;
- except for some bare soil surfaces, urban areas always have the highest temperature during the day. The lowest day temperatures are noticed for certain forest types (Picea);
- during the night, except for water bodies, urban agglomerations are also highest in temperature;
- T_{night} values are always highest for water surfaces;
- temperature differences, $T_{\text{day}} - T_{\text{night}}$, are lowest for the open water category;
- albedo values are highest for grassland and for bare soil (dunes) and lowest for water surfaces.

Average values for ATI are indicated in Table III.2.5. From these preliminary values it is anticipated that major land-use classes can be separated by the ATI-products and that even forest species (Fagus, Quercus, Picea, Pinus) may be discriminated.

Table III.2.5. Apparent Thermal Inertia (Average Value) of Major Land-Use Classes (Belgium) Heat Capacity Mapping Mission: Sept. 16, 1979

Land-Use Class	ATI
Open Water:	522.9185
Forest: Fagus	94.5649
Quercus	87.4339
Picea	74.5640
Pinus	66.6631
Mixed Species	77.4054
Urban Land:	61.3251
Grassland:	56.3060
Dunes and Sands:	53.1287

D. Summary of Significant Results

The following significant results have been obtained:

- 1) Broad temperature patterns, optically distinguished on NMAPW-visualization computer printouts, correspond fairly well to that of the Belgian geographic regions. Such correspondence was observed on night- and on day thermal recordings.
- 2) The comparison of limits on the Belgian pol-der soils association map with EXIO-temperature printouts, reveals good correlations for the more humid soil associations (high clay content, inadequate drainage).

- 3) During the night, cities and even small urban areas (1 or 2 pixels) could be distinguished due to their relative high radiant temperature. These areas could also be marked out individually by EXIO-temperature slicing.
However, differences between forest species cannot be inferred only from their temperature range, although it appears that during the night deciduous forests are somewhat higher in radiant temperature as compared to coniferous forest. During the day, forests were observed to be relatively cooler than surrounding areas. By means of the NMAPW-classification and visualization program, it was possible to delineate forests and to calculate their areal extent through pixel counting (cf. following examples):
 - a. Meerdaal forest (13.19 km^2):
51 HCMM pixels = 12.76 km^2
 - b. Heverlee forest (5.5 km^2):
24 HCMM pixels = 6.0 km^2 .
- 4) Although temperatures remotely sensed over soil surfaces may be subject to a rapid change, some conclusions could be drawn

from them as to surface or subsoil characteristics: relation with surface type or land-use category, distinction between certain soil units.

- 5) The study of general thermal characteristics of land surfaces, and the more so if it is to be performed at a regional or even larger scale, can best be approached by intercomparison of relative temperature ranges. Results from such comparisons are likely to be more related to surface and/or subsurface characteristics than the momentary absolute temperature (radiance) level of a particular feature or land-use class.
- 6) The Apparent Thermal Inertia (ATI) pertaining to major land-use classes of Belgium were calculated. From preliminary average values it is anticipated that major land-use classes (i. e. open water, forests, urban land, grassland, bare soil) can be separated by the ATI-product and that even forest species (Fagus, Quercus, Picea, Pinus) may be discriminated. It should be remarked that these ATI-values are obtained through optical registration procedures using digital printouts of day and night radiance data.
- 7) In performing HCMM-data analysis, a combination of digital together with optical interpretation methods proved to be most appropriate. It consisted basically in the optical superposition (Zoom Transfer Scope) of maplike computer classifications with thematic maps and imagery (e. g. Landsat). Such procedure was necessary as a continuous comparison had to be made with ground information or former classifications. Landsat imagery was most useful for pixel locating purposes on the HCMM computer printouts (classifications). In this manner the Landsat image was also con-

sidered as containing part of the recent ground information needed for a specific thermal interpretation.

- 8) It is clear that the accuracy of proposed methods will depend on the degree of spectral homogeneity of each area or feature studied. Due to the low pixel resolution (500 x 500 m) of the Heat Capacity Mapping Mission, especially with respect to the high degree of parcelling encountered over the Belgian territory, some spectral inhomogeneity is to be expected. Obviously this relatively "coarse" spatial resolution might interfere with all interpretation results obtained and a higher resolution would have been more appropriate for thermal studies on land surfaces in Belgium.

References

- J. ANNAERT, C. CHRISTIANS and B. DE SMET; Landbouwkaart van België, 1959, 1 : 500,000; Atlas van België, blad Nr. 35 (1966).
- Bestuur van Waters en Boszen (1957); Wouden. Types van Bestanden 1957, 1 : 500,000; Atlas van België, Blad 29 A.
- H. GULINCK and R. GOMBEER; "Bodemkundige Interpretatie van Multispektrale Landsatopnamen over enkele Geografische Streken van België". *Pedologie*, 27, 3, 291-312 (1978).
- Instituut tot Aanmoediging van het Wetenschappelijk Onderzoek in Nijverheid en Landbouw; Agronomische Kaart van de Zeepolders, 1 : 100,000; Centrum voor Grondonderzoek, IWONL.
- MARÉCHAL and TAVERNIER (1970); Bodemassociatiekaart 1 : 500,000; Atlas van België, Blad 11 B.
- B. TURNER, D. APPLEGATE and B. MEREMBECK (1978); "Satellite and Aircraft Multispectral Scanner Digital Data User Manual, ORSER", Pennsylvania State University, USA.

3. HCMM Potentialities for the Deduction of Physiographic Lineaments of the Pô Valley in Northern Italy

B. Marcolongo
Consiglio Nazionale delle Ricerche
Padova, Italia

E. Barisano
Unité Géographique de Télédétection
Université Catholique de Louvain, Belgique

Introduction. Basic Approach

The aim of this research was to evaluate the influence of static physiographic aspects (geology, hydrogeology, pedology) on the HCMM thermal response in relation to the dynamic aspects (vegetation cover, land-use, etc.). The approach adopted is based on the deduction of reciprocal inferences between buried structures and surface patterns. Indicators such as vegetation and humidity content of the subsoil insaturated region are evaluated qualitatively in the thermal imagery by examining "structural distributions" as well as "thermal anomalies".

A number of existing physical maps (orographical-hydrographical), integrated by a few Landsat false colour composites (when available) are employed as a "ground truth".

During interpretation, special attention is given to the tone as well as to the analysis of forms and their spatial distribution (morphology and structure).

This approach leads to thematic maps mainly of hydrogeological character of the area covered by HCMM. An original type of legend illustrates the logical passage between geomorphological, vegetational-anthropologic aspects of the identified surfaces and the

buried hydrological aspects deduced (see Fig. III.2.38). In Fig. III.2.39 a theoretical logical model of the thermal behaviour of various earth bodies is reported. It was set up as a valid scheme for HCMM imagery interpretation and can be improved. The role of thermal inertia properties of materials appears evident for interpretation and classification in the hydrogeological field both structural and applied.

Zone Investigated. HCMM Imagery and Maps Used

The area investigated encompasses the whole Po Valley, in Northern Italy. It is one of the most interesting examples of a South-European hydrological basin. It was selected for interpretation mainly due to the availability of "ground-truth" cartographic documentation. The HCMM imagery for this investigation is provided by a section of an HCMM scene of 3 June 1978 (day and night). These images have a low cloud cover. Their densitometric and scanning quality is very good. A Test-Image (TI) for the same date has been also utilized for a preliminary interpretation.

The Standing Order (SO) imagery utilized were:

Day-VIS A-A0038 - 12460-1 (Fig. III.2.40)

Day-VIS A-A0038 - 12460-2 (Fig. III.2.41)

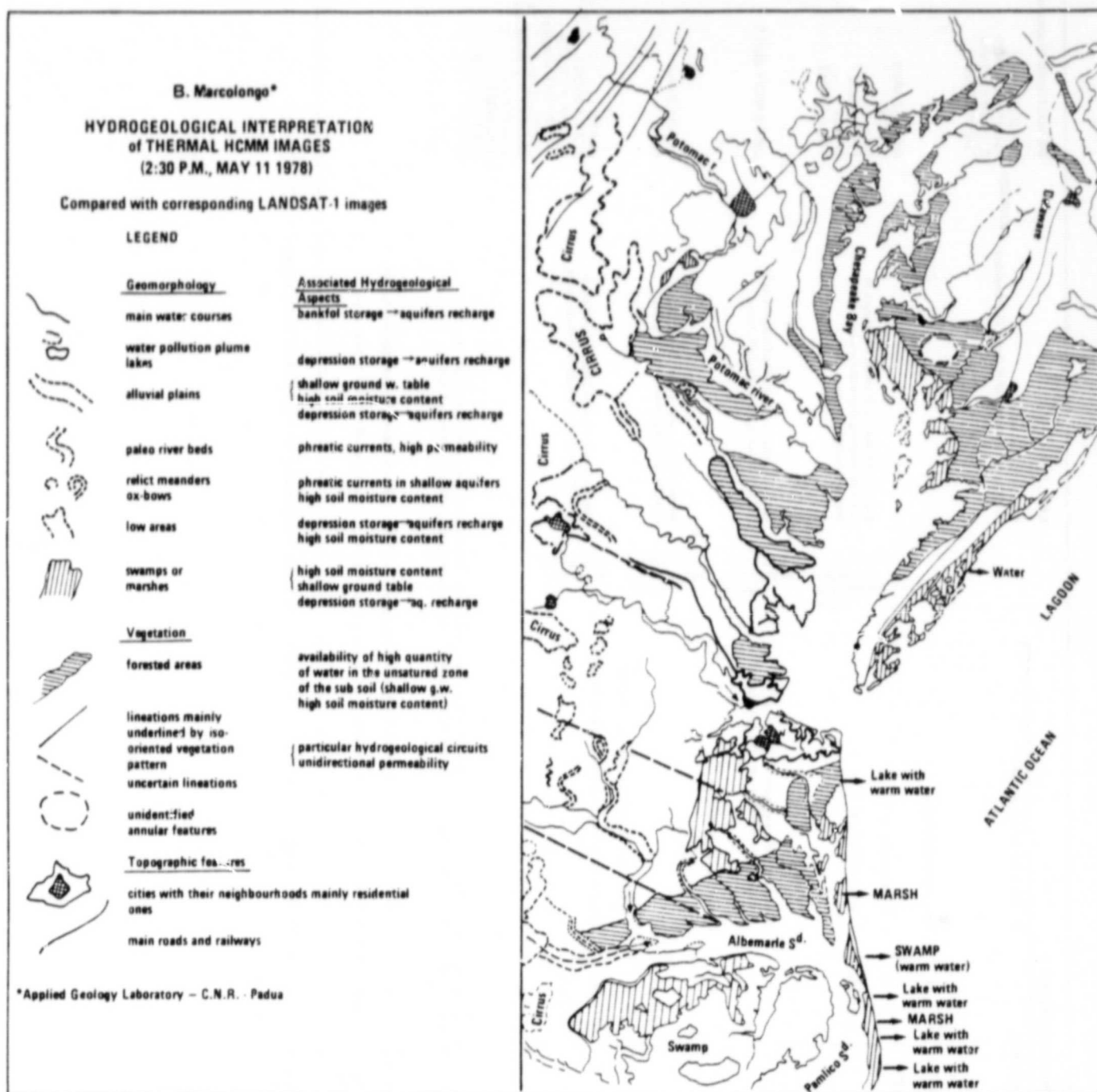


Fig. III.3.38.

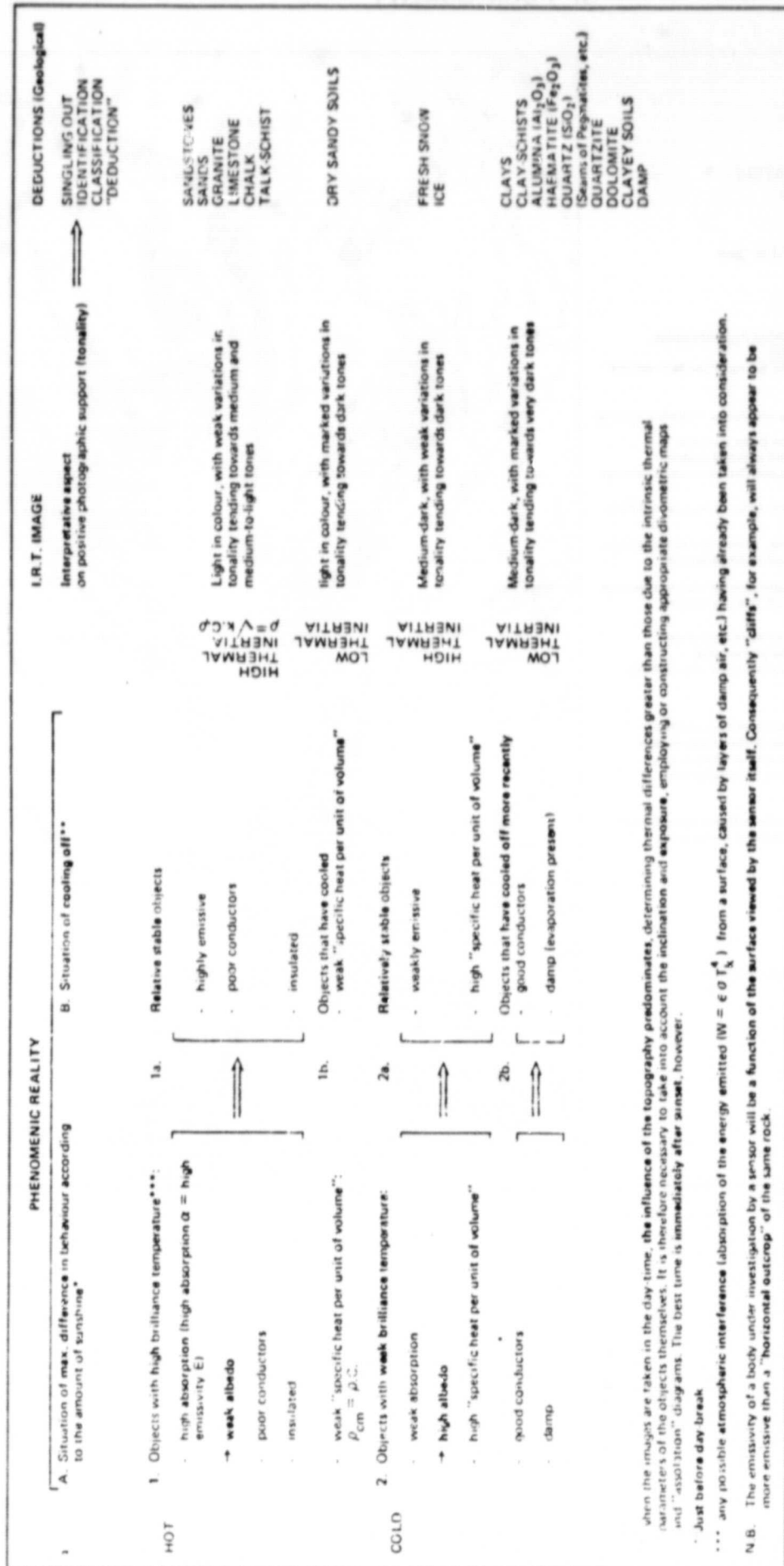


Fig. III.2.39. Methodological scheme for the interpretation of thermal infra red images (taken from Cl. TORRES, 1973, and integrated by B. MARCOLONGO, 1978).

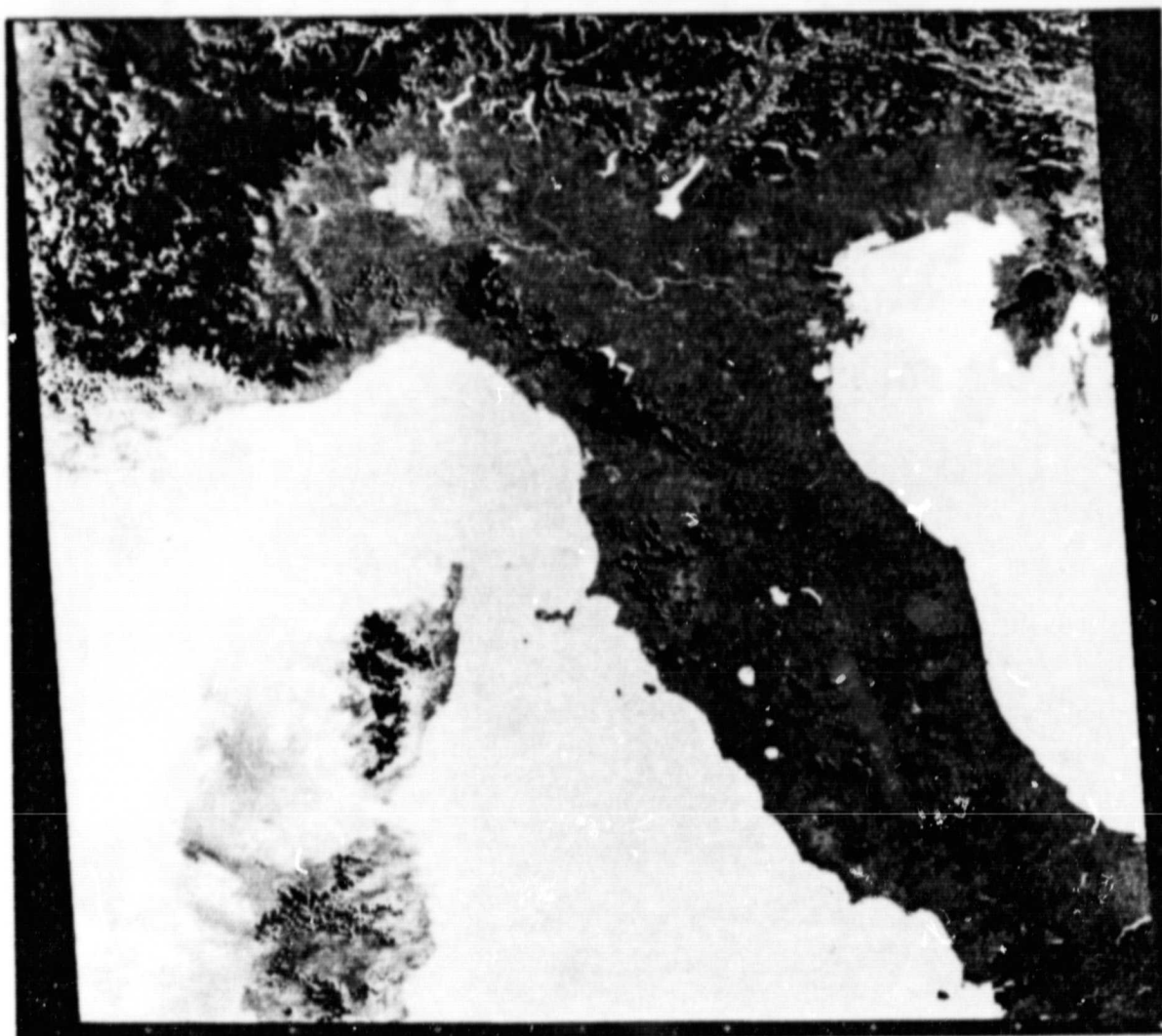


Fig. III.2.40. DVIS-HCMR albedo image of Northern and Central Italy (3 June 1978, scale $\sim 1:4,000,000$).

ORIGINAL PAGE IS
OF POOR QUALITY

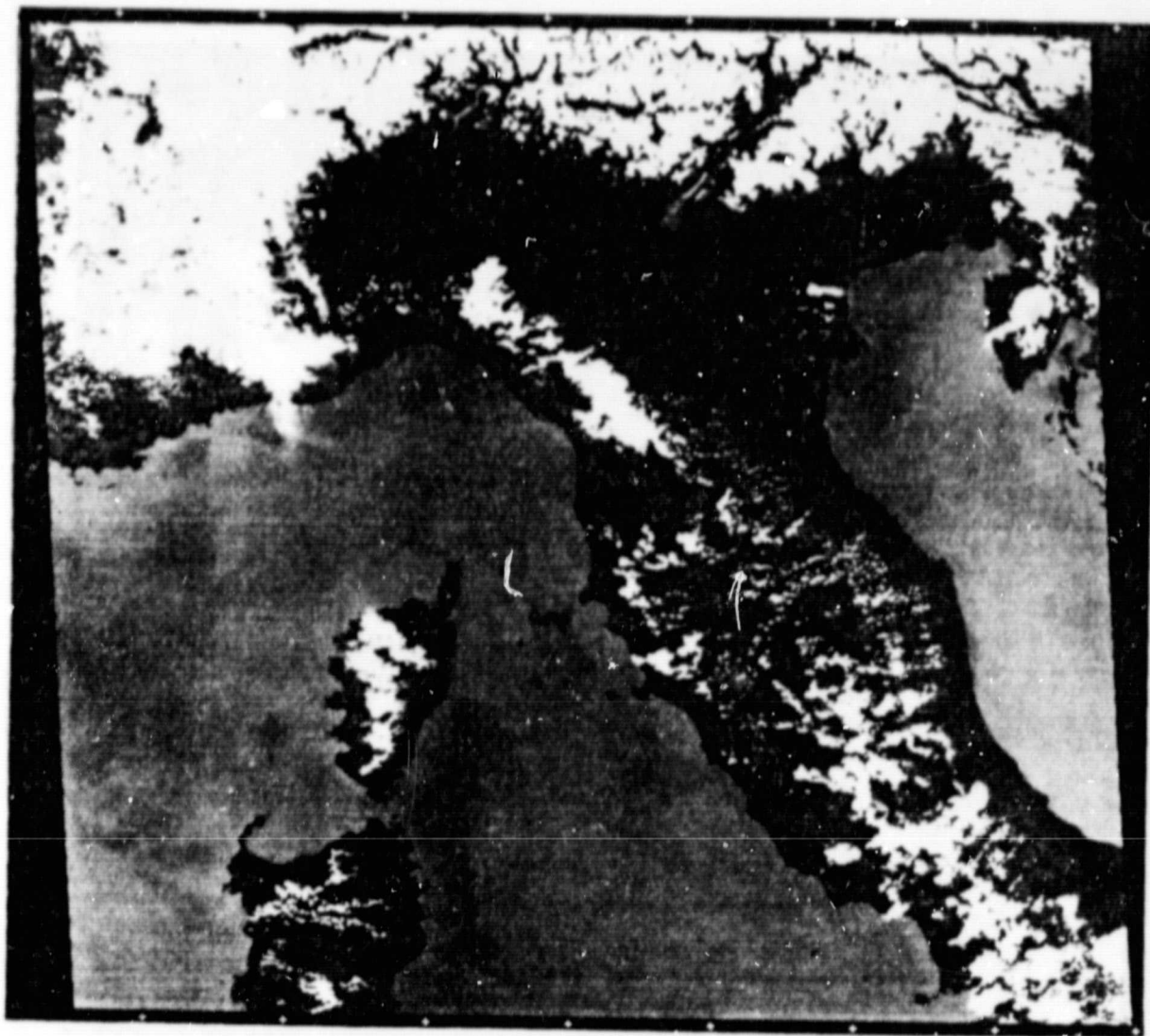


Fig. III.2.41. DIR HCMR thermal image of Northern and Central Italy (3 June 1978, scale $\sim 1:4,000,000$).

ORIGINAL PAGE IS
OF POOR QUALITY

Night-IR A-A0038 - 01491-3 (Fig.III.2.42)

The Test Image (TI) imagery utilized was:

Night-IR A-A0038 - 01491-3 (Fig.III.2.42)

The thematic maps used were:

hydrologic map	1 : 1, 500, 000
geologic map	1 : 1, 000, 000
pedologic map	1 : 1, 000, 000
soil potentiality map	1 : 1, 000, 000
land-use map	1 : 1, 000, 000

The last one is a remapping of an original map 1 : 250, 000 made by the Italian Ministry of Agriculture and Forestry.

Method and Activity Performed

Instrumentation

The interpretation of the HCMM scene was performed in an analog way using an OMI stereo-plotter (analog-anamorphic), a densitometer and an equidensitoscope. The superposition of HCMM thermal images on basic maps or Landsat transparencies was possible with an error of 2 HCMM pixels.

Four colour levels were utilized by electronic density slicing.

Analysis Support of Methodological Process

Fig.III.2.42a illustrates the block-diagram of the various interpretation steps:

- Image visualization is first made on the HCMM transparencies at $\sim 1 : 4, 000, 000$ original scale in order to find control points for further cartographic approach with stereoplotter.
- The first interpretation process step is based on grey tone discrimination. Boundaries between homogeneous zones are traced out (structure and texture). Without delimiting isophenic zones (i.e. creating genuine land-

scape families) one respects, as much as possible, the intrinsic physical realities which have been recognized on the scene. Oceanographic and urban boundaries are purposely considered apart. Attention is devoted to physiographic boundaries only.

- The cartographic classification-deduction-interpretation phase, done with the stereo-plotter is the successive key-step of the analysis. Information from the stereo-plotter and colour density slicing leads to definitive interpretation results which are transferred on to the final deduced physiographic map.

Superposition-Interpretation Procedure

The analog-anamorphic interpretation was made after superposing a sector of the HCMM images on the corresponding entire extent of the hydrological map 1 : 1, 500, 000. The analysis of the other maps, 1 : 1, 000, 000 was performed on an enlargement of the hydrogeological deduced map where the unknown boundaries were reported for comparison. Afterwards the first deduced map was superposed on the remaining thematic maps. As a result of this approach a final deduced thematic map is obtained for each HCMM image (monotemporal analysis).

Figs.III.2.43, 44, 45 represent the final interpretation maps of the HCMM scene of 3 June 1978 for DVIS, DIR and NIR. One can notice that they are denominated "hydrogeological" maps: this depends on the legend where hydrogeological terms are dominant. But they contain a lot of information deduced from the other thematic maps 1 : 1, 000, 000 and reported in the analytic tables (see 4.1).

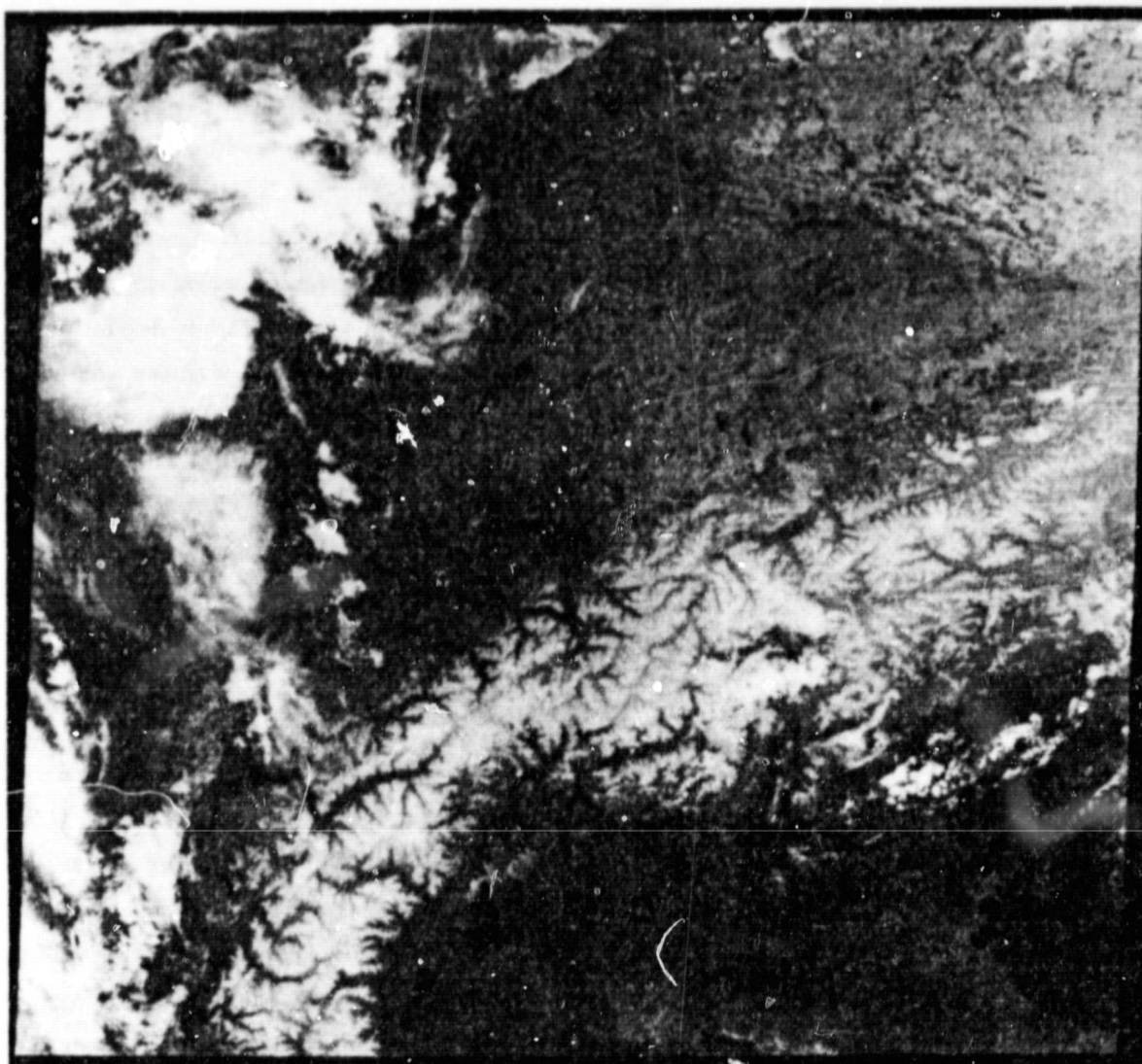


Fig. III.2.42. NIR HCMR thermal image of Northern and Central Italy (3 June 1978, scale 1:4,000,000).

ORIGINAL PAGE IS
OF POOR QUALITY

ORIGINAL PAGE IS
OF POOR QUALITY

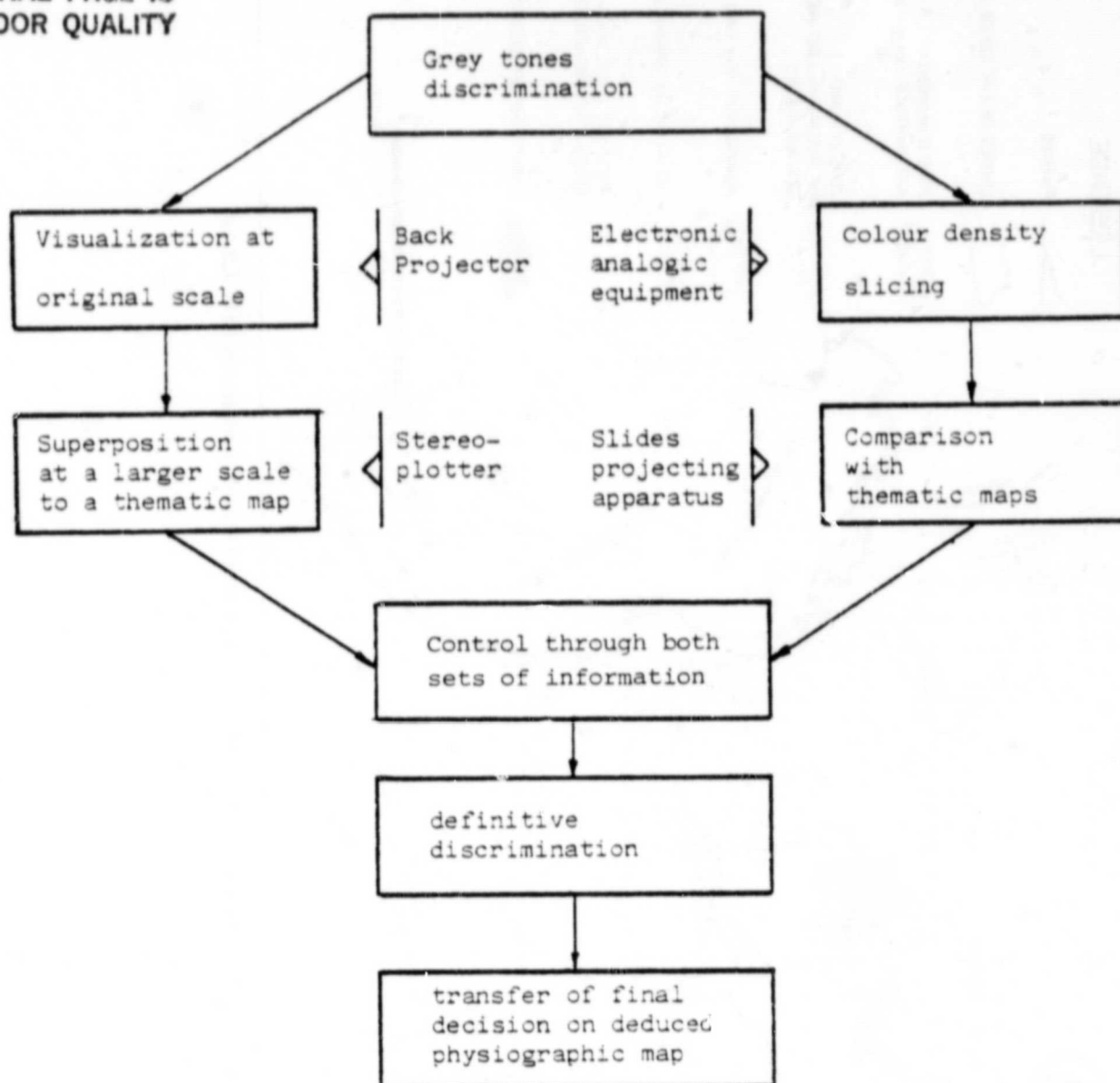


Fig. I/1 2.42a. Block diagram of the analog interpretation approach of HCMM imagery of the Po Valley (Northern Italy).

ORIGINAL PAGE IS
OF POOR QUALITY

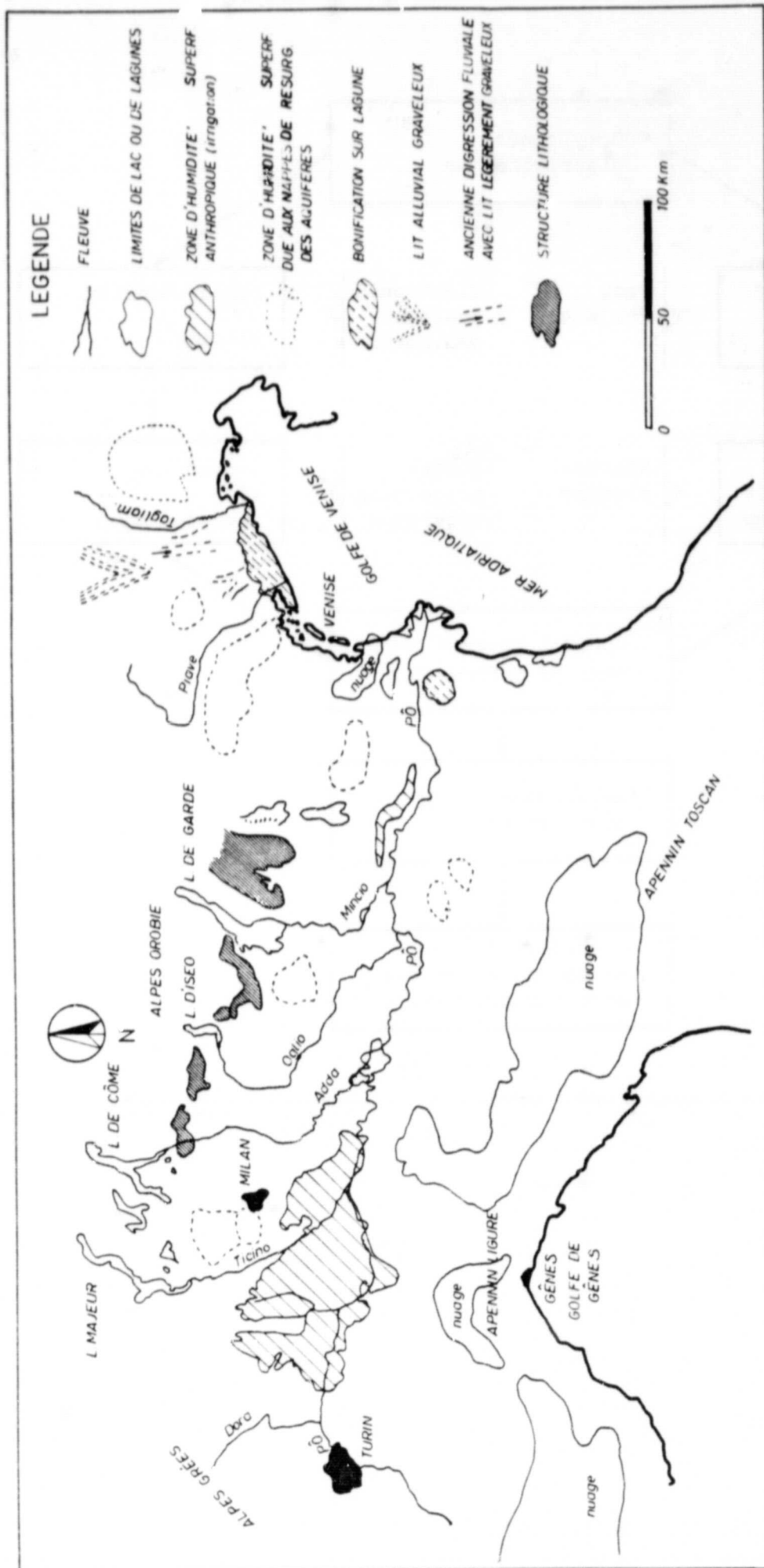
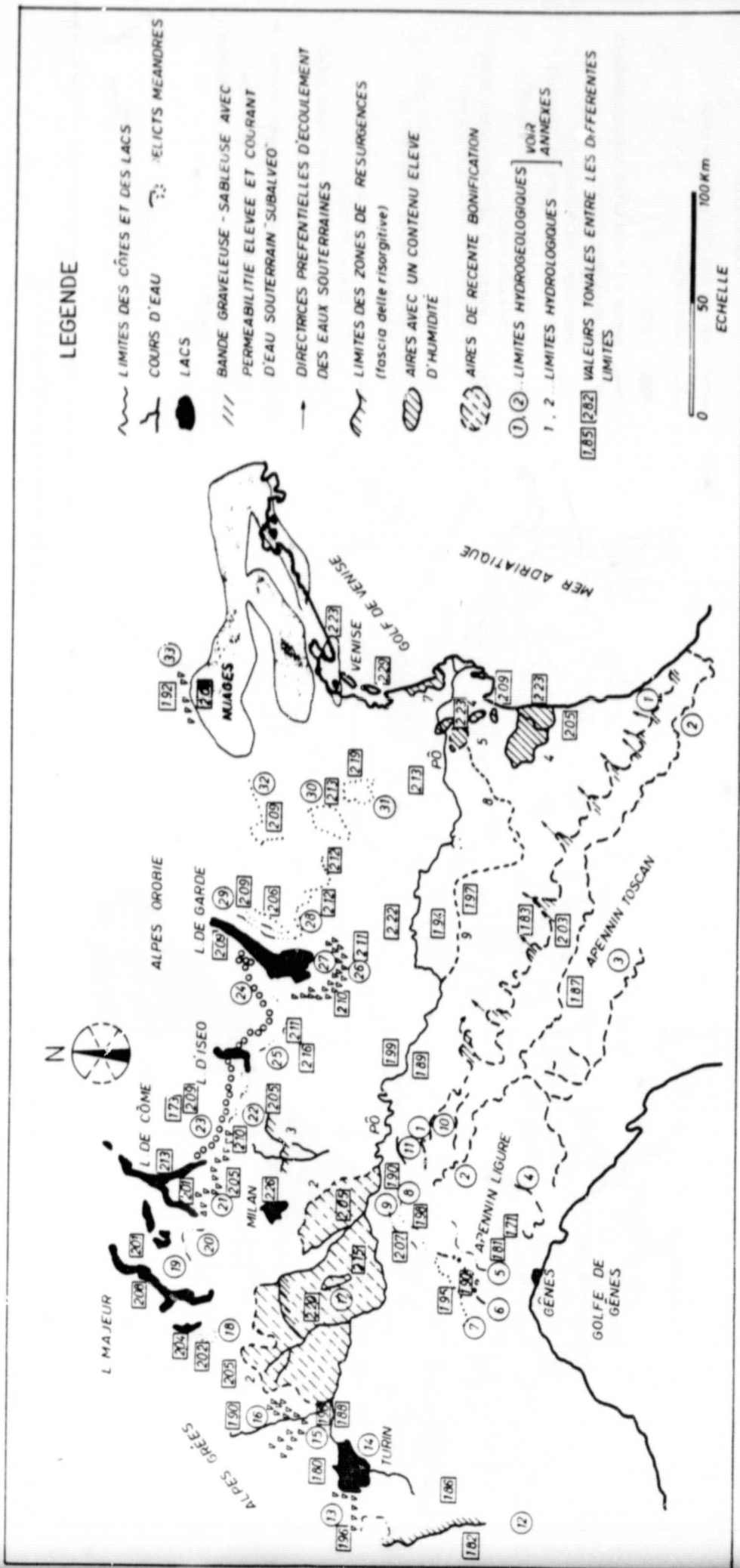


Fig. III.2.43. Map of the principal hydrological aspects of the Po Valley derived from the interpretation of a HCMM panchromatic image (mission of the satellite EXPLORER-A DAY-VIS 1.30 p.m., 3 June 1978).

ORIGINAL PAGE IS
OF POOR QUALITY



Fig. III.2.44. Map of the main hydrological aspects of the Po Valley derived from the interpretation of a HCMM thermic image (mission of the satellite EXPLORER-A, DAY-IR, 1.30 p.m., 3 June 1978).



ORIGINAL PAGE IS
OF POOR QUALITY

Fig. III.2.45. Map of the main hydrological aspects of the Po Valley derived from the interpretation of a HCMM thermal image (mission of the satellite EXPLORER-A, NIGHT-IR 2.30 a.m., 3 June 1978).

ORIGINAL PAGE IS
OF POOR QUALITY

TABLE III.2.6. DVIS HCMM image (3 June 1978, 1.30 p.m.)

Physiographic Subject (class)	Boundaries Length (km)	Parameters	
		A%	B% (±)
Geology	1713	71	67
Hydrogeology	1966	82	79
Pedology	1014	42	35
Soil Utilization	534	22	12
Soil Potentiality	346	4	4
Total	2424	(±) 268 km are of physiographically insignificant subjects	

TABLE III.2.7.

Physiographic Class	Degree of Significance
Hydrogeology	very significant
Geology	significant
Pedology	little significance
Land-Use	very little significance
Soil Potential Affec.	insignificant

TABLE III.2.8. NIR HCMM image (3 June 1978, 2.30 a.m.)

Physiographic Subject (class)	Boundaries Length (km)	Parameters	
		A%	B% (±)
Geology	416	17	27
Hydrogeology	1022	41	65
Pedology	1016	41	36
Soil Utilization	72	3	5
Soil Potentiality	900	36	29
Total	2482	-	-

TABLE III.2.9.

Physiographic Class	Degree of Significance
Hydrogeology	Significant
Pedology	Little significance
Geology	Very little significance
Soil Potential Affec.	Very little significance
Land-Use	Insignificant

Results

Classification of Identified Structures and Probabilities of Correlation with Actual Physiographic Lineaments

One defines "structure" as a set of objects forming a homogeneous class with respect to their spectral response.

The fundamental problem of structure classification is to determine - through an appropriate and simple procedure - the degree of correspondence between the structures identified on the thermal HCMM images and the physiographic characters (geologic, pedologic, hydrologic, etc.) of the land under investigation. This can be achieved through the analysis of the physiographic mean of the separation boundaries between structures, i.e. by means of the following procedure:

- A) 1. Adding up measured lengths of boundaries of each physiographic class (geology, hydrology, land-use, etc.)
2. Adding up measured lengths of all boundaries on the image
3. Calculating the percentages
- . for each class referred to the whole boundaries set,
 - . id. but excluding the contribution of the classes insignificant for the image interpretation.
- B) 1. Establishing a qualitative table of the identified structures
2. Deducing an importance list of classes (physiographic subjects).

These procedures have been applied to the DVIS and NIR images of 3 June 1978 (see Tables III. 2, 6 and 7).

Discussion of the Results of HCMM Imagery Interpretation

Classifying identified physiographic structures has shown that hydrological characteristics offer the best identification out of the HCMM images. It has been also confirmed that the success of the inductive interpretation approach of satellite thermal imagery is based on the correlation between buried structures and surface patterns which are characterized by typical indicators (i.e. water content of insaturated subsoil zones, vegetation type, etc.).

1. Day-VIS Image (3 June 1978, 1.30 p.m.)

As a first step it was considered useful to interpret the DVIS image due to the complementary role of their information to the Day-IR and Night-IR images.

The following information has been obtained:

1. The hydrogeological network (rivers, lakes, lagoons) stands out very clearly and details can be easily identified.
2. The surface moistured areas are well defined and can be recognized. This top soil humidity is mostly of anthropic origin and has been localized within the late-reclaimed areas, i.e. Novara waterways, reclaimed land around Ferrara.
3. The deeper moistured areas are more difficult to recognize. Nevertheless, analogic superposition on the hydrologic thematic map 1 : 1,000,000 led to a clear localization using shape-and-tone analysis. The best results were found for areas with strong imbibition.
4. Large urban agglomerations have been easily identified.
5. Relief does not stand out at all.

2. Day-IR Image (3 June 1978, 1.30 p.m.)

The following physiographic characteristics were deduced:

lithology: some deep lithologic structures were singled out with great precision

morphology: from a morphological point of view it has been found that relief boundaries can be well characterized.

Small scale of HCMM demonstrates contributing to a simplification of such boundaries within the scene context.

hydrography: the main hydrographic network results depicted by a very good contrast with the environment.

Only minor canalization networks and small rivers are difficult to recognize. Lake borders and coast lines are well depicted.

hydrology: surface-moisture areas are very difficult to define into boundaries instead of the deep-moisture ones. It is possible to identify zones of upwelling, displaying the transition from highland aquifers (generally of restricted area) to lowland aquifers (more diffused). Preferential directions of underground water drainages are also identifiable.

The most relevant thermographic aspects of this image may be summed up as follows:

hottest points: agglomeration (urban and industrial), bottom of valleys

warm zones: mostly situated in lowlands with various thermal gradients depending on texture and/or morphology

cold points: distributed mainly in highlands, along the Alpine area and the

Apennine Chains.

Lakes and sea appear cold, due to their high thermal inertia.

In conclusion, the DIR Image contribution is quite significant for the characterization of lithological and hydrogeological structure, but it only contributes on a small scale to defining humid areas.

3. Night-IR Image (3 June 1978, 2.30 a.m.)

As for DIR this type of image was the object of a thorough analysis. The following physiographic characteristics were deduced:

lithology: information obtained does not appear to be as comprehensive as for IR Day-Image. Nevertheless, the possibility of individualizing some buried structures was verified, mainly along the Alpine arc (the boundary zone with lowlands) and within the hilly area of "Colli Euganei" near the city of Padua, where the identification turned out to be very satisfactory.

morphology: relief does not stand out clearly

hydrography: the hydrographical network is not easily identifiable. In practice one can identify only the Po river. Lake contours are very difficult to individualize.

hydrogeology: surface-moisture zones can be defined pretty well: irrigated areas are distinguishable from moistured areas by re-ascending underground waters. The latter areas extend along the foot of the Apennines. Inversely, deep-moisture areas are difficult to define.

The most relevant thermographic aspects of

this image may be summarized as follows:

- hottest points: cities and humid zones (irrigation, reclamation) lagoons, and sea
- warm points: plains, lakes, some mountain slopes in valleys and humidity bands along Apennines
- cold points: highlands.

In conclusion the NIR image appears to be a very significant contribution for highly surface-saturated zone characterization. It appears to be less important for a structural re-composition (relief, morphology). Information provided for lithological characterization is rather contributive.

References

1. AMERICAN SOCIETY OF PHOTOGRAMMETRY; "Manual of Remote Sensing - Volume I: Theory, Instruments and Techniques", Falls Church, Virginia, 1975.
2. E. BARISANO; "Contribution à l'évaluation des potentialités des images thermiques de satellite (HCMM-Explorer 1) pour la déduction d'aspects physiographiques: Applications à la plaine du Pô (Italie du Nord)", Mémoire présenté pour l'obtention du grade d'Ingénieur agronome (UCL-LLN) 1979.
3. H. G. GIERLOFF; "Orbital Remote Sensing of Coastal and Offshore Environments. A Manual of Interpretation". Walter de Gruyter, Berlin, New York, 1977.
4. M. C. GIRARD and C. M. GIRARD; "Les fonctions et les traitements des images satellites. Méthodes d'emploi en pédologie", 1er Colloque de Pédologie et Télédétection, AISS, Rome, 1977.
5. G. M. LECHI, B. MARCOLONGO and A. M. TONELLI; "The Principal Hydrogeological Aspects of the Eastern Venetian Plain as Identified by Multispectral Photography from Satellites", Bollettino della Società Italiana di Topografia e Fotogrammetria, No. 1, 1978.
6. NASA - National Aeronautics and Space Administration; "Heat Capacity Mapping Mission (HCMM) Users' Guide", Goddard Space Flight Center, Greenbelt, Md., 1978.
7. B. MARCOLONGO, G. M. LECHI and A. M. TONELLI; "Applicazioni delle immagini multispettrali da satellite alla individuazione di materiali da costruzione sulla coltivazione di pietre e minerali litoidi", Associazione Mineraria Subalpina, Torino, Italia, 1974.
8. B. MARCOLONGO; "Fotointerpretazione sulla pianura alluvionata tra i fiumi Artico e Brenta, in rapporto alle variazioni del sistema idrografico principale". Studi trentini di Scienze Naturali, Trento, 1973.
9. B. MARCOLONGO and M. MASCELLANI; "Satellite Images and their Treatments Applied to the Identification of the "Roman Reticulum" in the Venetian Plain", XXXVI Photogrammetric Work, Stuttgart, 1977.
10. B. MARCOLONGO; "Photointerpretation Applied to Soil Characterization, to Determination of Moisture Content and to Hydrological Study", International Ispra-Courses on Remote Sensing Application in Agriculture and Hydrology, 1977.
11. ORSTOM; "Les satellites d'observation de la Terre: Landsat". Documentation technique No. 34, Paris, 1977.
12. A. M. TONELLI; "Introduzione al Remote Sensing e alle sue applicazioni", ARCO, Milano, 1978.
13. Cl. TORRES; "La Thermographie. Questions techniques et problèmes de l'interprétation", Revue Photo-Interprétation, Edition Techniques, Paris, 1973.
14. L. VAN WAMBEKE; "Les techniques et les applications de la télédétection", CCR-Ispra, Rapport de mission, 1971.
15. H. T. VERSTAPPEN; "Remote Sensing in Geomorphology", Elsevier Scientific Publishing Company, Amsterdam, Oxford, New York, 1977.
16. J. WILMET; "Interprétation des images des satellites Landsat en vue d'études urbaines et régionales", Société Française de Photogrammétrie, No. 70, 1978.
17. R. S. WILLIAMS Jr. and D. W. CORTES; "A New Window on our Planet", Geological Survey Professional Paper 929, US Government Printing Office, Washington, 1976.

ORIGINAL PAGE IS
OF POOR QUALITY

4. Remotely Sensed Thermal Data for Localization of Frost Prone Areas and the Evaluation and Monitoring of Low Altitude Breezes

ORIGINAL PAGE IS
OF POOR QUALITY

A. Wind-Induced Microclimatic Differences Detected from Thermal Scanner Data

W. Nübler
Geographisches Institut I der Universität
Freiburg, Deutschland

Introduction

Since more advanced remote sensing methods have been available, the solution of climatological questions as the evaluation and monitoring of wind action has always been looked upon as one promising application.

A reserved attitude is still prevalent on whether and to what extent a climatological interpretation of remotely sensed thermal data can be given for such micro- and meso-climatological applications.

In fact, thermal scanning means recording the radiation emitted by the earth's surface, while the climatologist is concerned with the air layer above this surface. Although it is evident that the lower boundary layer of the atmosphere is influenced by the underlying surface, interrelations are so complex that unequivocal interpretation is very difficult to obtain. But under certain conditions micro-

climatic differences can definitely be deduced from thermal scanner data. The possibilities and limitations of tracing cold air in thermal images have been covered (Nübler, 1978) and the effects of low-altitude breezes are here investigated and reported.

Interpretation of MSS Aircraft Data.

The effort made by the Geographisches Institut I der Universität Freiburg was concentrated on two examples of the wind effect on the city of Freiburg and an area situated 8 km northwest in the Rhine Valley.

The experiments in the investigation area "Black Forest-Rhine Valley" included some flight campaigns with a multispectral scanner (Bendix M²S) taking place under the sponsorship of the Deutsches Flugzeugmessprogramm (DFP) in 1976.

Each campaign comprised flights, three times a day, at three different levels (1000, 2000 and 4000 m above ground level). The data recorded in the 8-14 μ m thermal channel were processed with the digital image processing system DIBIAS of the DFVLR in Oberpfaffenhofen/Munich.

A rough representation of the test area is given in Fig.III.2.46. It shows the Black Forest-Rhine Valley boundary and the isolated Kaiserstuhl, a mountainous area of about 90 km². The two examples will show the greater part of the city of Freiburg and a 16 km² area situated in the Rhine Valley; these areas are shaded in Fig.III.2.46.

recording wind speed and wind direction. Of these, Feldberg (1486 m) is the highest point of the Black Forest and therefore is nearest to free atmosphere conditions over Southwest Germany. Of the remaining three stations, Bremgarten represents best the Rhine Valley. In Freiburg and - less frequent - Bad Krozingen wind direction is influenced by valley winds from the Black Forest.

City of Freiburg

Figure 4a is a thermal image of Freiburg taken before sunrise on 1 April 1976 from an altitude of 4000 m. Surface temperatures (ST) range from below 0°C to over 10°C. Air temperatures were recorded simultaneously and ranged from 6.2 to 10.4°C.

The distribution of ST corresponds to what one would expect: for example the wooded hillslopes east of the city appear with high ST as radiational cooling can be compensated for by upper and warmer air. Normal too, is that the lowest ST occur over short grass as e. g. on the airfield near the northwest corner or that the city centre with its concentration of massive buildings has relatively high ST. It should be noted, however, that the southern part of the city centre displays considerably lower ST compared to the northern part, although the type and density of the buildings are the same. On the other hand, the southwestern suburbs are in large areas 2 to 3°C warmer than the adjacent northwestern suburbs, although here again the structure is

similar. This can be seen best in Fig.III.2.49b, an equidensity representation of Fig.III.2.49a.

After applying a digital low-pass filter the 0... 5°C range of the original data (Fig.III.2.49a) is split into 5 grey tones representing 1°C each; white is lower than 0°C, black is warmer than 5°C.

The problem of differing ST in regions of the town with comparable structure can be explained by the influence of a local circulation system.

Under anticyclonic conditions at night cold air flows from the slopes and valley of the Black Forest towards the Rhine Valley. The wind field in the urban area of Freiburg under the influence of a well developed mountain wind system is shown in Fig.III.2.47a. -47b shows that a similar wind field occurred when the thermal image (Fig.III.2.49a) was recorded on 1 April 1976 between 5 a. m. and 6 a. m.

Although the general wind direction is West to Southwest (Feldberg), in Freiburg southeasterly wind prevails throughout the night.

Due to the topographic situation, with the city centre slightly north of the opening of the Dreisam valley, this stream of cold air reaches only the southern part of the city centre, cools it and displaces its heat island westwards, thus warming the western suburbs. This explanation is confirmed by extensive air temperature measurements and by registrations of wind speed and wind direction.

This means that when the structure of the surface cover is known and corroborative evidence from ground truth measurements is available, the cooling of surfaces by cold-air flows and the extent of their influence can be deduced from thermal images.

Rhine Valley

In the second example it is more evident that wind must have shaped the distribution of ST.

ORIGINAL PAGE IS
OF POOR QUALITY

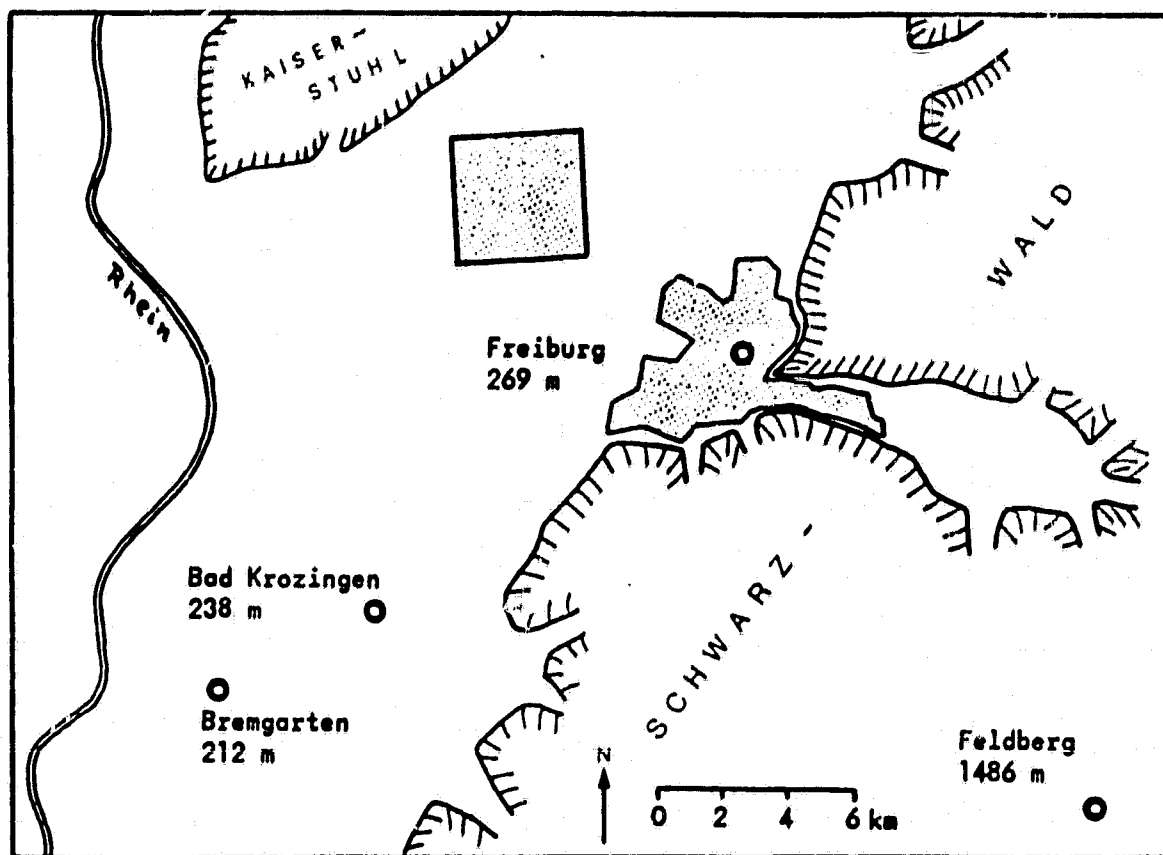


Fig. III.2.46. Topographic sketch of the investigation area (circles: Windstations listed in Figs. III.2.47b and III.2.48; shaded: Urban area of Freiburg i.Br. and area represented in Fig. III.2.50.

ORIGINAL PAGE IS
OF POOR QUALITY

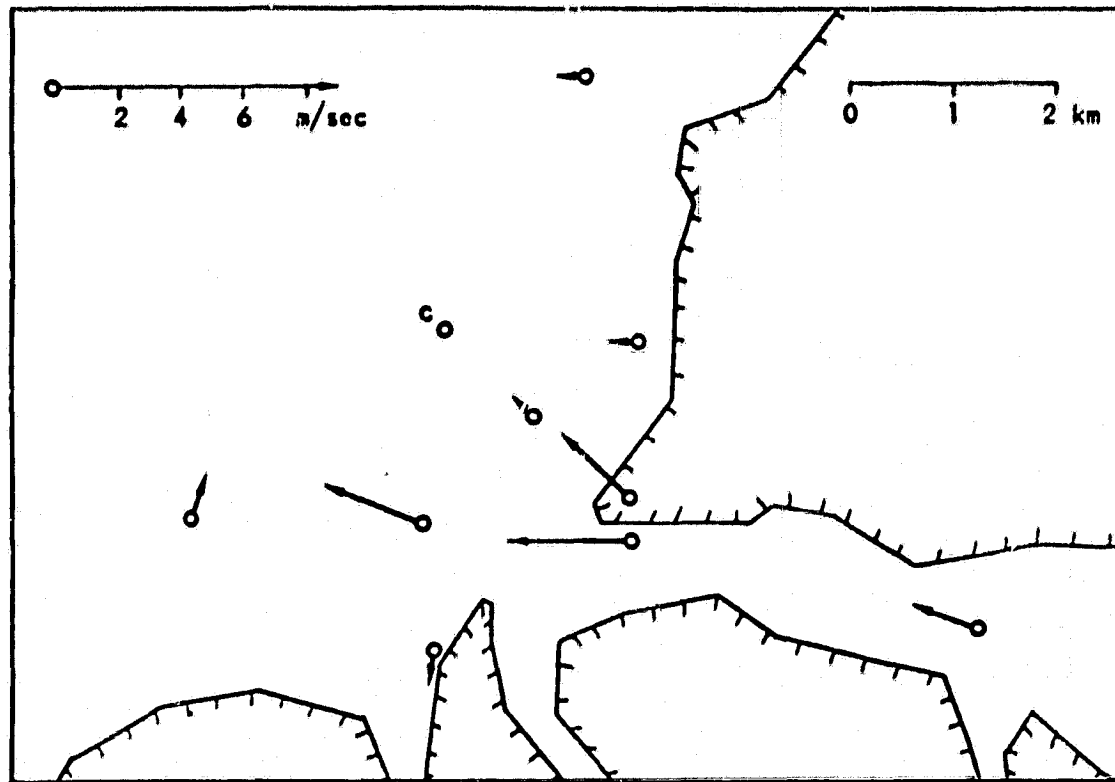


Fig. III.2.47a. Wind speed and wind direction at 10 stations in the urban area of Freiburg under the influence of the mountain wind system (20.9.71, 5 h). The solid line delimits the Black Forest - Rhine Valley boundary; see also Fig. III.2.46.

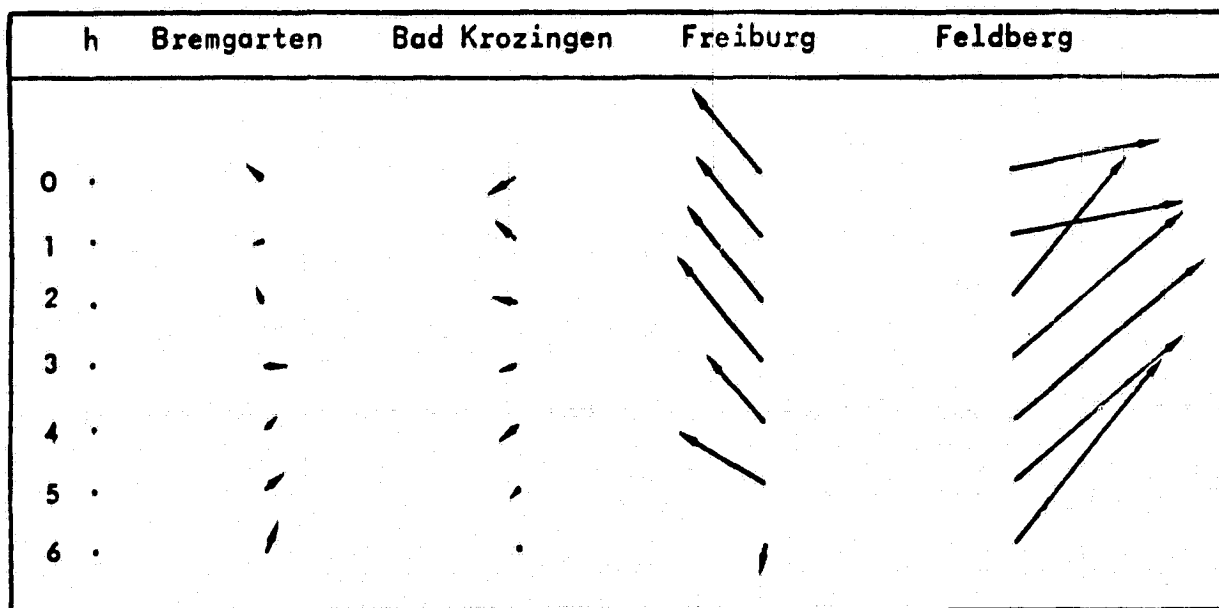
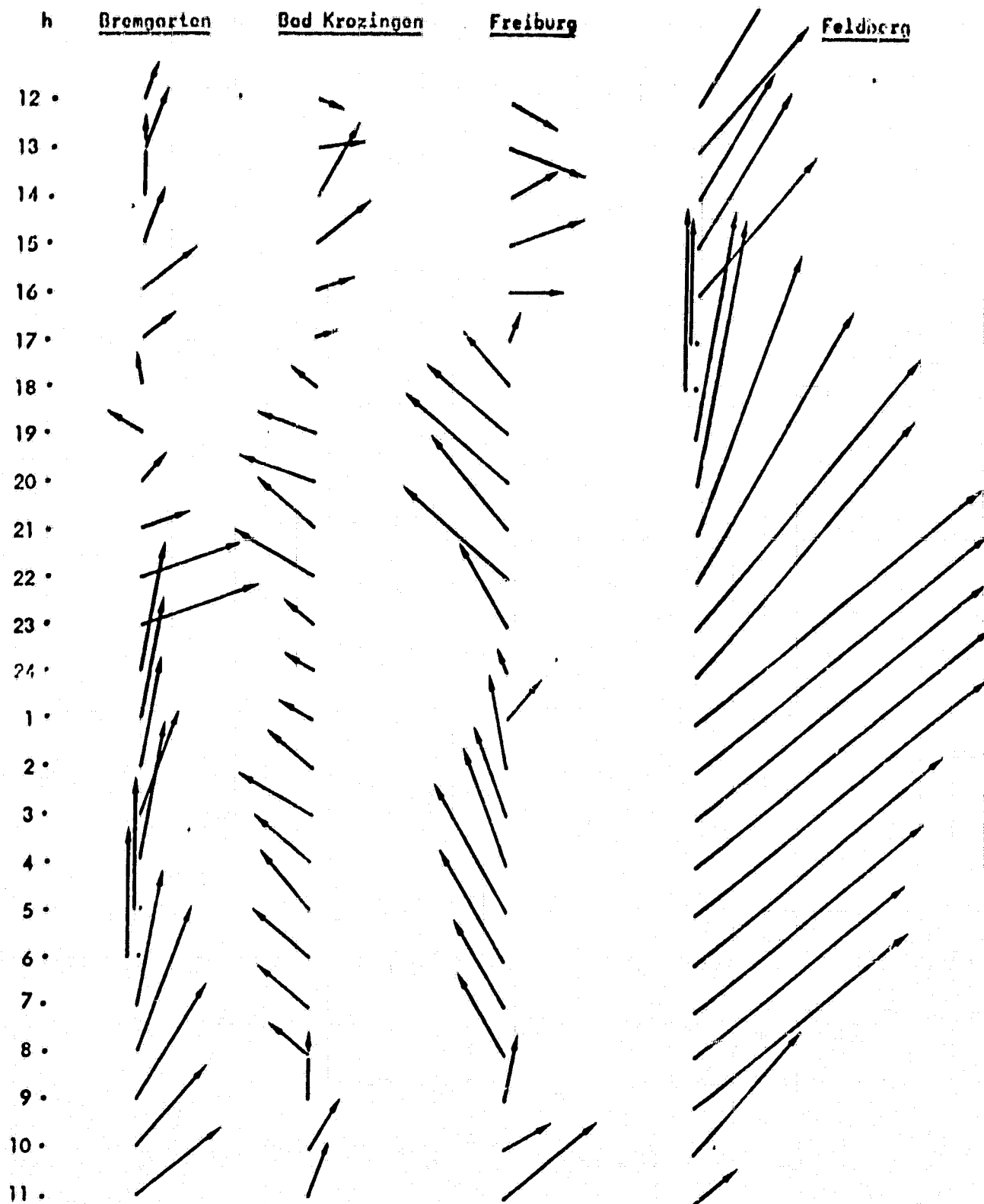


Fig. III.2.47b. Wind speed and wind direction at the 4 stations shown in Fig. III.2.46 (1.4.76, 0-7 h) 0 2 4 m/sec

Fig. III.2.48. Wind speed and wind direction (1.4.76, 12 h - 2.4.76, 12 h). 0 2 4 m/sec



The area covered in Fig.III.2.50a is situated 8 km northwest of Freiburg in the Rhine Valley (see Fig.III.2.46). The villages Gottenheim and Umkirch are near the upper left and lower right corners, respectively. The region is partly wooded and partly open field. The thermal image was recorded from an altitude of 2000 m on 2 April 1976, before sunrise.

Again the forests are warmest with ST between 5 and 10°C. The most remarkable feature, however, are narrow zones of lower ST on most northern margins of forest areas. It is clear from the two facts that the formation of these thermal shades is a wind effect: a) they are all oriented, even streamlined, in the same direction, although the fields north and south of the patches of wood are exactly of the same type, and b) they do not occur on other recordings of the same region, i. e. with different weather conditions.

However, at that stage it was not yet possible to demonstrate quantitatively alterations of ST in a thermal shade. By the use of a calibrated scanner together with digital image processing, this may be now achieved. Figure 5b shows that ST in thermal shade areas differ $> 5^{\circ}\text{C}$ from ST in the open parts of the region.

More detail is given in Fig.III.2.51a/b which was recorded from an altitude of 1000 m and consequently has a better resolution (pixel size $2 \times 2 \text{ m}$). It may be noticed that even a row of trees along a road causes differences in ST of 6°C in the adjacent fields. Another marked feature is the strict north-south orientation of the thermal shade contours.

So far the argument that the described thermal shades are wind-induced, rests on indirect evidence. However, Fig.III.2.48 reveals that the registration of wind direction supports this

view: in fact there was a fairly strong southern wind in the Rhine Valley (Bremgarten 5.3 m/s) which prevailed, more or less unchanged in direction, for over 5 hours, after which, at 5.40 a.m. the thermal image was recorded. This direction corresponds to a continuous and strong (16.0 m/s) south-westerly wind at the Feldberg station. Nevertheless, easterly directions prevailed throughout the night in Bad Krozingen and Freiburg.

It is clear, then, that the thermal shades on the northern margins of forests are due to southern wind. The physical explanation would be the following: radiative cooling produces low ST and consequently cold air near the ground. Where this air is exposed to a continuous wind, it is mixed with warmer air from upper layers. Any obstacles disturbing the windflow, however, will reduce wind speed to such an extent that mixing, on their leeward side, is also reduced and the cold air can accumulate. Everywhere on the open fields ST would, without wind-induced mixing, correspond to those in the thermal shade areas. In this case, contrary to the first example, wind action generates higher ST in the thermal image than there would be without wind.

Conclusions

It has been demonstrated that the interpretation of thermal images can lead to the detection of wind-induced microclimatic differences. One example shows that the cooling of otherwise warmer surfaces can be attributed to wind. On the other hand, in the second example, higher ST in an otherwise colder environment - as seen from the low ST in wind-sheltered areas - can also be the result of wind action. Therefore, the conclusion drawn from these two examples must be, that, although thermal images are a unique tool to delimit the extent of wind

ORIGINAL PAGE IS
OF POOR QUALITY

ORIGINAL PAGE IS
OF POOR QUALITY

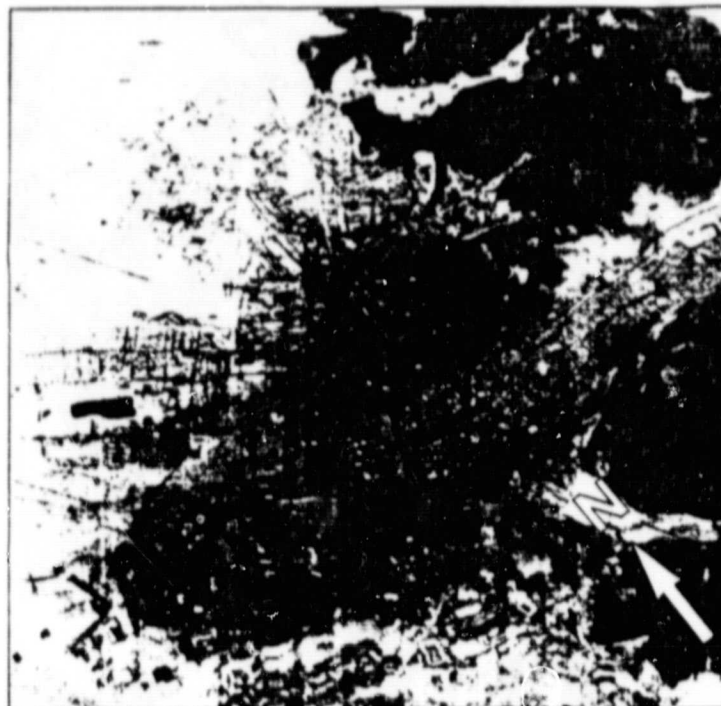


Fig. III.2.49a. Thermal image of Freiburg i.Br. The dark area near the middle left margin is the airfield, the city centre is at the same height farther to the right (1.4.76, 5 h, altitude 4000 m).

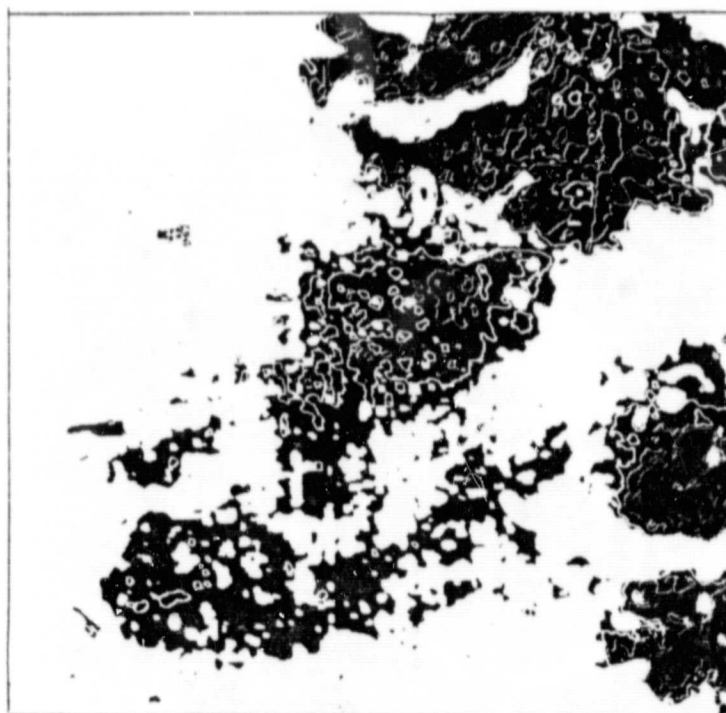


Fig. III.2.49b. Same image as III.2.49a, equidensity representation, 1°C - grey tones ranging from 0° (white) to 5° (black).

ORIGINAL PAGE IS
OF POOR QUALITY



Fig. III.2.50a. Thermal image of a $4 \times 4 \text{ km}^2$ area in the Rhine Valley 8 km northwest of Freiburg i.Br. The terrain is partly wooded, the villages Gottenheim and Umkirch are in the upper left and lower right corners respectively (2.4.76, 5.25 h, altitude 2000 m).

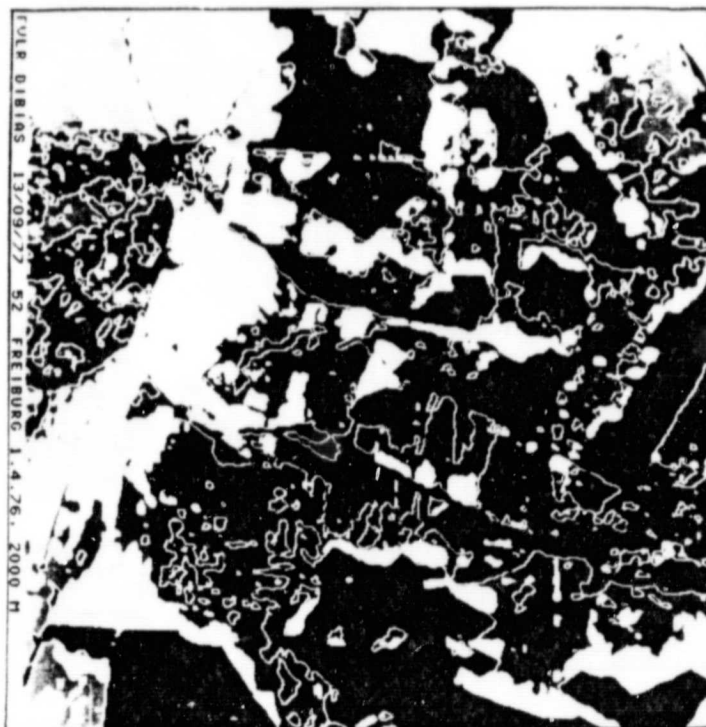


Fig. III.2.50b. Same image as III.2.50a, equidensity representation, 1°C - grey tones ranging from 0° (white) to 5° (black).

ORIGINAL PAGE IS
OF POOR QUALITY



Fig. III.2.51a. Thermal image of the central part of the area represented in Fig. III.2.50a/b (2.4.76, 5.40 h, altitude 1000 m, i.e. not enlarged from Fig. III.2.50).



Fig. III.2.51b. Same image as III.2.51a, equidensity representation, 1°C -grey tones ranging from 1° (white) to 4° (black).

effects, for a correct interpretation ground truth data are essential.

References

1. H. GOSSMANN and W. NÜBLER; "Oberflächentemperatur und Vegetationsverteilung in Freiburg", *Bildmessung und Luftbildwesen*, 45 (1977), 105-113.
2. F.H. HIRT; "Infrarot-Wärmeaufnahmen: Die Darstellung der Grossstadtlandschaft Ruhrgebiet im Wärmebild". In: *Schriftenreihe des SVR*, Nr. 58, Essen 1975, 99-122.
3. K.G. LENHART; "Mögliche Anwendungen von Meteosat für die Fernerkundung". *Bildmessung und Luftbildwesen*, 46 (1978) 113-122.
4. D. LORENZ; "Problems of Airborne Infrared Scanning in Meteorology". *Arch. Met. Geophys. Bioclim.*, B 21 (1973a), 125-146.
5. D. LORENZ; "Die radiometrische Messung der Boden- und Wasseroberflächentemperatur und ihre Anwendung auf dem Gebiet der Meteorologie". *Z. f. Geophysik*, 39 (1973b), 627-701.
6. J.O. MATTSSON; "Mikro- och lokalklimat-indikering medelst infrarödtermografi". *Svensk Geogr. Arsbok*, 43 (1967), 191-211.
7. J.O. MATTSSON; "Microclimatic Conditions in Forest Areas Studied with Infrared Technique". *Oikos*, 21 (1970), 174-184.
8. W. NÜBLER; "Konfiguration und Genese der Wärmeinsel der Stadt Freiburg". *Diss.*, Freiburg, 1977.
9. W. NÜBLER; "Möglichkeiten des Nachweises von Kaltluftsammlgebieten und Kaltluftbewegungen aus Thermalbildern". In: *Berichte zum Symposium Flugzeugmeßprogramm*. Bundesministerium für Forschung und Technologie, Forschungsbericht W 78-04, Bonn 1978, 207-216.
10. < RPU > Lufthygienisch-meteorologische Modelluntersuchung in der Region Untermain. 3. Arbeitsbericht, Frankfurt 1972.
11. P. STOCK; "Interpretation von Thermalbildern der Stadt Dortmund". *Bildmessung und Luftbildwesen*, 43 (1975), 144-151.
12. W. WEISCHET; "Stadtklimatologische Konsequenzen von Line-Scanner-Aufnahmen der Oberflächentemperaturen im Tagesgang". In: *Symposium Erderkundung (DFVLR)*. Porz-Wahn, 1975, 459-467.

ORIGINAL PAGE IS
OF POOR QUALITY

B. Thermal Imagery as a Tool to Delimit Vineyard Sites liable to Cold-Air Damage

W. Endlicher
Geographisches Institut | der Universität
Freiburg, Deutschland

Introduction

The wine-growing legislation in the European Community requires a strict delimitation of the area provided for the growing of quality grapes. All these decisions are taken by a group of experts. In the integral part of their expertise the influence of topoclimatic factors such as inclination and exposition, the absolute height over sea level and the risk of frost damage must be considered. This is the consequence of the fact, that in Central Europe vines grow near their polar frontier. It is not difficult to calculate the input of solar energy on slopes with different orientations and to predict the physiologic reactions of the plant. However, it is still a problem to fix the lowest altitude of vine-growing in a hilly terrain. The limitation factor is the radiation frost in spring and autumn, which makes the cultivation of vines in valley bottoms impossible. Although the quality and quantity of grapes is strongly influenced by lakes of cold air, in most parts of German wine-growing areas there are only estimations of the extension of cold air areas liable to frost damage. Experts in viticulture and agrotopoclimatology are searching for solutions to this problem. Many of them look upon remote sensing techniques as possible tools in this respect.

In doing so, attention must be given to the different scales of the region concerned. In considering regions like the Upper Rhine Valley, the Rhone Valley or the Champagne, the employment of satellite data may be useful in de-

termining the cold air influence in a scale of some 250 - 1000 km². For the scale of some 100 km² and smaller, however, we must still utilize thermal images from air planes.

Methods and Data Used

UF/GI used the same DFP's flight campaign data sets as for wind-induced microclimatic difference detection. Multi-spectral scanner images of the Kaiserstuhl were produced. This little mountainous region in the southern part of the upper Rhine Valley is well known for its famous vineyards.

The examination of the spring campaign showed that it was not possible to determine stagnant cold air from the temperature of the bare soil. Its temperature differs with the pedologic factors such as type, water content, heat capacity of the bedrock etc., its representation in a thermal image is, therefore, determined by a multitude of interrelated factors. On the contrary, from the beginning of July the vine leaves form a rather homogeneous cover which has a much more moderate heat capacity than the bare soil. Therefore, it is possible - if topography and vegetation cover of an area are known - to infer from the temperature of the vegetation - in this case vine and tree leaves - the temperature of stagnant cold air. The following thermal images date back to the calm, clear night of July 16, 1976, in the hours before sunrise. The flight heights were 3600 m and 800 m above ground level. Parallel to the flight campaigns, mobile measurements of the air temperature in 0.7 m and 2 m above the ground level in the test sites were made. The digital image processing consisted of three parts: in the first step, enhanced original thermal images were generated for a qualitative interpretation. In the second step equidensities

of surface temperature at intervals of 1°C were made and covered with pseudo-colours. Thirdly, these equidensities were transferred to a topographic and vegetation map.

Delimitation of Cold Air Influence

Subregional Scale. Entire Kaiserstuhl, ca. 100 km², 180-550 m above sea level

Fig.III.2.52 is an enhanced thermal image of the Kaiserstuhl subregion from 3600 m above ground level. An interpretation of the image shows three zones of different grey tone: A dark one which represents the rather low temperatures of the Upper Rhine Plain, a medium one which comprises the slopes and a light one forming a sort of horseshoe which shows the warm forests of the mountain ridge. In the eastern part of the image 21 valleys may be distinguished with cold surface temperature entering from the plain into the hills having higher temperatures. In the south-western part, the warmer slopes are dominating as the relief is steeper and consequently the cold air originating from these slopes can flow off directly into the plain. The western valleys (3 G, 4 F) which have very low surface temperatures are well known for their increased frost risk. The vine-grower avoids planting vines in these valley bottoms. The high surface temperatures of the central part may be explained by the different energy balance of a forest. The cooling of the tree leaves - some 10 m above ground level and 200 m above the plain - is reduced by the screening of tree tops against the sky and by the energy of the relatively warm air above the boundary layer inversion.

Fig.III.2.53 shows a map of the Kaiserstuhl with isanomales of the surface temperature. The 0°C -line represents the medium surface temperature of the plain. The map shows the very

sharp delimitation of the Kaiserstuhl, really a warm island in the middle of the cold plain. The vine slopes are $2-3^{\circ}\text{C}$ warmer than the plain, the mountain ridge more than 3°C , in most parts more than 4°C .

Local Scale. The Vineyards of a Single Kaiserstuhl Village, ca. 1 km²

To delimit cold air influence in the scale of single hills and slopes, it is necessary to digitally enlarge a part of Fig.III.2.52 in Fig.III.2.54 can now see some more details which are important for the appraisal of cold air influence. Very striking are the low surface temperatures in the Schambach Valley (3/4 F/I), although there are numerous fruit trees. The forest situated on the top of the mountain ridge and the buildings and streets of the village have the highest surface temperatures. The isanomales of the surface temperature in Fig.III.2.55 permit a very detailed delimitation of the areas influenced by the cold air. It was possible to show by mobile measurements of air temperature in 10 clear nights, that the limits of relatively cold surface temperatures and air temperatures correspond very well in the valley bottoms as well as on the lower parts of slopes. It would, therefore, not be very reasonable to transform the fruit trees and vegetable fields in the Kaiserstuhl valleys nor the greenland and corn fields of the Upper Rhine Plain into vineyards as there is evidence of nightly cold air layers in these parts.

Stagnant Cold Air on a Single Vine Terrace, ca. 0.01 km²

The detection of surface temperature in a scale of acres or hectares is only possible if the height of the flight is reduced to 1000 - 2000 m above ground level. Fig.III.2.56 shows the equidensities of surface temperature of a single vine terrace (2.4 ha) taken from

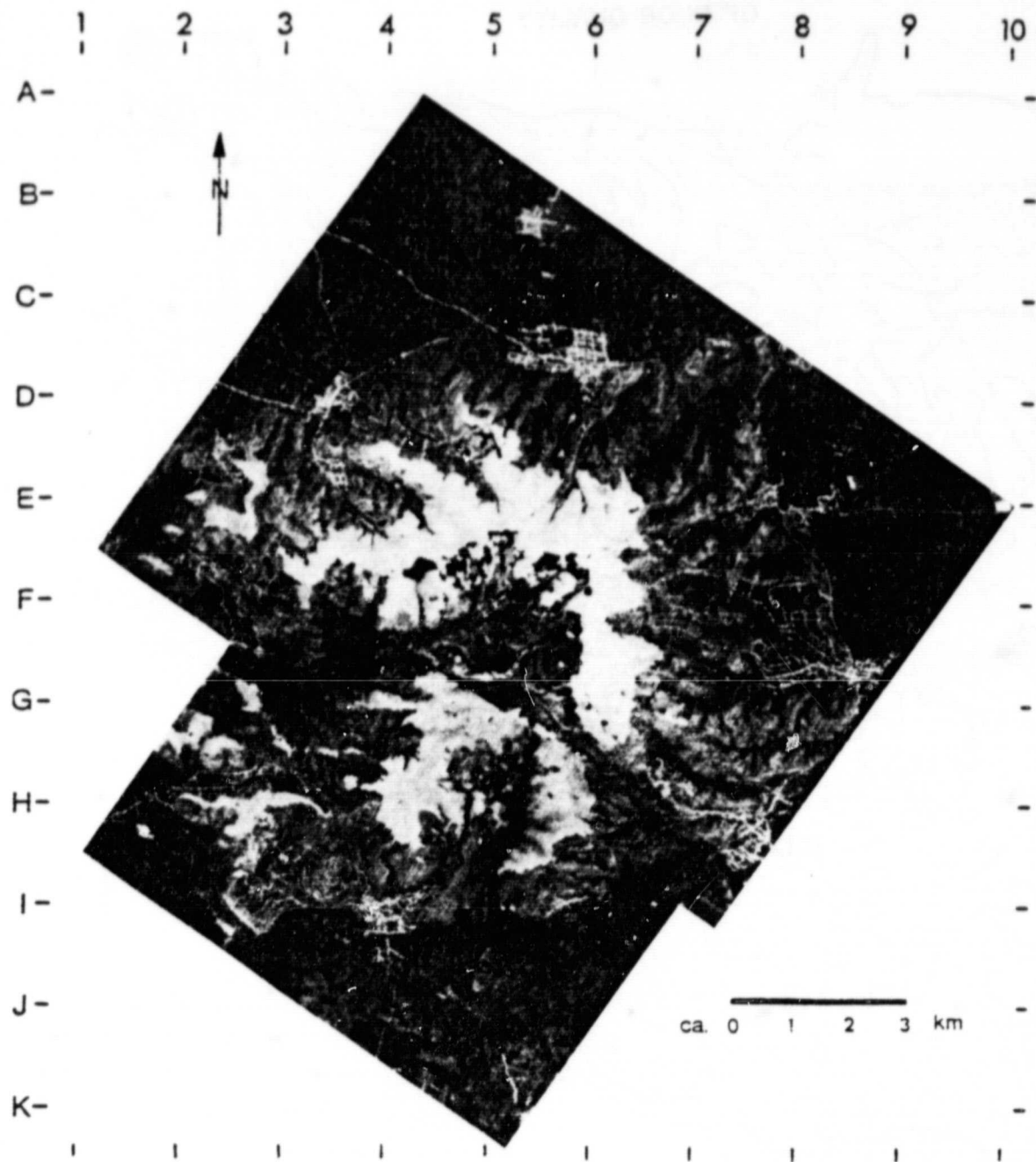


Fig. III.2.52. Enhanced thermal images of the entire Kaiserstuhl from 3600 m over ground; 16.7.76, 2.21-2.27 and 3.34-3.36 CET; light: relatively high surface temperature, dark: relatively low surface temperature.

ORIGINAL PAGE IS
OF POOR QUALITY

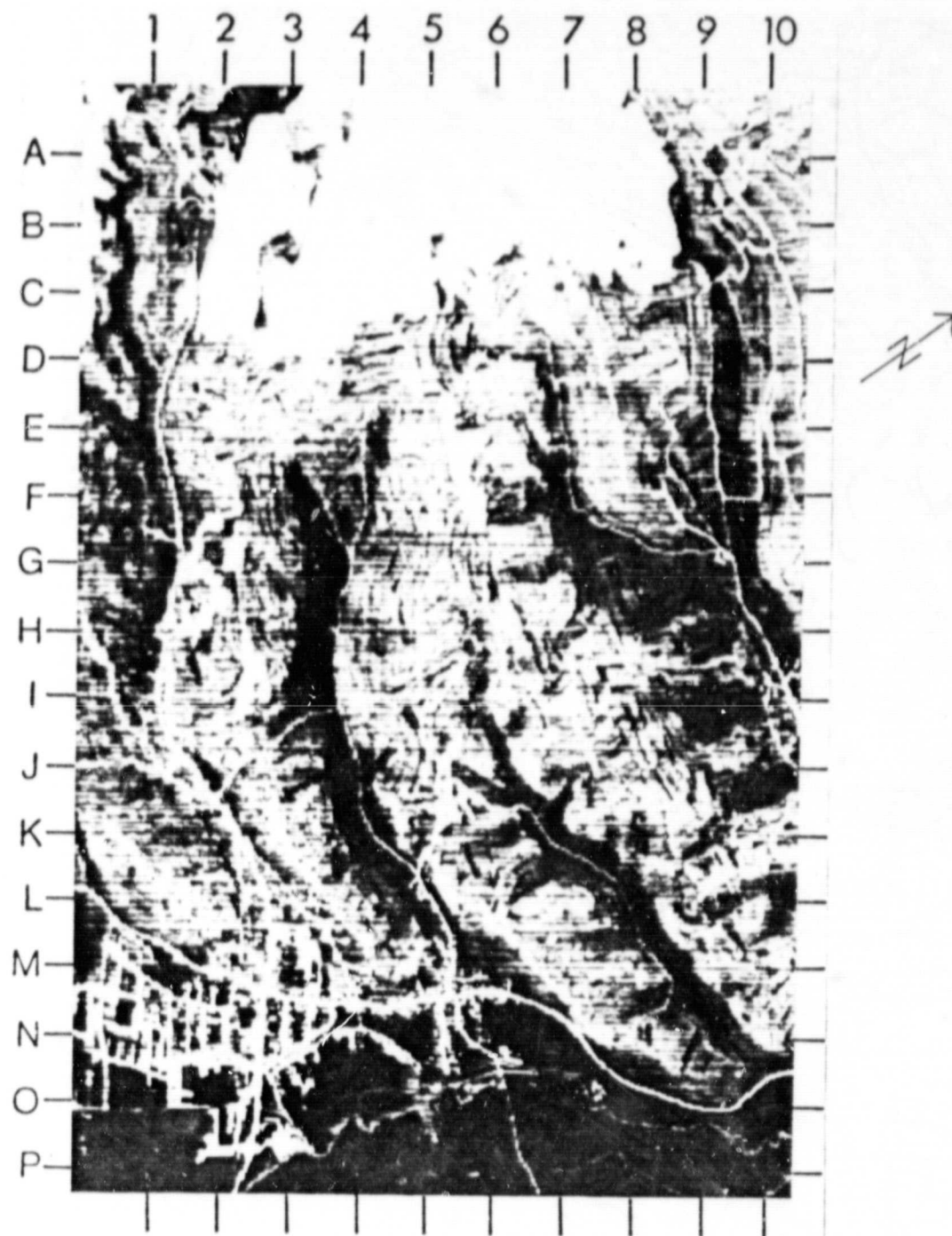


Fig. III.2.54. Enhanced thermal image of the Eastern Kaiserstuhl from 3600 m over ground; 16.7.76, 2.21-2.27 CET; light: relatively high surface temperature, dark: relatively low surface temperature.

ORIGINAL PAGE IS
OF POOR QUALITY



Fig. III.2.55. Topography and vegetation cover of the Eastern Kaiserstuhl with isotherms of surface temperature (after equidensities from the thermal image, Fig. III.2.54); 0°C - isoline: mean surface temperature of the Upper Rhine Plain: ca. 12°C (without correction of atmospheric influences).

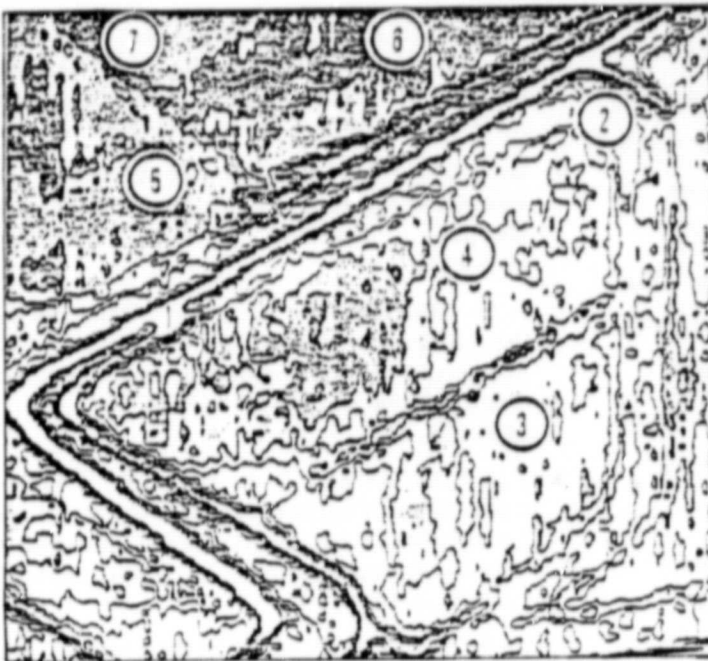


Fig. III.2.56. Thermal image (equidensities) of a large terrace; 16.7.76, 4.14 CET, 750 m over ground. Equidensities:

- 1) $> 18.0^{\circ}\text{C}$ blacktop roads
- 2) $15.5-16.0^{\circ}\text{C}$ terrace slope
- 3) $15.0-15.5^{\circ}\text{C}$: exterior part of the large terrace, small terrace eastward
- 4) $14.5-15.0^{\circ}\text{C}$: interior part of the large terrace
- 5) $14.0-14.5^{\circ}\text{C}$: terrace
- 6) $13.5-14.0^{\circ}\text{C}$: Balschental-Valley
- 7) $13.0-13.5^{\circ}\text{C}$.

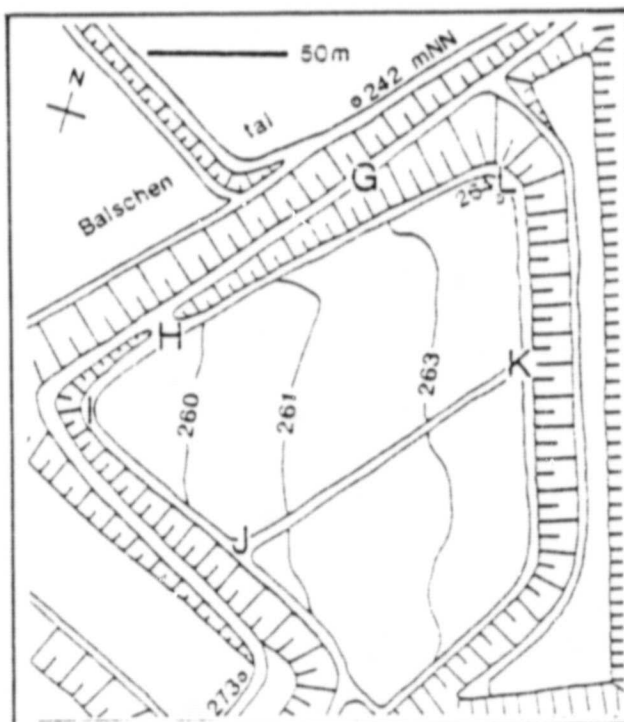


Fig. III.2.57. Topography of a typical large terrace (GT)

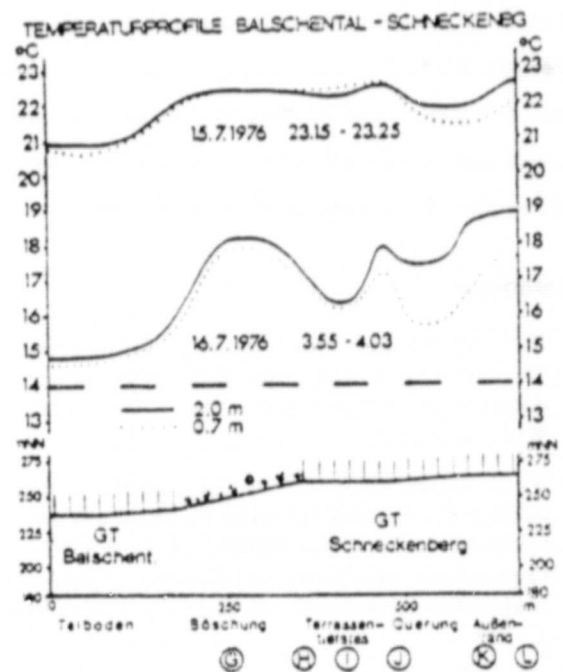


Fig. III.2.58. Air temperature profiles over large terraces (GT) recorded simultaneously with the airborne measurements of surface temperature.

750 m above ground level. The newly formed large terraces are inclined against the slope, as it is shown on the topographic draft (Fig.III.2.57). The surface temperatures on Fig.III.2.56 as well as the air temperatures on Fig.III.2.58 show that the terrace forms a "cold air trap". At the inner part of the terrace, the temperatures are nearly as low as at the valley bottom. The influence of cold air in all calm, clear nights of the year and the frost risk in spring and autumn is enlarged. This is an example which indicates that the remodelling of agricultural landscapes, with the formation of new terraces, initiated to facilitate economic procedures in agriculture, is not compatible with the demands of agrotopoclimatology.

Conclusions

Digital processed thermal imagery seems to be a very suitable tool to delimit frost prone areas. However, the contours of the terrain and nature and height of its vegetation cover should be known in order to avoid incorrect interpretations. Proceeding on this assumption, the precision of this investigative method surpasses by far all other conventional techniques for the mapping of frost hollows.

References

1. N. J. BECKER; "Ökologische Kriterien für die Abgrenzung des Rebgeländes in den nördlichen Weinbaugebieten". Die Wein-Wissenschaft, 32 (1977), 77-102.
2. W. ENDLICHER; "Zum Temperaturverhalten auf Großterrassen in Strahlungsnächten anhand von Meßfahrten, Frostkartierung und Thermalbildern". Die Wein-Wissenschaft, 32 (1977), 174-188 u. 309.
3. W. ENDLICHER; "Geländeklimatologische Untersuchungen im Weinbaugebiet des Keiserstuhls". Diss. Geowiss. Fak. Universität Freiburg (1978), 309 p.
4. R. GEIGER; "The Climate near the Ground", Harvard University Press, Cambridge, Mass. (1965), 611 p.
5. H. GOSSMANN; "Radiometrische Oberflächentemperaturmessung und Thermalbild als Hilfsmittel der Umweltforschung". Beihefte Geogr. Rdsch. 7 (1977), 101-112.
6. D. LORENZ; "Problems of Airborne Infrared Scanning in Meteorology", Archiv Met. Geophys., Bioklim., Ser. B 21 (1973), 125-146.
7. J. O. MATTSSON; "Thermal Patterns in the Landscape Recorded with Infrared Technique and Simulated in Model Experiments". Geografiska Annaler, Ser. A 51 (1969), 219-238.
8. P. R. NIXON and T. A. HALES; "Observing Cold-Night Temperatures of Agricultural Landscapes with an Airplane-Mounted Radiation Thermometer", J. Appl. Meteorol., 14 (1975), 498-505.
9. R. B. STEWARD, E. I. MUKAMMAL and J. WIEBE; "The Use of Thermal Imagery in Defining Frost Prone Areas in the Niagara Fruit Belt", Remote Sensing of Environment, 7 (1978), p.187-202.

ORIGINAL PAGE IS
OF POOR QUALITY

5. Geographic Measurements on METEOSAT-1 and HCMM Imagery Recorded over Northern Africa

R. Gombeer
Laboratorium voor Bodemgenese en Bodemgeographie,
Katholieke Universiteit Leuven, België

Introduction

In this study an experiment has been made to correlate area measurements obtained from HCMM with those obtained through a Meteosat image analysis of the same areas.

The Meteosat satellite is stationed in a geostationary orbit at nearly 36,000 km above the Equator and the Greenwich meridian (0 degrees N, 0 degrees E). Radiance data from the full Earth disk are acquired every 30 min. by a three-channel radiometer. It operates in the visible region of the electromagnetic spectrum (0.4-1.1 μm), in the infrared region (10.5-12.5 μm) and in the water vapour emission band (5.7-7.1 μm). The spatial resolution in the visible band is 2.5 km at the sub-satellite point, and 5 km in the other bands. The unique orbital position (synoptic overview) of the Meteosat spacecraft and the high repetition rate (half hourly) of its imaging radiometer are particularly useful for studies of large-scale features and for analysis of short-lived phenomena. The high image repetitivity also ensures the recording of radiance data, at random visibility, over areas which are cloud-covered most of the time.

The objective of this study was to examine whether measurements on small-scale synoptic imagery could assist in the monitoring of transitory phenomena on the ground like flooding, grass fires, etc. The zone selected for this experiment is in North Africa (Tunisia).

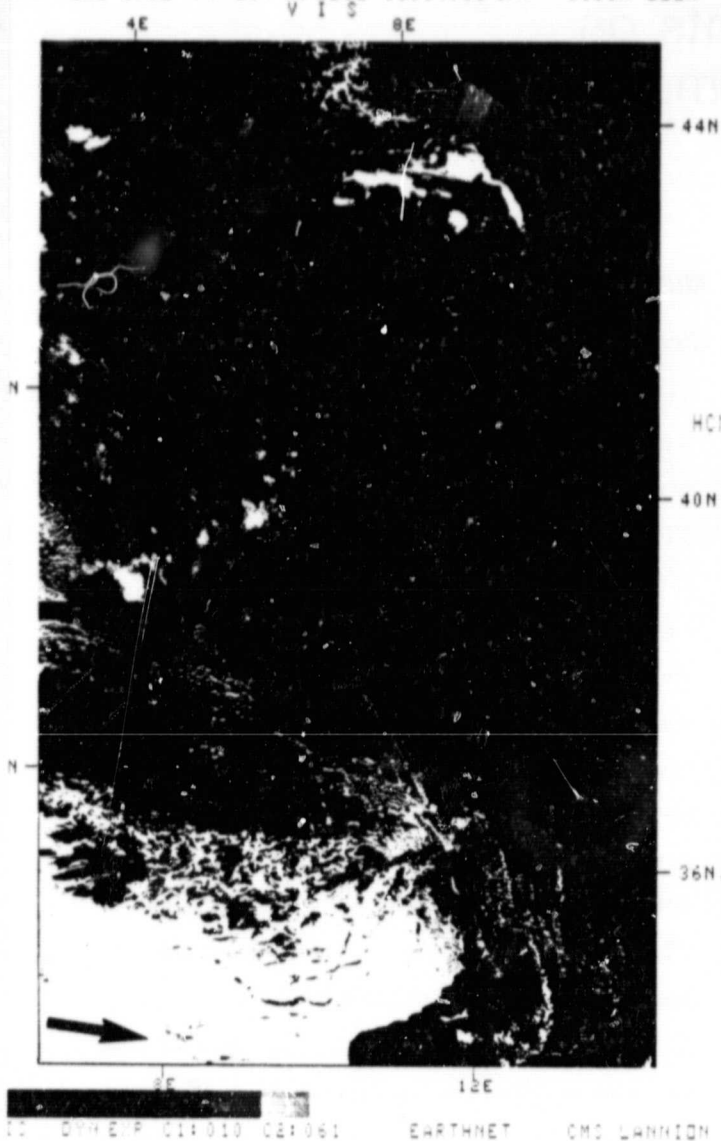
Method

Quantimet 720 Image Analyser

The electronic image analysis was performed with basic Quantimet 720 equipment (Cambridge Instruments), comprising an epidiascope, a Vidicon camera with aspherical Canon lens (FS 55 mm, $f/1.2\text{SSC}$), a display and system control unit with shade corrector, Standard Detector, Densitometer, Image Editor and Variable Frame and Scale Module. The electronic light pen (Image Editor) and the Variable Frame and Scale Module are both interactively connected with each individual image detector (Standard Detector/Densitometer). The epidiascope projects a specimen image onto the face of a vidicon tube. The image so formed is scanned by a 720-line vidicon scanner and is digitized spatially into a standard matrix of 500,000 picture points with a variable live-frame (Variable Frame and Scale Module) represented on the display. The output of the scanner is passed to a detector (Standard Detector or Densitometer) that selects features for measurement in terms of their common grey-level characteristics. The signal of a detector can be amended by direct manual interaction on the display with the aid of a light pen (Image Editor Module). Each performed operation is displayed on the screen, showing detected features, the measurement being made on them and the digital results (Gombeer and D'Hoore, 1979).

ORIGINAL PAGE IS
OF POOR QUALITY

CHR DRB 8712 79 339 05 DECE 11.34.55 GMT QUICK LOOK



HCHR DRB 8727 79 340 06 DECE 11.52.52 GMT QUICK LOOK

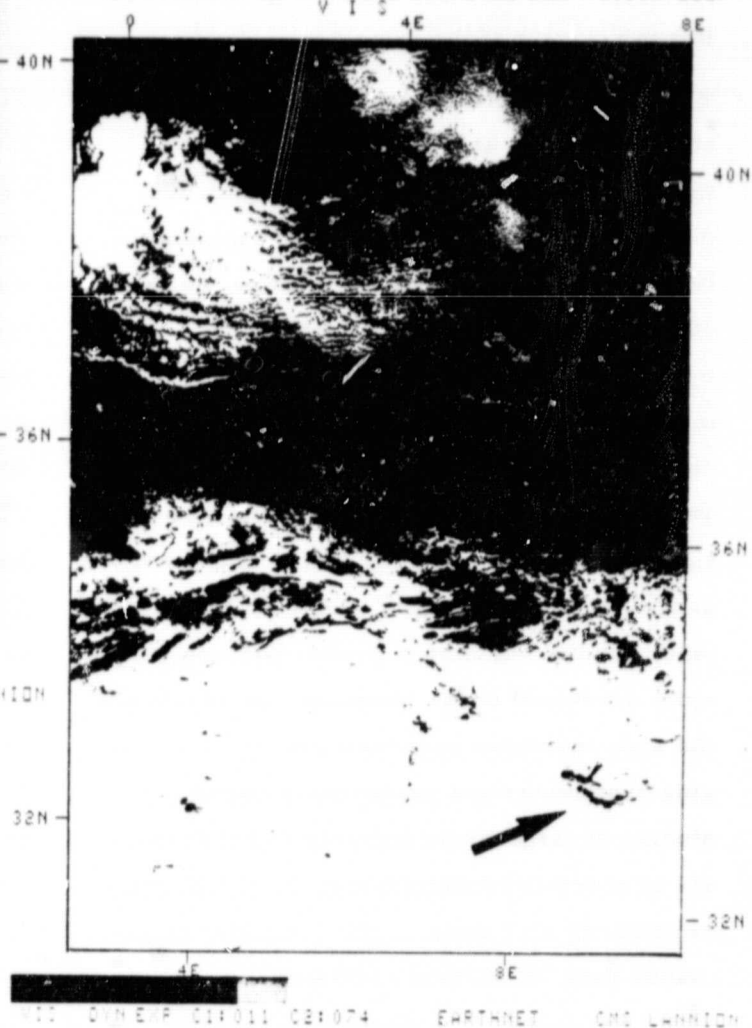


Fig.III.2.59. HCMM recordings (VIS) over Chott El Djerid (Dec. 5 and 6, 1979)

ORIGINAL PAGE IS
OF POOR QUALITY

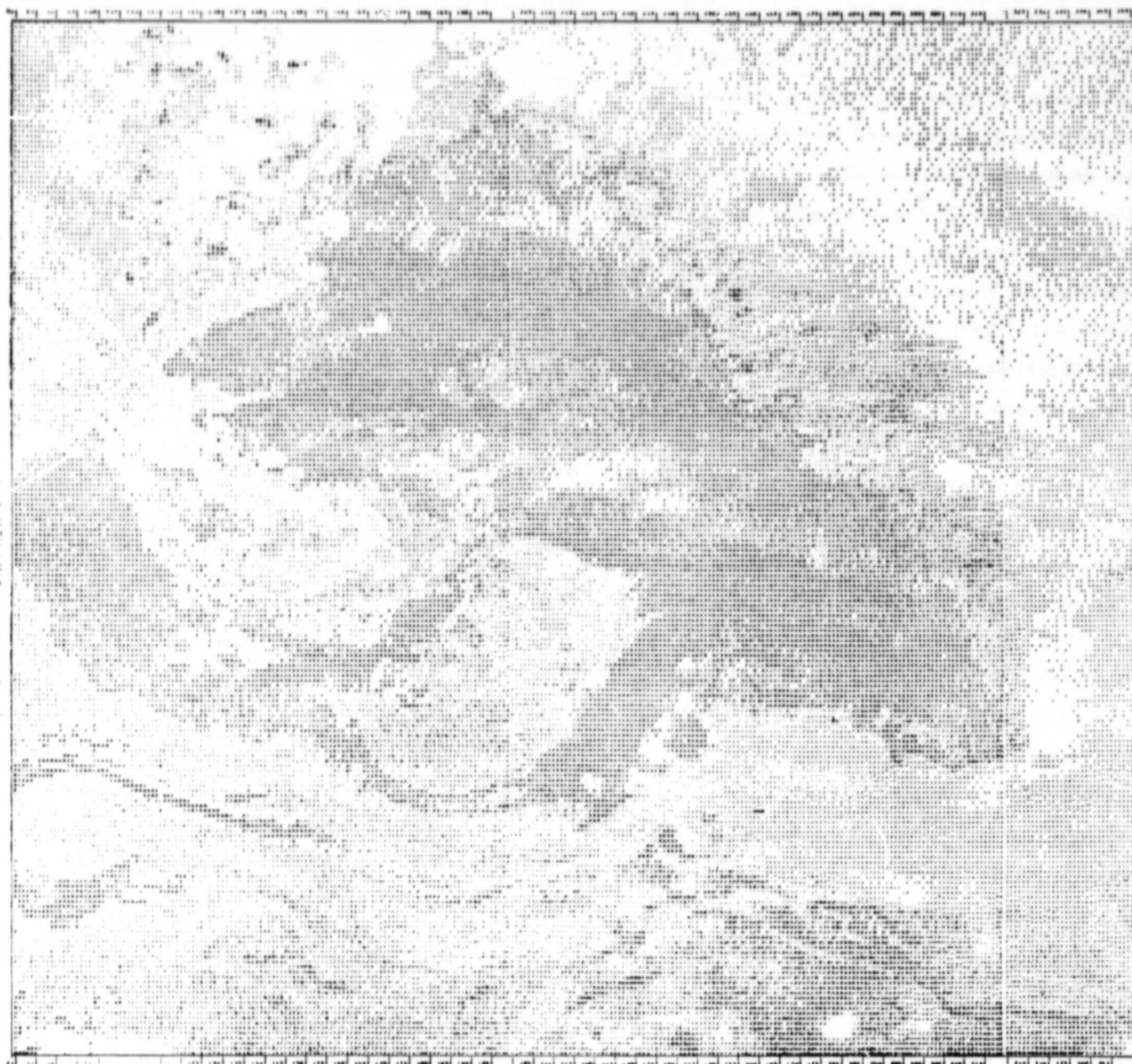


Fig.III.2.60. Collage of visualization printouts of the HCMM VIS band. Chott El Djerid (Tunisia), Dec. 1979.

Procedure

The limit of each soil unit to be measured was drawn from the FAO-map (1:5,000,000, 1973) on transparent paper on which areas were circumscribed and measured with the electronic pen on the video display after calibration of the instrument. Meteosat images used for analysis were good quality paper prints of recordings all from the visible wavelength channel (0.4-1.1 μm) at different dates (Table III.2.11). The HCMM satellite imagery used were transparencies from the visible band (0.55-1.1 μm) of the Heat Capacity Mapping Radiometer. Areas were measured directly on these images, represented on the display, with the aid of the light pen (Image Editor). Patches that appeared as homogeneous in grey value on the image or homogeneous pattern of such patches were manually delineated. Such patches were previously identified by optical comparison of the imagery with soil and other maps. The scale of the imagery was calculated by comparing distances between two reference points (easy to locate on coastlines) both on the image and on the soil map (1:5,000,000 approx.).

Results

Chott Djerid areas (Tunisia) can be easily depicted on Meteosat-imagery (visible channel) through their dark spectral signature (Gombeer, 1980). These halomorphic soils (solonchaks) (Table III.2.10) are generally fine-textured, have hydromorphic properties and they may be occasionally flooded. Both features (flooding and hydromorphy) generally facilitate detection of such areas in the visible wavelength band. Areas measured are indicated in Table III.2.11, from which it can also be seen that the areal extent of the flooding varies at different recording dates. In this respect the large

Melrhir and Rharsa Chott areas seem to be only partially flooded (on 13 Sept., 1979) and they were measured separately (two small patches) on the imagery. At the same recording date the deduced Djerid area closely corresponds to the mapped soil unit (4.717 km^2). The flooded total area of Chott Djerid was also measured on imagery obtained from another satellite: the Heat Capacity Mapping Mission. The HCMM is a polar orbiting sun-synchronous satellite with a higher geometric resolution (500 m) than Meteosat (2.5 km). Measurements were performed on two quick-look images corresponding to two adjacent orbit strips (films) with a slight overlap (5 and 6th December 1979) (Fig. III.2.59). Individual areas (two parts) measured on each film strip were summed up. The scale of both quick-look images was calculated as described before:

- a) recording on 5-12-79: 1 : 8,033,707 (appr.)
- b) " " 6-12-79: 1 : 8,105,263 (")

The Chott Djerid areal extent measures:

- a) Djerid, part 1, on 5-12-79: 399.85 km^2
- b) Djerid, " 2, " 6-12-79: 4403.51 "
- c) Djerid, total area : 4803.36 "

This area fairly corresponds with that measured on the Meteosat recording of Sept. 13 1979 (Table III.2.11) and also with that of the mapped Djerid soil unit (FAO).

For comparison purposes it was also attempted to calculate the areal extent of Chott Djerid from HCMM digital data (Fig. III.2.60). Data from the visible band (6th December 1979) were visualized with the NMAPW-programme. Pixels (500 x 500 m) classified as flooded areas were counted and in this way a total area of 4884 km^2 could be deduced (cfr. Table III.2.11).

The areal extent of salt pans (Etosha, Makarikari, Salinas (Mauret), as deduced from

ORIGINAL PAGE IS
OF POOR QUALITY

TABLE III.2.10. Soil units and soil associations (FAO, 1973)
over the areas studied (Africa).

Area	Soil Units
(1) <u>Chott Djerid</u> Tunisia	Z ₁₆ - 3a (with sodic phase) (Solonchaks orthic) Associations: Z ₁ and Z ₂ (Solonchaks _g gleyic ^c and takyric)
(2) <u>Chott Melrhir</u> Algeria	Z ₁₇ -3a (Solonchaks orthic) Associations: Z _g (Solonchaks gleyic)
(3) <u>Salinas</u> Mauretania	Salt flats
(4) <u>Etoha pan</u> S.W-Africa	Z ₁₂ - 1/2 a (Solonchaks gleyic) Associations: Z ₁ (Solonchaks orthic) Inclusions: Q _a (Arenosols albic)
(5) <u>Makarikari</u> Botswana	Z ₁₇ - 1/2a (Solonchaks orthic) Associations: J _e (Fluvisols eutric) Z ₁ ^c (Solonchaks takyric) Inclusions: Q (Arenosols), S (Solo- netz)
(6) <u>Okavango</u> Botswana	J _e 59-1a (Fluvisols eutric) Associations: Z (Solonchaks), Q (Arenosols) Inclusions: G (Gleysols)

Textural classes: 1 Coarse textured (sands)
2 medium textured (loam, silts)
3 fine textured (clays)
Slope classes : a level to gently undulating
b rolling to hilly
c steeply dissected, mountainous

TABLE III.2.11. Area measurements on METEOSAT-imagery and comparison with measurements on the FAO soil map of Africa.

Soil units and features measured	Area measurements with QUANTINET 720 (in km ²)		Image Recording Date	Original image scale (approx)	Remarks
	FAO soil map (\pm 1/5,000,000)	METEOSAT imagery (vis-channel)			
1. <u>Chott Djerid</u> TUNISIA	4717.34 id. id.	4271.60 4387.88 4882.85	14/4/78 2/9/78 13/9/79	1/15,287,000 1/15,385,000 1/8,276,000	flooded area flooded area flooded area
2. <u>Chott Melrhir (Rharea)</u> ALGERIA	3400.94	2162.72	13/9/79	1/8,276,000	two flooded areas measured separately
3. <u>Salinas (salt flats)</u> MAURETANIA	3543.15	3028.08	30/3/78	1/17,250,000	highly reflective (whitish) area
4. <u>Etosha pan</u> S.W. AFRICA	5386.44 id.	5582.74 5764.00	21/8/78 13/9/79	1/17,544,000 1/8,772,000	highly reflective (whitish) area
5. <u>Makarikari pan</u> BOTSWANA	10949.55 id.	11190.86 11270.62	21/8/78 13/9/79	1/17,544,000 1/8,772,000	highly reflective (whitish) area
6. <u>Okavango Swamp</u> BOTSWANA	27709.40 id.	14982.78 14523.29	21/8/78 13/9/79	1/17,544,000 1/8,772,000	area mixed with burnt patches no burnt areas present
7. <u>Burnt patches</u> S.W. of Okavango S. of Okavango	- -	6311.40 8613.38	21/8/78 21/8/78	1/17,544,000 1/17,544,000	dark-gray to black features (oriented)

TABLE III.2.12. The annual precipitation (approximately) and its broad distribution over the African areas studied (Jackson, 1961).

Area	Annual precipitation
(1) <u>Chott Djerid</u> (Tunisia)	150 mm (approx.) Well distributed from September - March
(2) <u>Chott Melrhir</u> (Algeria)	113 mm (approx.) Distributed from March - April and from September - December
(3) <u>Salinas</u> Mauretania	100 mm (approx.) From August - September
(4) <u>Etosha</u> (S-W Africa)	517 mm (approx.) Dry season from May - October
(5) <u>Makarikari</u> Okavango (Botswana)	433 mm (approx.) Dry season from May - October

ORIGINAL PAGE IS
OF POOR QUALITY

Meteosat-imagery, does correspond with units mapped on the FAO-soil map. Salt pans are generally detected through their very white appearance (high reflectance) on the visible band recordings.

Large burnt patches were observed on a Meteosat image recorded on 21 August 1978 over the southern part of Africa. These patches were located in a Botswana area described by Eyre (1968) as thorn-tree tall-grass savannah.

A majority of the savannahs are located in climates with pronounced wet and dry seasons. They also prevail in tropical areas of impermeable soil and poor drainage and where man periodically burns off the vegetative cover to expand the grassland area. In many regions the savannah vegetation pattern is considered to be the result of drainage and soil condition but also of human intervention (frequent fires, grazing) (Eyre, 1968). Generally, bush fires are started purposely to clear away the old dry grass in order to stimulate growth of young grass in the following season. However, fires may also be started for hunting purposes or can start accidentally. Because of their uncontrolled progress and the complete destruction of all plant material, fires have been subject to many studies. Moreover, the intensity of a fire and its destructive power will depend on the dry season time (drought, available material to burn). Annual late season fires generally have a large effect on the vegetation pattern as most of the trees are eliminated and a grass cover will expand now over the area. Frequent late season bush fires are also indicated to be detrimental to soil fertility (litter destruction, nitrogen loss etc.) (Jones and Wild, 1975).

The areal extent of two large burnt areas,

located near the Okavango swamp (Botswana), was measured (Table III.2.11). They were both noticed on a Meteosat recording during the mid-dry season (Table III.2.12) when the vegetation is progressively becoming dry over this savannah area. For the total burnt surface, an area of approx. $15,000 \text{ km}^2$ was found and it should also be mentioned that in the same Okavango area no burnt patches were present on another recording from a corresponding period in 1979 (13/9/79, end of dry season). It is clear that the synoptic (continental) overview and especially the high repetition of the Meteosat observations can be used to detect such fire, to deduce when and where it might have started and to monitor its daily progress. The optical analysis of the single image studied, already indicates that at the date of 21.8.1978, the burning front apparently moved in the NE-direction. This may be deduced from its black elongated, sharp boundaries almost perpendicular to the NE-direction.

Conclusions

The quantitative analysis (Image Analyser Quantimet 720) of Meteosat imagery indicates that flooded areas can be properly measured as well as the areal extent of grass and bush fires. Obviously, small scale satellite imagery with high repetitivity (half hourly), as acquired from the geostationary Meteosat, can be used to quickly demarcate such areas and to monitor their extensions (regressions) and their effects.

However, errors in the area determination using imagery may arise from the:

- original scale (enlarged or small) and quality of the imagery used for quantitative analysis,
- geometric deformation (Earth curvature or

oblique view) of the imagery as it is recorded over the entire African continent (geostationary orbit),

ORIGINAL PAGE IS
OF POOR QUALITY

- calculation of the exact scale factor of the imagery and of the FAO-soil map (map projection used),
- optical distinction of image grey-tones and manual delimitation of boundaries with the Quantimet light pen on the video display,
- spectral discrimination of features and boundaries to be measured and as registered by the visible wavelength channel (Meteosat and HCMM).

Areas deduced from HCMM imagery and from digital data do correspond with those measured on Meteosat images, although the Meteosat satellite has a lower geometric resolution (2.5 km).

References

1. Cambridge Instruments: Quantimet 720 Instruction Manual and Technical Data Sheets, Royston, U.K.
2. S. R. EYRE; "Vegetation and Soils. A World Picture". E. Arnold, London (1968).
3. FAO/UNESCO; "Soil Map of the World - Scale 1 : 5,000,000". Sheets VI(1), VI(3) (1973).
4. R. GOMBEER and J. D HOORE; "Quantimet 720 Aided Analysis of Remote Sensing Imagery and of Related Ground Truth Documents". Microscopica Acta, Suppl. 3, 121-126 (1979).
5. R. GOMBEER; "Soil and Land-Use Distribution as Discernible on Meteosat-1 Imagery over W-Africa". Pedologie, 30, 1, 127-136 (1980).
6. S. P. JACKSON; "Climatological Atlas of Africa". CCTA/CS Joint Project 1, Lagos (1961).
7. M. J. JONES and A. WILD; "Soils of the West African Savannah", Techn. Comm. No. 55, Commonwealth Bureau of Soils, Harpenden, U.K. (1975).
8. J. MORGAN; "Introduction to the Meteosat System". Meteosat Data Management Dept. (ESOC), Darmstadt (1978).

Part 3 - Anthropogenic Heat Release

H. Gossmann
Geographisches Institut der Universität
Freiburg, Deutschland

R. Gombear
Laboratorium voor Bodemgenese en Bodemgeografie,
Katholieke te Leuven, België

ORIGINAL PAGE IS
OF POOR QUALITY

Surface Temperature Distribution for the City of Freiburg

The long delay in the distribution of HCMM data and the high percentage of cloud cover of the images of the middle European test site received, have seriously delayed work on this subject.

In the preparatory phase, work was carried out in Germany on wind-induced micro-climatic differences detected from thermal scanner data. The study treated a mixed urban-rural area. Details are given in Chapt. 4, A.

A first evaluation of the usefulness of HCMM thermal data for defining the surface temperature of built-up areas was carried out on scene AA0034.0213.0.3 (May 30, 1978) for the city of Freiburg (48°N , $9^{\circ}50'\text{E}$).

After geometric correction of the data on a scale 1 : 200,000 and smoothing of the pixel edges, the resulting image was compared with surface temperatures measured with an airborne thermal scanner from a height of 4000 m. The results are presented in Figs. III.3.1 and 2.

Though the dates of the aircraft and satellite scene are different and also due to the fact that uncertainties in the calibration of the HCMR made it impossible to compare absolute temperatures, the temperature pattern on the two scenes is rather similar.

Urban Agglomerations and Cold Air Accumulations and Stream in Germany

The data base for this investigation was provided by a segment of the same HCMM scene AA0034.0213.0.3 of May 30, 1978. It encompasses the Upper Rhine Valley between Basel ($47^{\circ}33'\text{N}$, $7^{\circ}36'\text{E}$) and Frankfurt ($50^{\circ}7'\text{N}$, $8^{\circ}36'\text{E}$) and the surrounding highlands.

Surface Temperatures of Settlements

It was to be expected that heat islands from large cities would be depicted in the HCMM image because of their high surface temperature. However, it became evident that much smaller settlements can evoke a signal, under favourable circumstances, down to a size of 2,000 inhabitants.

Prerequisites for this phenomenon are a densely built-up village centre and placement in a horizontal, unforested environment. Otherwise, the weak signal emitted by the settlement would be masked by other effects on the thermal pattern. The thermal effect of such small villages situated in concave terrain is especially cancelled out by the influence of the relief.

However, not all of the villages with the above mentioned favourable conditions are represented by a warm spot on the HCMM image, as

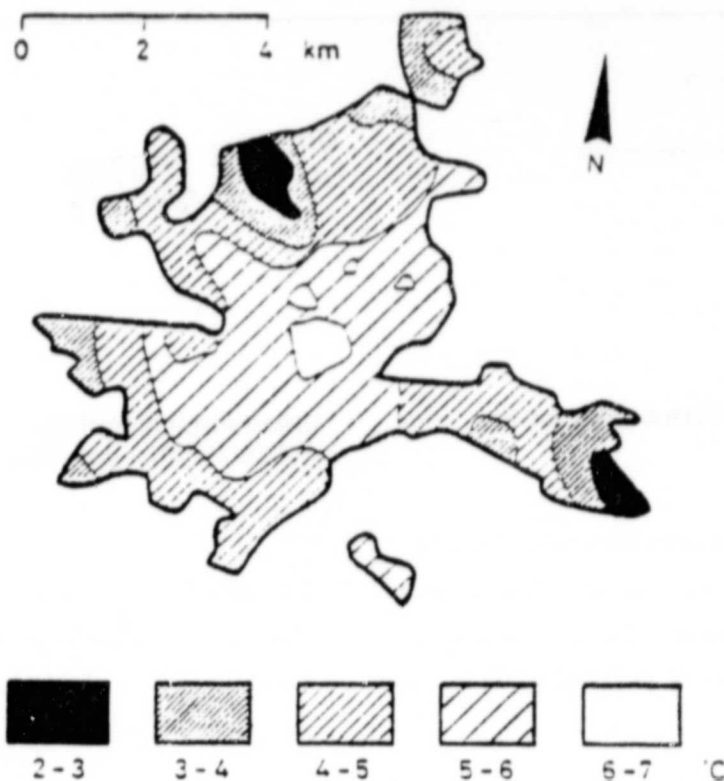


Fig. III.3.1. Surface-temperature distribution within the city of Freiburg on 5.30.79, 2:13 GMT (preliminary calibration), as revealed by the HCMM thermal-image following "fine" rectification and "smoothing" of the pixel edges.

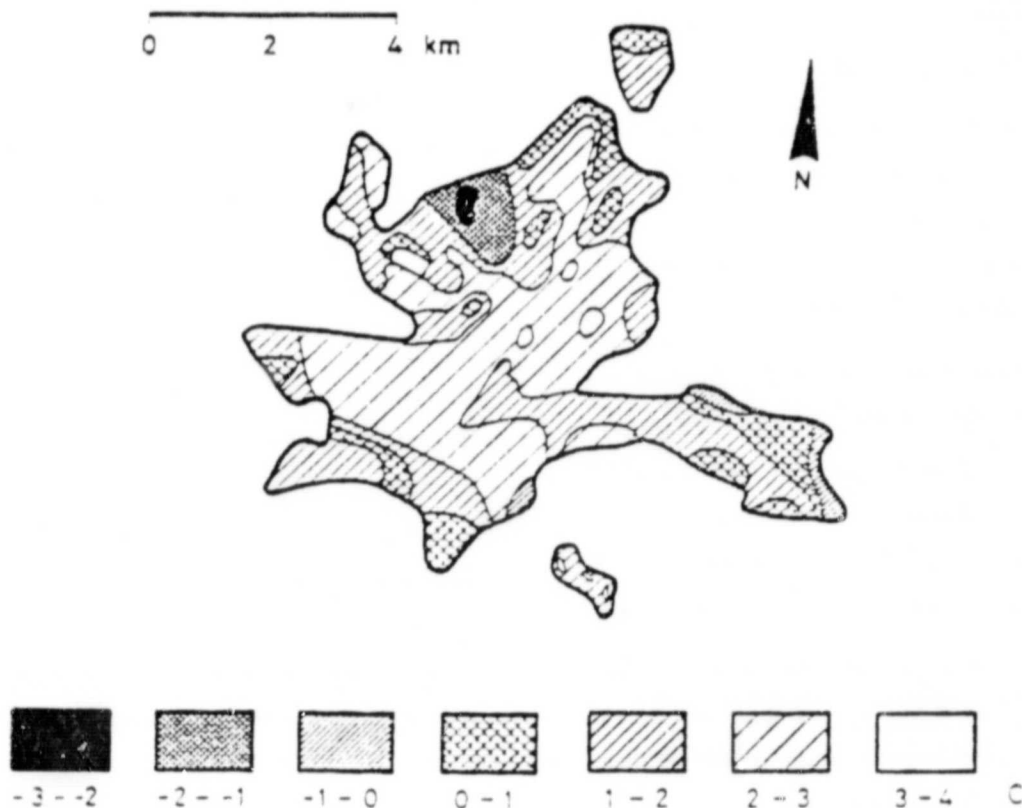


Fig. III.3.2. Surface-temperature distribution within Freiburg, taken from an aircraft scanner thermal image from 4.1.76, 3:40 GMT, 4000 m height above ground, resolution of the original pixels: 10 m.

the recorded phenomena are very small with reference to the means provided by geometric as well as radiometric resolution. The effect is of the same magnitude as the random noises produced by VHRR. Thus, it is possible that the heat island of a village can be simulated or suppressed in each individual case. At the same time, the identification of a village depends on whether its area is depicted in a single pixel or whether it is distributed on several picture elements. A signal on the thermal image can be expected only in the first case.

The situation is less equivocal when we consider larger villages and smaller towns with an average size of approx. 10,000 inhabitants. These are clearly identified as heat islands by reason of their elevated surface temperature. The core area of every larger city with tens of thousands of inhabitants is registered as a heat island with temperatures a few degrees higher than its surroundings.

The difference in temperature between the centres of cities such as Mannheim/Ludwigshafen (cf. Fig. III.3.3) and Strasbourg (cf. Fig. III.3.4) and their environments increases to over 4°C . The area of higher surface temperature extends beyond the urban built-up area to the surroundings because of the flow of warm air in the boundary layer. The suburban area is much warmer on the leeward than on the windward side of the cities.

Industrial Complexes

On comparing different industrial areas, it becomes apparent that different levels of energy consumption are identified on the thermal image even though it is impossible to quantify the respective heat emission of an automobile plant and a chemical factory from the difference in the temperature reading. It is difficult

to interpret these readings definitively because the thermal image by itself cannot be used to establish decisively whether the high temperatures of chemical plants registered by the HCMM are really higher surface temperatures or whether they must be attributed to the masking effect of warmer exhaust gases containing aerosols.

Cold Air Reservoirs and Cold Air Streams

With reference to the problem of cold air accumulation in concave areas and its outflow from valleys, the following statements can be made:

1. The fact that broad and shallow valley expanses are generally depicted as cold areas independent of their surface coverage, supports the theory that the thermal image can identify areas in which cold air collects and either comes to rest or flows onward very slowly down the valley. By contrast, in narrow valley areas, those sections where cold air escapes quickly, are registered as warm areas. Furthermore, in contrast to cold air reservoirs, the areas in front of the mouths of valleys were nowhere registered as particularly cold areas. This signifies that basins accumulating cold air are depicted by the satellite thermal image, but that the route taken by the cold air and the extension of cold air at the mouth of a valley is ignored.
2. It is generally agreed that elevated grassland is the main producer of cold air and that it is a prerequisite for the night-time streams of cold air at the mouths of valleys as grassland gets colder than adjoining forests. Our examples show, however, that extensively or completely forested areas can also create cold air accumulation. Basically, this was to be expected. From



Fig. III.3.3. Mannheim/Ludwigshafen (80,000 Inh.)



Fig. III.3.4. Strassburg/Kehl (Aggl. 355,000 Inh.)

the point of view of the heat budget, elevated forest areas with their higher surface temperatures must surely radiate more energy and thus the net radiation is even more negative than over grasslands. Therefore, forests have to withdraw a larger quantity of energy from the air via the sensible heat flux and so contribute substantially to the cooling of the air. Forests do not produce air that is as cold as that of grassland in corresponding locations but they produce it in greater quantities.

Urban Heat Islands and Thermal Effluents in Belgium

The City of Brussels

The urban heat island of Brussels can be typically depicted by a Night-IR (16 Sept., 1979) temperature slicing (EXIO-programme) in which a gradual decrease in temperature is noticed from the inner city towards its boundary (Fig.III.3.5). The temperature difference between the warmest part of the city (class 1) and the surrounding countryside (class 7) is of the order of 5°K , showing that the thermal characteristics of urban areas are in marked contrast to those of the adjacent (rural) area. Obviously, thermal contrasts will also depend on topographic situation and are expected to be greatest for sheltered cities with light winds. Temperature differences are also noticed to be well marked during still-air conditions, especially at night (Barry and Chorley, 1972). The factors responsible for creation of a heat island are the direct production of heat by combustion and the gradual release of heat stored during the day by the brickwork, concrete and similar construction materials.

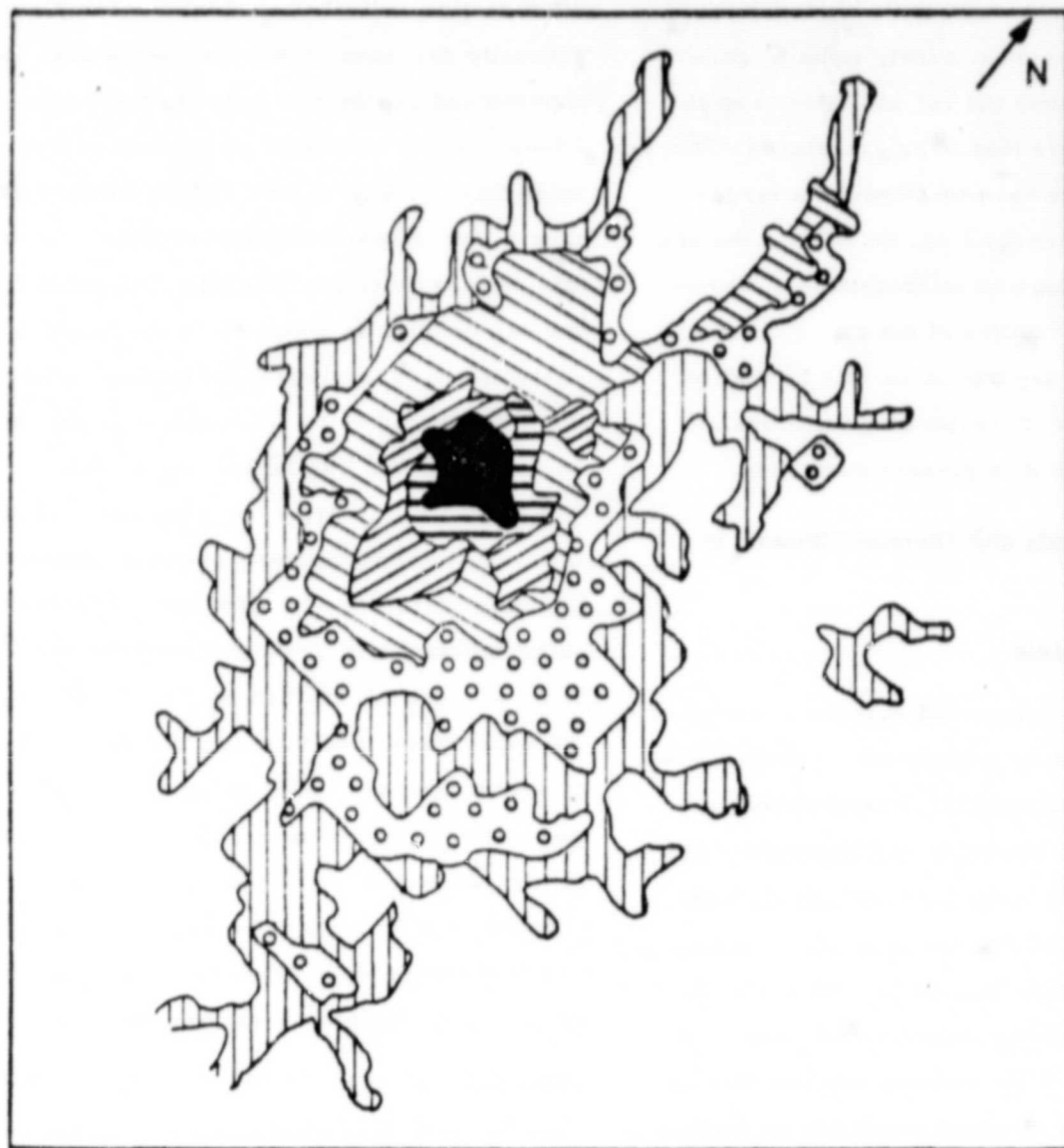
An EXIO-temperature slicing of the Day-IR recording (16 Sept., 1979) over Brussels also shows a tendency of decreasing temperatures

out from the city's central parts (Fig.III.3.6). In the direction indicated as AA', the temperature gradually decreases from the centre over the suburbs and residential areas to the Zonien-Forest, which is located south-east of Brussels (class 8, Fig.III.3.6). During the day forests have a low radiant temperature range; therefore forest limits can be clearly delineated and can be used as a reference for location purposes. City temperatures during the day are also noticed to be substantially higher than during the night. The factor responsible for this is direct insolation but it may also be the active heat production of a complex nature (buildings, factories, traffic etc.), the latter being substantially greater during the day. Some of these effects can be detected through the appearance, and this only during the day, of several sectors being highest in temperature over the Brussels agglomeration. Apparently, these "hotter" urban sub-islands (class 1, Fig.III.3.6) are located along the axis BB' which corresponds essentially with industrial areas, large factories, railway stations.

Other thermal representations of the Brussels Heat Island are shown in Figs.III.3.7 and 8, corresponding both to night-infrared recordings on 30/5/1978 and on 28/7/1978. Comparing the three night recordings it is observed that temperature differences between the warmest city centre and the coolest parts of the surrounding land, are of the same order (6.5°K).

Date	Channel	$T_{\text{max}}^{\bullet)}$ (city)	$T_{\text{min}}^{\bullet)}$ (land)	$\Delta T^{\bullet)}$
30/5/78	night-IR	287.84	281.08	6.76
28/7/78	"	282.90	276.59	6.31
16/9/79	"	273.49	266.98	6.51
16/9/79	day-IR	292.25	279.98	12.27

$\bullet)$ in $^{\circ}\text{K}$




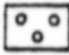


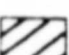


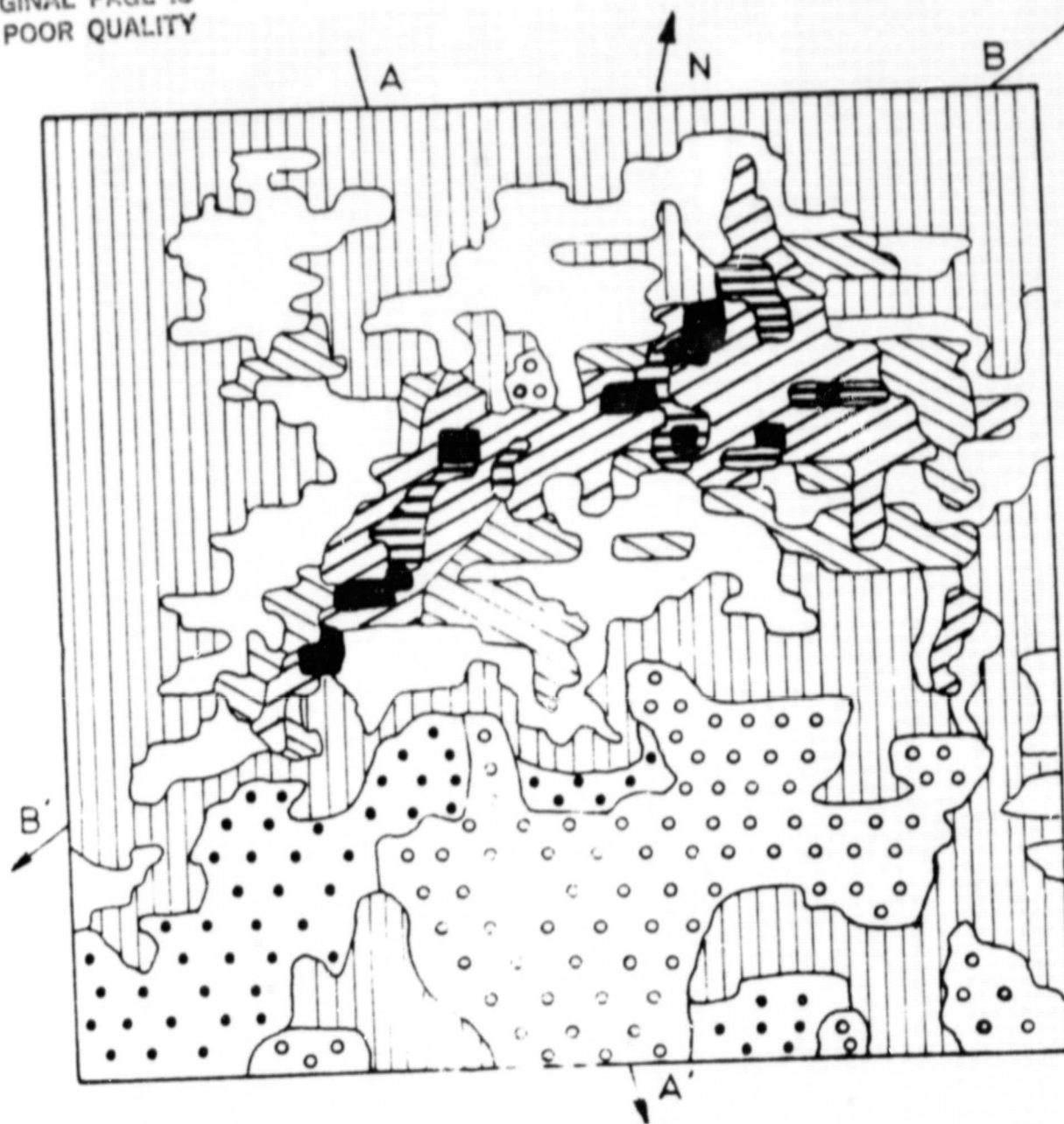
Class			
1		273,49°K	5  271,50 - 271,09°K
2		273,09°K	6  270,69 - 270,28°K
3		272,69°K	7  269,88 - 266,98°K
4		272,30 - 271,90°K	

Fig. III.3.5. The Urban Heat Island of Brussels. (Night-IR, 16.9.79) EXIO temperature slicing.

ORIGINAL PAGE IS
OF POOR QUALITY



Class	
1	292,25 - 291,25° K
2	290,91 - 290,57° K
3	290,23 - 289,55° K
4	289,21 - 288,87° K
5	288,53 - 287,84° K
6	287,49 - 286,10° K
7	285,75 - 284,33° K
8	283,98 - 279,98° K

Fig. III.3.6. The Urban Heat Island of Brussels. (Day-IR, 16.9.79) EXIO temperature slicing.

IN: 11:00 640
ING: 11:00 750
I INCREMENT 1

OF THIS STRIP 750
OF THIS STRIP 1

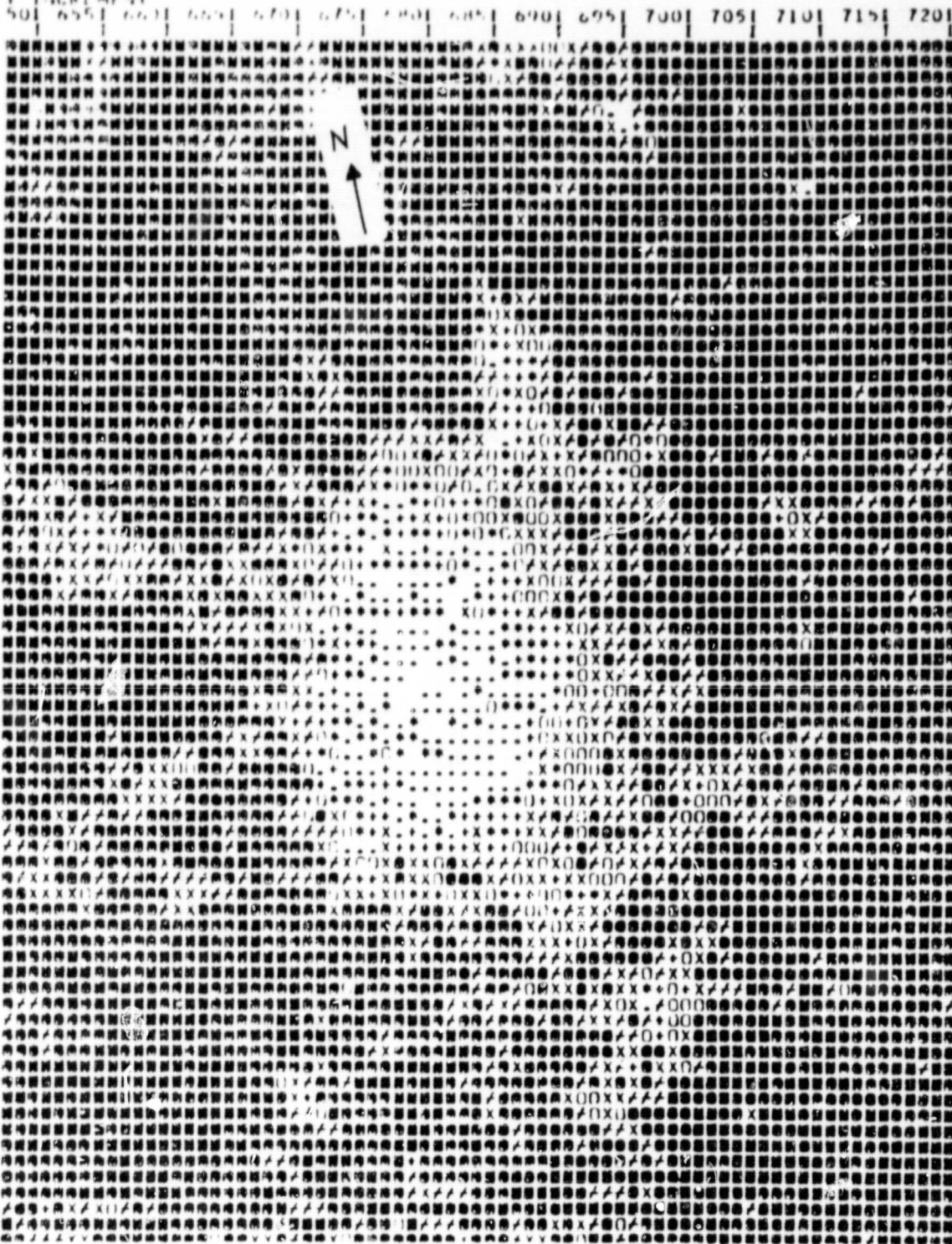


Fig. III.3.7. The Urban Heat Island of Brussels. (Night-IR, 30.5.78) EXIO temperature slicing.

ORIGINAL PAGE IS
OF POOR QUALITY

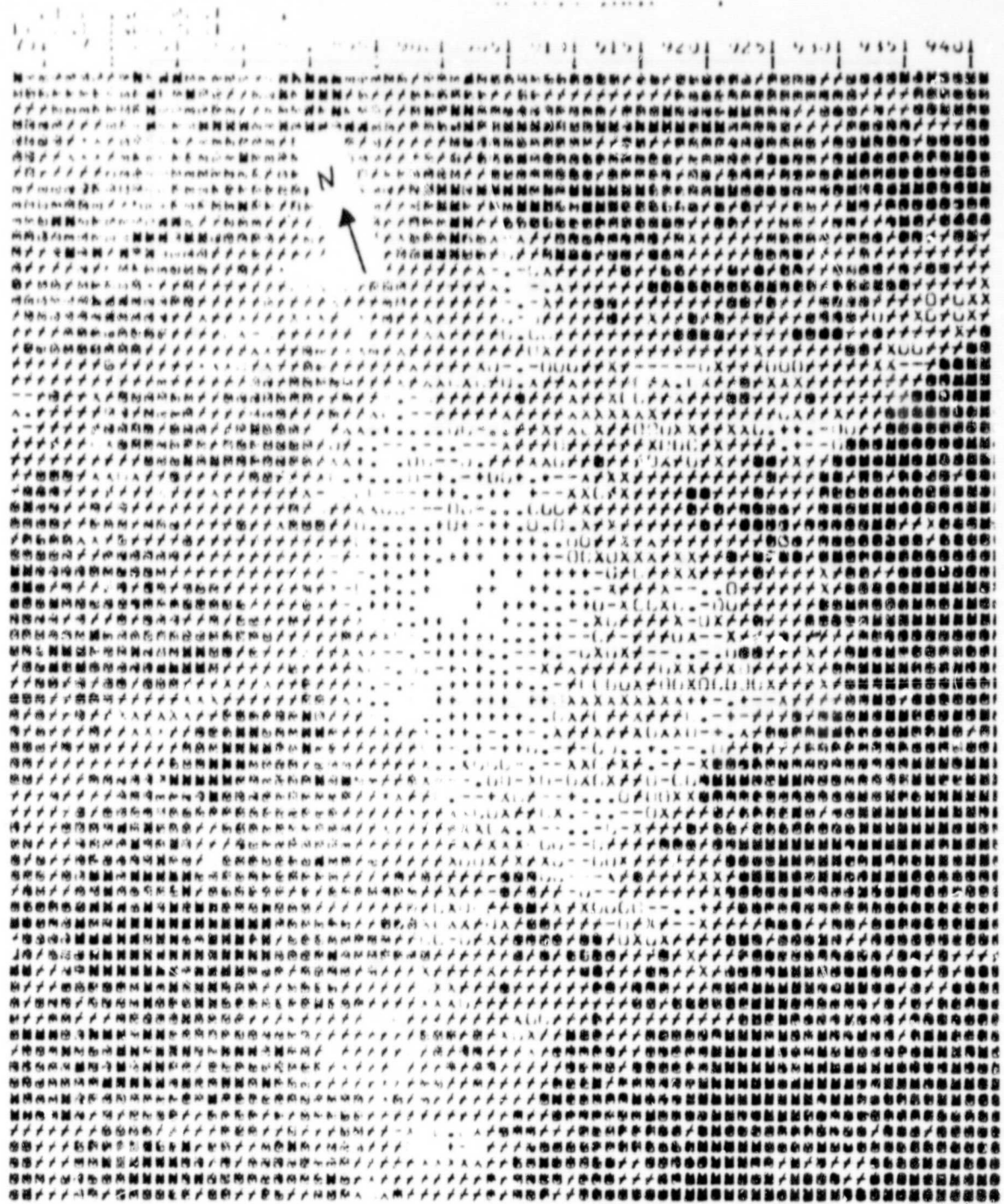
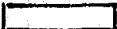

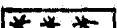











Fig. III.3.8. The Urban Heat Island of Brussels. (Night-IR, 28.7.78) EXIO temperature slicing.

Legend of Fig. III.3.7. (Night-IR 30.5.78).

<u>Class</u>	<u>Temperature</u>
	287.84 - 287.15°K
	286.80 - 286.45°K
	286.10°K
	285.75°K
	285.40°K
	285.04°K
other	284.69 - 281.08°K

Legend of Fig. III.3.8. (Night-IR, 28.7.78).

<u>Class</u>	<u>Temperature</u>
	282.90 - 282.54°K
	282.18 - 281.81°K
	281.45°K
	281.08°K
	280.71°K
	280.35°K
other	279.98 - 276.59°K.

ORIGINAL PAGE IS
OF POOR QUALITY

However, during the day (16 Sept. 79) the temperature difference is substantially higher (12.27°K). Such a high temperature difference indicates that the surface temperatures of urban areas are not related to their air temperature. In fact, air temperature differences between cities and rural land are generally much smaller (2°K).

Schelde-River and Doel's Nuclear Plant

The Schelde River and parts of its estuary are well depicted by the temperature pattern in Figs.III.3.9 and 10. During the day a decrease in temperature is observed (dark symbol = cool, white = warm) following the river's course through Antwerp's industrial areas towards its mouth. This pattern may be related, to some extent, to tidal streams. It was verified that on Sept. 16, 1979 a condition of high tide prevailed at Antwerp at 11.55 MET. On the night recording on the same day, several sand-banks or tidal flats are exposed in the river (see Fig.III.3.10, arrows).

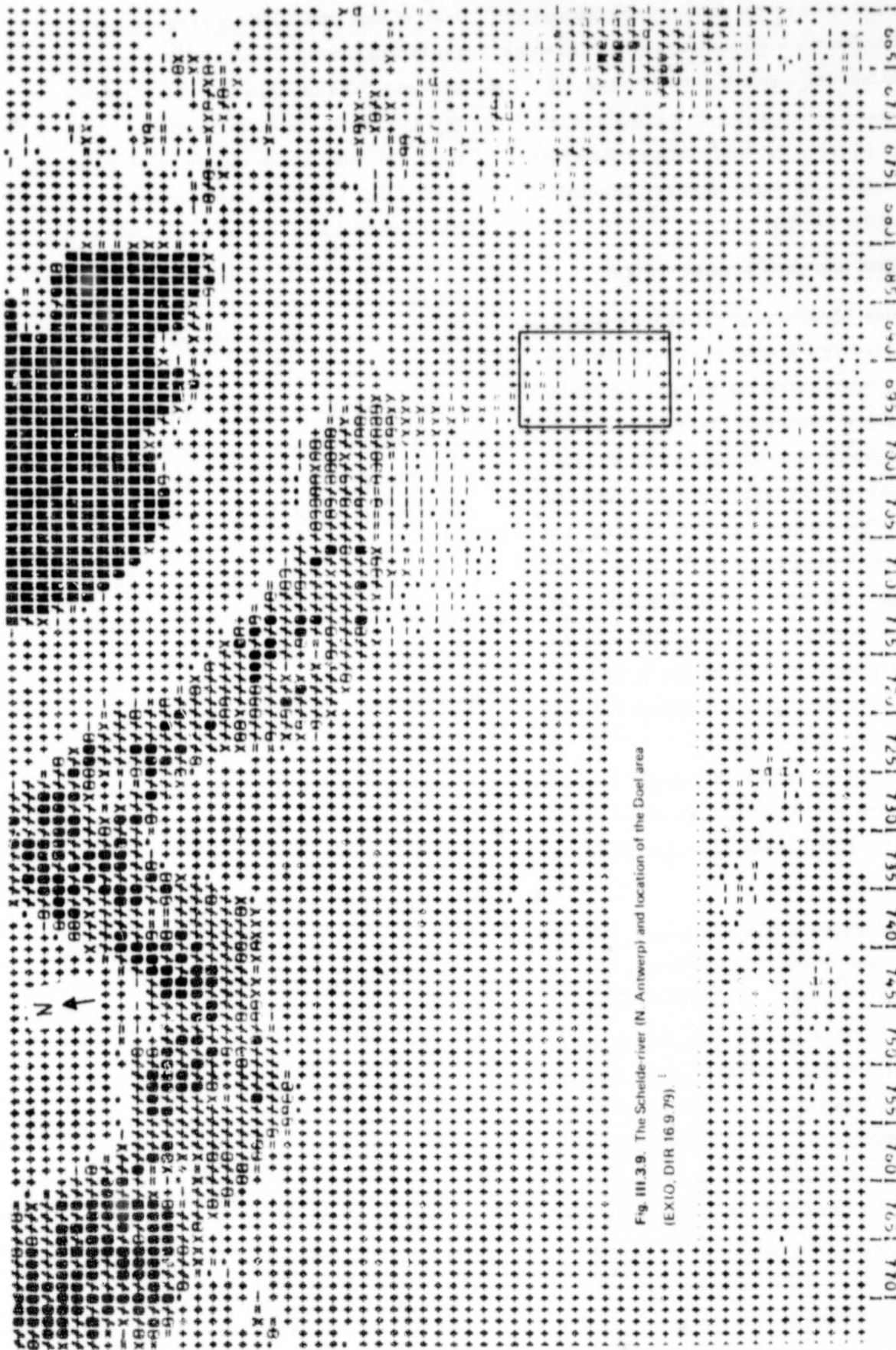
They now become visible as cooler areas, with respect to the water surface, and are represented on the EXIO-print by a dark printing symbol.

The nuclear power plants of Doel are located on the left bank of the Schelde River, i.e. approximately in the centre of the rectangle in Fig.III.3.9. Two nuclear reactors are operational (Doel-1 and 2), two others are under construction (Doel-3 and 4). Water from the reactor cooling cycles is discharged ($2 \times 40,000 \text{ m}^3/\text{h}$) in the Schelde. At the point of discharge, the temperature of this water is about 11°C higher compared to the temperature of the river-water taken up for cooling. The infra-red count of each pixel was determined by means of the STATS-programme and this for the whole rectangular area indi-

cated in Fig.III.3.9. When the constructed pixel matrix was optically superposed (ZTS) on a topographic map (Fig.III.3.11), a temperature anomaly became apparent in the polderland and another in the Schelde River. In the polderland, the pixels with highest surface temperatures (high pixel counts) correspond with the power plant construction area. In the Schelde River, the warmest pixel (count 69) contains the water discharge point of the power plant. Its integrated real surface temperature was calculated as 23.4°C , applying the temperature correction factor ($+9.28^{\circ}\text{C}$) derived from calibration procedures. The temperature difference between this "discharge" pixel and the mean river temperature is of the order of $+4^{\circ}\text{C}$. Also note the high surface temperatures recorded over industrial areas, located on the right riverbank, as compared to the mean temperatures of the polderland.

References

1. E. C. BARRETT and L. F. CURTIS; "Introduction to Environmental Remote Sensing". Chapman and Hall, London, (1976).
2. R. G. BARRY and R. J. CHORLEY; "Atmosphere, Weather and Climate". Methuen & Co. Ltd., London, (1972).
3. H. GOSSMANN and W. NÜBLER; "Oberflächentemperatur und Vegetationsverteilung in Freiburg". Bildmessung und Luftbildwesen, 45, 105-113 (1977).
4. NASA; "Heat Capacity Mapping Mission Users' Guide". Goddard Space Flight Center, Greenbelt, USA (1979).
5. W. NÜBLER; "Wind-Induced Microclimatic Differences Detected from Thermal Scanner Data". Tellus Newsletter No. 5, 1-11 (1978).
6. F. F. SABINS; "Remote Sensing. Principles and Interpretation". Freeman & Co., San Francisco (1978).
7. P. STOCK; "Interpretation von Wärmebildern der Stadtregion von Essen". Proc. Int. Symp. on Remote Sensing for Observation and Inventory, Freiburg (BRD), vol. II, 1017-1029 (1978).



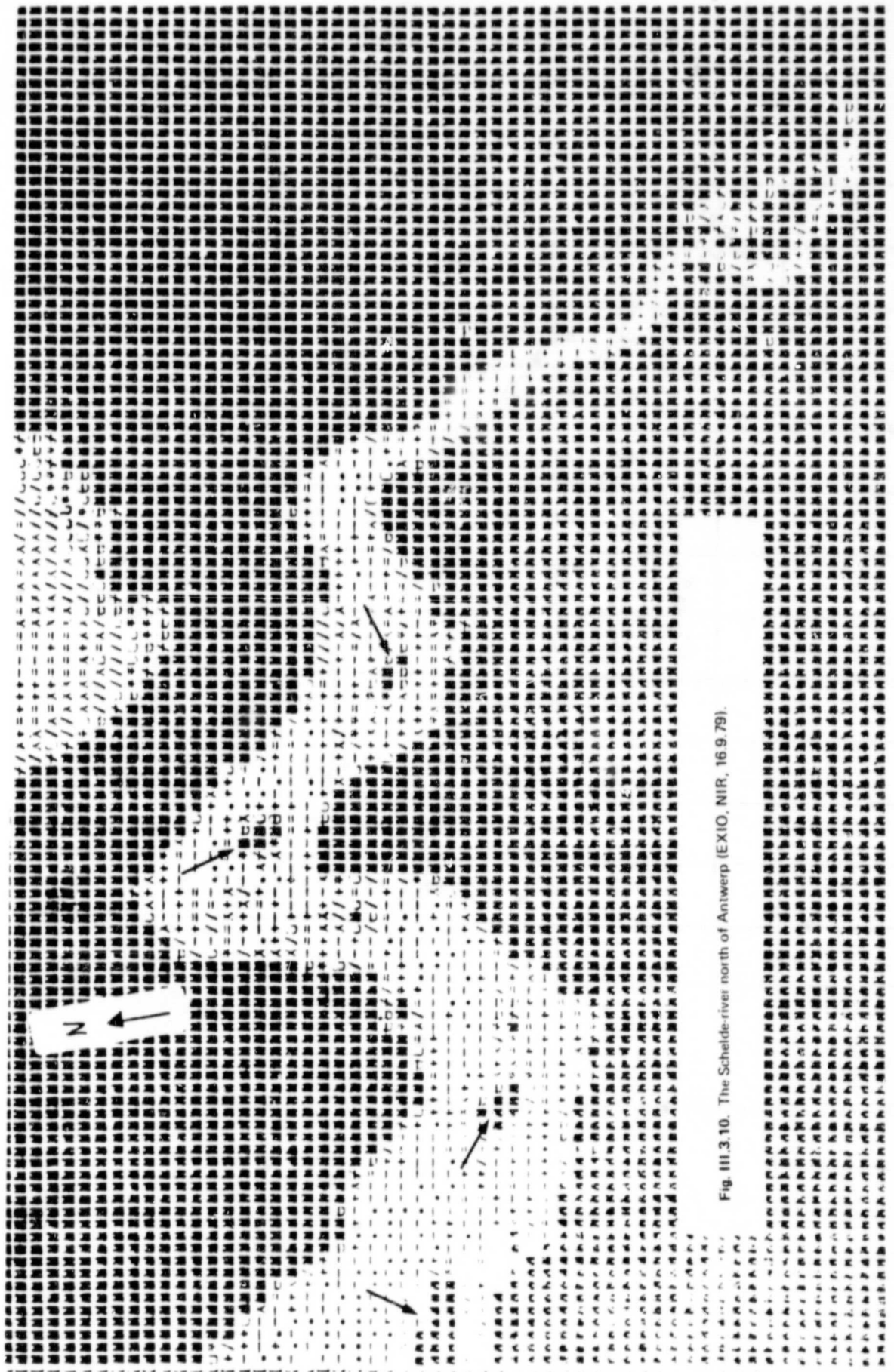


Fig. III.3.10. The Schelde-river north of Antwerp (EXIO, NIR, 16.9.79).

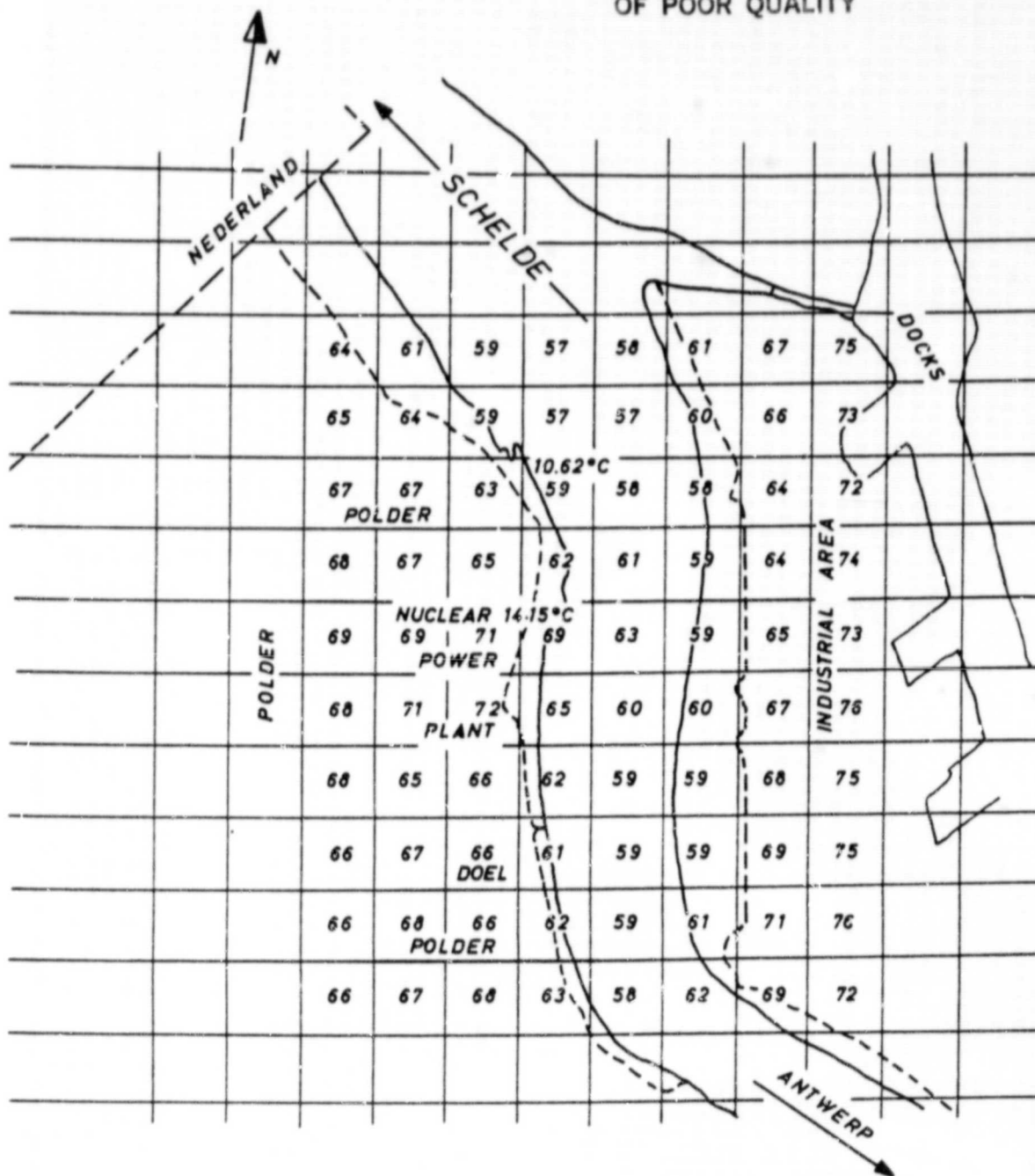


Fig.III.3.11. HCMM-infrared pixel counts represented for the DOEI area (day-ir, 16.9.79).

Part 4 : HCMM Satellite Data Calibration and Atmospheric Corrections

ORIGINAL PAGE IS
OF POOR QUALITY

Introduction

In contrast to many uses of multispectral data such as furnished by the satellites of the LANDSAT series, the exploitation of the thermal, and also albedo, data provided by the HCMR necessitates its proper calibration relative to values measured on the ground. The reason for this apparent difference between multispectral and thermal data resides in the fact that the interpretation of thermal data requires an understanding of the physical processes responsible for a certain surface temperature or surface temperature difference (PRICE 1980) and, therefore, the temperatures or temperature differences both spatial and temporal as measured on the ground have to be known.

The difference between the interpretation of MSS and thermal data is only apparent, because a deeper going and deterministic interpretation of MSS data encounters the same problems as that of thermal data. The interpretation of the MSS-data of the CZCS of the Nimbus-7 satellite (STURM 1980) is an example of the development in this direction.

Prior to the HCMM, the calibration of satellite thermal data, or more generally, its comparison with ground measured temperatures has mostly been carried out for sea water temperatures.

A comparison between sea surface temperature (SST) measurements from the NOAA-4 satellite and from an underflight with an airborne radiometer was carried out in the Gulf of Lyon (ALBUISSON et al. 1979).

Comparison with ship-born SST measurements were made for NOAA-3, NOAA-4 and NOAA-5 (TABATA 1980, BROWN 1980) and in-situ measured thermal gradients were compared with results obtained from NOAA-5 (WALD and NIHOUS 1980). Thermal data from METEOSAT were checked with SST measurements from a North-Sea platform (GRASSL and KOEPKE 1980).

In all these calibration attempts, agreement between satellite and "ground" measured SST was 1°C or better. One has to add, that the sea surface represents a relatively homogeneous medium both in regard to temperature and to thermal emissivity, and that the range of temperatures observed is usually rather limited. At maximum this range covers from

0 - 30°C and on individual scenes the range is of a few degrees only. Furthermore, temporal changes of temperature are rather slow.

The situation is quite different for the temperature of land surfaces such as observed by the HCMR. These surfaces not only show a rather great spatial heterogeneity both in regard to temperature and emissivity, but also temporal changes of temperature are rather rapid. In addition, the temperature range observed on an individual scene is more extended and is shifted upwards and may reach from 20°C to more than 50°C, the total range being from below 0°C to more than 50°C. Comparisons have been carried out between the temperature of land surfaces measured by thermistors and hand-held radiometers and measurements with an airborne Nimbus Medium Resolution Infrared Radiometer (MARLATT 1967), but no comparisons with satellite data are known.

Calibration of satellite data implies the use of atmospheric corrections and therefore the present part will first deal with atmospheric corrections before treating the results of the calibration of the HCMR data proper.

Atmospheric Corrections

Even under clear sky conditions the atmosphere is not completely transparent for infrared radiation in the "windows" of the elec-

tromagnetic spectrum. The atmosphere not only causes a shift in the level of the temperatures of the earth surface, but also a smoothing of the actual spatial and temporal differences in surface temperature.

An example of the order of magnitude of this effect is given in Table III. 4.1 for a dry and an irrigated surface of the Crau.

In this example, the atmospheric corrections were as high as 13.5°C and they almost doubled the temperature difference between irrigated and dry plots, as well as the daily temperature amplitude. Therefore, atmospheric corrections are not only necessary for absolute, but also for relative measurements, including thermal inertia.

A number of methods have been developed to calculate atmospheric corrections.

The RADTRA Model

This model has been developed by RANGASWAMY and SUBBARAYUDU (1978) under contract by NASA and has subsequently been made available to HCMR investigators. In this model, the attenuation of infrared radiation by the atmosphere is being estimated by solving the equation of radiative transfer. Calculations for the 10.5 to 12.5 μm wave band are performed by dividing the atmosphere into different layers and taking for each separate layer the mean values for mass absorption coefficient, temperature and vapour pressure. The radiance at the top of layer n then equals the sum of the transmitted radiance of layer (n-1) and the emitted radiance of layer n:

$$R(\nu, n) = R(\nu, n-1) \exp(-k_n x_n) + R_a(\nu, n)$$

$$[1 - \exp(-k_n x_n)] \quad (W \cdot m^{-2} \cdot sr^{-1}) \quad (4.1)$$

where R is the total radiation per unit of frequency interval, R_a the radiation emitted by layer n, ν the radiation frequency (μm^{-1}), k_n the mass absorption coefficient of layer n

Time	Site	T _{sat} , °C		ΔT, °C day/night		ΔT, °C dry/irr.	
		uncorr.	correct.	uncorr.	correct.	uncorr.	correct.
Night	Irr.	14.7	15.3			1.0	1.8
	Dry	15.7	17.1	15.7	27.8		
Day	Irr.	26.9	36.5	12.2	21.2	4.5	8.4
	Dry	31.4	44.9				

Table III.4.1. Surface temperature of the Crau measured on 28.7.78 by the HCMR, with and without correction by the "Window" model for the effect of the atmosphere (SEGUIN and REINIGER).

($\text{g}^{-1} \cdot \text{cm}^2$) and x_n the optical path lengths ($\text{g} \cdot \text{cm}^{-2}$).

R_a can be calculated by substituting the mean air temperature of layer n into Planck's equation.

As the atmospheric attenuation in the 10.5 to 12.5 μm wave band is mainly caused by water vapour molecules, the optical path length x_n can be expressed as:

$$x_n = \rho_v \cdot \Delta h \quad (\text{g} \cdot \text{cm}^{-2}) \quad (4.2)$$

where ρ_v is the water density ($\text{g} \cdot \text{cm}^{-3}$) and Δh the thickness of layer n (cm).

According to BIGNELL (1970) the mass absorption coefficient k_n can be described as:

$$k_n = f_1(T)k_1 \frac{(P_n)}{10^5} + f_2(T)k_2 \frac{(e_n)}{10^5} \quad (\text{g}^{-1} \cdot \text{cm}^2) \quad (4.3)$$

where

$$f_1(T) = 1 - 0.005 (303 - T_n) \quad (4.4)$$

$$f_2(T) = 1 + 0.02 (303 - T_n) \quad (4.5)$$

T_n is the mean air temperature (K) of layer n , e_n the mean partial pressure of water vapour of layer n (Pa), P_n the mean pressure of layer n (Pa), $k_1 = 0.10$ and a value of 3.2 ($\text{g}^{-1} \cdot \text{cm}^2$) was used for k_2 .

With this method upward radiation can be calculated at each altitude. From Planck's formula an equivalent black-body temperature $T_{bc}(h)$ can be calculated. The difference between surface temperature T_c and $T_{bc}(h)$ is the correction for the attenuation of thermal infrared radiation by the atmosphere:

$$T_{\text{corr}} = T_c - T_{bc}(h) \quad (\text{K}) \quad (4.6)$$

The RADTRA-model was used and tested by NIEUWENHUIS (1980 a) who found that according to BIGNELL (1970) a value of $k_2 = 10.0$ should be employed in the model. This change has a considerable effect on the

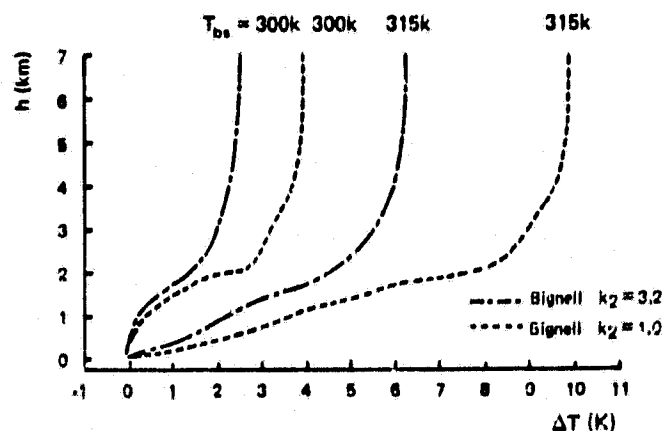


Fig.III.4.1. Atmospheric temperature corrections (ΔT) on July 31, 1978 as calculated with the RADTRA-model for two surface temperature. Transmission of the atmosphere is calculated for two values of k_2 : 3.2 and 10.0 $\text{g}^{-1} \cdot \text{cm}$. (NIEUWENHUIS 1980).

atmospheric corrections especially for the higher correction values as shown in Fig. III.4.1. Following this change, a number of errors were detected in the RADTRA-model which was completely re-written by PRICE (1980) in the form of the "WINDOW-model". Consequently, this model was used for most of the atmospheric corrections in this report.

Independently, a correction program KORR has been developed by WIENERT (1980) which follows basically the same approach. In this program the radiative transfer equation was integrated over the 10.5-12.5 μm interval and was not quasi-monochromatically evaluated for a wavelength of 11.5 μm . As shown in Fig. III.4.2, these two approaches may lead to atmospheric corrections differing by up to 2°C. This difference increases with scan angle. When the atmospheric correction was calculated monochromatically with the KORR-model, the same results were obtained as with the WINDOW model, showing that this was effectively the cause of the discrepancy between the two models. The results of these calculations are presented in Table III.4.2.

The Linear Model

In this model it is likewise assumed, that an

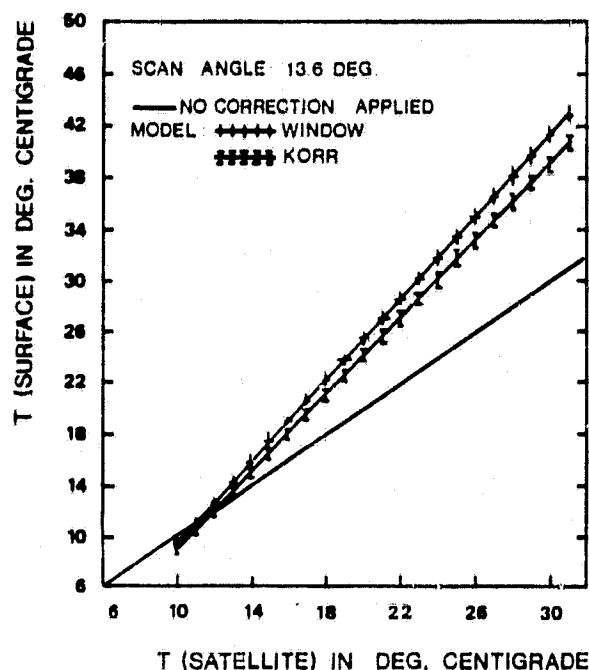


Fig. III.4.2. Atmospheric correction due to water vapor absorption (HCMM) calculated with Hannover radiosonde data 22 June 1979, 00 UT (WILMERS and WIENERT 1981).

$\theta = 30^\circ$		$\theta = 30^\circ$		
T_{sat}	T_s (KORR)	T_s (WINDOW)	T_s (KORR)	T_s (WINDOW)
10	8.8	9.3	8.4	9.3
12	12.3	12.5	12.1	12.8
14	15.6	15.8	15.7	16.3
16	18.9	19.1	19.3	19.8
18	22.1	22.2	22.8	23.2
20	25.3	25.4	26.3	26.5
22	28.5	28.5	29.7	30.0
24	31.7	31.6	33.1	33.3
26	38.0	37.8	39.8	40.0
30	41.1	41.1	43.1	43.2
31	42.6	42.7	44.8	44.7

T_{sat} = surface temperature in °C measured by the satellite
 T_s (KORR) = surface temperature in °C corrected with "KORR"
 T_s (WINDOW) = surface temperature in °C corrected with "WINDOW"
 θ = scan angle in degrees

Table III.4.2. Comparison of atmospheric corrections by "KORR" monochromatically calculated for a wavelength of 11.5 μ m with "WINDOW" for 22 June 1979, 00 UT (WILMERS and WIENERT 1981)

atmospheric attenuation in the 8-14 μ m band is caused by water vapour molecules only. Applying a linear expansion of Planck's formula, BECKER (1978) has derived that:

$$T_{bs}(h, \theta) = T_{bs} + \frac{AW(h)}{-\cos \theta} (\theta(h) - T_{bs}) + \delta \quad (K) \quad (4.7)$$

where h = altitude (m), θ = angle of observation, T_{bs} = black body temperature of the surface (K), $W(h)$ = total water content of the atmosphere over the column of length h ($g \cdot cm^{-2}$), A = constant characteristic of the atmosphere ($cm^2 \cdot g^{-1}$), δ = correction, which can be neglected to first order, $\theta(h)$ an effective atmospheric temperature (K).

The effective atmospheric temperature is defined as:

$$\theta(h) = \frac{\sum_{n=1}^N W_n T_n}{\sum_{n=1}^N W_n} \quad (K) \quad (4.8)$$

According to a first order approximation the temperature correction for atmospheric attenuation is:

$$T = T_{bs}(h, \theta) - T_{bs} = \frac{AW(h)}{\cos \theta} (\theta(h) - T_{bs}) \quad (4.9)$$

Results obtained with this model have been compared with the RADTRA-model. (NIEUW-ENHUIS 1980 a) and they are shown in Fig. III.4.3. The factor A has been calculated assuming that for a surface temperature equal to the temperature of the lower atmosphere, the corrections as calculated by both models are the same at the top of the atmosphere. As can be seen in Fig. III.4.3, agreement between the two models was within 1°C.

In both the RADTRA-WINDOW-KORR and in the simplified linear model, radiosonde data on pressure, temperature and humidity are required. In eq. (4.9) however, $W(h)$ and $\theta(h)$ can be eliminated by measuring the radiation temperatures of the surface in two different wave length bands.

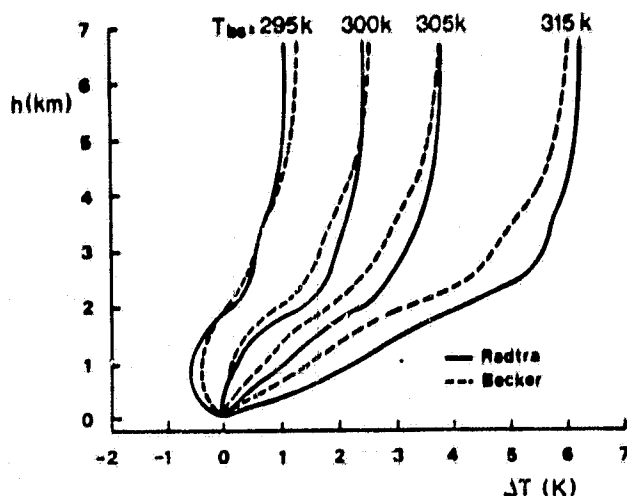


Fig. III.4.3. Atmospheric temperature corrections (ΔT) depending on height (h) above the earth surface for different surface temperatures as calculated both with the RADTRA-model and BECKER's model for July 31, 1978. The observation angle is zero (NIEUWENHUIS 1980).

These are:

$$T_1(h, \theta) = T_{bs} + \frac{A_1 W(h)}{\cos \theta} (\theta(h) - T_{bs}) \quad (K) \quad (4.10)$$

$$T_2(h, \theta) = T_{bs} + \frac{A_2 W(h)}{\cos \theta} (\theta(h) - T_{bs}) \quad (K) \quad (4.11)$$

The radiation temperature of the soil surface T_{bs} is found by combining the eqs. (4.10) and (4.11):

$$T_{bs} = \frac{T_1(h, \theta) + T_2(h, \theta)}{2} + (T_1(h, \theta) + T_2(h, \theta)) \bar{A} \quad (K) \quad (4.12)$$

where

$$\bar{A} = \frac{A_1 + A_2}{2(A_2 - A_1)}$$

Calculations with eq. (4.12) are only accurate, if the difference in atmospheric transmission in the two wave length bands is large enough. This approach (IMBAULT 1980, DESCHAMPS and PHULPIN 1980) was not tested in the present work.

Data Calibration

Data calibration refers almost exclusively to

thermal infrared data of the HCMR and only a short comment will be given on the albedo data.

Thermal Infrared Data

The calibration procedure consisted in comparing the satellite measured surface temperature, T_{sat} , with the ground measured surface temperature as the satellite should have measured it after atmospheric correction, T_{sat}^* . The atmospheric corrections were calculated with the WINDOW model unless stated otherwise. The WINDOW model, like the model of BECKER (1978) proposes a linear relation between a radiometric temperature measured on the ground, T_g , and the temperature "seen" by the satellite. This relation is given by:

$$T_{sat}^* = a T_g + b \quad (4.13)$$

where T_{sat}^* = radiometric temperature to be measured by the HCMR ($^{\circ}K$), T_g = radiometric temperature measured on the ground ($^{\circ}K$). The coefficients a and b in eq. (4.13) were calculated by the WINDOW program. Especially for water temperatures, the kinetic temperature T_s , and not the radiometric temperature T_g , was measured on the ground. The relation between the two temperatures is given by

$$T_g = (1 - \epsilon) T_a + T_s \quad (4.14)$$

where T_s = kinetic temperature measured on the ground ($^{\circ}K$), T_a = radiative temperature of the atmosphere ($^{\circ}K$), ϵ = thermal emissivity.

Except in one case, only the emissivity correction was taken into account and the correction for reflection, $(1 - \epsilon) T_a$, was neglected.

The results of the calibration attempts are summarized in Table III.4.3 which contains 45 data points for two of which no ground data are yet available. The data cover a period

AL	Date	Scene	T _g , °C	T _{sat} , °C	T _{sat} , °C	T _Δ	Location and author	
34	30.5.78	AA-0034.0213.0.3	8.6	8.6	9.0	-0.4	Pine forest, S.Germany	(1)
--	--	--	14.1	13.6	10.4	3.2	Grass-airfields, Belgium	(2)
38	3.6	AA-0038.0148.0.3	12.5	11.9	13.3	-1.4	Lac Leman	(3)
54	19.6	AA-0054.0145.0.3	16.9	15.0	6.1	8.9	Steinhuder Meer, N.Germany	(4)
82	17.7	AA-0082-0208.0.3	18.3	17.1	11.9	5.2	Lac Leman	(3)
--	--	--	15.7	16.0	10.5	6.4	Crau, grass irrig.	(5)
--	--	AA-0082.1303.0.2	18.3	17.4	14.1	3.3	Lac Leman	(3)
--	--	--	39.8	34.3	25.0	9.3	Crau, grass irrig.	(5)
--	--	--	49.0	40.9	30.9	10.0	Crau, grass dry	(5)
93	28.7	AA-0093.0212.0.3	18.6	16.6	10.9	5.7	Lac Leman	(3)
--	--	--	15.1	14.4	8.7	5.7	Crau, grass irrig.	(5)
--	--	--	17.7	15.8	9.1	6.7	Crau, grass dry	(5)
--	--	AA-0093.1307.0.2	18.6	16.9	14.4	2.5	Lac Leman	(5)
--	--	--	41.3	29.5	20.8	8.7	Crau, grass irrig.	(5)
--	--	--	53.0	35.8	27.5	8.3	Crau, grass dry	(5)
96	31.7	AA-0096.1226.0.2	15.0*	11.0		4.0	North Sea	(6)
--	--	--	22.0	16.0		6.0	Lake IJssel	(6)
--	--	--	35.0**	27.0		8.0	Land surface, the	(6)
--	--	--	50.0**	36.0		14.0	Netherlands	(6)
108	12.8	AA.0108.0151.0.3	9.9	11.2	6.1	5.1	Crau, grass irrig.	(5)
--	--	--	13.6	13.7	7.9	5.8	Crau, grass dry	(5)
--	--	AA-0108.1247.0.2	28.9	24.9	19.4	5.5	Crau, grass wet	(5)
--	--	--	50.3	40.5	25.6	14.9	Crau, grass dry	(5)
118	22.8	AA.0118.1232.0.2	18.7	17.3	15.7	1.6	Lac Leman	(3)
135	8.9	AA-0135.1249.0.2	17.2	15.2	10.5	4.7	Lac Leman	(3)
145	18.9	AA-0145.1237.0.2	16.2	15.1	11.8	3.3	Lac Leman	(3)
198	10.11	AA-0198.0123.0.3	-3.0	-2.7	-7.3	4.6	Fog, Rhine Valley	(1)
--	--	AA-0198.1221.0.2	10.0	9.5	3.5	6.0	Lac Leman	(3)
422	22.6.79	Orb. 8246/ 5N	22.4	17.7	8.6	9.1	Steinhuder Meer	(4)
423	23.6	6268/ 6D	14.9	14.1	9.2	4.9	Lac Leman	(3)
433	3.7	6409/16N	16.3	13.8	5.3	8.5	Lac Leman	(3)
444	14.7	6579/11D	18.1	15.2	8.9	6.3	Lac Leman	(3)
459	29.7	6801/10D	18.1	17.3	15.2	2.1	Lac Leman	(3)
492	31.8	7283/11N	17.6	15.4	8.7	6.7	Lac Leman	(3)
497	5.9	7364/16D	17.4	16.1	10.3	5.8	Lac Leman	(3)
498	6.9	7372/ 1N	17.4	15.5	8.8	6.7	Lac Leman	(3)
503	11.9	7446/ 6N	17.3	13.7	8.7	5.0	Lac Leman	(3)
508	16.9	7520/11N	17.1	15.1	8.9	6.2	Lac Leman	(3)
--	--	7527/11D	17.1	15.3	10.0	5.8	Lac Leman	(3)
--	--	--	21.1	19.2	12.6	5.6	Grass airfields***, Belgium	(2)
518	26.9	7675/ 5D	15.8	14.5	6.6	7.9	Lac Leman	(3)
519	27.9	7690/ 6D	15.8	13.9	7.2	6.7	Lac Leman	(3)
528	6.10	7823/15D	17.8	14.1	11.0	3.1	Adriatic Sea	(7)
710	5.4.80	10523/16N			0.9		Lac Leman	(3)
761	26.5.80	11291/10N			5.2		Lac Leman	(3)

Table III.4.3 List of HCMR thermal calibration data.

AL = days after launch.

SCENE = scene identification, given by number of orbit and path night/day for data from CMS-Lannion.

T_g = radiometric temperature measured on the ground.

T_{sat} = theoretical ground temperature viewed by satellite taking into account atmospheric effects.

T_{sat} = radiometric temperature actually measured by the satellite.

ΔT = T_{sat} - T_{sat}.

Remarks: + T_g = Kinetic ground temperature,
T_{sat} = satellite measured temperature
corrected for atmospheric effects.

++ T_g = Radiometric ground temperature mea-
sured by airborne scanner, T_{sat} = sa-
tellite measured temperature corrected
for atmospheric effects.

+++ T_g = Measured at 2-cm depth

Authors (1) Gossman (Univ. Freiburg)
(2) Gombeer (Univ. Louvain)
(3) Reiniger (JRC Ispra)
(4) Wilmers and Wienert (Univ. Hannover)
(5) Seguin (INRA Avignon), Reiniger (JRC Ispra)
(6) Nieuwenhuis (ICW Wageningen)
(7) Maracci (JRC Ispra)

from 30 May 1978, 34 days after launch (AL) of the satellite to 26 May 1980, 761 days after launch. The radiometric surface temperatures range from -3.0°C to 53.0°C . The location and the authors of the various calibration attempts are listed in the rightmost column of Table III. 4, 3 and the procedures used will be treated in the following.

1. Pine forest and fog surface (H. Gossmann, Geographisches Institut I der Universität Freiburg)

a) Pine forest

The geometrical correction procedure described elsewhere in this report (III. 2) had permitted to identify a pine forest of about 1 km^2 on the HCMM scene of May 30, 1978, 02.13 UT. In this forest, the Climatological Station (Messtation) Hartheim is being operated by the Institute of Meteorology of Freiburg University, measuring air temperature, humidity and windspeed at two heights above the canopy, as well as the vertical radiation fluxes. The results are registered as hourly means or the sum total per hour, respectively^{*}). The hourly totals of the long wave radiation fluxes measured at the climatology station served to calculate the course of the surface temperature of the tree canopy over a 5 hour period, assuming various values of thermal emissivity. (Table III. 4. 4 and Fig. III. 4. 4).

The interpolation to the passage of the satellite at 02.13 UT (03.13 Central European Time, MEZ) gave the following temperatures:

for $\epsilon = 1$	7.7°C
for $\epsilon = 0.9$	9.6°C

^{*}) These data were made available by Prof. Dr. A. Kessler and Dr. L. Jaeger of the Meteorological Institute, Freiburg University. Their helpful cooperation is gratefully acknowledged.

Time	23-24	0-1	1-2	2-3	3-4	GMT
Outgoing longwave radiation (E)	133.77	133.04	129.77	128.59	134.66	Joule cm ² hr
	3.7158	3.6956	3.6047	3.5719	3.7406	Watt 10 ³ cm ²
Incoming longwave radiation (A)	114.15	110.84	108.81	108.10	110.88	Joule cm ² hr
	3.1708	3.0817	3.0225	3.0306	3.0800	Watt 10 ³ cm ²
Equivalent blackbody radiation (S) and surface temperature (T)						
a) for $\epsilon = 1$ $S = E$	284.2	283.8	282.0	281.4	284.6	T (K)
	11.05	10.85	8.85	7.25	11.45	T (°C)
b) for $\epsilon = 0.9$ $S = (E - A) \cdot 10^9$	285.4	285.2	283.4	282.5	286.0	T (K)
	12.25	12.05	10.25	9.35	12.85	T (°C)

Table III.4.4. Calculation of the surface temperature from the longwave radiation fluxes (GOSSMANN 1980 a).

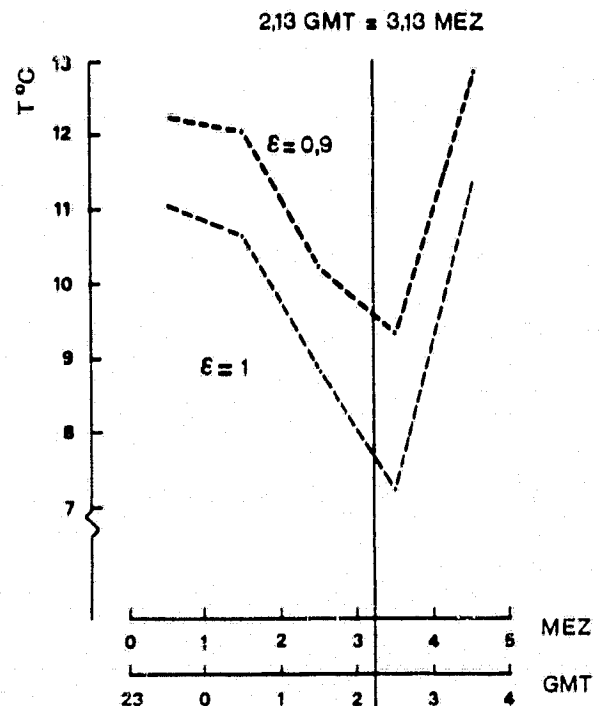


Fig. III.4.4. Surface temperature of the pine forest near Hartheim between 29.5.78 23.00 UT and 30.5.78 04.00 UT, calculated from the measured longwave radiation fluxes for two values of the thermal emissivity (GOSSMANN 1980 a).

Assuming the thermal emissivity of the pine forest to be similar to that of other forms of vegetation, i. e. have values between 0.97 and 0.98, the surface temperature of the canopy (T_g) would be in the range of $9.0 \pm 0.2^\circ\text{C}$. In the calculation of T_g the atmospheric reflection was taken into account. The atmospheric corrections calculated with the WINDOW model using radiosonde data from Stuttgart affected T_g by less than 0.1°C . The satellite measured surface temperature (T_{sat}) was between 8 and 9°C and differed by less than 1°C from the expected temperature T_{sat}^* . A possible source of error may be a certain inhomogeneity of the surface observed. Furthermore, it should be noted that the canopy temperature was derived by interpolation from hourly mean temperatures. The minimum of the curves in Fig. III.4.4 being an hourly mean value, it is somewhat higher than the lowest temperature which would have been observed approximately around 03.00 UT. Therefore, also the temperature found by interpolation for 02.12 UT is too high by a few tenths of a degree. Further details may be found in GOSSMANN (1980 a, b)

b) Fog surface

On the HCMM night scene of November 10, 1978 (A-A0198-01230-3), a continuous high-lying fog layer covering Southern Germany could be identified. The fog layer also showed up clearly on the temperature and humidity profile of the atmosphere measured by radiosonde Stuttgart at 00 UT.

In the calibration procedure it was assumed that the emissivity of the fog layer was equal to 1.0 and that its temperature remained constant between 00 and 01.23 UT. Taking the temperature of the fog layer as given by the radiosonde and correcting for the influence of the atmosphere above the fog, the HCMR should have measured a temperature of -2.7°C . Actually, a temperature between -6.8 and -7.8°C was measured by the HCMR.

2. Grass-airfields (R. Combeer, Laboratorium voor Bodemgenese en Bodemgeografie, Katholieke Universiteit, Leuven)

Comparison between satellite registered temperatures and soil temperatures were performed on a night infrared recording (02.13 UT) of 30 May 1978 (scene A-A0034-02130-3) and on a day-infrared registration (11.46 UT of 16 September 1979 (recorded by CMS Lannion, France)). Both HCMM-scenes are of good quality and show the Belgian territory to be completely cloud-free.

The HCMM digital data were visualized by means of the NMAPW-programme as a brightness classification printout at an approximate scale of 1/200,000 (Fig. III.4.5). Airfield areas were located and delimited through optical superposition of this printout with road and/or topographic maps using a Zoom Transfer Scope. The scan direction of the HCMM Radiometer was indicated for each scene on each map to be superimposed with the printout. This direction could be determined by a number of reference points which were located on the same scanline and which could be clearly identified and localized both on the maps and on the computer print (forest edges, lakes, small urban areas). As printouts are somewhat (scale) deformed, maps were stretched perpendicular to the on-map indicated HCMR scan direction and scale adjustments were made in order to achieve optimum congruency.

Stretch factors were determined from the geometry of pixels which are represented by different printing symbols (according to their classification) on the NMAPW-lineprint (cfr. Fig. III.4.5).

For the HCMM-scene recorded on 16 September 1979, the delimitation of airfields was greatly facilitated using NMAPW-printouts of both the visible and the IR-channel. On a printout of the visible channel (which is congruent with

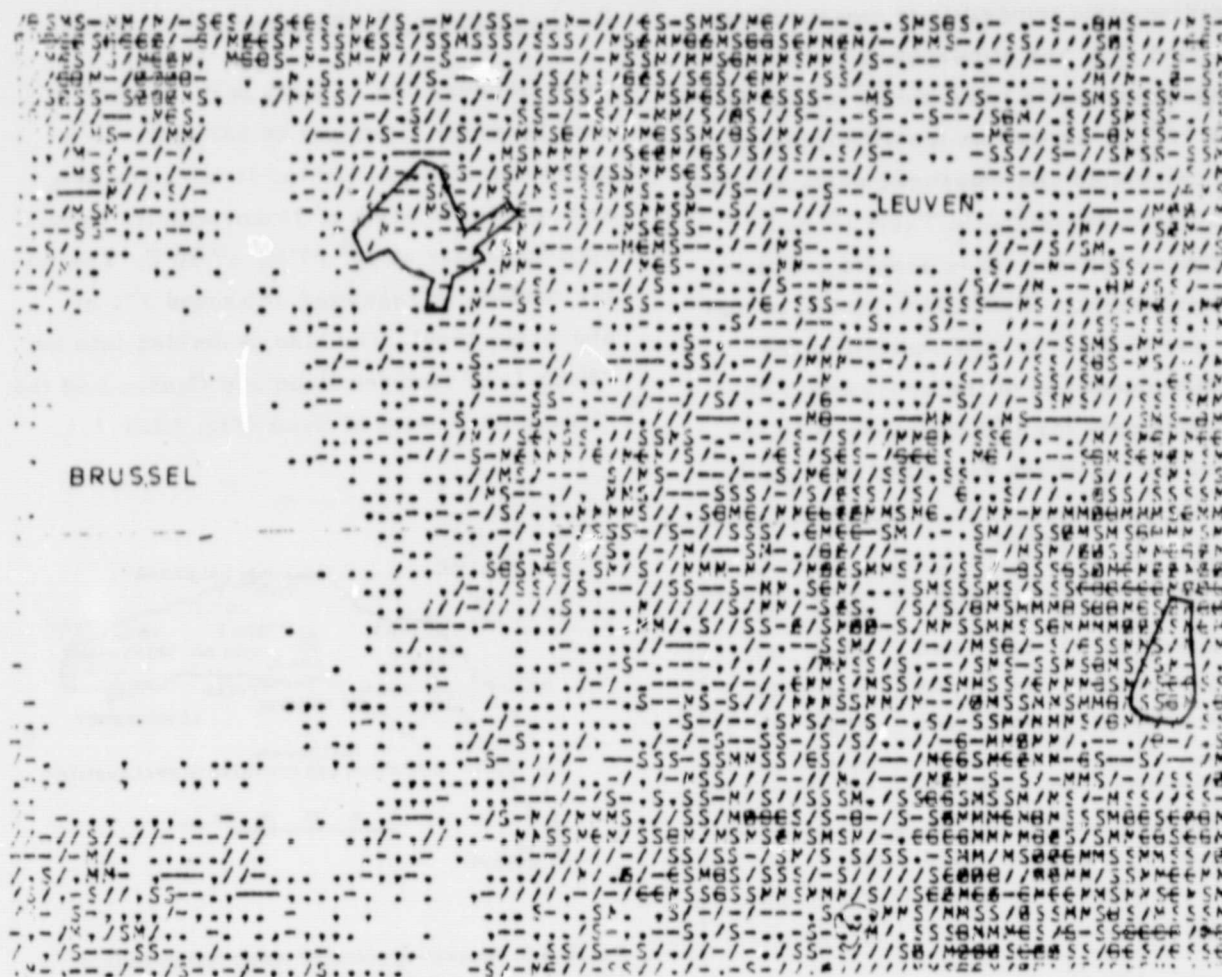


Fig.III.4.5. The delimitation of Zaventem (upper area) and Beauvechain (lower area) airfields on a NMAPW-visualization printout (Night-IR, 30 May 1978) (GOMBEER 1980).

the day-IR band) the localization of airfields was achieved using the position of urban areas as a reference.

Such areas stand out clearly (low reflectance) and are easy to locate on a printout of the VIS-channel. This technique proved to be necessary for geographic areas (Leemstreek, Coastal area) without any forested parts (e.g. Oostende, St. Truiden, Bierse). In forested areas (Ardennes) or especially in cases where forests were located in the vicinity of the airfield, the positioning of the latter was greatly facilitated on a day-IR printout, on which forests stand out by their low temperature range (e.g. Kl. Brogel, Spa).

Ground temperatures (T_g) were provided by the meteorological stations (Regie der Lucht-

wegen, Directie Meteorologie) located at 14 airfields distributed over the Belgian territory. These soil temperatures are recorded continuously (day and night) by electrical resistance thermometers placed at different soil depths (2, 5, 10, 20, 50 and 100 cm). In this calibration study the temperatures at a depth of 2 cm (grass covered soil) were used.

These kinetic temperatures (T_g) were converted to radiometric temperatures, T_r , using an emissivity of 0.989 (BECKER et al. 1980). The atmospheric corrections were calculated with the WINDOW program using radiosonde data from Uccle. In contrast to former results, measurements from corresponding night and day radiosonde ascensions were available for the calculations.

The radiometric temperature measured on the ground (T_g), the atmospheric correction and the temperature to be measured by the HCMR (T_{sat}^*), as well as the difference between calculated and measured surface temperature are presented in Table III.4.5. Differences between these results and those calculated earlier (REINIGER 1980) are due to the use of the WINDOW instead of the RADTRA model and of the appropriate day radiosonde data for 16 September 1979 instead of the nighttime data used previously.

	Airfield	T_g °K	Atmos., °K corr.	T_{rat} °K	T_{sat} °K	$T_{sat}^* - T_{sat}$ °K
May 30, 1978	Zaventem	287.7	-0.6	287.1	284.4	2.7
	Beauvechin	287.2	-0.5	286.8	283.1	3.7
	St. Truiden	287.4	-0.0	286.9	283.4	3.5
	Goetsenhoven	286.5	-0.2	286.3	282.9	3.4
	Munte	287.6	-0.5	287.1	284.1	3.0
	Mean					3.3 ± 0.4
September 16, 1979	Melsbroek	296.8	3.3	293.5	289.3	4.2
	Deurne	295.7	3.1	292.6	287.5	5.1
	Chievres	293.4	2.7	290.7	284.3	6.4
	Kl. Brogel	294.5	2.9	291.6	285.8	5.8
	Oostende	296.3	3.2	293.1	287.0	6.1
	Koksijde	294.8	2.9	291.9	287.5	4.4
	St. Hubert	290.7	2.2	288.5	282.1	6.4
	Spa	291.9	2.4	289.5	282.6	6.9
	Mean					5.7 ± 1.0

Table III.4.5 Ground temperatures, satellite temperatures and atmospheric corrections for the HCMR passes of 30 May 1978 and 16 September 1979. All temperatures are radiative temperatures. (GOMBEER 1980)

The mean difference between the measured and the calculated surface temperature during the night of 30 May 1978 was 3.3°C for the five airfields; while the daytime difference on 16 September 1979 was 5.7°C. In evaluating these results, one has to take into account the heterogeneity of the pixels comprising the airfields as well as the fact that on the ground, surface temperatures were measured at a depth of 2 cm. Between this depth and the true surface temperature differences of a few degrees are easily possible.

3. Lac Léman (P. Reiniger, JRC, Ispra)

Lake Geneva (Lac Léman) is the largest Alpine lake with a surface of 581 km² and a maximum depth of 310 m. It is 73 km long and reaches a width of 14 km with its center approximately at 46° 27'N, 6° 30'E. The water surface is regulated at around 372 m above sea level. The lake is divided into the "Petit Lac" between Nyon and Genève and the "Grand Lac" west of Nyon (Fig. III.4.6.).

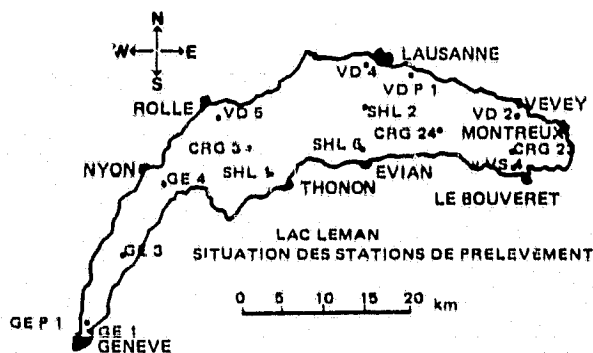


Fig. III.4.6. Measuring points of water temperature in Lake Geneva (from "Rapport sur les études et recherches entreprises dans le bassin lémanique" Campagne 1978).

Its size, the availability of water surface temperatures and a considerable number of suitable HCMR scenes make of the lake a rather attractive reference target for calibration of the HCMR.

a) Lake surface temperatures

The "Commission internationale pour la protection des eaux du Lac Léman contre la pollution" measures, among other parameters, water temperatures at monthly intervals at 15 points in the lake (Fig. III.4.6). Surface temperatures from 10 points in the "Grand Lac" published by the Commission internationale (1978, 1979) were used in this investigation. For each month of 1978 and 1979 the lake temperature was calculated as the mean of the temperature at the 10 measuring points and a seasonal lake temperature curve was con-

structed. The kinetic temperature was transformed into the radiometric surface temperature (T_g) using an emissivity of 0.9815 (BECKER et al. 1980). The effect of the heat flow at the water-air interface (HASSE 1971, PAULSON and PARKER 1972) was not taken into consideration.

b) HCMM scenes

Computer compatible tapes of 22 satellite scenes between 3 June 1978 and 26 May 1980 were employed. The scenes are listed in Table III.4.3. The scenes were visualized on a video screen and the lake surface was delimited using the IMREG program of the Laboratory of Image Processing (LIP). In most cases, this could be done directly on the thermal image, except for the autumn scenes where the temperature contrast between water and land was not sufficient. In these cases, the visible channel was employed to delimit the lake area. The area close to the shore was excluded to avoid using mixed land-water pixels.

The delimitation process was checked on printout maps of the lake surface temperature and on the histograms of the temperature distribution. Slight problems were posed by the contrails of aircraft, as a major European N-S airline passes over the lake. Areas covered by contrails or clouds visible on the video display were excluded from the lake surface.

For the remaining surface of the lake, the mean satellite measured surface temperature (T_{sat}) and its standard deviation were then calculated.

c) Atmospheric corrections

Atmospheric corrections were calculated with the WINDOW model using atmospheric soundings from Payerne, 30 km N.E. of the Lake. Night (00.00 UT) and day (12.00 UT) radiosonde data on magnetic tape were provided by the Zentralamt des Deutschen Wetterdienstes, Offenbach am Main. Formerly

(REINIGER 1980) only nighttime radiosonde data from the European Meteorological Bulletin were available.

4. Steinhuder Meer (F. Wilmers and U. Wienert, Institute for Meteorology and Climatology at the University of Hannover)

During the Joint Measuring Campaign of June 1979 at Ruthe, Northern Germany, water temperatures of a lake, Steinhuder Meer, and of an irrigation pond were taken for the calibration of thermal aircraft and HCMR data. The temperature sampling points on the lake and the superimposed grid of the HCMM scene are shown in Fig. III.4.7.

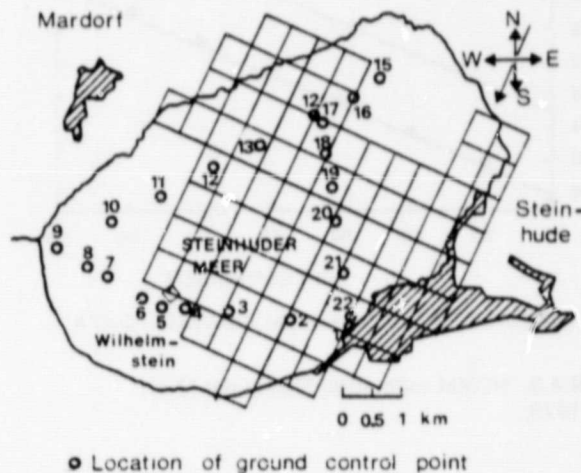


Fig.III.4.7. Control points on Lake Steinhude and grid of pixels from June 22nd 1979, 00:25 GMT.

Unfortunately, during the night of a valid HCMM overpass on 22 June 1978, continuous water surface temperatures were only recorded at the irrigation pond, too small to show up on the satellite scene. Therefore, a relation was established between water surface temperatures of the lake and of the irrigation pond and using this relation, night lake surface temperatures were deduced from daytime lake surface temperatures measured on 22 June 1979. For the calibration of 16 June 1978 only one measurement of the water surface temperature was available.

Atmospheric corrections were calculated with the KORR model (WIENERT 1980) and the WINDOW model. The resulting calibration curve of the HCMR for 22 June 1979 is shown in Fig. III.4.8 indicating an offset of the calibration of 10.1°C . Correcting for thermal emissivity, this offset is reduced to 9.1°C . Further details of the calibration procedure, as well as the influence of various thermal emissivities and of reflection are given in an extensive report (WILMERS and WIENERT 1981).

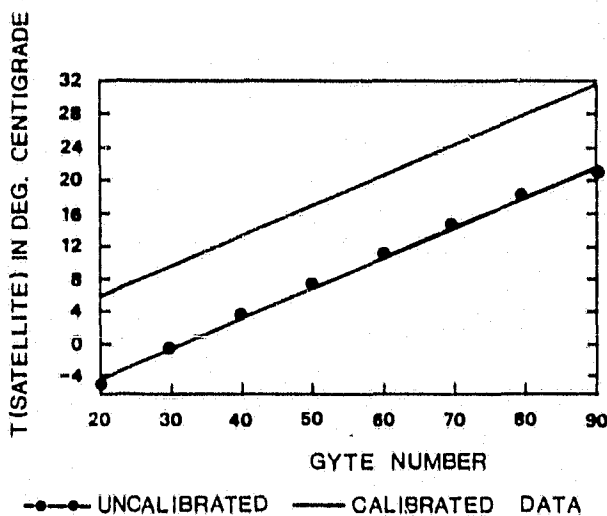


Fig. III.4.8. HCMR calibration Steinhuder Meer, 22.6.1979;

5. Crau-grassland. (B. Seguin, Bioclimatologie INRA-Avignon, P. Reiniger, JRC, Ispra)

During the summer of 1978 (July-October) and from April 1979 to March 1980, the surface temperature of one irrigated and one dry grassland plot was monitored with a Heiman KT-24 infrared radiometer. The radiometers were installed in two measuring stations which formed a part, respectively of an irrigated zone of $10 - 30 \text{ km}^2$ and of a dry zone of about 100 km^2 . These two measuring stations directly furnished the values of T_g for the calibration. Three night/day passes of the satellite, i.e. 6 scenes of the summer of 1978 were geometrically rectified and superimposed on a topographic map on a scale

1 : 250,000. In this way, the location of the measuring station could be identified on the HCMR scene and the corresponding satellite measured temperature (T_{sat}) could be obtained.

The fact that even "homogeneous" land surfaces present considerable temperature differences and that the geometrical correction is not better than ± 1 pixel, may lead to differences in T_{sat} of up to 2°C . This effect is especially noticeable as one measuring station was established rather close ($\sim 500 \text{ m}$) to the border between the irrigated and the dry zone. Day and night (00.00 and 12.00 UT) radiosonde data from Nimes, distant about 30 km from the site were used in the WINDOW program for atmospheric corrections to calculate T_{sat}^* . The radiosonde data on magnetic tape were provided by the Zentralamt des deutschen Wetterdienstes, Offenbach am Main. The results of this calibration attempt are presented in Table III.4.3.

6. Land and water surface. The Netherlands (G.J.A. Nieuwenhuis, ICW, Wageningen).

The calibration attempt was carried out at the occasion of an underflight experiment with a 4-channel thermal scanner carried out on 31 July 1978 in the Province of Drenthe. Ship-born water temperatures of the North Sea and Lake IJssel were obtained. These measurements were not converted to radiometric temperatures.

Over land the maximum and minimum temperatures observed on the airborne scanner served as ground temperature (T_g) for comparison with the satellite measurements. Atmospheric corrections were calculated with the RADTRA model using a value of $K_2 = 10.0$ and radiosonde data from De Bilt. The corrections were applied to T_{sat} and not to T_g as in the other calibration attempts.

7. Adriatic Sea (G. Maracci, JRC, Ispra)

The sea surface temperature was measured

from an oceanographic platform situated off the coast of Venezia (45° 19' N, 12° 31' E). The measurement was carried out with a PRT-5 radiometer, vertically 8-10 m above the sea surface and simultaneously with the passage of the satellite. During the day-time passage the transmittance of the atmosphere was likewise measured with a 4-channel LANDSAT-compatible radiometer (EXOTECH mod. 100). The HCMM surface temperature was taken as the mean of 58 pixels around the platform with a standard deviation of 0.4°C. Atmospheric corrections were calculated with the WINDOW model using atmospheric soundings from Udine, 100 km to the N.E. of Venezia. The results are presented as part of Table III.4.3.

Comparison with Thermal Data from Other Satellites

A first comparison was carried out with data from NOAA-5 and from TIROS-N. Superposition of the scenes was carried out by CTAMAN-Ecole des Mines, Sophia Antipolis. The comparison with NOAA on 17 July 1978 concerned an area of 643 NOAA-5 pixels in the Mediterranean Sea, south of Marseille.

HCMM scenes AA. 0082-0208.03

AA. 0082-1340.0.2

NOAA-5 passage: 08.35 UT

The following temperatures were recorded (°C):

HCMM/Night	NOAA-5	HCMM/Day
14.1 ± 0.5	26.3 ± 0.5	16.5 ± 0.8

showing a difference of 10 - 12°C between the radiometers of the two satellites, the HCMR giving the lower temperature.

The comparison with TIROS-N on 31 August 1979 again concerned the Mediterranean Sea south of Marseille and, in addition, a dry and an irrigated area of the Crau.

HCMM scenes: Orbit 7283, equator crossing time 00.30 UT;

Orbit 7290, equator crossing time 11.50 UT;

TIROS-N 14.01 UT

The following temperatures were recorded by the two satellites (°C):

	HCMM/Night	HCMM/Day	TIROS-N
Sea	10.8	11.5	19.3
Crau-dry	6.9	25.9	32.8
Crau-air	5.7	21.1	28.3

The daytime temperatures observed by the HCMR were lower by 6.9 - 7.8°C than those indicated by TIROS-N.

Conclusions

Analysing the calibration data concentrated in Table III.4.3, a few conclusions may be attempted:

1. From 34 to 528 days after launch (AL) there seems to be no long time trend in the calibration of the HCMR. The regression of ΔT on the number of days after launch, AL, is given by the equation

$$\Delta T = 5.85 + 4.53 \times 10^{-4} AL$$

with a highly non-significant regression coefficient of $R^2 = 7.72 \times 10^{-4}$.

2. The intercept of the above regression equation of 5.85 indicates that the offset of 5.5°C which had been introduced into the calibration equation of the HCMR after the validation study by SUBBARAYUDU (1979) was not valid during the whole period investigated. The differences of between 7 - 12°C with temperatures measured by NOAA-5 and TIROS-N point in the same direction.

3. The linear regression of T_{sat}^* , the theoretically correct satellite temperature, on T_{sat} , the actual temperature given by the HCMR is represented by the equation:

$$T_{sat}^* = 7.55 + 0.95 T_{sat}$$

The regression was established for 39 of the 43 points in Table III.4.3 excluding point (6).

Again, the intercept of 7.55 shows that the offset of 5.5°C should be abandoned. The low regression coefficient $R^2 = 0.64$ indicates that the relation is not linear or that the ground or satellite measurements, or both, do not form homogeneous populations. This could point to sporadic changes in scanner performance.

4. The assumption that the calibration of the HCMR is not linear is statistically supported by the parabolic regression of T_{sat}^* on T_{sat} given by:

$$T_{sat}^* = 6.87 + 0.7 T_{sat} + 0.01 (T_{sat})^2$$

with a regression coefficient $R^2 = 0.89$. When drawing conclusions, though, one should consider that the high temperatures responsible for this non-linear regression were all measured with the same type of radiometer on the Crau test site (5). Therefore, erroneous readings at high temperatures of this radiometer are not to be excluded, though independent measurements in the Netherlands (6) seem to speak against this hypothesis.

5. The hypothesis of sporadic changes in the calibration is not to be excluded as 38 days after launch, calibration results over a pine forest in Germany (1) and over Lake Geneva (3) agree with those of SUBBARAYUDU (1979) at White Sands. This is no longer the case 54 days after launch.

6. One may conclude that much additional work is needed on the calibration of thermal infrared data from satellites. Data from different satellites should be intercalibrated and suitable reference surfaces should be delimited and monitored regularly.

Albedo

No ground measurements of albedo were carried out for calibration purposes and, therefore, data from the literature had to be used to comment the albedo values furnished by the HCMR in the 0.55 - 1.1 μm band.

Table III.4.6 presents the albedo measured

	17.7.78	28.7.78	12.8.78
Crau irrig.	0.16 \pm 0.012	0.15 \pm 0.012	0.14 \pm 0.017
Crau dry	0.16 \pm 0.010	0.16 \pm 0.010	0.14 \pm 0.012
Medit. sea		0.13 \pm 0.004	0.04 \pm 0.007

Table III.4.6. Satellite measured albedo of an irrigated and of the dry zone of the Crau and of a part of the Mediterranean Sea (REINIGER et al. 1981).

by the HCMR over an irrigated and over a dry grassland area of the Crau (Southern France) and over the Mediterranean Sea. These values are on the low side compared with results of ground measurements of albedo found in the literature. On a grassland site about 30 km from the Crau, albedo values ranging from 0.19 - 0.27 were observed (SEGUIN 1978), while measurements from a helicopter over natural pastures in Israel gave a value of 0.19 in the dry and of 0.29 in the rainy season (STANHILL 1970). The albedo of water is given as a rather constant value of 0.05 (MONTEITH 1973).

The differences of 20-40% between the albedo measured by the HCMR and those measured on the ground can be explained by the effect of the atmosphere, which can be assumed to have this order of magnitude. It should further be noted that albedo on the ground is measured in the 0.4 - 3.0 μm band compared to 0.55 - 1.1 μm for the HCMR.

The albedo of the Crau in Table III.4.6 compares well with that measured by NIMBUS II over the coastal region of Israel with values of 0.15 - 0.20 on 30 June 1966 and 0.10 - 0.15 on 5 July 1966 (POUQUET and RASCHKE 1968).

References

- ALBUISSON M., PONTIER L. and WALD L., 1979. A comparison between sea surface temperature measurements from satellite NOAA-4 and from airborne radiometer Aries. *Oceanologia Acta* 2 (1), 1-4.
- BECKER F., 1978. Température superficielle de la mer et la transmission atmosphérique par radiométrie différentielle. *Sci. Techn. CNEXO, Actes colloq. No. 5*, 141-160.
- BECKER F., NGAI W. and STOLL M., 1980. An active method for measuring thermal infra-red effective emissivities: Implications and perspectives for remote sensing. Invited paper, COSPAR, Budapest, also *Tellus Newsletter No. 21*, JRC, Ispra, 18 pp.
- BIGNELL K.J., 1970. The water vapour infrared continuum. *Quart. J. Roy. Meteor. Soc.* 96, 390-403.
- BROWN O.B., 1980. SST interannual variability in the Arabian Sea. COSPAR/SCOR/IUCRUM Symp. on Oceanography from Space, Venezia, 26-30 May, 1980.
- COMMISSION INTERNATIONALE pour la protection des eaux du Lac Léman contre la pollution, 1978. Rapports sur les études et recherches entreprises dans le bassin lémanique. Lausanne.
- COMMISSION INTERNATIONALE pour la protection des eaux du Lac Léman contre la pollution, 1979. Rapports sur les études et recherches entreprises dans le bassin lémanique. Lausanne.
- DESCHAMPS P.Y. and PHULPIN T., 1980. Atmospheric correction of infrared measurements of sea surface temperature using channels at 3.7, 11 and 12 μm . *Boundary-Layer Meteorology* 18, 131-143.
- GOMBEER R., 1980. The comparison of HCMM-satellite registered surface temperatures with ground temperature measurements over Belgium: A calibration study. *Tellus Newsletter No. 18*, JRC, Ispra, 16 pp.
- GOSSMANN H., 1980a. A calibration attempt of HCMM scene AA-0034.0213.0.3 of May 30, 1978. *Tellus Newsletter No. 18*, JRC, Ispra, 6 pp.
- GOSSMANN H., 1980b. Satelliten-Thermabilder. Ein neues Hilfsmittel Geographischer Forschung? Die Analyse einer HCMM-Aufnahme der Oberrheinebene und ihrer Randgebirge. *Habilitätsschrift Univ. Freiburg*.
- GRASSL H. and KEOPKE P., 1980. Corrections for atmospheric noise and surface reflectivity in satellite borne SST-measurements. COSPAR/SCOR/IUCRUM Symp. on Oceanography from Space, Venezia, 26-30 May, 1980.
- HASSE L., 1971. The sea surface temperature deviation and the heat flow at the sea-air interface. *Boundary-Layer Meteorology* 1, 368-379.
- IMBAULT D., 1980. Determination of sea surface temperature by I.R. differential radiometry. COSPAR/SCOR/IUCRUM Symp. on Oceanography from Space, Venezia, 26-30 May, 1980.
- MARLATT W.E., 1967. Remote and in situ temperature measurements of land and water surfaces. *J. Applied Meteorology* 6, 272-279.
- MONTEITH J.L., 1973. *Principles of Environmental Physics*. Edward Arnold (Publishers) Ltd., London, 241 pp.
- NIEUWENHUIS G.J.A., 1980a. Influence of the atmosphere on thermal infrared radiation. *Tellus Newsletter No. 14*, JRC, Ispra, also published as *Nota 1159*, ICW, Wageningen.
- NIEUWENHUIS G.J.A., 1980b. Application of HCMM-satellite and airplane reflection and heat maps in agro-hydrology. *Tellus Newsletter No. 19*, JRC, Ispra, 18 pp.
- PAULSON C.A. and PARKER T.W., 1972. Cooling of a water surface by evaporation, radiation and heat transfer. *J. Geophys. Res.* 77, 491-495.

- POUQUET J. and RASCHKE E., 1968. A preliminary study of the detection of geomorphological features over northeast Africa by satellite radiation measurements in the visible and infrared. NASA, TND-4648.
- PRICE J. C., 1980. On the atmospheric correction to satellite thermal infrared measurements. GSFC, communication to HCMM investigators.
- PRICE J. C., 1981. The contribution of thermal data in Landsat multispectral classification. Photogram. Engng. and Rem. Sens. 47 (2), 229-236.
- RANGASWAMY S. and SUBBARAYUDU J., 1978. Program RADTRA to compute atmospheric attenuation correction. Systems and Applied Sciences Corporation, Riverdale, Maryland 20840. NASA contract NASS-24272.
- REINIGER P., 1980. Calibration of HCMM thermal data. Tellus Newsletter No. 18, JRC, Ispra, 19 pp.
- REINIGER P., HUYGEN J., MEGIER J. and SEGUIN B., 1981. Estimates of regional evapotranspiration in south-eastern France using thermal and albedo data from the Heat Capacity Mapping Mission Satellite. First Thematic Conference "Remote Sensing of Arid and Semi-Arid Lands, Cairo, Egypt, Nov. 1981.
- SEGUIN B., 1978. Estimates of regional ET from HCMM data: Summary of 1977 experiment and final arrangement for 1978 in Southeastern France Test Site. 2nd Meeting of Tellus Project Working Group II, Wallingford, February 21-22, 1978.
- STANHILL G., 1970. Some results of helicopter measurements of the albedo of different land surfaces. Solar Energy 13, 59-66.
- STURM B., 1980. Atmospheric correction of satellite and aircraft remotely sensed data in the visible spectral range and quantitative determination of suspended matter in the surface layer of water bodies from remotely sensed upwelling spectral radiance. EARSEL Summer School, Dundee, 1980.
- SUBBARAYUDU J., 1979. Heat Capacity Mapping Mission (HCMM) Validation Study. Final Report. Report No. R-SAG-3/79-01, Systems and Applied Sciences Corporation, Riverdale, Maryland 20840.
- TABATA S., 1980. On the accuracy of satellite observed sea surface temperatures. COSPAR/SCOR/IUCRUM Symp. on Oceanography from Space, Venezia, 26-30 May, 1980.
- WALD L. and NIHOUS G., 1980. Ligurian Sea: Annual variation of the sea-surface thermal structure as detected by satellite NOAA-5. Oceanologica Acta 3 (4), 465-469.
- WIENERT U., 1980. Versuch einer quantitativen Oberflächentemperaturanalyse von Flugzeugscanneraufnahmen im thermischen Infrarot. Diplomarbeit, Inst. for Meteorology and Climatology at the University of Hannover (unpublished).
- WILMERS F. and WIENERT U., 1981. Calibration of the Heat Capacity Mapping Radiometer in the thermal infrared at Lake Steinhude in June 1979. Report on contract No. CN 05 9941 with JRC, Ispra, Institute for Meteorology and Climatology at the University of Hannover.

Part 5 - Development and Application of Auxiliary Methods and Techniques

1. Usage of Filtering Techniques for Scaling-up Simulation

V. Di Gennaro
Centro Studi Applicazioni Tecnologie Avanzate
Bari, Italia

Introduction

It is well known that the grey level of image pixels depends on the radiance coming, in a particular spectral range, from the ground areas corresponding to the pixels. If each area is homogeneous no problem exists in its interpretation; if, on the contrary, a lot of different objects are contained, they contribute, in different ways, to the overall grey level of the pixel.

The problem becomes more important as greater dimension pixels are involved, i.e. the problem must be faced to understand the informative content of the data.

Images from HCMM are a typical example of this with their pixels, dimensioned 500 x 500 m. It is then necessary to study the so-called scale effect to understand how detailed information aggregates give rise to low or very low resolution data as they are detected, for example, from a high altitude platform.

The first question to which this work was devoted was the simulation of HCMM data starting from better resolution ones.

The following approach was adopted however:

- to determine a methodology which permits the correlation of different resolution data;
- to test the methodology for the simulation of slight altitude increase (usage of aircraft

data);

- to simulate if possible HCMM images.

The methodology is based on filtering techniques in the hypothesis that all changes due to altitude increase can be represented by a point spread function. These aspects, together with a "practical" introduction to the filtering technique, are particularly stressed all along the work. As will be seen, no attempt is made, however, to simulate HCMM data; attention is mainly focused on the scale effect in its general aspects, also for its importance in problems such as registration between images.

Scale Effect : Theoretical Model

Possible Reduction Methods

At first sight the simulation of an altitude increase of acquisition platform consists of an image reduction and this is equivalent to a suitable smoothing. This can be achieved by two methods:

- a) neighbourhood averaging techniques,
- b) filtering techniques.

- a) Neighbourhood averaging techniques.

These consist of an arithmetical or weighted average of the grey values on a number of pixels equal to the reduction factor (for example 4 x 4 pixels if the reduction factor is 16 : 1).

b) Filtering techniques. If this operation is realized in the spatial domain, it consists of the convolution of the image with the weighting mask and then of the decimation of the points according to the appropriate scale factor.

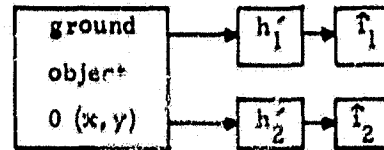
It is interesting to note that the former approach can be viewed as a particular case of the filtering technique where the filter dimensions are equal to the reduction factor. In this case the two steps of convolution and decimation give an output equal to the averaging approach output.

In both cases the weighting mask has the role of a Point-Spread Function (PSF), so its shape (and hence the Modulation Transfer Function (MTF) shape) should represent the physical characteristics of the process.

The averaging approach is certainly very convenient from a computer time point of view, but it is considerably limited for accurate simulations. The weighting mask must have, in fact, a Fourier transform as similar as possible to the MTF process itself. Since the more PSF samples there are, the better the transform shape can be controlled, it is convenient to use large dimensioned masks. In the averaging technique, however, mask dimensions are fixed by the scale factor so that for small reductions very little mask must be used with the consequent impossibility of controlling the MTF shape.

Discrete Image Formation Process

To understand how the function simulating a scaling up can be obtained, it is worthwhile examining the mathematical processes generating discrete images. In a general manner, the imaging process at the two altitudes can be briefly represented as follows:



where \hat{I}_1 is the discrete image at lower altitude q_1

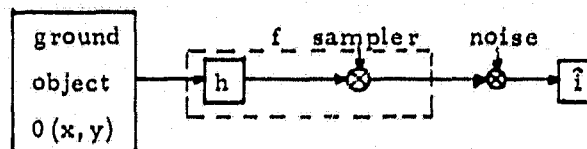
\hat{I}_2 is the discrete image at higher altitude $q_2 = Kq_1$ ($K > 1$)

h_1' is the global PSF for image formation at altitude q_1

h_2' is the global PSF for image formation at altitude $q_2 = Kq_1$ ($K > 1$).

This means that the same ground object is seen in different manners (i.e. with different PSFs) and so different images are obtained.

The figure below shows a more detailed representation of discrete image formation process:



i.e. each PSF is seen as composed of a continuous PSF followed by a sampler.

The assumption is made that the signal-to-noise value is sufficiently high so that the noise can be ignored.

It is interesting to carry out a graphical derivation (in one-dimensional form) of the process.

The assumption is made that SIPSF are involved, so that the degrading process can in the same way be represented by its MTF.

The ground object corresponding to the image being considered is represented by the function $O(x)$ (Fig.III.5.1) while it is assumed that the continuous PSF h_1 is given by Fig.III.5.1b). The integration performed on the photodetector surface is mathematically represented by the convolution of $O(x)$ with $h_1(x)$ (i.e. the multiplication of $O(f)$ and $H_1(f)$ (Fig.III.5.1c).

ORIGINAL PAGE IS
OF POOR QUALITY

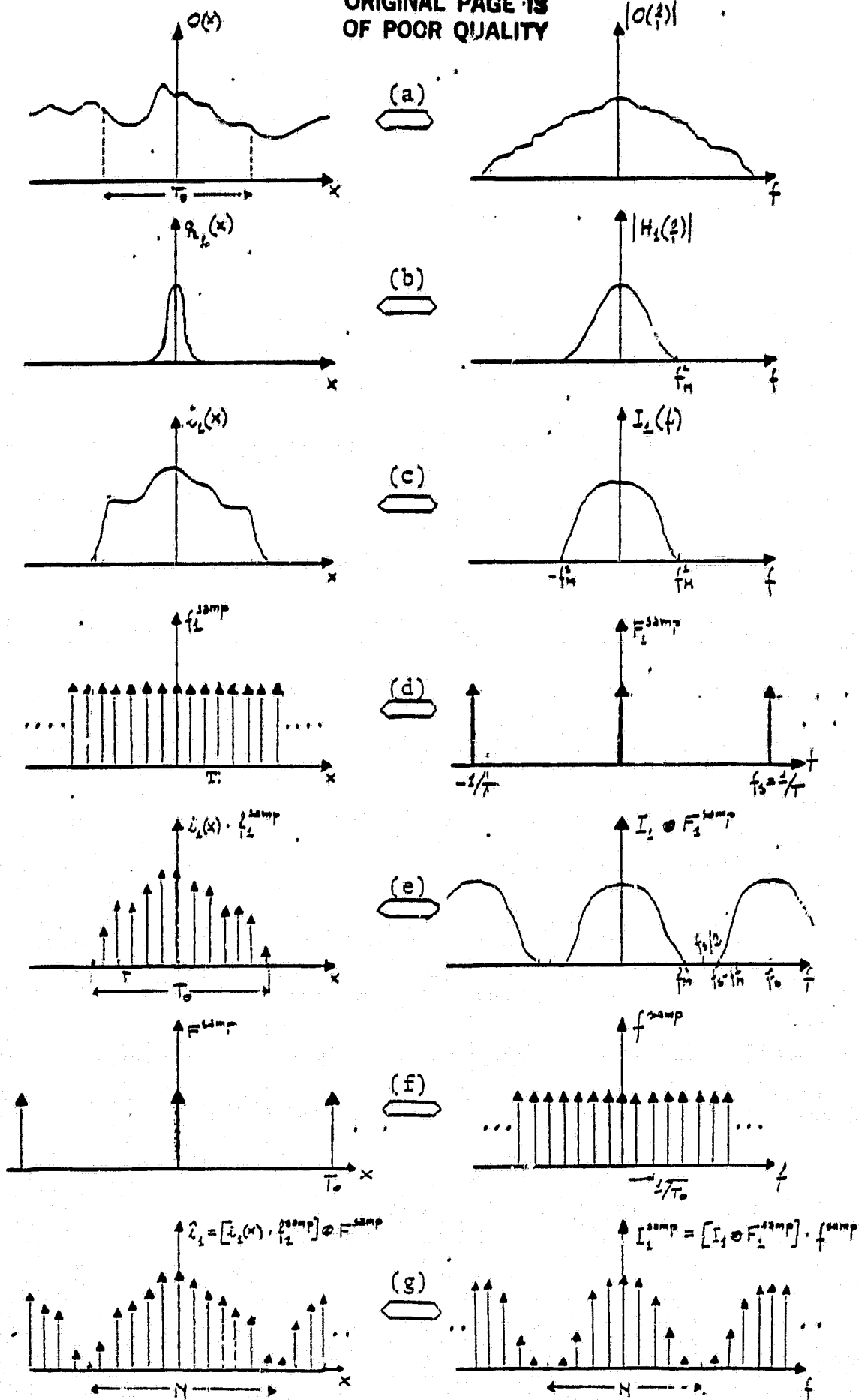


Fig. III.5.1.

ORIGINAL PAGE IS
OF POOR QUALITY

The assumption can be made that the convolution output has its spatial frequency content limited to a f_M^1 frequency. The filtered image is then spatially sampled. The assumption can be made that the sampling system works so that the image has neither overlaps nor gaps between pixels. Referring, for example, to the scan in the flight direction, this condition is satisfied by the frequency.

$$f_s = \frac{V/h}{n\alpha}$$

where V = platform velocity

h = platform altitude

n = number of sensors

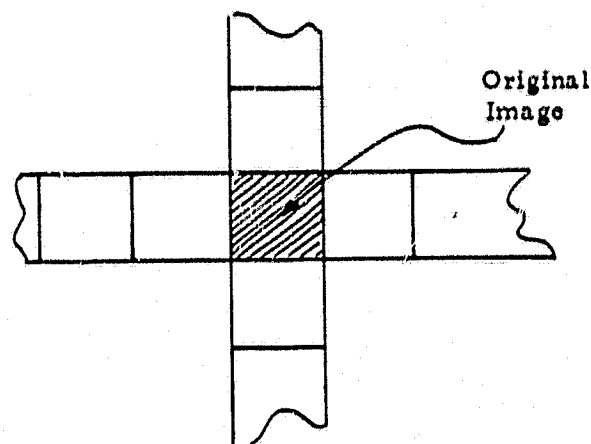
α = instantaneous field of view (IFOV).

With this assumption and supposing the sampler is an ideal Dirac delta function, it can be written

$$f^{\text{samp}} = \sum_{j=-\infty}^{+\infty} \delta(x - j\Delta x_{\text{samp}}) \quad (1)$$

where Δx_{samp} is the pixel dimension depending on the altitude and system IFOV. It is assumed that for q_1 altitude $\Delta x_{\text{samp}} = T$ (see Fig. III.5.1d). As it is easily understood the sampling is equivalent to a multiplication in space domain, i.e. a convolution in frequency domain. The result is shown in Fig. 1e. It must be noted that if the folding frequency ($f_s/2$) is less than f_M^1 (i.e. if data are undersampled), the aliasing phenomenon appears.

To provide a mapping between transform domain and image space and to permit transformed data to be handled by computer, it is necessary to discretize also the Fourier domain. The so-called Discrete Fourier Transform (DFT) is accomplished by sampling the continuous Fourier transform by means of an f^{samp} with $1/T_0$ frequency step (Fig. III.5.1f); this produces the iteration of the space signal as it appears from Fig. III.5.1g. For the two-dimensional case, this periodicity is equivalent to the situation depicted as follows:



From this it follows (ref. /2/) that when finite extent discrete arrays are involved, "circular convolution" must be used.

It must be noted that in the frequency domain a number of samples is generated equal to spatial domain one (for primary components). This number is obviously $N = T_0/T$.

The same graphical derivation can be carried out for the upper altitude (q_2) image, i_2 . The input (ground object $o(x)$) is the same as in Fig. III.5.1.a. Generally, the acquisition system is a different one so a new PSF, $h_2(x)$ is now involved; referring to the case of a loss of resolution, the width of its non-zero region is, however, greater than the lower altitude one.

In this particular case the acquisition system is the same, the upper altitude PSF can be assumed to be carried out only by means of geometrical properties; other effects due to altitude increase (just like atmospheric effects, etc.) are not taken into account. In this hypothesis the timescaling relation is used (ref. /3/), i.e. if K is the altitude factor, then

$$\begin{aligned} h_2(x) &= h_1(x/K) \\ H_2(f) &= KH_1(Kf) \end{aligned} \quad (2)$$

If the two altitudes are twice the other, the

$h_2(x)$ can be represented as in Fig.III.5.2b where $f_M^2 = 1/2 f_M^1$; Fig.III.5.2c shows the convolution of this PSF with the ground object.

Also the pixel dimensions are obtained by means of the scaling of the lower altitude pixel, i. e. now $\Delta x_{\text{samp}} = 2T$, as can be seen in Fig.III.5.2a; the result of the sampling is represented in Fig.III.5.2e. It is obvious that now the sample's number is half the lower altitude one. The step corresponding to Fig.III.5.2f and Fig.III.5.2g is equivalent to that seen in Figs. III.5.1f and III.5.1g.

Determination of a Scale-Change Function

A Fourier transform pair $g \leftrightarrow G$ which permits one to carry out \hat{i}_2 directly from \hat{i}_1 must be defined. This pair must satisfy the relations

$$\mathcal{J}_2 = \mathcal{J}_1 \cdot G \quad (3a)$$

$$\hat{i}_2 = \hat{i}_1 \bullet g \quad (3b)$$

where with \mathcal{J}_1 (\mathcal{J}_2) the DFT of \hat{i}_1 (\hat{i}_2) is denoted, i. e. a complex function. It immediately appears that such a determination can be easily made in the frequency domain. In fact, if

$$\begin{aligned} \mathcal{J}_1(u, v) &= I_1(u, v) \exp [i \psi(u, v)] \\ \mathcal{J}_2(u, v) &= I_2(u, v) \exp [i \phi(u, v)] \\ G(u, v) &= G(u, v) \exp [i \rho(u, v)] \end{aligned} \quad (4)$$

Solving the equation (3a) gives $G(u, v) = G(u, v) \exp [i \rho(u, v)]$ where

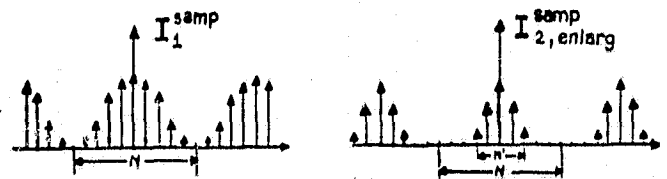
$$\begin{aligned} G(u, v) &= I_2(u, v) / I_1(u, v) \\ \rho(u, v) &= \phi(u, v) - \psi(u, v) \end{aligned} \quad (5)$$

Liv and Gallanger give a detailed description of the problems involved in minimizing the error between \mathcal{J}_2 and $\mathcal{J}_1 \cdot G$ functions. The main problems concern \hat{i}_1 and \hat{i}_2 phases choice; in the present form phases are, however, neglected so that the model is restricted to magnitude values, i. e.

$$G = G(u, v) = I_2(u, v) / I_1(u, v) = I_2^{\text{samp}} / I_1^{\text{samp}} \quad (6)$$

It is not so easy to solve equation (3b) if an operation inverse to the convolution were to be used.

In order to realize a significative comparison, the same number of samples, for the two altitudes spectra, should be used. Because I_2^{samp} has the primary component with N' samples, it is convenient to enlarge it up to N samples by adding zeros. Then the spectra to be compared are:



Referring to the primary component N samples, it is possible to write

$$I_{2, \text{enlarg}}^{\text{samp}} = O(f) \cdot H_2(f) \cdot f^{\text{samp}} \quad (7)$$

$$I_1^{\text{samp}} = O(f) \cdot H_1(f) \cdot f^{\text{samp}}$$

so it is true that

$$G = \frac{I_{2, \text{enlarg}}^{\text{samp}}}{I_1^{\text{samp}}} = \frac{H_2'(f)}{H_1'(f)} \quad (8)$$

$$\text{where } H_{1, 2}'(f) = H_{1, 2} f^{\text{samp}} \quad (9)$$

is the acquisition system's continuous MTF sampled with $1/T_0$ step.

The expression (8) states clearly that the G function can be carried out either directly from the data or from information on the acquisition system.

Since spatial filters are passive devices, they do not amplify the signal. The G function then must satisfy the constraint

$$G(u, v) \leq 1$$

While this must be tested for different sensors, it is automatically true when H_2 is carried out by the scaling of H_1 ; this also pre-

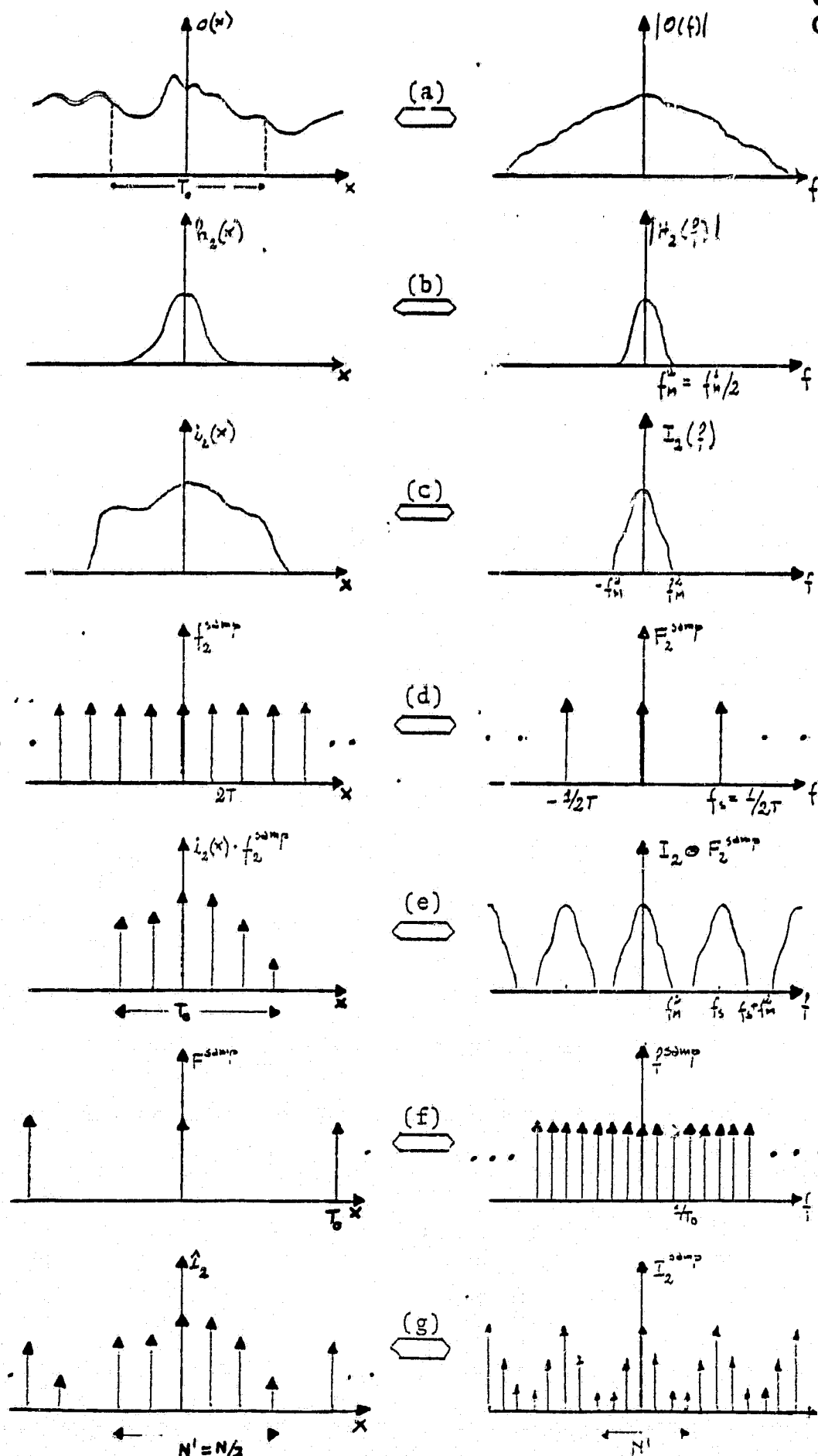


Fig. III.5.2.

vents any problem coming from H_1 zeros. The g function is obtained by means of the Inverse Discrete Fourier Transform (IDFT). This g is constituted of N samples, but only a few of them are different from 0.

Before applying the proposed method for a generical scaling-up, it is better to verify it by performing the filtering in order to re-obtain \hat{i}_2 starting from \hat{i}_1 . This operation can be performed either in the spatial or in the frequency domain.

In the latter one, for I_2^{samp} to be re-obtained, the multiplication of G and I_1^{samp} must be realized. This gives, however, $I_{2,\text{enlarg}}^{\text{samp}}$ so it is necessary to reduce it by dropping $(N-N)/2$ zero value points at each edge.

The filtering in the spatial domain is obtained making a convolution of i_1 with the g samples. The output consists of N samples T -spaced whose spectrum is just I_2^{samp} . If a decimation of samples is made with a factor K equal to the scale factor (in the particular case of 2.2 $K = 2$), I_2^{samp} is just obtained. The decimation is in fact equivalent to the convolution in the frequency domain with a pulse train, spaced $1/KT$.

This produces a loss of a part of the spectrum due to the aliasing; this part is, however, just the one containing zero values so that the final result is similar to Fig. III. 5. 2g.

It must be observed that the considered model is based on the assumption of the existence of a unique MTF for each altitude, i. e. in the hypothesis of shift-invariant PSF. If this is not true, the model is no longer applicable in its present form.

Scale Effect : Operative Approach

The problem involved in the simulation of a higher altitude image are:

- determine the appropriate scale change filter,
- perform the filtering operation.

Determination of the Scale Change Filter

To solve the problem with a deterministic approach, it is necessary not to consider data any longer, but to use only a priori information. Referring to expression (8) the G filter can be carried out by means of ratioing discrete MTFs.

This obviously requires the exact knowledge of transfer functions at each altitude; if these are not known, they must be constructed from the knowledge of imaging processes, of all degradation sources involved and of their models.

A quick survey of the principal degradations of an acquisition system is reported in App. II of /26/ but it appears evident that it is a very hard job to use this approach for carrying out the global transfer function. On the assumption, however, that the lower altitude MTF is known and if the image is seen at the upper altitude, but the same acquisition system is desired, it is possible to easily arrive at the G function.

According, in fact, to expression (2), the G filter project procedure can be schemed as in Fig. III. 5. 3.

It must be noted that the time-scaling property can be indifferently applied, either in space domain or in the frequency domain.

The significance of the operation $G = H_2/H_1$ is the one explained in § 2. 3.

Neglecting the phase term, the function

$$G_{m,n} = \begin{cases} \frac{H_{2m,n}}{H_{1m,n}} & \text{if } \frac{H_{2m,n}}{H_{1m,n}} \leq 1 \\ 1 & \text{if } \frac{H_{2m,n}}{H_{1m,n}} > 1 \end{cases} \quad (10)$$

ORIGINAL PAGE IS
OF POOR QUALITY

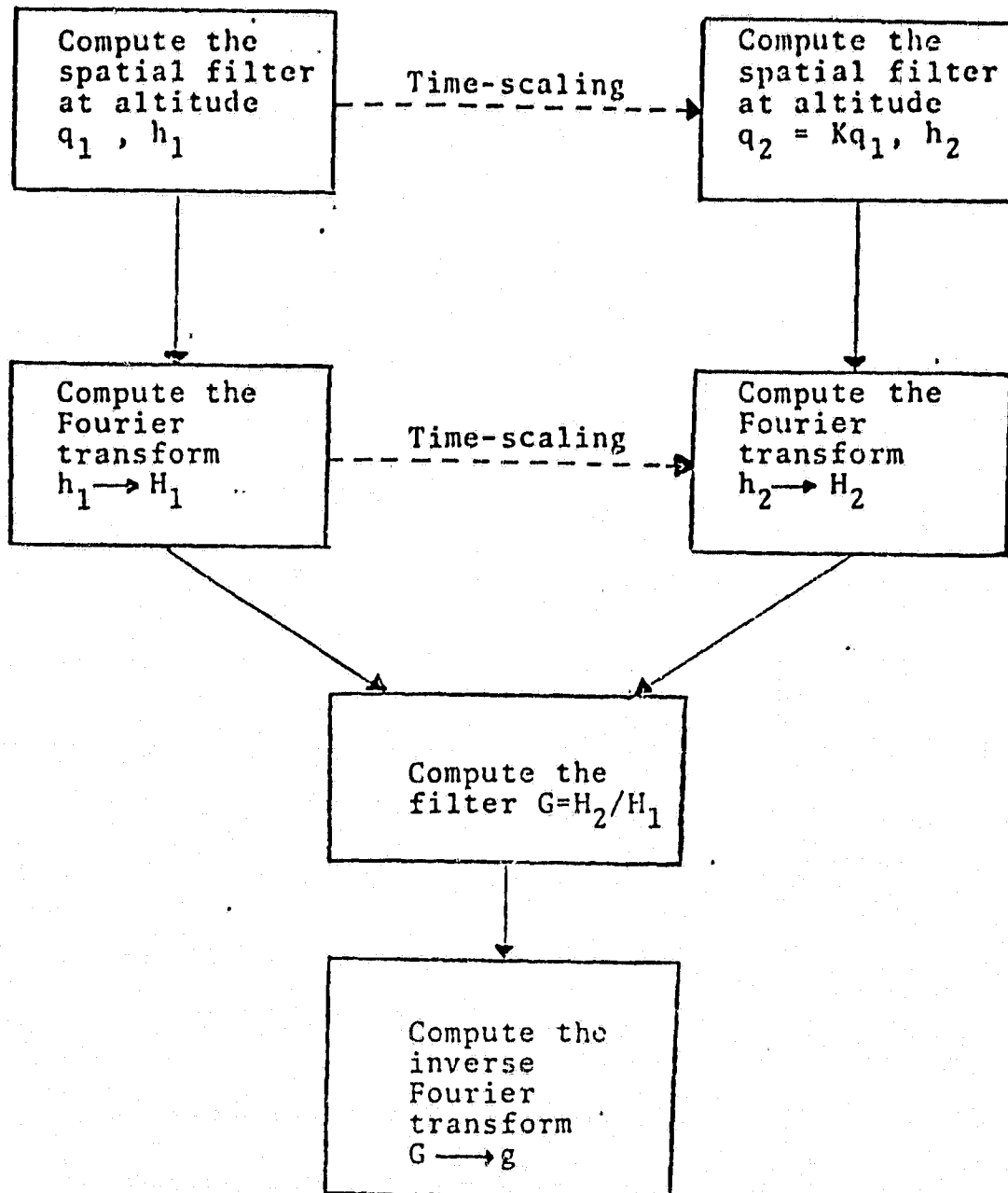


Fig. III.5.3. Scheme of the G filter project procedure

is computed.

If the modulation transfer function information is not available, the scale change filter must be evaluated directly from the data.

According to expression (6) the empirical approach is realized by ratioing the two altitudes image's spectra.

For the use of the Fourier techniques to be meaningful, it is necessary to remove from the images all the shift-variant effects. Apart from the eventual SVPSF components of the acquisition system, there are some standard SV effects related to the acquisition itself. The actual procedure should consist of a deconvolution for these SVPSFs, but empirical methods are usually employed to correct data.

In a first approximation two kinds of effects must be eliminated. The first is the so-called panoramic effect. This is due to the variation of the ground resolution when the view angle is changed (see Fig. III. 5. 4).

If this geometrical effect is left uncorrected, it gives incorrect spatial frequency values, especially for aircraft data where panoramic effect is more relevant. The correction can be done by using resampling techniques which obviously yield an increase of the sample number in the direction normal to flight-line.

Another effect depending on the position in the image plane is that due to the different atmospheric thickness for nadir and off-nadir observations. This yields a symmetrical lowering of the values at image edges with respect to actual values.

Instead of the deconvolution approach, this effect can be statistically corrected by means of best-fit techniques. The assumption is made that for almost uniform regions in the image, the profile of the average values of the columns in this region can be fitted with a

second order polynomial.

An example of this kind of correction is reported in Figs. III.5.5 and III.5.6. The first shows a corrected and an uncorrected 3000 m aircraft image, while Fig. 6 shows the profiles of average values of the columns (averaged on a number of lines). Actually there are two competing atmospheric effects present in remotely sensed data (ref. 5). The first is the attenuation which reduces the magnitude of sensed radiation.

The second is an active effect represented by scattering and/or emission. The balance between them depends on the scan direction relative to the sun's position. If the scanner looks toward the sun, the dominant effect is the attenuating one. The opposite effect dominates if the scanner looks away from the sun. It follows that the proposed correction is not completely exhaustive while a third-order curve should be necessary for a better correction; no attempt has however been made.

Another effect is that coming from atmospheric thickness increase due to platform altitude increase. As ref. 6 leads to simulating the increase of optical thickness, a linear transformation can be used which is independent of starting haze level, but dependent of added layer. It can then be considered shift-invariant and nothing has been done to take it into account.

When all known shift-variant effects have been removed both from lower and upper altitude images, Fourier techniques can be applied (in the assumption of SIPSF of the instrument).

In the following step the Fourier transform of "corrected" images at different altitudes must be calculated.

Given a discrete image in the form of the finite sequence $\{i(n_1, n_2)\}$, $n_1 = 0, \dots, N-1$, $n_2 = 0,$

ORIGINAL PAGE 19
OF POOR QUALITY

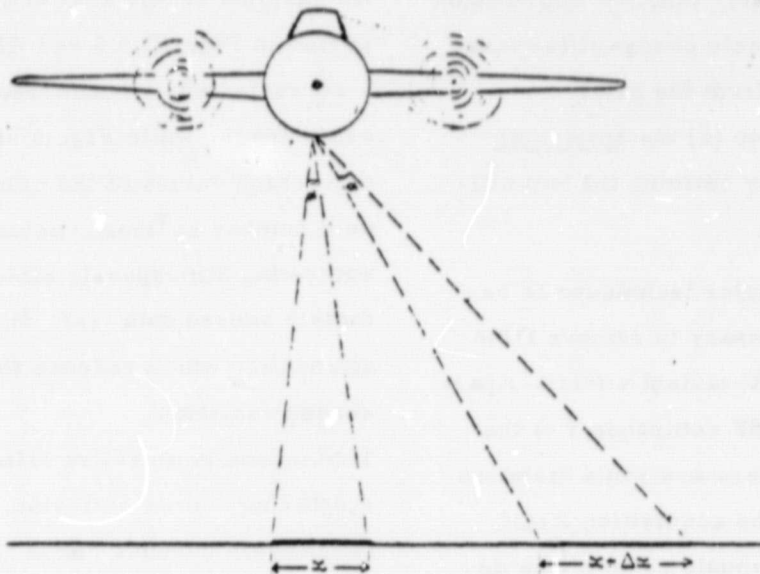


Fig. III.5.4.

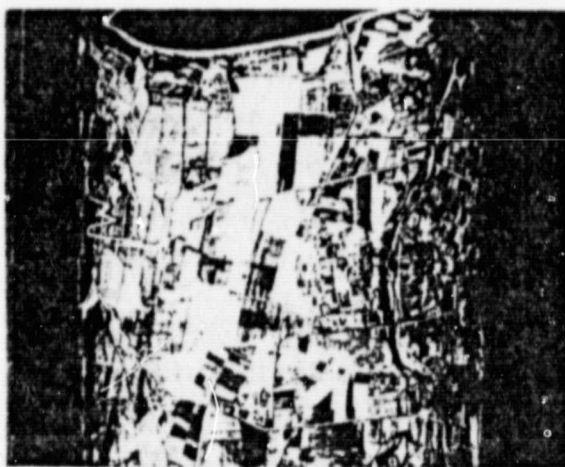


Fig. III.5.5a. uncorrected



Fig. III.5.5b. corrected

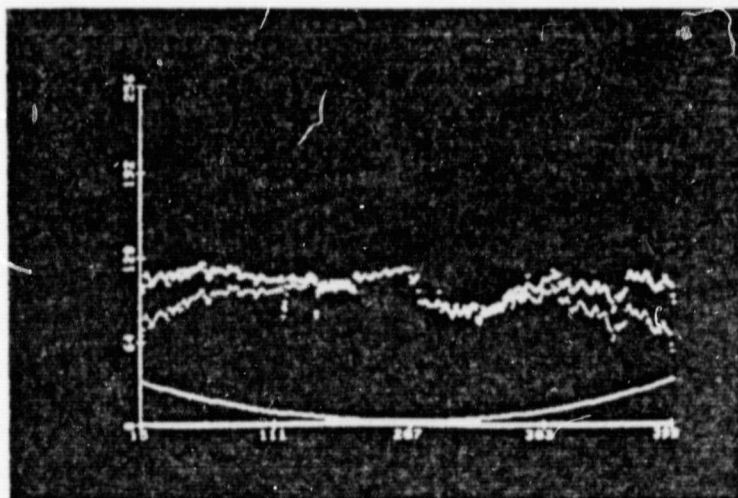


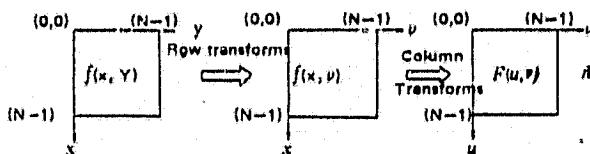
Fig. III.5.6.

..., N-1, its two-dimensional discrete Fourier transform is obtained as the z-transform along the two circles $z_1 = e^{j\omega_1}$, $z_2 = e^{j\omega_2}$ so that the transform is

$$\begin{aligned} I(k_1, k_2) &= I(z_1, z_2) \Big|_{z_1 = \exp [j(2\pi k_1/N)]}, \\ z_2 &= \exp [j(2\pi k_2/N)] = \\ &= \sum_{n_1=0}^{N-1} \sum_{n_2=0}^{N-1} i(n_1, n_2) \exp [-j(2\pi k_1 n_1/N)] \\ &\quad \exp [-j(2\pi k_2 n_2/N)] \end{aligned}$$

with $k_1 = 0, \dots, N-1$, $k_2 = 0, \dots, N-1$.

From an implementation point of view this two-dimensional transform is obtained by performing two one-dimensional transforms as is shown hereunder:



It must be noted that the result has a phase in which the meaningful parts of the transform are at the corners of the display. To help visual examination of the transform, it is convenient to shift the origin in the centre of the $N \times N$ points frequency domain. This is obtained either by re-ordering transform coefficients or by making use of the translation property of the Fourier transform pair

$$f(x, y) \exp [j2\pi(u_0 x + v_0 y)/N] \Leftrightarrow F(u - u_0, v - v_0) \quad (12)$$

i. e.

$$i(n_1, n_2) \exp [j(2\pi k_1 n_1/N)] \exp [j(2\pi k_2 n_2/N)]$$

$$\Leftrightarrow j(m_1 - k_1, m_2 - k_2)$$

if the shift is $k_1 = k_2 = N/2$ then

$$\begin{aligned} \exp [j2\pi(k_1 n_1 + k_2 n_2)/N] &= e^{j\pi(n_1 + n_2)} = \\ &= (-1)^{n_1 + n_2} \end{aligned} \quad (13)$$

so that by multiplying the pixel of coordinates (n_1, n_2) by $(-1)^{n_1 + n_2}$, the requested transform is obtained.

The software in its present form (implemented on IBM 370/158) produces only the spectrum of the image, i. e. being generally the Fourier transform complex

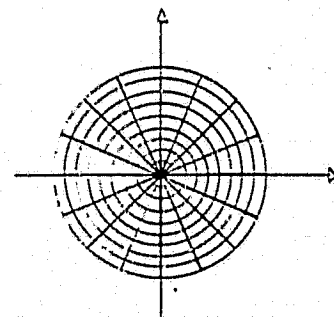
$$F(u, v) = R(u, v) + j I(u, v) \quad (14)$$

the available data are

$$|F(u, v)| = [R^2(u, v) + I^2(u, v)]^{1/2} \quad (15)$$

After the two altitude images' spectra are obtained, in accordance to (6), the scale change transfer function is carried out by ratioing these spectra. This ratio can be performed either on a point-to-point basis or in an integrated manner.

The first approach is certainly more general, but it is also more subjected to local fluctuations. The integrated approach consists in subdividing the original spectra into a lot of little areas as is shown in the following sketch:



The ratio of partial energies of corresponding regions gives the shape of the G function. On the assumption of circular symmetry of the scale change filter, the regions to be ratioed can simply be the rings.

With respect to the proposal to obtain the scale change function for whatever altitude increase, two cases can occur:

i) if only the data of two altitudes are avail-

able, it is possible to determine only one G function. Supposing the acquisition system used is the same, in order to simulate other altitude data, the system MTF must be known. It is then necessary to proceed by attempts with the following steps:

- the hypothesis is made that the system MTF belongs to a certain class of filters,
- by means of time-scaling and of the model the corresponding code change filter is carried out,
- a comparison between supposed and true scale change function is realized which gives an answer as to how good the choice is.

When the system MTF is carried out, other altitude increases can be simulated with the method shown in Fig.III.5.3.

- ii) If at least data of three altitudes are available, it is possible to determine at least two G functions. Writing these functions using the altitude factor as a parameter, it is possible to directly obtain the G filter for whatever altitude increment.

Comparison Techniques between True and Simulated Images

After filtering has been performed, some methods must be established to carry out the comparison between simulation output and true image. A pixel-to-pixel comparison must be disregarded because such an approach presupposes a very accurate registration between images. Also taking into account the phase factor and on the hypothesis that images do not have any geometrical distortions, the registered averaged error for N reduction factor is $1/2 N$ of the low resolution pixel dimension. It follows that for small reductions (such as aircraft data simulations), this error would be

rather high.

Instead of local techniques it is then convenient to use image global information. These techniques can be summarized as follows:

- i) image analysis in the space domain,
- histogram comparison
 - entropy computation for the two images.
- Referring to ref. 11 it is possible to define the entropy of an image as

$$S = - \sum_{i=1}^N p_i \log_2 p_i \quad (16)$$

where p_i denotes the i^{th} level probability (it is interesting to note the introduction, in the same paper, of a specific entropy, i.e. a value independent of image area). This method permits to realize a comparison of two images simply by the comparison of two numbers.

- ii) Image analysis in the frequency domain,

- computation of spectra correlation.
- In the transform domain the problems arising from a point-to-point comparison are smaller than in the space domain. Here, in fact, the registration of two spectra gives no problem unless the original flight lines were not perfectly parallel; in that case the true and simulated image spectra are slightly rotated one with respect to the other. If this is not the case, it is possible to estimate the similarity between images by means of a measure of correlation of spectra. Any of the known fidelity functions (ref. 12, vol. 3.1., 1.4.2.3) can be used; the sum of absolute values of differences will be used in the following.
- Spectra energy computation in corresponding regions.
- If an accurate registration between spectra is not possible, an averaging tech-

nique must be used. Remembering that the energy of a signal is the square of its spectrum, the total energy of the Fourier transform of each image is calculated adding the energy at each point (u, v)

$$E_T = \sum_{u=0}^{N-1} \sum_{v=0}^{N-1} E(u, v) \quad (17)$$

with $u, v = 0, \dots, N-1$.

Calculating then the energy enclosed in circles or circular rings with origin at the centre of the frequency domain, it is possible to compare the corresponding energy percents β of the two spectra. This is obtained by calculating

$$\beta = 100 \left[\sum_u \sum_v E(u, v) / E_T \right] \quad (18)$$

where the summation indices range over the samples lying inside the circles of the rings.

Another averaging technique makes use of circular sectors. If, however, a rotation between spectra is present, the circles/rings method must be preferred.

Application Example

Just as an example of the use of techniques seen in the previous paragraphs, a simulation of an aircraft day image in the infra-red channel is now examined. The data collection was made during the 1978 Joint Flight Experiment on test site Sibari by means of a Bendix MSS. During this campaign, data were detected at different aircraft altitudes (500, 1000, 1800 and 3000 m) but as a first attempt only 500 - 1000 m simulation had been put into practice.

The region considered (seen at 500 m) is reported in Fig.III.5.7.

According to the procedure described in § 3.1, the following steps have been implemented:

- correction of 500 m and 1000 m original images,

Since the Bendix' PSF is not known, the only corrections made concern the optical depth increase for scan angle and the panoramic effect. About the former, the correction has been calculated first referring to an almost uniform region and has then been applied to the whole 500 m image. Fig.III.5.8 shows the profiles (averaged on a number of lines) of the uncorrected and the corrected image. The same procedure has been repeated for the 1000 m image. The panoramic effect has been corrected resampling data (with a cubic polynomial) in the scanning direction. Using 803 input samples, the algorithm has produced 1256 output pixels. A visual effect of this correction is shown in Fig.III.5.9, where uncorrected images (Fig.III.5.9a) is compared with the corresponding panoramic effect-corrected image (Fig.III.5.9b). The two images are left-aligned (corresponding to the flight-line) so that the pixel number increase becomes evident (a symmetric effect on the other side).

- Choice of test area.

The simulation procedure is performed on a segment 512 x 512 pixels dimensioned. In the whole region of Fig.III.5.7, the area shown in Fig.III.5.10 has been chosen because of the presence of spatial structures. For homogeneous areas, in fact, the scaling-up output is independent of the PSF used, so this case is not meaningful for the test.

The scale change procedure should give an output similar as much as possible to the true 1000 m image (reported in Fig.III.5.11).

- Fourier spectra computation.

The developed software in its present form, neglects the phase information; besides, since the dynamic range of transform is very

ORIGINAL PAGE IS
OF POOR QUALITY

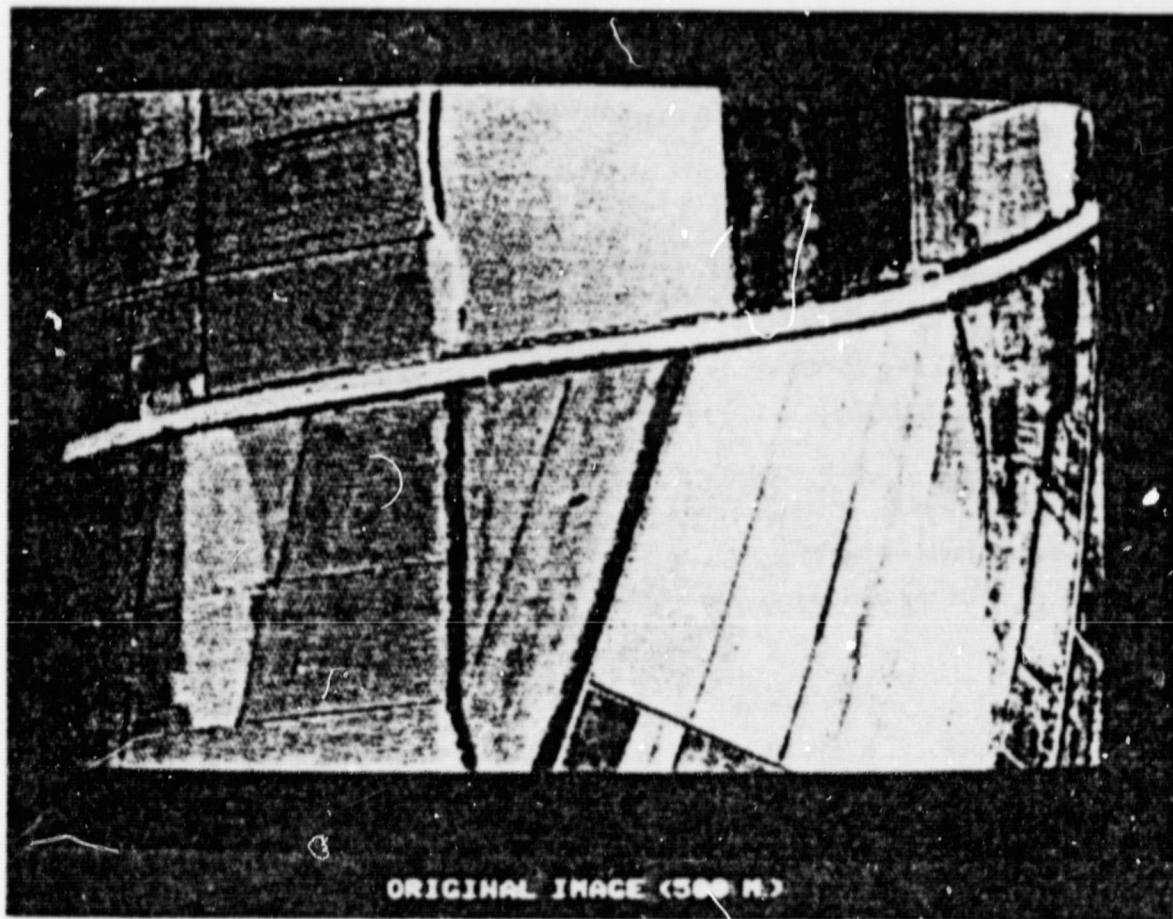


Fig. III.5.7.

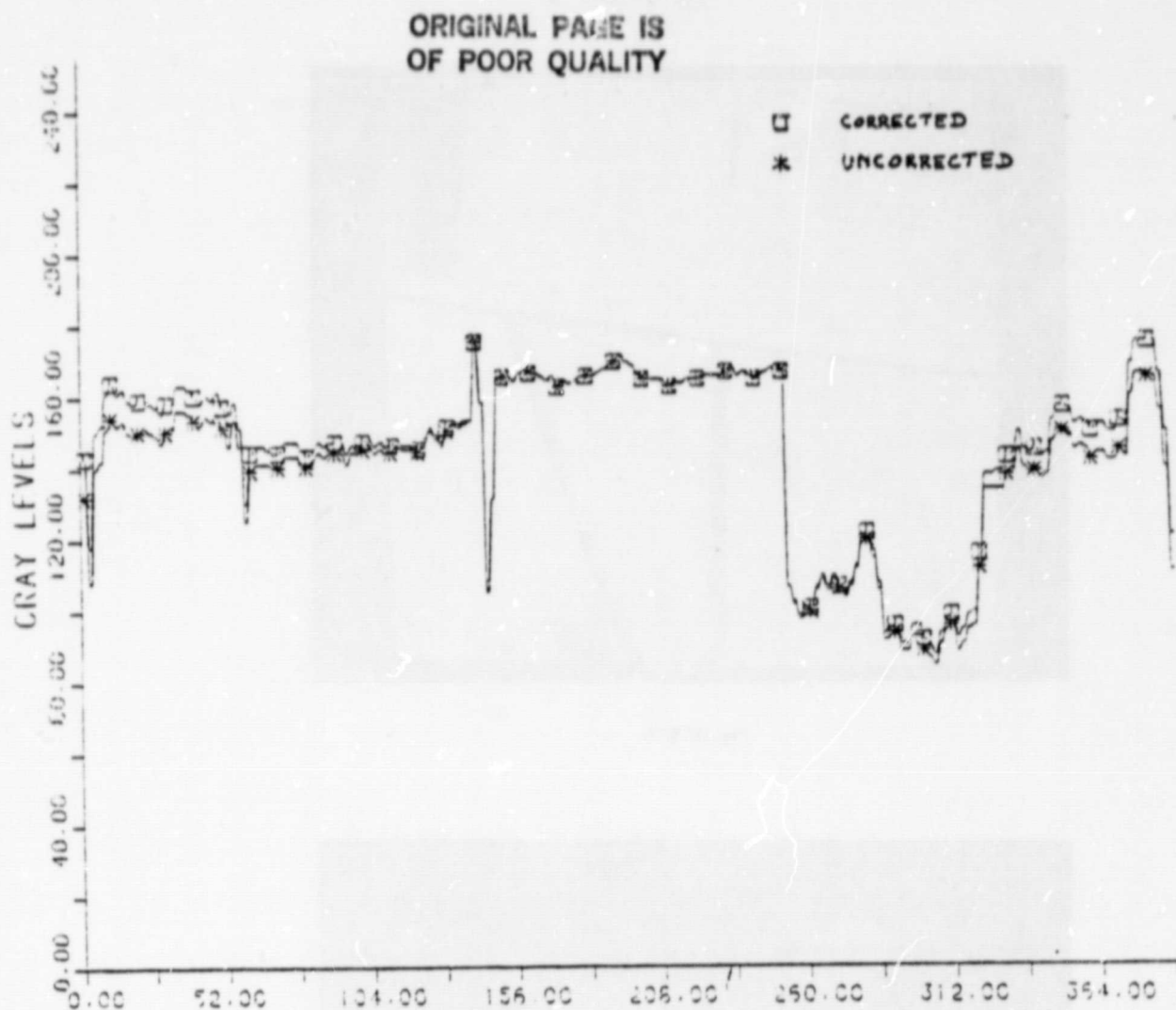


Fig. III.5.8.

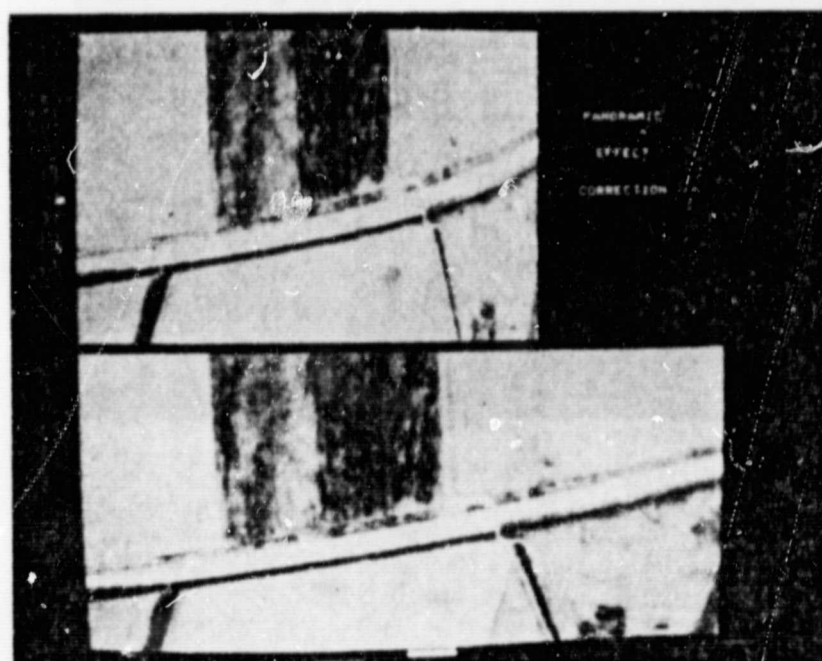


Fig. III.5.9.

ORIGINAL PAGE IS
OF POOR QUALITY

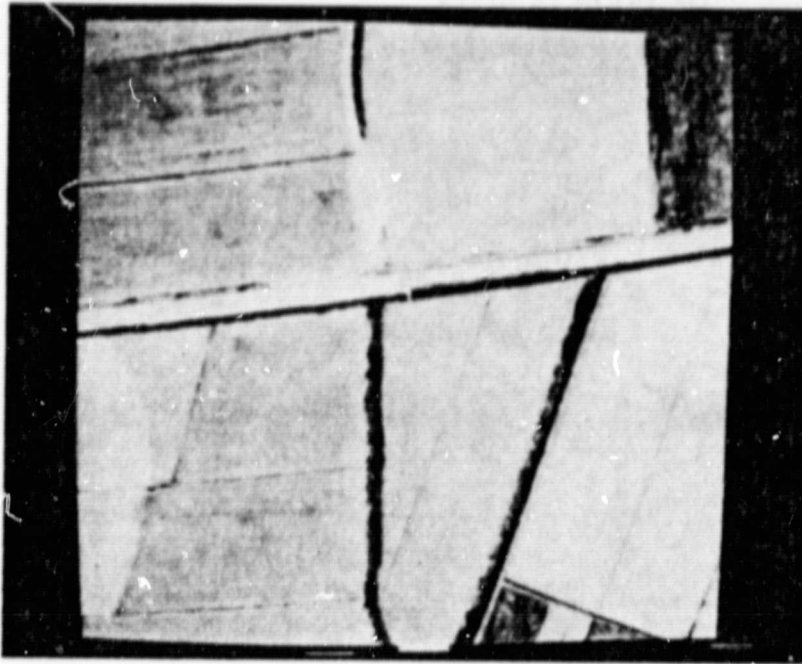


Fig. III.5.10.

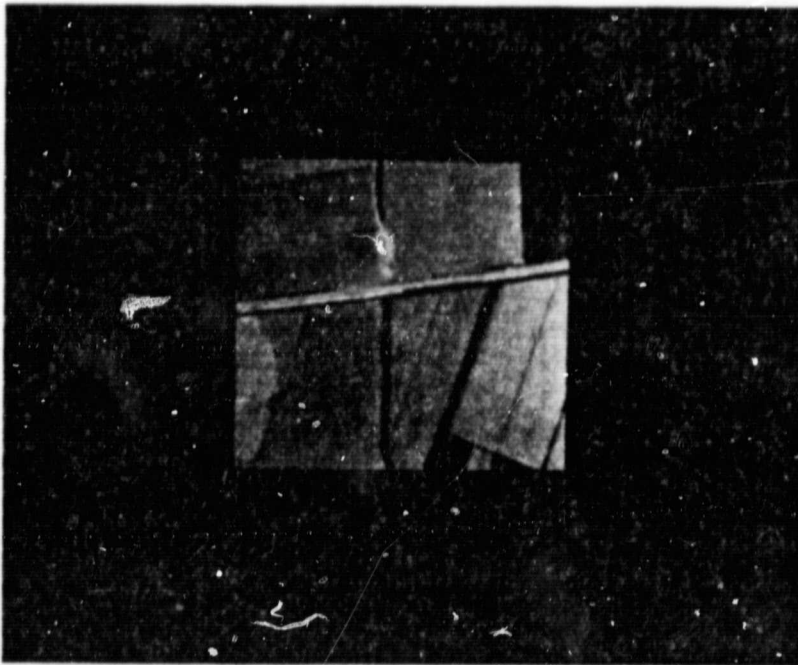


Fig. III.5.11.

large and in order to display it in image form on an I^2S imaging system, it is necessary to compress the coefficient values in byte format. The whole spectrum range is then linearly subdivided into 256 levels. Images of Figs.III.5.10 and 11 are used as input to the Fourier spectrum computation program. The resulting outputs are reported in Figs.III.5.12 and 13, respectively. For visual reasons they report the quantity $1 + \log_{10}|H|$.

As has been stated in § 2.2, the spacing between frequency samples is the same, i. e., $\Delta u = 1/T_0$ where $T_0 = N\Delta x$.

In this case for 500 m image spectrum $\Delta x \approx 1.25$ m, $N = 512$ while for 1000 m image spectrum, $\Delta x \approx 2.5$ m, $N = 256$. It follows that the frequency domain dimensions are (see also ref. 8):

$$512 \Delta u = \frac{1}{1.25}$$

$$256 \Delta u = \frac{1}{2.5}$$

The maximum revealable frequencies are

$$0.5 \frac{1}{1.25} = 0.4 \text{ cycles/m}$$

$$0.5 \frac{1}{2.5} = 0.2 \text{ cycles/m.}$$

- Ratio of spectra

As has been stated in § 4, the ratio of spectra can be realized either in an integral mode or in a point-to-point mode.

An example of the former approach is reported in Fig.III.5.14 which shows one of the rings into which the Fourier plane can be subdivided. The technique used is, however, the local ratio one; the (normalized) output is in Fig.III.5.15. The presence of structures in the spectrum can be ascribed to a little non-compensated rotation between the two original images spectra.

- Determination of an analytical scaling-up filter.

As has been stated in § 3.1, it is convenient

to determine which class of analytical filters fits the true scaling-up filter.

In this case it has been seen that the ratio of a Butterworth filter of the order 3 and a cut-off frequency 120 with its scaled version produces a G function which resembles the shape of the G filter (Fig.III.5.16).

According to the model, the acquisition chain object-data at 500 m altitude can then be represented by an MTF shaped just like a Butterworth filter ($f_{\text{cut}} = 120$; order 3) so the corresponding G filter for whichever other altitude increase can be easily carried out.

- Scaling-up simulation.

The image filtering has been performed in the space domain. Frequency domain filtering requests, in fact, the multiplication of the spectrum by the filter. Since both have a quantification error and because the result must be re-quantified and antitransformed, referring to the present software, this approach would be meaningless (for a good treatment of quantification techniques see ref. 9, chapt. 7). The two-dimensional spatial array obtained from G anti-transformation has been convolved with the image of Fig.III.5.11, and the result has been compared with Fig.III.5.12.

- True and simulated images comparison.

Referring to the techniques exposed before, the histograms of the whole images have been obtained (Fig.III.5.17). Evidently, there is no similarity between them. This effect becomes, however, less evident if the histograms regarding a region, symmetrical with respect to the flight-lines, are considered (Fig.III.5.18). The difference still remaining between them can be further reduced by means of a linear transformation. Calling, in fact, x_1, M_1, S_1 (x_2, M_2, S_2) the grey level, the average value and the variance of the simula-

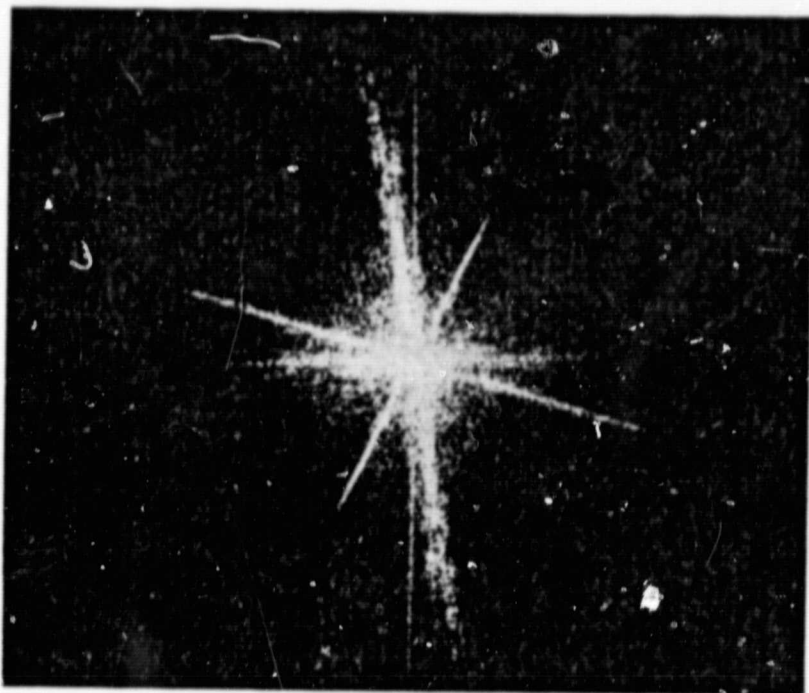


Fig. III.5.12.

ORIGINAL PAGE IS
OF POOR QUALITY

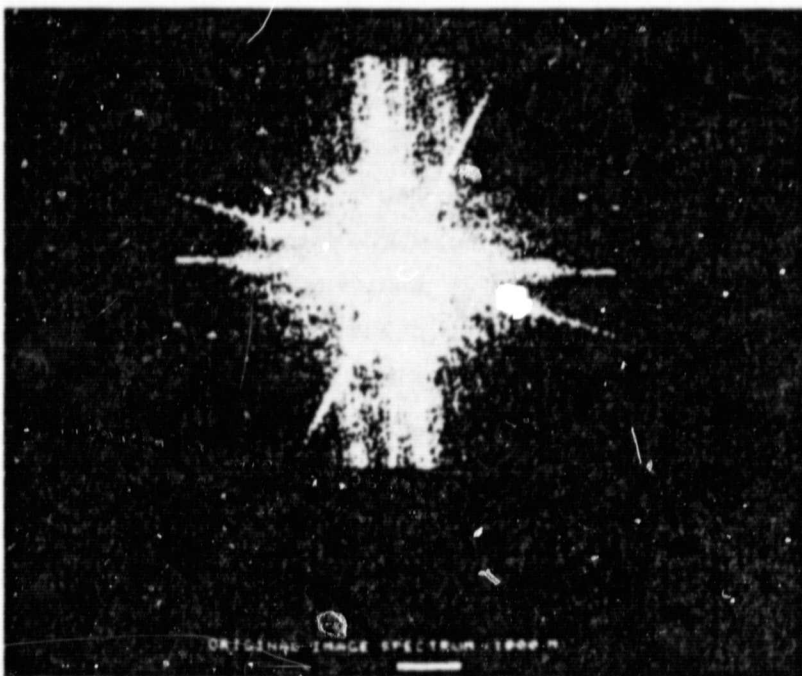


Fig. III.5.13.

ORIGINAL PAGE IS
OF POOR QUALITY

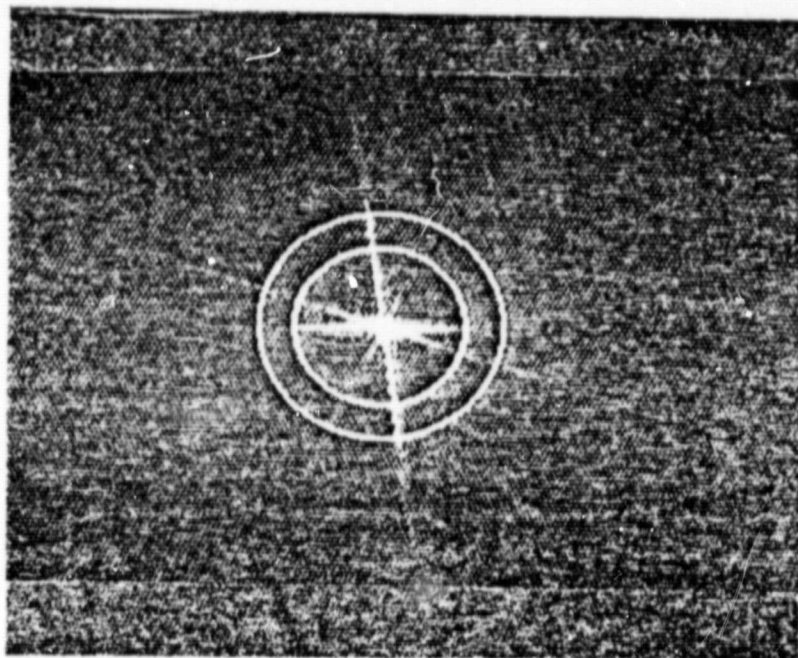


Fig. III.5.14.

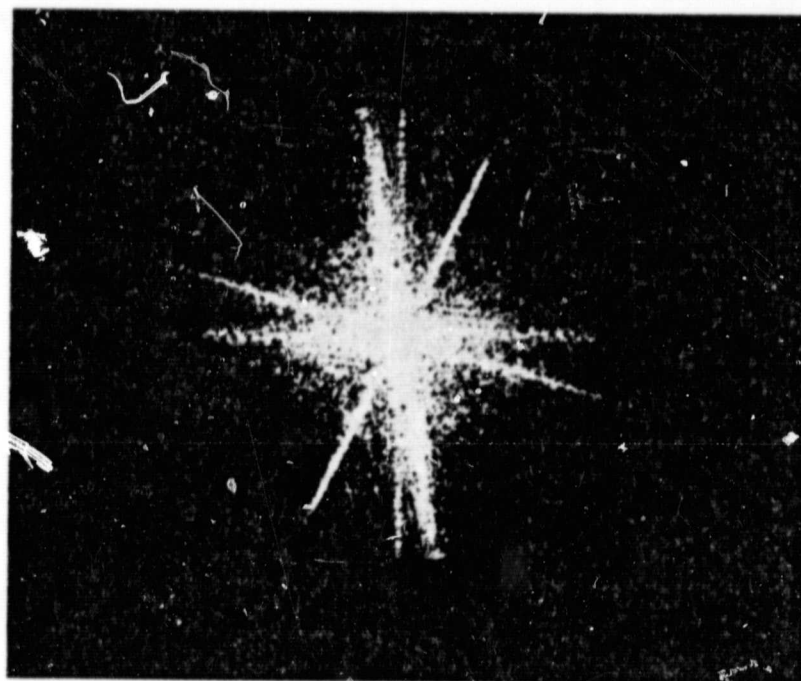


Fig. III.5.15.

ORIGINAL PAGE IS
OF POOR QUALITY

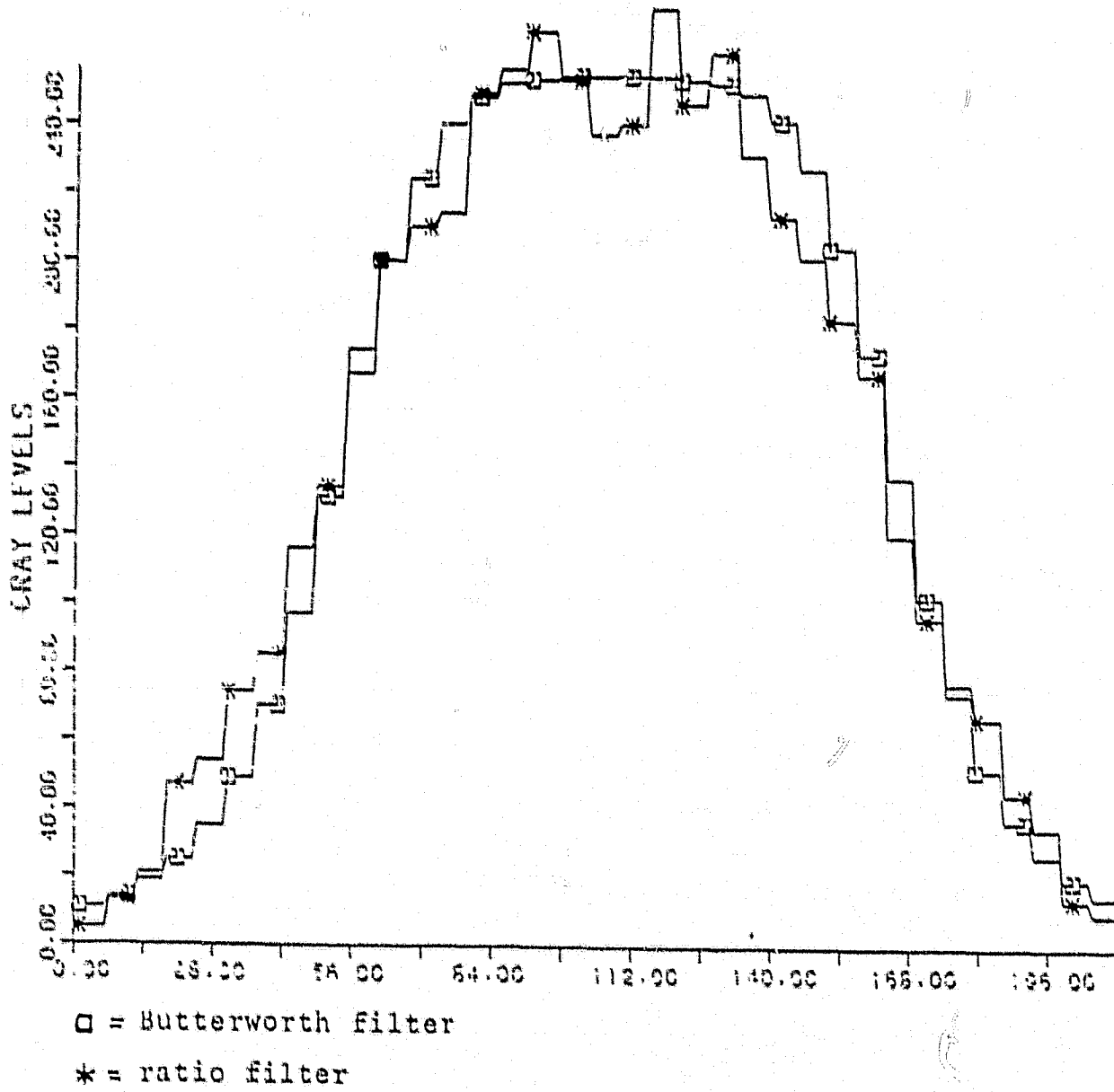


Fig. III.5.16.

ORIGINAL PAGE IS
OF POOR QUALITY

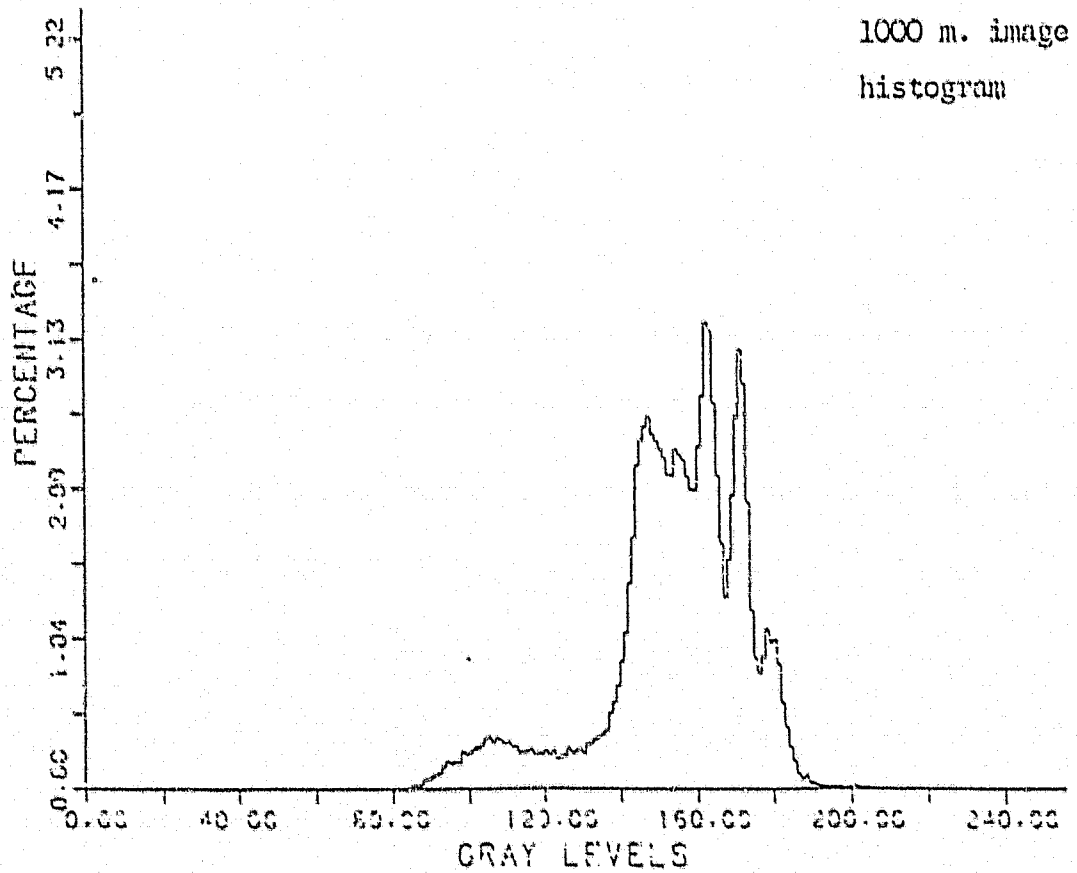
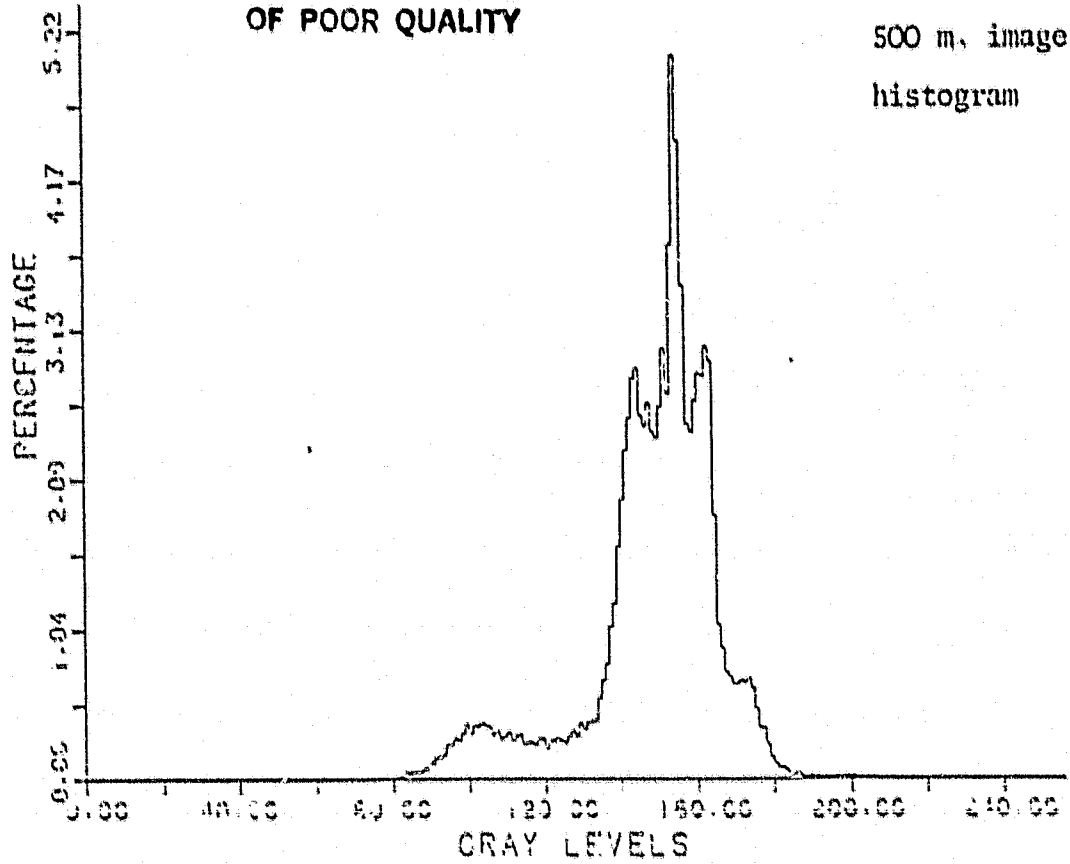


Fig. III.5.17.

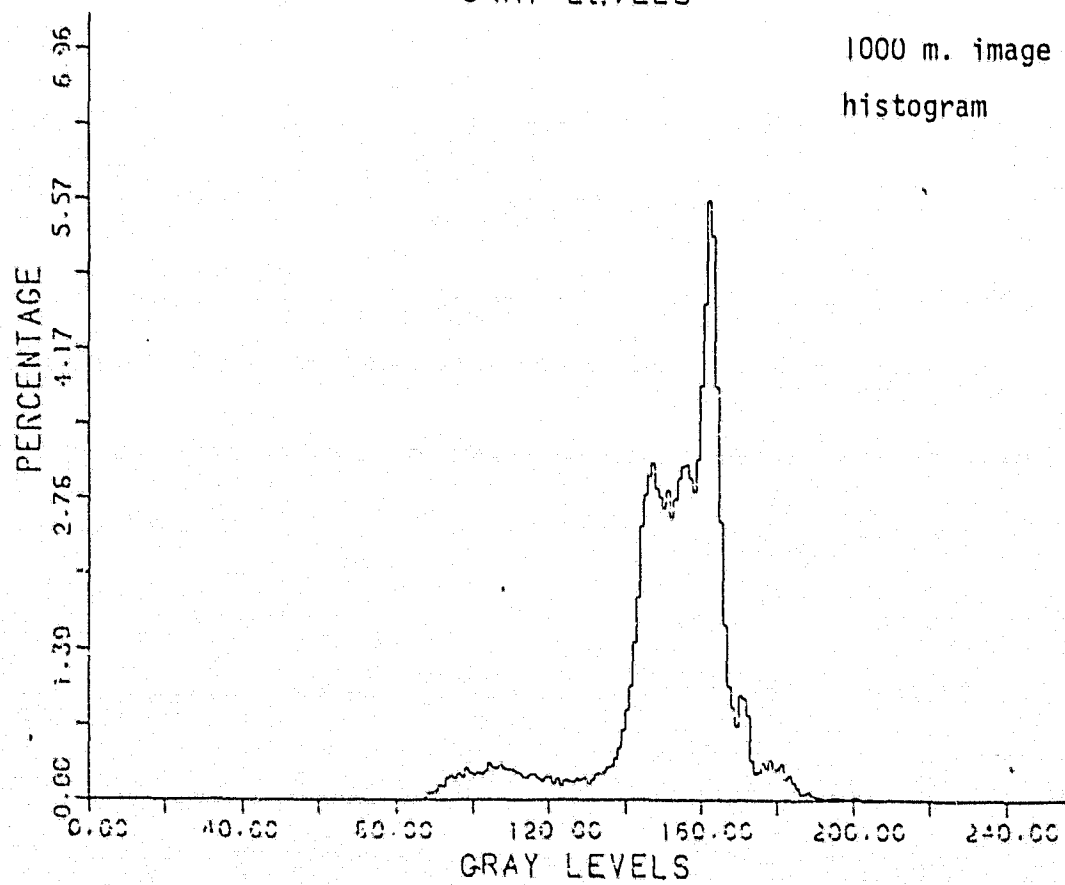
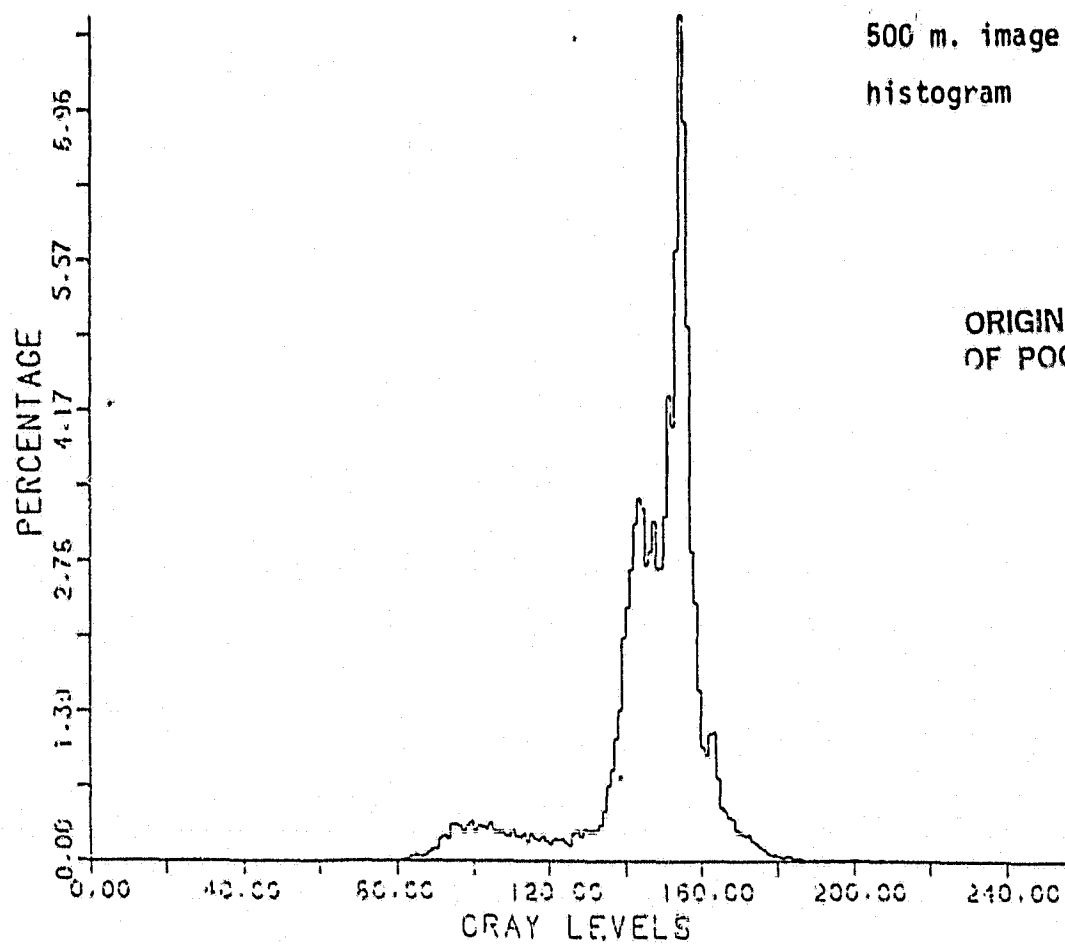


Fig. III.5.18.

ORIGINAL PAGE IS
OF POOR QUALITY

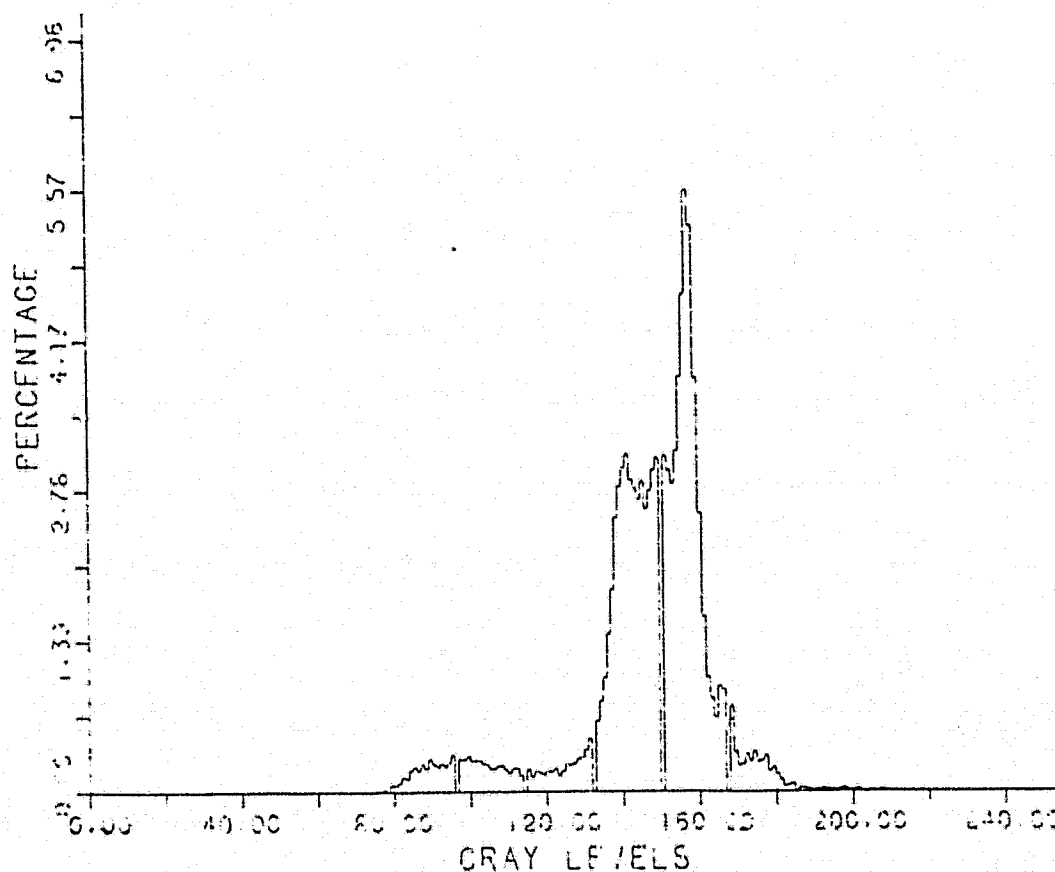
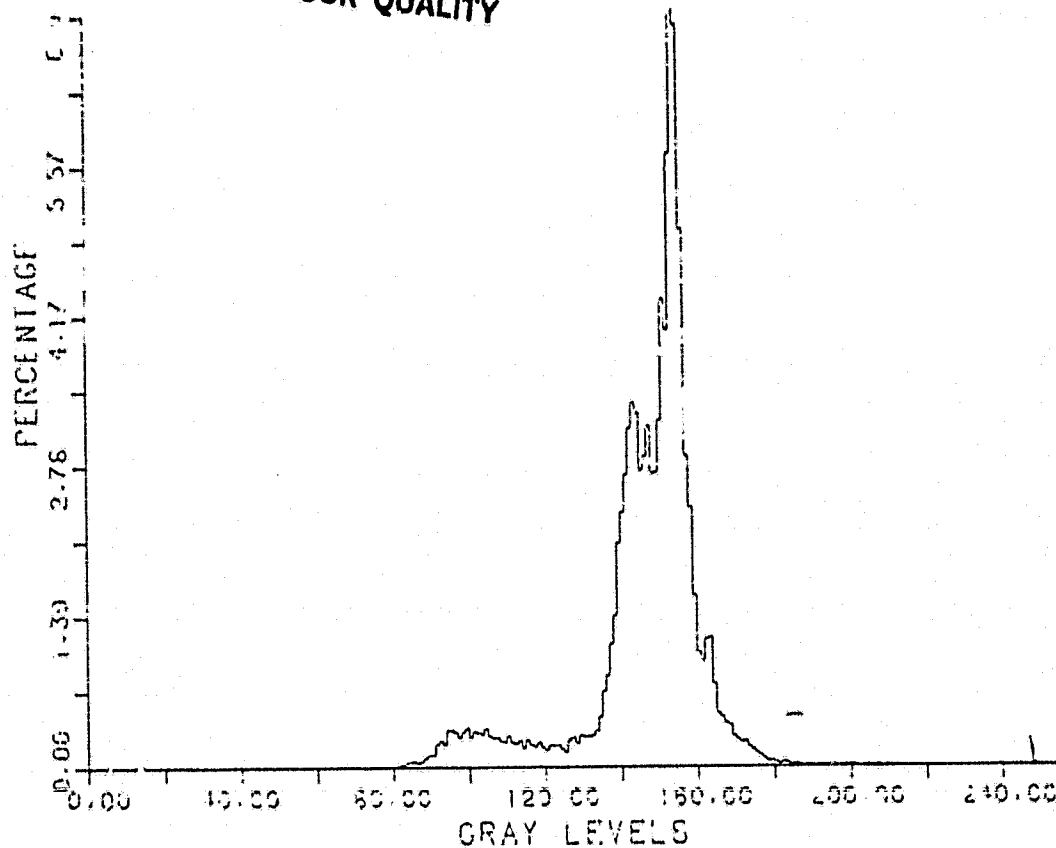


Fig. III.5.19.

ted (original) image, respectively, a new image was obtained with grey values x'_1 carried out by means of the relation

$$x'_1 = ax_1 + b$$

$$a = \frac{S_1}{S_2}$$

$$B = M_2 - aM_1$$

Figure III.5.19 shows the comparison between the original and the new simulated image histograms.

The hypothesis can be made that this linear transformation accounts for atmosphere increase with altitude.

When the transformation was applied to the whole image, no improvement was obtained.

Two possible causes are suggested to justify this result:

- along-flight direction pixels correlation (the correction of panoramic effect was realized, in fact, only in the scanning direction without considering the enlargement of the pixel also in the flight direction),
- shift-variant components present in the Bendix MSS PSF.

As a further comparison method, the simulated image (complete) Fourier spectrum has been compared with the original one. From a visual inspection the filtering output is too lacking in high frequencies with regard to the true 1000 m image, i.e. the filter used was revealed as the incorrect one.

As an experiment, all the operations were repeated with the Lanczos-Cappellini filter with parameters $N = 16$; $\alpha = 0.25$; $m = 15$. Histograms and spectra reveal, however, no meaningful improvement with respect to the first attempt.

Conclusions

The most important results of this work can be summarized as follows:

- singling out of main problems which must be faced in scaling-up simulations,
- determination of a simulation method,
- software implementation of the method.

The lack of information on the acquisition system used did not permit the realization of an exhaustive test of the proposed scaling-up methodology.

Moreover, HCMM images have not been simulated, also because of the difficulty of registering the few pixels coming from test site data with a whole HCMM scene.

Further developments can, however, be proposed to improve the method. They can be summarized as follows:

- utilization of atmospheric models to take into account the increase of the atmospheric layer,
- correction of panoramic effect also in the flight direction,
- better registration between the two altitudes starting images (if a rotation must be performed, it is convenient to subdivide it into two opposite half-rotations; this avoids the resampling affecting the two images in different manners,
- introduction of the phase term in the Fourier transform computation and use of non-integer values for the transform itself.

Besides, the module could be developed to carry out the scale change filter in a parametric form using the data of three altitudes; this avoids, in fact, the step of the determination of instrument MTF.

Many of its aspects make the proposed empi-

rical approach useful only for the simulation of different altitudes data detected by the same acquisition system. If, on the contrary, images detected by different systems must be simulated, only the deterministic approach can be used. The problem must then be faced to know, with a sufficient approximation degree, the MTF of the acquisition system, followed by applying the method of Fig.III.5.3.

References

1. MUNDIE and others; "System Design Considerations for Advanced Scanners for Earth Resource Applications", Proc. IEEE, Vol. 63, No. 1, Jan. 1975, p. 95.
2. ROSENFELD and KAK; "Digital Picture Processing", Academic Press (1976).
3. BRIGHAM; "The Last Fourier Transform", Prentice-Hall, Inc.
4. LIU and GALLANCHER; "Optimum Fourier Transform Division with Magnitude Constraint", Journ. Opt. Soc. Am., Vol. 64, No. 9, Sept. 1974, p. 1227.
5. TURNER, MALILA and NALEPKA; "Influence of the Atmosphere on the Remotely Sensed Data", Proc. Soc. Ph. Opt. Instrum. Eng., Vol. 51, August 1974, p. 101.
6. POTTER; "Haze and Sun Angle Effects on Automatic Classification of Satellite Data and Correction", Proc. Soc. Ph. Opt. Instrum. Eng., Vol. 51, August 1974, p. 73.
7. CAPPELLINI et al.; "Digital Filters and their Applications", Academic Press (1978).
8. GONZALES and WINTZ; "Digital Image Processing", Addison-Wesley (1977).
9. ANDREWS; "Computer Techniques in Image Processing", Academic Press (1970).
10. PRATT; "Digital Image Processing", Pre-publication copy.
11. LECHI; "Le carte tematiche e le loro risoluzioni", Proc. II Site Conference Varenna, Sept. 1979 (not yet published).
12. CSATA - ESOC Contract; "An Image Processing Support Software (IPSS). Contr. No. 2800/76/D/IM/SC, Bari, April 1978.
13. The Optical Industry and Systems Directory; Encyclopedia, Vol. 2 (1979).
14. KIDD and WOLFE; "Performance Modeling of Earth Resources Remote Sensors", IBM Journ. Research and Development, Jan. 1976, p. 29.
15. O'NEILL; "Transfer Function for an Annular Aperture", Journ. Opt. Soc., Vol. 46, No. 4, April 1956, p. 285.
16. PAPOULIS; "System and Transforms with Applications in Optics", Mc Graw-Hill, (1968).
17. STOKSETH; "Properties of a Defocused Optical System", Jour. Opt. Soc. Am., Vol. 59, No. 10, October 1969, p. 1314.
18. LERMAN and SHANNON; "Two-Dimensional Image Prediction and Enhancement", Proceedings SPIE, Vol. 10 (1967).
19. BARBE; "Imaging Devices Using the Charge-Coupled Concept", Proc. IEEE, Vol. 63, No. 1, Jan. 1975, p. 38.
20. HUFNAGEL and STANLEY; "Modulation Transfer Function Associated with Image Transmission through Turbulent Media", Jour. Opt. Soc. Am., Vol. 54, 1964, p. 52.
21. ABOUTALIB and SILVERMAN; "Restoration of Ratio-Degraded Images", IEEE Trans. Circuits Syst. CAS-22, 1975, p. 278.
22. Proceedings CALTECH/JPL Conference on Image Processing, Technology, Data Sources and Software for Commercial and Scientific Applications (1976).
23. Istituto Elettrotecnica, Genova-Esoc Contract Study on the Use of the Fast Fourier Transform in Spectral Analysis. Contr. No. 486/73 ESA (ESRO) CR-468, Genova, Sept. 1975.
24. KULHANEK; "Introduction to Digital Filtering in Geophysics", Elsevier (1976).
25. HUAN; "Picture Processing and Digital Filtering", Springer Verlag (1975).
26. SCALE EFFECTS. HCMM Data Simulation Usage of Filtering Techniques for Scaling-up Simulations. Contract CSATA-JRC-Ispra, No. 960-78-10 SISP I.

ORIGINAL PAGE IS
OF POOR QUALITY

2. An Active Method for Measuring Thermal Infrared Effective Emissivities; Implications and Perspectives for Remote Sensing

F. Becker, W. Ngai and M.P. Stoll
Groupe de Recherches en Télédétection Radiométrique
de l'Université Louis Pasteur, Strasbourg, France

Introduction

Remote sensing in the thermal infrared bands as 9-14 μm is very interesting because it provides a means to measure the energetic response of the Earth to its excitation by the sun. However, several problems have to be solved before a relevant quantitative interpretation of the data can be made.

First, the radiance of a pixel depends not only on its surface temperature, but also on its emissivity and corollary on the radiance of its surroundings. Therefore, it is generally not possible to interpret a variation of radiance in the thermal infrared bands in terms either of a temperature variation or of an emissivity variation. Furthermore, it may happen in natural media, that some interesting effects may be more or less hidden because they increase the emissivity while they decrease the surface temperature, reducing the variation of the radiance. This is the case for soil moisture, for instance.

Consequently, emissivities are very interesting to know, not only because they are an essential factor to obtain accurate measurements of surface temperature by radiometry (remember that at 10 μm a relative error $\frac{\Delta \epsilon}{\epsilon}$ of 1% may lead to an error $\Delta T = 0.6^\circ\text{C}$ at a surface temperature of 300°K), but also because they may be very useful indicators of specific properties

of the surface itself.

Unfortunately, these emissivities and surface temperature are defined for homogeneous surfaces. Thus, they cannot be used to express the radiance observed from generally much larger than characteristic areas of homogeneous components, at least in European countries. It will therefore be necessary to introduce new parameters, namely the effective emissivity and temperature, in order to describe these heterogeneous surfaces as if they were homogeneous.

The two main problems which have to be solved for interpreting quantitatively remote sensing data in the thermal infrared bands are then:

- i) to define unambiguously the effective parameters, i. e. to relate them to the well defined corresponding parameters for homogeneous surfaces,
- ii) to measure directly these effective parameters, for both homogeneous and heterogeneous surfaces with a remote sensing method.

Radiometry for Heterogeneous Media

Statement of the problem

In natural media, the observed surfaces are seldom homogeneous because they are formed

with many different sub-elements, each having its own characteristic parameters. This situation occurs very frequently when the Earth is observed from satellites in the direction θ, ϕ . It results that

$$R_{\lambda}(\theta, \phi) = \sum_{i=1}^N \epsilon_i(\theta, \phi) P_i(\theta, \phi) R_{\lambda}^0(T_i) \quad (1)$$

where $R_{\lambda}^0(T_i)$ is the radiance of a black body at temperature T_i given by the Planck's formula, and $P_i(\theta, \phi)$ is the partition function of the pixel given by

$$P_i(\theta, \phi) = \frac{\Lambda_i(\theta, \phi)}{\alpha \Sigma} = \frac{d\omega_i(\theta, \phi)}{d\omega} \quad (2)$$

with the constraint

$$\sum_{i=1}^N P_i(\theta, \phi) = 1 \quad (3)$$

Generally, the emissivities $\epsilon_{i\lambda}$ will not depend on the angle, and the angular distribution will be given by the partition functions $P_i(\theta, \phi)$ of the pixel.

For a pixel formed with flat surfaces, without any shadowing effect, the partition function does not depend on the angles θ and ϕ . On the same line, the emittance of the surface $d\Sigma$ given by

$$E = \int_0^{\infty} d\lambda \int_{\text{hemisphere}} R_{\lambda}(\theta, \phi) \cos \theta d\Omega \quad (4)$$

can be written simply

$$E = \sigma \sum_{i=1}^N \bar{\epsilon}_i \bar{P}_i T_i^4 \quad (5)$$

with

$$\bar{\epsilon}_i = \frac{\int_0^{\infty} d\lambda R_{\lambda}^0(T_i) \int_{\text{hemisphere}} \epsilon_{i\lambda}(\theta, \phi) P_i(\theta, \phi) \cos \theta d\Omega}{\left[\int_0^{\infty} d\lambda R_{\lambda}^0(T_i) \right] \left[\int_{\text{hemisphere}} P_i(\theta, \phi) \cos \theta d\Omega \right]} \quad (6)$$

and

$$P_i = \frac{1}{\pi} \int_{\text{hemisphere}} P_i(\theta, \phi) \cos \theta d\Omega \quad (7)$$

If the partition functions do not depend on the angles θ, ϕ , then $\bar{\epsilon}_i$ is the regular averaged emissivity of the element i while $P_i = \bar{P}_i$. The problem to be solved can be stated now in the following terms: is it possible to write both expressions (1) and (5) simultaneously as:

$$R_{\lambda}(\theta, \phi) = \tilde{\epsilon}_{\lambda}(\theta, \phi) R_{\lambda}^0(\tilde{T}) \quad \text{and} \quad E = \tilde{\epsilon} \sigma \tilde{T}^4 \quad (8)$$

with

$$\tilde{\epsilon} = \frac{\int_0^{\infty} d\lambda R_{\lambda}^0(\tilde{T}) \int_{\text{hemisphere}} \tilde{\epsilon}_{\lambda}(\theta, \phi) \cos \theta d\Omega}{\sigma \tilde{T}^4} \quad (9)$$

where $\tilde{\epsilon}_{\lambda}$ and \tilde{T} will be respectively the effective emissivity and temperature.

Effective parameters

The various temperature T_i over a pixel are not very different from each other and thus from the effective temperature \tilde{T} (generally $\frac{T_i - \tilde{T}}{\tilde{T}}$ is less than 10%). It is therefore possible to express, with a good approximation, the Planck function $R_{\lambda}^0(T_i)$ and T_i^4 near the maximum of emission as:

$$R_{\lambda}^0(T_i) \cong R_{\lambda}^0(\tilde{T}) \left[1 + 5 \frac{(T_i - \tilde{T})}{\tilde{T}} \right]$$

and

$$T_i^4 \cong \tilde{T}^4 \left(1 + 4 \frac{(T_i - \tilde{T})}{\tilde{T}} \right)$$

It is then easy to show (ref. 4, 5) that formulae (1) and (5) can be rewritten unambiguously as:

$$R_{\lambda}(\theta, \phi) = \tilde{\epsilon}_{\lambda}(\theta, \phi) R_{\lambda}^0(\tilde{T}) [1 + 5h_{\lambda}(\theta, \phi)]$$

and

$$E = \tilde{\epsilon} \sigma \tilde{T}^4 [1 + 5h] \quad (10)$$

with

$$\tilde{\epsilon}_{\lambda}(\theta, \phi) = \sum_{i=1}^N P_i(\theta, \phi) \epsilon_{i\lambda}(\theta, \phi)$$

and

$$\tilde{T} = \sum_{i=1}^N \bar{P}_i T_i \quad (11)$$

ORIGINAL PAGE IS
OF POOR QUALITY

where the heterogeneity factors h_λ and \bar{h} are given by

$$h_\lambda(\theta, \phi) = \frac{\sum_{i=1}^N (T_i - \bar{T}) P_i (\epsilon_{i\lambda} - \bar{\epsilon}_\lambda)}{\bar{\epsilon}_\lambda \bar{T}_\lambda} \quad (12)$$

and

$$\bar{h} = \frac{\sum_{i=1}^N (T_i - \bar{T}) \bar{P}_i (\bar{\epsilon}_i - \bar{\epsilon})}{\bar{\epsilon} \bar{T}} \quad (13)$$

The effective emissivity and temperature are defined by equations (12) and (13). These definitions are significant if equations (8) and (9) are valid with an accuracy of at least 1%, in order to define the radiometric temperature with an accuracy of 0.5°C. This means that the heterogeneity factors must satisfy the inequalities $h_\lambda < 0.002$ and $\bar{h} < 0.002$ (14).

The typical example of Table III.5.1 shows that these inequalities are generally fulfilled.

Parameters	ϵ	$T^\circ\text{C}$	P_i
Water	0.983	17	0.3
Bare soil	0.8	35	0.2
Grass land	0.97	20	0.5
Effective Parameters	0.94	22.1	1
Heterogeneity factors $h = \bar{h} = 0.0017$			

TABLE III.5.1. Typical values of the characteristic parameters of sub-elements constituting a pixel. The heterogeneity factor fulfills (16) and it is easy to check that the emittance, for instance, is accurate to better than 3%.

As a conclusion, if the heterogeneity factors \bar{h} and h_λ satisfy (16), which is generally true, it is possible to introduce effective parameters which are characteristic of the equivalent homogeneous pixel. These parameters have many interesting properties which have been discussed in reference 4 and will not be reproduced here. However, in order to be operational,

these effective parameters must be measurable at any scale. Let us discuss this question in the following section.

A Method to Measure Effective Emissivities

Principle of the method

If a surface is not too heterogeneous, i. e. if the condition (16) is fulfilled, the spectral radiance $R_\lambda^N(\theta, \phi)$ may be most generally written as:

$$R_\lambda^N(\theta, \phi) = \bar{\epsilon}_\lambda(\theta, \phi) R_\lambda^0(\bar{T}) + \iint_{\text{hemisphere}} \bar{\rho}_{b\lambda}(\theta, \phi; \theta', \phi') H_\lambda(\theta', \phi'; T_e) \cos \theta' d\Omega' \quad (15)$$

where the first term of the right hand side of expression (17) is the emitted radiance discussed before and the second term is the reflected radiance due to the irradiation by the surroundings (the sun, the atmosphere, near surroundings such as trees, etc.) which is supposed to have an equivalent radiance $H_\lambda(\theta', \phi', T_e)$.

The parameter $\bar{\rho}_{b\lambda}(\theta, \phi; \theta', \phi')$ is the effective spectral bidirectional reflectivity. In stationary conditions and for media which do not transmit radiative energy (as for natural media) it can easily be shown with the arguments given before that:

$$\bar{\epsilon}_\lambda(\theta, \phi) = 1 - \bar{\rho}_{b\lambda}(\theta, \phi) = 1 - \iint_{\text{hemisphere}} \bar{\rho}_{b\lambda}(\theta, \phi; \theta', \phi') \cos \theta' d\Omega' \quad (16)$$

The measurement of $\bar{\epsilon}_\lambda$ appears to be a very hard task even if $R_\lambda^N(\theta, \phi)$, \bar{T} and $H_\lambda(\theta', \phi', T_e)$ are known. In fact it is not possible to extract simply $\bar{\epsilon}_\lambda$ from (17) because $\bar{\rho}_{b\lambda}(\theta, \phi; \theta', \phi')$ is not simply expressed in terms of $\bar{\epsilon}_\lambda$, unless some severe approximations are done:

- Either $\bar{\rho}_{b\lambda}(\theta, \phi; \theta', \phi')$ does not depend on the angles (which is generally not true as will

be seen below).

- ii) Or the equivalent radiance of the surroundings is isotropic (which is no longer true mainly for clear sky).

With these approximations and using (18), expression (17) can be rewritten as

$$\tilde{\epsilon}_{\lambda}(\theta, \phi) = \frac{R_{\lambda}^N(\theta, \phi) - B_{\lambda}(T_e)}{R_{\lambda}(\bar{T}) - B_{\lambda}(T_e)} \quad (17)$$

where $B_{\lambda}(T_e) = \frac{1}{\pi} \iint_{\text{hemisphere}} H_{\lambda}(\theta', \phi', T_e) \cos \theta' d\Omega'$.

In case i) $\tilde{\epsilon}_{\lambda}$ and R_{λ} do not depend on the angles (θ, ϕ) , while in case ii) $B_{\lambda}(T_e) = H_{\lambda}(T_e)$.

Besides the fact that the previous approximations have to be checked, expression (19) shows that three types of measurement have to be done in order to obtain with passive radiometry:

- i) A measure of $R_{\lambda}^N(\theta, \phi)$, the radiance of the medium,
- ii) A measure of \bar{T} in order to get $R_{\lambda}^0(\bar{T})$, which is very difficult in natural media and implies sometimes to modify the surrounding effects,
- iii) A measure of $B_{\lambda}(T_e)$, the average over the upward hemisphere of the radiance of the surroundings.

The various existing methods for measuring emissivities of natural media are based on equation (19). Although they may be fast, they cannot avoid a direct measurement of the effective surface temperature nor the evaluation of the radiation of the surroundings, which may be very important in the thermal infrared bands and may change drastically during a day or during the measurement itself.

In order to overcome all these difficulties and to avoid any non-radiometric measurements, it is necessary to modify somehow expression

(17). The best way is to add an external pulsed source. If this source, chopped at a frequency $\omega/2\pi$, irradiates the surface in the direction (θ_1, ϕ_1) and is seen from this surface within the solid angle $d\Omega_1$, the radiance $dR_{\lambda}(\theta, \phi)$ of the irradiated surface will become:

$$dR_{\lambda}(\theta, \phi, \omega t) = R_{\lambda}^N(\theta, \phi) + \rho_{b\lambda}(\theta, \phi; \theta_1, \phi_1) R_{\lambda e}(\theta_1, \phi_1; \omega t) \cos \theta_1 d\Omega_1 \quad (20)$$

where $R_{\lambda e}(\theta_1, \phi_1, \omega t)$ is the pulsed radiance of the source.

If the electric signal recorded by the radio-meter is filtered so that unwanted frequencies are blocked, the detection system will be sensitive to R_{λ}^N . Therefore the recorded radiance may be written:

$$dR_{\lambda}(\theta, \phi) = \tilde{\rho}_{b\lambda}(\theta, \phi; \theta_1, \phi_1) R_{\lambda e}(\theta_1, \phi_1) \cos \theta_1 d\Omega_1 \quad (21)$$

here $\tilde{R}_{\lambda e}$ is proportional to the radiance of the external source.

From this equation the effective emissivity is given by

$$\epsilon(\theta, \phi) = 1 - \iint_{\text{hemisphere}} \frac{dR_{\lambda}(\theta, \phi)}{\tilde{R}_{\lambda e}(\theta_1, \phi_1)} \quad (22)$$

Advantages and disadvantages

Comparing (19) and (22), it becomes evident that this active method eliminates the effects of the surroundings and the measurement of the effective surface temperature T . However, these advantages are partially offset by:

- i) A more complex calibration procedure, $R_{\lambda e}$, has to be known;
- ii) The necessity to measure $dR_{\lambda}(\theta, \phi)$ over all the upward hemisphere in order to obtain $\tilde{\epsilon}_{\lambda}$ from (22). We shall see below how to reduce this constraint.

However, if the surface is assumed to reflect isotropically expression (22) becomes for an irradiation in the direction of the nadir:

$$\tilde{\epsilon}_{\lambda} = 1 - \pi \frac{dR_{\lambda}}{R_{\lambda e} d\Omega} \quad (23)$$

which leads to one measurement (dR_{λ}) instead of three.

Furthermore, the necessity of measuring the angular distribution of the reflected radiance is not a disadvantage since it gives a complete overview of the angular behaviour of the emissivity and adds interesting information on the structure of the surface. Finally, another appears if one estimates the possible precision given by this method. Since the relative accuracy of the emissivity is related to the relative accuracy of the reflectivity by

$$\frac{\Delta \epsilon}{\epsilon} = \frac{1 - \epsilon}{\epsilon} \frac{\Delta \rho}{\rho} \quad (24)$$

the relative accuracy of ϵ may be larger by a factor 3 (for $\epsilon = 0.75$) to 50 (for $\epsilon = 0.98$) than the relative accuracy of the reflectivity. As a consequence, a relative accuracy of some ‰ is easily attainable even using rough instrumentation.

A simple realization of the required instrumentation

A preliminary version of the measuring system has been designed to fulfill the following requirements:

- i) It must allow measurements in the field;
- ii) It must possess all the angular degrees of freedom for both the source and the detector with an angular resolution not less than $1-2^{\circ}$;
- iii) It must give effective emissivities in the spectral domain of the 8-14 μm window;
- iv) It must be as cheap as possible.

A block diagram of the system is given in Fig. III,5.20. The infrared goniometer and associated electronics have been built by the Groupe de Télédétection de Strasbourg under a CNES contract. The noise equivalent temperature, $NET \approx 0.01^{\circ}\text{C}$.

Preliminary results demonstrated the great stability of the system.

The accuracy of the method was checked through direct measurement of pure water emissivity, using an aluminium plate as a reference. Afterwards one measured the emissivity of a very heterogeneous medium: a sample of grass (95% cover and 3 cm height). The various results obtained confirmed the goodness of the active method proposed which gives an accuracy of a few ‰ even for large emissivities.

Implications and Perspectives for Remote Sensing Applications

In principle, the method proposed can be extended to aircraft or spacecraft or aircraft remote sensing, since it is a pure radiometric method which leads directly to effective parameters, the only relevant ones at this altitude. In order to verify experimentally this capability, a programme is in progress at Strasbourg involving various controlled heterogeneous media with well defined heterogeneity factors. The spectral analysis of these effective emissivities can be done as well since we have a large spectral band source.

Furthermore, this method allows a good separation of the effects of the surface temperature and emissivity. Therefore, it could be possible including correlations with a passive method, to obtain both the effective emissivity and surface temperature, knowing the averaged irradiation due to the surroundings.

ORIGINAL PAGE IS
OF POOR QUALITY

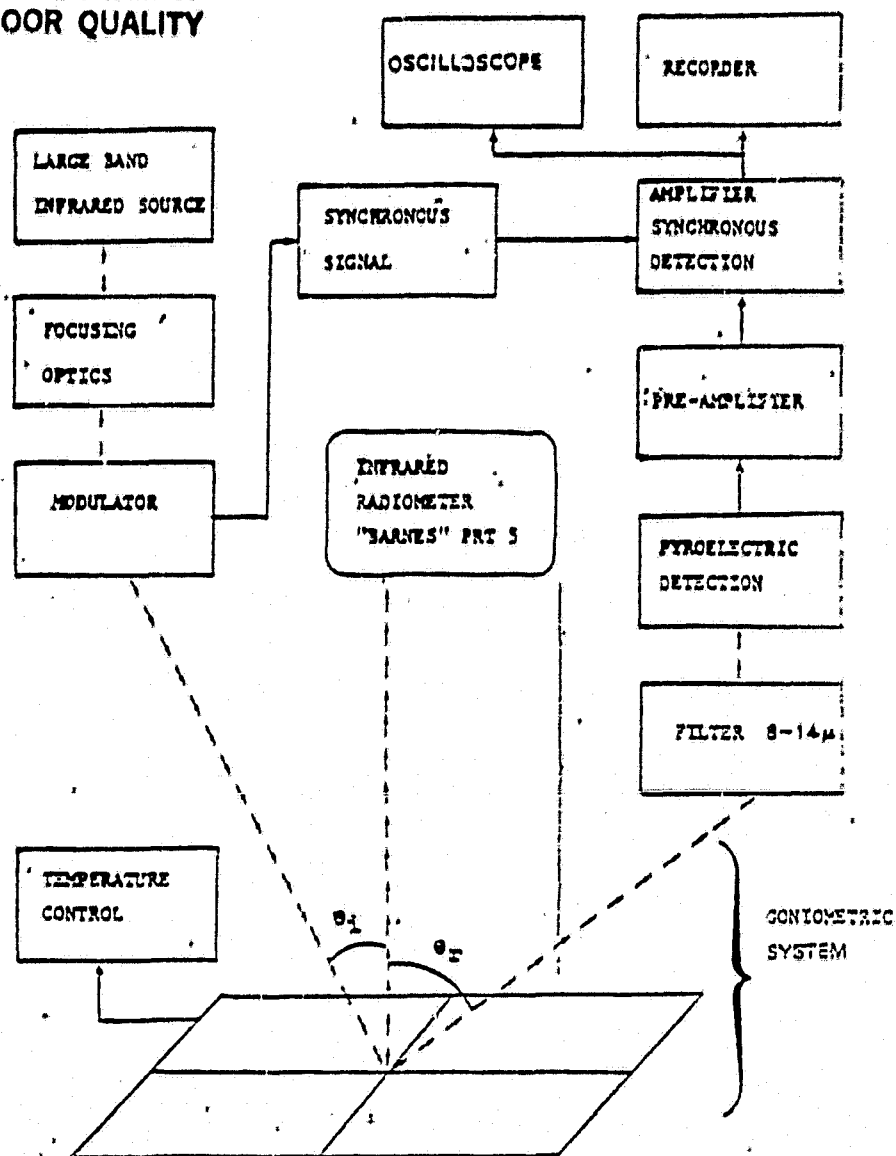


Fig. III.5.20. Schematic diagram of the measuring system.

However, the extrapolation to aircraft and spacecraft remote sensing is not a simple task. There are several problems and we shall discuss two of them which are very important.

The first problem deals with the physics of the measure itself. The proposed method requires in principle an integration of the reflected radiance over the complete upward hemisphere and this is not possible because only backscattering can be measured as in radar techniques. It will be necessary therefore to relate this backscattering to the emissivity. A programme is in progress at Strasbourg to solve this problem. The second problem deals with the instrumentation capabilities. The energy recorded in a given direction will be very small as it can be estimated easily as follows. For a nadir observation of a surface of bidirectional reflectivity ρ_b , the ratio of the recorded to the emitted power can be written:

$$\frac{P_r}{P_s} = \rho_b \frac{d_s d_\omega}{x^2} G \quad (31)$$

where d_s and d_ω are respectively the entrance window area and the IFOV solid angle of the detector, x is the altitude and G an efficiency factor. Values of the ratio P_r/P_s for typical values of the parameters entering formula (31) are given in Table III. 5. 2:

TABLE III.5.2. Some values of the ratio P_r/P_s for aircraft (A) and spacecraft (S) remote sensing (for $G=1$).

Parameter	ρ_b	d_s	d_ω	A	S	$\frac{P_r}{P_s}$ $\frac{A}{S}$
Dry sand	0.048	0.8	$5 \cdot 10^{-4}$	4,000	800,000	1.2 -12 10
Water	0.006	0.8	$5 \cdot 10^{-4}$	4,000	800,000	1.5 -13 10
Grass	0.003	0.8	$5 \cdot 10^{-4}$	4,000	800,000	7.5 -14 10

The threshold of detectivity will not be reached if the source power is not large enough. It will

therefore be necessary to have a powerful well focused source such as a CO_2 laser. We are therefore building a new goniometer with such a laser to have a better understanding of the possible spatial extension. Although it is too early to give a definitive statement concerning its possible extension to aircraft or spacecraft remote sensing, the method which we proposed and used is already in its simple form a powerful and accurate tool for measuring spectral effective emissivities in situ and at low altitudes.

References

1. N. J. BECKER; "Ökologische Kriterien für die Abgrenzung des Rebgebietes in den nördlichen Weinbaugebieten" Die Wein-Wissenschaft, 32 (1977), p. 77-102.
2. W. ENDLICHER; "Zum Temperaturverhalten auf Großterrassen in Strahlungsnächten anhand von Messfahrten, Frostkartierung und Thermalbildern." Die Wein-Wissenschaft, 32 (1977), p. 174-188 & 309.
3. W. ENDLICHER; "Geländeklimatologische Untersuchungen im Weinbaugbiet des Kaiserstuhls". Diss. Geowiss. Fak. Universität Freiburg 1978, 309 pp.
4. R. GEIGER; "The Climate near the Ground", Harvard University Press, Cambridge, Mass. (1965) 611 pp.
5. H. GOSSMANN; "Radiometrische Oberflächen-temperaturmessung und Thermalbild als Hilfsmittel der Umweltforschung". Beihefte Geogr. Rdsch. 7 (1977) p. 101-112.
6. D. LORENZ; "Problems of Airborne Infrared Scanning in Meteorology". Archive Met., Geophys., Bioklim., Ser. B 21 (1973) p. 125-146.
7. J. O. MATTSSON; "Thermal Patterns in the Landscape Recorded with Infrared Technique and Simulated in Model Experiments". Geografiska Annaler, Ser. A 51 (1969) p. 219-238.
8. P. R. NIXON and T. A. HALES; "Observing Cold-Night Temperatures of Agricultural Landscapes with an Airplane-Mounted Radiation Thermometer"; J. Appl. Meteorol., 14 (1975), p. 498-505.
9. R. B. STEWARD, E. I. MUKAMMAL and J. WIEBE; "The Use of Thermal Imagery in Defining Frost Prone Areas in the Niagara Fruit Belt". Remote Sensing of the Environment, 7 (1978), p. 187-202.

3. Data Processing Methods

ORIGINAL PAGE IS
OF POOR QUALITY

A. Digitizing of Grey Levels on Auxiliary Maps

H. Gossmann
Geographisches Institut I der Universität
Freiburg, Deutschland

P. Haberhacker
DFVLR, Institut für Nachrichtentechnik
Oberpfaffenholten, Deutschland

Introduction

The preparation of auxiliary (maps) data to be superimposed to the HCMM data has been obtained by microdensitometric scanning of $6 \times 6 \text{ cm}^2$ slides.

Digitizing of the maps' grey levels has presented considerable difficulties. It proved to be impossible to carry out the digitalization of a grey tone scale with more than two levels in one step. Furthermore, because of vignetting effects, the binary black and white prints also show a strong distortion of the image contents. Using the relief map as an example, the solution of this problem is described below.

Separation of Grey levels for a Relief Map

When it became apparent that the separation of the grey values for the digitalization of the five elevations on the relief map would not be possible, using the available apparatus, the elevations were removed one by one from the

original map according to the strip mask procedure. They are thus represented on the film by black patches. These five photos, to which scanning markers were added, as well as a sixth transparency, which contains only scanning markers, are designated I_1, I_2, I_3, I_4, I_5 and T corresponding to the following legend:

I_1	0 - 200 m
I_2	200 - 400 m
I_3	400 - 700 m
I_4	700 - 1000 m
I_5	> 1000 m
T	scanning markers only.

In the digitalization the most exact coordination of the five images that was possible, was achieved by careful adjustment of each image on the scanning frame, using a magnifying glass and the pass markers. The numerical fields (matrices) thus produced are called $I'_1, I'_2, I'_3, I'_4, I'_5$, and T' . The superposition of any two of the I_i in the interactive colour monitor (COMTAL) of the DIBIAS-system showed that because of smaller fitting errors and a little play in the scanning frame of the digitizer, the digitized elevations levels did not completely fit together. The overlaps and gaps which thus arose have been made visible by colour representation and could be corrected by shifting individual images by one to two pixels. The

necessary shifts correspond to errors in the scanned images of 1/20 mm and 1/10 mm, respectively.

In this way the five digital elevation-images could be joined together to form a map, provided each were already binary. But this is not the case, since even in the scanning of a black and white print far more than just two grey tones will appear in the digitalized image. This is caused by:

- vignetting effects (shadowing on the edges) during the photographic production of the respective copy I_1 ,
- vignetting effects from the digitizing device,
- eclipse- or illumination-effects at the borders of bright and dark.

Because of vignetting, a white background becomes darker towards the edges of the image, but the black elevation representations are also subject to this distortion (Fig.III.5.21a). The threshold, which must be established to produce a binary scene, would therefore be position-dependent. As a corrective measure the digital image T of the completely white transparency T has been used. Since it was produced under the same conditions as the images I_1', \dots, I_5' , T contains the same vignetting-effects (Fig.III.5.21c).

By subtracting the grey values of the image T from those of I_i' , one obtains images I_i'' which are free of vignettes. The equation as $I_i'' = I_i' + 180 - T$ (MM-Module of the DIBIAS-System). Accordingly, the cross section of the image I_1' which appears in Fig.III.5.21b obtains after correction the shape shown in Fig.III.5.21d.

Even after correction of vignetting there remains at the dark-bright edges a gradual transition from white to black (Fig.III.5.21d). Therefore, for the construction of the binary image in each case a threshold value must be estab-

lished which ascribes the grey values in the transition zone to either black or white. If this value becomes too large, then fine white structures disappear in the black environment. The opposite occurs if the threshold value is too small. This threshold value (grey value 144) was ascertained interactively on the monitor screen. Finally, every elevation was characterized by a definite grey value according to the statement

$$I_i'' = g_i \text{ if } I_i'' < 144 \\ \text{otherwise}$$

with the following values for g_i :

Image	Elevation	Characterizing Grey Value g_i
I_1''	0 - 200 m	230
I_2''	200 - 400 m	180
I_3''	400 - 700 m	130
I_4''	700 - 1000 m	80
I_5''	> 1000 m	30

Following this preparation, the five individual images have been merged by the ME-module into a five-channel image and then assembled by the MM-module according to the following formula for forming a relief map with the five elevations in one channel:

$$R = (K1 \text{ NE } 0) * (K2 \text{ EQ } 0) * (K3 \text{ EQ } 0) * \\ (K4 \text{ EQ } 0) * (K5 \text{ EQ } 0) * K1 + (K1 \text{ EQ } 0) * \\ (K2 \text{ NE } 0) * (K3 \text{ EQ } 0) * (K4 \text{ EQ } 0) * \\ (K5 \text{ EQ } 0) * K2 + (K1 \text{ EQ } 0) * (K2 \text{ EQ } 0) * \\ (K3 \text{ NE } 0) * (K4 \text{ EQ } 0) * (K5 \text{ EQ } 0) * K3 + \\ (K1 \text{ EQ } 0) * (K2 \text{ EQ } 0) * (K3 \text{ EQ } 0) * \\ (K4 \text{ NE } 0) * (K5 \text{ EQ } 0) * K4 + (K1 \text{ EQ } 0) * \\ (K2 \text{ EQ } 0) * (K3 \text{ EQ } 0) * (K4 \text{ EQ } 0) * \\ (K5 \text{ NE } 0) * K5.$$

The relief maps which are produced in this way still show gaps (grey value = 0) at the borders between adjoining elevations. These arise during the removal of the eleva-

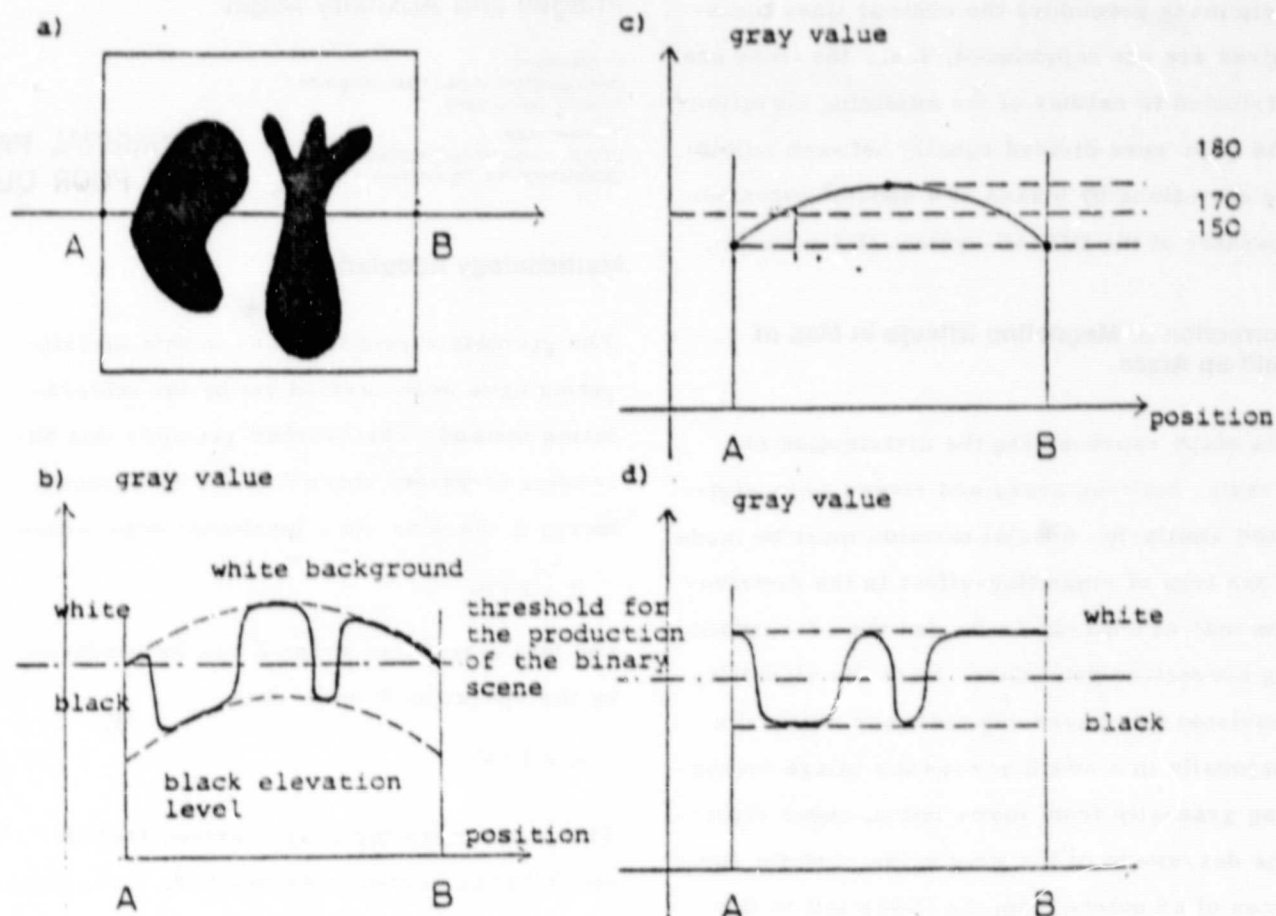


Fig. III.5.21. Sketches representing the suppression of vignetting in digitalized maps prior to the production of a binary scene.

- Because of position-dependent illumination of the image during the photographic production of the image-copy and during scanning undesired light intensity oscillations become evident in the images I_1' .
- Profile of section AB from Fig. III.5.21a in the case of a typical edge-shadowing.
- A section in a completely white image ("vignetting-image" T') corresponding to the profile of section AB in Fig. III.5.21a.
- Result of correction by means of the equation $I'' = I_1' + 180 - T'$ (Subtraction of the vignetting-image from the respective scene and shift of the values into a region of medium grey tones).

ORIGINAL PAGE IS
OF POOR QUALITY

tions from the original map, because with the strip mask procedure the contour lines themselves are not reproduced, i. e., the lines are attributed to neither of the adjoining elevations. The gaps were divided equally between adjoining elevations by means of a special extension operator of the DIBIAS-system (BS-module).

Correction of Magnetizing Effects in Map of Built-up Areas

The maps representing the distribution of forests, built-up areas and rivers were digitized similarly. Special mention must be made of the type of vignetting-effect in the distribution map of built-up areas and the corresponding correction procedure. Here the vignetting consisted in a darkening tendency which ran diagonally in a swath across the image increasing gradually from lower left to upper right. The decrement of the grey value of white surfaces of 25 points from the lower left to the upper right corner has been ascertained by means of microdensitometric sections parallel to the diagonal. By addition of a correction term the grey values have been standardized in the following equation, thus:

$$GR_{\text{new}} = GR_{\text{old}} + (ZE - SP) \cdot 25/ZZ$$

GR = gray value, ZE = line number,
SP = column number, ZZ = number of
lines in the image.

B. Geometric Rectification of HCMM Images and Auxiliary Maps

H. Gossmann
Geographisches Institut der Universität
Freiburg, Deutschland

P. Haberhacker
DFVLR, Institut für Nachrichtentechnik
Oberpfaffenhofen, Deutschland

ORIGINAL PAGE IS
OF POOR QUALITY

Methodology Adopted

The geometric rectifications in this investigation have been carried out by the interpolation method. This method assumes that between a distorted scene V and a reference image R there exists a functional dependence

$$R = F(V)$$

and that a rectified scene E can be produced by the operation F on V, thus

$$E = F(V).$$

The parameters for F are derived from R and V by the control point method, i. e., corresponding control points are sought in the reference image R and the distorted scene V and their respective coordinates are determined in both coordinate systems. This alignment results in a transformation equation, by which all points of the distorted scene can be related to the reference image.

The following symbols will be used in the equation below:

V	distorted scene
$\underline{v} = (v_1, v_2)^T$	position-coordinates of the distorted scene
$g_v(v)$	grey-value of the picture element having these coordinates
R	reference image
$\underline{r} = (r_1, r_2)^T$	position coordinates of the reference image
E	rectified scene
$\underline{x} = (x_1, x_2)^T$	position coordinates of the rectified scene

ORIGINAL PAGE IS OF POOR QUALITY

$g_E(\underline{x})$ gray value of the pixel
 having these coordinates.

The following relationship between the coordinates of the distorted and rectified scenes has been assumed:

$$\begin{aligned} v &= f(\underline{x}), \quad \text{or} \\ v_1 &= f_1(x_1, x_2) \\ v_2 &= f_2(x_1, x_2) \end{aligned}$$

If V is generated from E by means of a projection, then the transformations in x_1 and x_2 are linear (1st-order polynomial):

$$\begin{aligned} v_1 &= A_1 x_1 + A_2 x_2 + A_3 \\ v_2 &= B_1 x_1 + B_2 x_2 + B_3, \quad \text{or} \\ \underline{v} &= C \underline{x} + \underline{d} \end{aligned}$$

with $C = \begin{pmatrix} A_1 & A_2 \\ B_1 & B_2 \end{pmatrix}$ and $\underline{d} = (A_3, B_3)^T$.

For the rectification of satellite scenes a 2nd-order polynomial is often used instead of the linear equation:

$$\begin{aligned} v_1 &= A_1 x_1 + A_2 x_2 + A_3 + A_4 x_1^2 + A_5 x_1 x_2 + A_6 x_2^2 \\ v_2 &= B_1 x_1 + B_2 x_2 + B_3 + B_4 x_1^2 + B_5 x_1 x_2 + B_6 x_2^2. \end{aligned}$$

In order to calculate the unknown A_i and B_i the control points are used. The number of control points p must thereby be equal to the number k of unknown parameters which have to be calculated per transformation. With more control points available ($p > k$), the error which appears in the polynomial approximation of the function can be minimized by means of a least squares method.

By the rectification an appropriate coordinate pair (v_1, v_2) from the distorted scene is connected with the coordinates (x_1, x_2) in the rectified scene in accordance with the above equations. The grey value of this pixel is calculated from the distorted scene.

C. Registration of Night Thermal Data over Day Thermal and Visible Data

J. Dejece, J. Mégier
Laboratory for Image Processing
Commission of the European Communities
Joint Research Centre, Ispra Establishment
Ispra, Italy

Introduction

The MSS data acquired during the JFE aircraft flights of Grendon, UK and Pattensen, Germany, were utilized for a detailed application of the TELL-US model which uses the day and night temperatures T_d and T_n at the same geographical point. Geometrical corrections on the night thermal data are needed to achieve superposition with the day visible-and-thermal data.

Day thermal and visible data are automatically registered for they were acquired during the same flight through the same instrument optics and with the same resolution. Night thermal data acquired during a previous flight, have the same resolution but they must be superposed by software to day data.

Method Used

The problem is to map the grid of night data on the grid of day data. This is obtained by using bivariate polynomials as mapping functions. A pixel with coordinates (x, y) , given by the line and column position in the day data, is thus the transformed element from a pixel with coordinates (u, v) in the night data such that:

$$\begin{aligned} u &= u(x, y) = \sum_{p=0}^N \sum_{q=0}^{N-p} a_{pq} x^p y^q \\ v &= v(x, y) = \sum_{p=0}^N \sum_{q=0}^{N-p} b_{pq} x^p y^q \end{aligned}$$

where u and v are calculated from x and y .

In the present case second order polynomials were chosen. The method uses ground control points which are common to day and night data

to determine the a and b coefficients by least square fitting. The fitting of the ground control points is performed in the untransformed grid (night data), rather than in the transformed grid (day data), as would seem more natural. The latter solution would indeed require to express the (x,y) coordinates as a function of the (u,v) i.e. to reverse the preceding expressions. The calculated (u,v) coordinates will not be generally integer and the nearest neighbour rule is applied to determine the pixel radiometric value. This simple procedure has been preferred in the present case to interpolation or convolution methods, in consideration of the average accuracy of the registration which in any case cannot guarantee less than two pixels.

Referring to the Grendon flight, as the complete strip of data is rather long (more than 4000 lines of 672 pixels), the registration is made for successive blocks of 672×300 points with 50% overlapping: 12 to 20 control points by block determine the respective pair of trans-

formation polynomials. Discontinuities between blocks are avoided by combining with variable weights the coefficients of the polynomials referring to two successive blocks. As the line of data processed moves from the centre of the first block to the centre of the second block, the weights relative to the first pair of polynomials are changed line by line from 1 to 0, the reverse being done for the second pair. The process is then repeated with the second and third blocks and so on.

Results Obtained

They are displayed in Figs. 1 and 2 of Part 1, Chapter 2, p.2.1.. The average registration error between ground control points was found to be 2.3 pixels with minimum 0 and maximum 7 pixels. The average registration error on the other points is not known but is very likely to have a similar value in this case of low order transformation polynomials.

ORIGINAL PAGE IS
OF POOR QUALITY

IV - Conclusions

Conclusions

PRECEDING PAGE BLANK NOT FILMED

The TELLUS project is terminated as NASA/HCM-025 Investigation. It is possible to draw-up, in a sort of wise man's retrospective criticism, a number of considerations about the approach adopted for the single investigation sections and of conclusions on the results obtained. Some thoughts can also be added with regard to the usefulness of day and/or night infrared remote sensors placed on board dedicated space missions such as HCMM.

Evapotranspiration and Soil Moisture

Evapotranspiration (ET) and soil moisture was the item of major interest in TELLUS. The greatest part of Coinvestigators participated in this effort. A systematic approach was adopted for the development and testing of algorithms using remotely sensed radiative temperature and albedo. It was confirmed to have been necessary because it provided the investigation with a deep understanding of the processes involved at the various investigation stages and it was the major premise for the blooming of so many models by the Institutes. All this should have also made it easier to develop some simple statistical empirical correlations for the various application cases. This purpose was only partially fulfilled. As a matter of fact this last phase could be considered referring more appropriately to the post-HCM-025 "continuing investigation phase" formerly announced in the TELLUS proposal. Evapotranspiration and soil moisture mapping was obtained as a result of the methodical Joint Flight Experiment applications on patches of homogeneous nature with regard to crops and soils. Moisture content in the upper soil layer was obtained from the thermal inertia with a tendency to underestimation. Nevertheless for the inhomogeneous soils and the rather dispersed and commixed crops situation such as we have in Western Europe, the relatively poor spatial resolution of HCMM lead to conclude that estimating soil moisture on a large scale does remain for the time being a difficult proposition.

For evaluation of the daily evapotranspiration the night thermal measurement seems to be of little contribution. On the other hand having one daily thermal measurement only shows not to be sufficient for middle Europe. The influence of meteorological variation (surface winds, clouds, cold fronts, etc.) would necessitate 2-3 or more temperature measurements per day. The more favourable meteorological conditions of the Mediterranean area should make future thermal satellites more suitable for evapotranspiration and soil moisture application in the Southern European countries. As a matter of fact a part of the TELLUS research effort was specifically devoted to testing the evapotranspiration algorithms in semi-arid conditions. This was made also in view of some possible extrapolations to the African continent as Commission initiatives in favour of the Developing Countries Associated to the European Community.

From the results obtained in the HCM-025 investigation it appears that the use of crop surface temperatures does not give better local estimate of evapotranspiration than other conventional methods. On a regional scale, HCMM (or similar) satellite day-time surface temperature could be usefully applied to estimates of evapotranspiration. This scale ranges from 1 km^2 to nearly $10^3 - 10^4 \text{ km}^2$, which is the width of the synoptical meteorological network in large

parts of Europe. The corresponding time scale would go from one to about 10 days, according to potential users, who could be found in agronomy (for predicting crop yields and scheduling irrigation) in hydrology (for establishing a regional water balance) and in regional climatology where the latent heat of evaporation is an important factor for the repartition of energy at the surface. These evapotranspiration estimates necessitate the elimination of atmospheric effects. Furthermore, if ET models developed for ground measured surface temperatures are to be employed, satellite measured surface temperatures have to be firmly correlated with these ground measured data. The critical point is a correct evaluation of the "roughness" parameter which has to be defined for each zone. An alternative solution could be seen in establishing some simplified relations directly between ET and satellite measured surface temperature. Encouraging results were obtained. Further experiments covering wide ranges of natural surfaces would be necessary to establish whether a unique set of empirical constants could be used in practice. On the other hand, HCMM day-time thermal images should permit to identify water stressed areas and to delimitate zones of ET by interpolating between the net of ground measuring stations.

Topography, Soils, Land-Use and Meteorology

The HCMM geometric resolution fits the mesoscale surface temperature distribution much better as far as its correlation with topography, soils, land-use and meteorology is concerned. Availability of day, night and day/night difference spatial temperature distribution was an incontestable privilege the HCM-025 investigators enjoyed. No other satellite has provided so far such a rich and diversified amount of thermal data. This was the general conclusion drawn by the Coinvestigators of the second section of TELLUS.

It followed also in this case a systematic approach was beneficial. The three-lines methodology adopted was based on the optical examination of 1) analogically superposed HCMM transparencies to thematic maps and LANDSAT scenes, 2) analogically superposed HCMM computer classifications to thematic maps and LANDSAT scenes, and 3) digital superposed HCMM thermal distributions to corresponding thematic and LANDSAT digital information in a high precision multichannel scene.

Merits and limitations of each different line can be put in evidence easily.

The first method fits well for deduction of physiographic lineaments of large basins only. Its interest resides in the attempt made to establish a logical link between geomorphological, vegetational (and anthropic) aspects of the surface and the buried aspects deduced. This work deserves some more application for its validation. An important point comes out of the confirmation of the different role of day-IR in respect to night-IR: the first appears to give a significant contribution for the characterization of lithological and hydrological structure, whereas the second shows to be of very significant contribution for highly surface saturated zones characterization and shows to be less important for a structural recomposition (relief, morphology).

The second and third method are suited for a more detailed utilization of HCMM data. No geometric/geographical correction was introduced. Utilization of LANDSAT imagery proved to be quite useful for locating pixels zone by zone.

The third method (purely digital superposition of geometric rectified data) looks very promising. The precision obtained is nearly one pixel error. Relief, waterways, forests, population and land-use can be compared with temperature as digital information. From the interpretation of thermal conditions of the various parts of the landscape made on such high-precision merged multichannel scene it resulted that HCMM harboured a surprising abundance of information easy to correlate and/or to be explained through topography, soil multiclass land-use structure at mesoscale. One advantage is that HCMM thermal information can also be numerically correlated with some population and land-use classes by multiple linear regression for statistical evaluations. Using deviations from regression, modification of surface temperature with changing land-use (i.e. cold air reservoirs, cold air streams build) can be detected. From all this one becomes convinced of the importance of having set up a methodology able to evolve numerically a

description of the thermal impact of various parameters on a regional scale and in representing various information spatially on computers. Also in this case the path is pointed out and it appears to be proper to a continuing investigation phase: the introduction of surface temperature as a parameter in heat budget deliberations.

As thermal mapper of day- or night-temperature, HCMM confirms to be more comprehensive than aircraft for studies on a regional scale (better evidence of thermal patterns not observed by irrelevant topographic details, more evidence of dependence of surface temperature on reliefs, contemporary observation of long distance points, etc.).

Calculation of thermal inertia (ATI) pertaining to major land-use classes indicated that major categories can be separated (even forest species appeared to be discriminated). Perhaps this discrimination work would have been more extended over the European test-sites if ATI / ΔT HCMM maps had reached TELLUS Coinvestigators in a due time from NASA. The importance of the role of ATI and the day/night daily temperature difference, ΔT , was so confirmed. From all above points, it should be emphasized that the joint utilization of LANDSAT and HCMM data with the support of thematic maps information demonstrated to be a key-point for the best interpretation of HCMM VIS/IR scenes.

The extension of these correlation studies to airborne applications gave some interesting results. The usefulness of airborne remotely sensed data for the localization of frost prone areas and the monitoring of low altitude breezes was demonstrated. In the first case digital processed thermal imagery appeared to be a very useful tool to delimit vineyard sites liable to cold air damage (until the surface dimension of one terrace). This result could help the wine growing legislation in the European Community which requires a strict delimitation of the area provided for the growing of quality grapes. The precision of this investigative method surpasses by far all other conventional techniques for the mapping of frost hollows.

Anthropogenic Heat Release

The result obtained in third investigation sector confirms the good HCMM satellites' pertinency to the evaluation of anthropogenic heat release on a regional scale. Day- and subsequent night-descriptions of surface temperature distribution appeared to be essential to assessments of thermal daily variability of heat sources on the scene. Spatial and radiometric HCMM's resolution showed to suffice to a good extent.

Application to urban heat-islands to local scale, involving geometric rectification and smoothing of pixel edges gave some results exceeding any expectation. Hotter sub-islands and industrial areas could be recognized. Temperature differences with surrounding rural areas were evaluated. Also in this case, following a suitable satellite data calibration, these data could be used as the necessary input to heat budget evaluations.

HCMM demonstrated to be useful also for detection and monitoring of thermal pollution of large water bodies. It permitted the evaluation of the difference between the temperature at the water discharge point of electricity generation plants and the mean river temperature. In this case some higher resolution satellites as Thematic Mapper should be considered more efficient (better description of the plume temperature gradient).

One of the major problems encountered in using HCMM data consisted in eliminating the effect of atmosphere on the HCMM temperature readings. Some correction methods were introduced but all show to be critical for different reasons (i.e. choice of the reference surface to be homogeneous and the temperature of which should be more accurate than 0.5°C). That confirms that a future suitable correction method should employ signals from two separate IR channels. Calibration of HCMM was the second main concern. One may conclude that the offset of 5.5°C introduced by NASA into the calibration of the HCM radiometer after their first ground check should be cancelled.

The solution of two momentous recurring problems in RS data measurement and interpretation was considered in TELLUS. The first difficulty concerns on-

field measurement of thermal IR emissivities. The active method based on a simple and stable ad hoc instrumentation which was realized is being improved as continuing investigation and it is expected to confirm soon to be a useful and accurate tool.

Having confronted, as mentioned before, the sometimes inadequate HCMM resolution in respect to soils inhomogeneity and crops commixture on the European scene, TELLUS interest was to investigate the informative content of large inhomogeneous pixels by "scaling" from smaller pixels information. Encouraging results were obtained from the simulation methodology adopted, which permits the correlation of different resolution data. This technique deserves further attention for development.

As a final consideration we assert that the TELLUS / HCM-025 coordinated effort provided the JRC and the European Coinvestigators with the privilege of facing unitedly a great deal of new RS. problems, the HCMM opportunity offered them through the National Aeronautics and Space Administration, Goddard Space Flight Center. TELLUS was able to give a solution to some of them, to the extent of saying "yes" or "no" with some indications on how to advance, for others. All this is a reward in itself to the effort produced.

List of TELLUS Newsletters

- TELLUS NEWSLETTER 1.

P. Boissard and Ch. Goillot.
Simulation of HCMM resolution from airborne thermal scanner data.

- TELLUS NEWSLETTER 2.

G. J. A. Nieuwenhuis and W. Klaassen.
Estimation of the regional evapotranspiration from remotely sensed crop surface temperatures.

- TELLUS NEWSLETTER 3.

J. Huygen and P. Reiniger.
A sensitivity analysis of the TERGRA model for the conditions of the Grendon test site (JFE/UK - 1977).

- TELLUS NEWSLETTER 4.

P. Boissard, P. Valéry, P. Belluomo and Ch. Goillot.
Assessing the heat budget at soil level by means of airborne thermography. Preview of HCMM capabilities.

- TELLUS NEWSLETTER 5.

W. Nubler.
Wind-induced microclimatic differences from thermal scanner data.

- TELLUS NEWSLETTER 6.

K. Gilman.
Movement of heat in soils.

- TELLUS NEWSLETTER 7.

W. Endlicher.
Thermal imagery as a tool to delimit vineyard sites liable to cold-air damage.

- TELLUS NEWSLETTER 8.

J. Huygen and P. Reiniger.
A test of the TELL-US Model for the conditions of the Grendon test site (JFE/UK-1977).

- TELLUS NEWSLETTER 9.

G. Maracci.
Comparison of spectral reflectances measured by airborne scanner and on the ground.

- TELLUS NEWSLETTER 10.

B. Marcolongo.
Hydrological interpretation of the first HCMM thermal image of Chesapeake Bay.
G. Gombeer.
Analysis of thermal infrared digital data recorded over Belgium by a heat capacity mapping mission (HCMM) night-pass.

- TELLUS NEWSLETTER 11.

J. Huygen.
Further developments of the TELL-US model:
I. An implicit finite difference scheme for the numerical approximation of the ground heat flux.
II. A simple algorithm for estimating the actual and potential evapotranspiration of vegetated surfaces from one remotely sensed surface temperature near the daily maximum.

- TELLUS NEWSLETTER 12.

H. Gossmann and P. Haberhacker.
Image processing of HCMM thermal images for superposition with other satellite imagery and topographic and thematic maps.

- TELLUS NEWSLETTER 13.

A. Perrier, B. Itier, P. Boissard, C. Goillot, P. Belluomo and P. Valéry.
A study of radiometric surface temperatures: their fluctuations, distribution and meaning. (French; English summary).

- TELLUS NEWSLETTER 14.

G. J. A. Nieuwenhuis.
Influence of the atmosphere on thermal infrared radiation.

- TELLUS NEWSLETTER 15.

M. Menenti.
Defining relationships between surface characteristics and actual evaporation rate.

- TELLUS NEWSLETTER 16.

B. Seguin and V. Petit.
The evaluation of evaporation by infrared thermography: A critical analysis of the measurements on the Crau test site.

- TELLUS NEWSLETTER 17.

H. Gossmann.

The influence of topographic structures on night-time surface temperatures: Evaluation of a satellite thermal image of the Upper Rhine Plain and the Surrounding Highlands.

- TELLUS NEWSLETTER 18.

R. Gombeer.

The comparison of HCMM-satellite registered surface temperatures with ground temperature measurements over Belgium. A calibration study.

H. Gossmann.

A calibration attempt of HCMM scene AA-0034.0213.0.3 of May 26, 1978.

P. Reiniger.

Calibration of HCMM thermal data.

- TELLUS NEWSLETTER 19.

G. J. A. Nieuwenhuis.

Application of HCMM satellite and airplane reflection and heat maps in agrohydrology.

- TELLUS NEWSLETTER 20.

H. Gossmann.

A study of the relation between nighttime surface temperatures and land-use, based on HCMM and Landsat images.

R. Gombeer.

Interpretation of nighttime infrared digital data recorded over Belgium by the Heat Capacity Mapping Mission.

- TELLUS NEWSLETTER 21.

F. Becker, W. Ngai and M. P. Stoll.

An active method for measuring thermal infrared effective emissivities implications and perspectives for remote sensing.

- TELLUS NEWSLETTER 22.

B. Marcolongo and E. Barisano.

Contribution à l'évaluation des potentialités des images thermiques de satellites (HCMM-Explorer 1) pour la déduction d'aspect physiographiques: application à la plaine du Po en Italie du Nord.

(French; English summary).

- TELLUS NEWSLETTER 23.

A. Hubaux and E. Scheffer.

Catalogue of Heat Capacity Mapping Mission (HCMM) data products achieved as part of the TELLUS Project at the Joint Research Centre, Ispra.

- TELLUS NEWSLETTER 24.

Working Group II of the TELLUS Project (P. Reiniger ed.).

Development and test of algorithms for the evaluation of evaporation and soil moisture from remotely sensed surface temperature and albedo.

- TELLUS NEWSLETTER 25.

F. Becker, R. Gombeer, H. Gossmann, G. Maracci, G. J. A. Nieuwenhuis, P. Reiniger, B. Segain, F. Wilmers and U. Wiernt (P. Reiniger ed.)

HCMM satellite data calibration and atmospheric corrections.

Abbreviations

AEM	Application Explorer Mission	JRC	Joint Research Centre, Ispra
AL	After Launch	LAT	Latitude
ATI	Apparent Thermal Inertia	LONG	Longitude
CC	Cloud Coverage	MDPF	Master Data Processing Facility, GSFC Greenbelt
CCT	Computer Compatible Tape	MSS	Multi Spectral Scanner
CEC	Commission of the European Communities, Brussels	MTP	Modulation Transfer Function
CMS Lannion		NASA	National Aeronautics and Space Administration
	Centre d'Etude de Météorologie Spatial, Lannion	NIR	Night Infrared
COI	Co-investigator	NT	Negative Transparency
DIR	Day Infrared	N	Night
DVIS	Day Visible	NER	Noise Equivalent Radiance
D	Day	N/D	Night-Day
DFT	Discrete Fourier Transform	NDN	Night-Day-Night
EC	European Communities	PC	Priority Coverage
EARTHNET		PI	Principal Investigator
	Section of European Space Research Institute, Frascati	PR	Progress Report
ESA	European Space Agency, Paris	PT	Preliminary Test
ETP	Evapotranspiration	PPL	Priority Processing List
GMT	Greenwich Meridian Time	PSF	Point Spread Function
GSFC	Goddard Space Flight Centre, Greenbelt, MD	QL	Quick Look
GDTA	Groupeement pour le Développement de la Télédétection Aérospatiale, Toulouse	RO	Retrospective Order
GT	Ground Truth	SEAL	Simplified Evaporation Algorithm
HCMM	Heat Capacity Mapping Mission	SC	Spacecraft
HCMR	Heat Capacity Mapping Radiometer	SO	Standing Order
HET	HCMM Experimental Team	TD	Temperature Difference
HOMP	Hotine Oblique Mercator Projection	TI	Thermal Inertia
HD	High Density	TN	TELLUS News, JRC Ispra
ET	Evaporation or Evapotranspiration	TNL	TELLUS Newsletter, JRC Ispra
IDTF	Inverse Discrete Fourier Transform	TS	Test Site
IPF	Image Processing Facility	TSC	Test Site Co-ordinator
HDT	High Density Tape	TSG	Test Site Group
ID	Identification	USWCL	U.S. Water Conservation Laboratory, Phoenix, AZ
IR	Infrared	VIS	Visible
IFOV	Instantaneous Field of View	WD	Delegation of the European Communities, Washington
IGN	Institut Géographique National, Paris	WG	Working Group
JFE	Joint Flight Experiment		